

Boma Phoebe Norman

The degradation of gas turbine blade materials and additively manufactured Alloy 625 in high temperature CO_2 environments

Cranfield University
Centre for Energy Engineering

PhD
Academic Year: 2021 - 2025

Supervisors: Andrew Potter
Associate Supervisor: Joy Sumner, Nigel Simms and Stefano Mori
July 2025



Centre for Energy Engineering
Energy and Power

PhD

Academic Year 2021 - 2025

Boma Phoebe Norman

The degradation of gas turbine blade materials and additively manufactured Alloy 625 in high temperature CO_2 environments

Supervisor: Andrew Potter
Associate Supervisor: Joy Sumner, Nigel Simms and Stefano Mori
July 2025

This thesis is submitted in partial fulfilment of the requirements for the degree of Energy and Power

© Cranfield University 2025. All rights reserved. No part of this publication may be reproduced without the written permission of the copyright owner.

Academic integrity declaration

I declare that:

- the thesis submitted has been written by me alone.
- the thesis submitted has not been previously submitted to this university or any other.
- that all content, including primary and/or secondary data, is true to the best of my knowledge.
- that all quotations and references have been duly acknowledged according to the requirements of academic research.

I understand that to knowingly submit work in violation of the above statement will be considered by examiners as academic misconduct.

Abstract

The need for a cleaner and more efficient method of electricity production has gained significant attention. The Allam cycle is a highly recuperated Brayton cycle that utilises supercritical (sCO_2) under conditions exceeding 760°C and 30 MPa, and presence of contaminants such as SO_2, H_2O, and N_2. The selection and durability of materials remain a critical concern. The influence of these impurities in sCO_2 environments, or how manufacturing techniques like traditional or additive manufacturing (AM), laser powder bed fusion (LPBF), affect oxidation behaviour, is not fully explored.

This thesis examines the high-temperature oxidation behaviour of nickel-based superalloys under Allam cycle conditions at atmospheric pressure, focusing on the effects of impurities, manufacturing techniques (LPBF), and surface conditions. Isothermal oxidation tests were conducted at 800°C in controlled gas environments. These included CO_2 + 2.7 mol% H_2O + 1.43 mol% N_2 + 0.17 mol% O_2 + 300 ppm SO_2 and CO_2 + 2.7 mol% H_2O + 0.17 mol% O_2. Contaminants degrade protective oxide scales, leading to internal oxidation and nitridation. Chromia-forming alloys, Rene 80 and IN738, exhibited accelerated mass gain and oxide breakdown, whereas alumina-forming alloys, CM247 and Marm247, demonstrated enhanced oxidation resistance. Thermal barrier coatings (TBCs), comprising YSZ and a bond coat system on CM247, provided further protection by limiting the ingress of reactive species and promoting the formation of stable thermally grown oxides.

Surface condition affects oxidation in LPBF Alloy 625. Polished, solution-treated samples had better chromia scales and lower oxidation rates than as-built or rough surfaces. Both polished and as-built samples, including wrought, formed chromia and Nb- and Mo-rich phases. Solution-treated LPBF showed improved resistance due to microstructure, leading to stable oxide layers and fewer ridge-like features compared to as-built. Although wrought alloy developed a thicker oxide, LPBF's slower-growing oxide indicates potential for long-term durability.

Keywords: Oxidation, Additive manufacturing, impurities, surface roughness, nickel-based superalloys.

Acknowledgements

They say it takes a village, and it truly does. I'm grateful to everyone who contributed to my PhD and journey. I wish to thank Joy Sumner, Nigel Simms, Andrew Potter, and Stefano Mori. To the friends I've made along the way, thank you for being part of the overall experience. Lastly, a shoutout to my parents, because without them, I wouldn’t be here to write this.

Table of Contents

Academic integrity declaration i
Abstract 1
Acknowledgements 3
List of Figures 7
List of Tables 12
List of Equations 14
List of Abbreviations 15
1 Introduction 17
1.1 Background 20
1.2 Research Challenges and current state of the art 23
1.3 Aim and Objectives 25
1.4 Scope of study 27
1.5 Significance of research 28
1.6 Contribution to knowledge 29
1.6.1 Conference presentation 29
1.6.2 Publications 30
1.7 Thesis Structure 31
2 Literature Review 32
2.1 Introduction 32
2.2 Power cycles 33
2.2.1 Brayton Cycle 35
2.2.2 Supercritical carbon dioxide (sCO_2) power cycles 39
2.3 sCO_2 Brayton Cycle 42
2.3.1 Configuration of CO_2 power cycles 42
2.4 Current state of the art of sCO_2 cycle 47
2.5 Application and advantages of sCO_2 cycles 48
2.5.1 Challenges 52
2.6 Materials in high temperature sCO_2 54
2.6.1 Superalloys 55
2.6.2 Additive Manufacturing 63
2.6.3 Failure mechanisms in extreme conditions 70
2.6.4 Protective treatments 80
3 Experimental procedures and microstructural analysis 82
3.1 Experimental approach 82
3.1.1 Rationale and significance of the testing approach 83
3.2 Experimental Procedures 85
3.2.1 Material selection 85
3.2.2 Preparation Prior to Exposure 87
3.2.3 Testing 89
3.2.4 Post-exposure 90

3.3 Characterization Techniques 92
3.3.1 Optical microscopy 92
3.3.2 Scanning Electron Microscopy (SEM) & Energy Dispersive X-ray Spectroscopy (EDX) 94
3.3.3 Electron probe microanalysis (EPMA) 97
4 Paper 1: Corrosion of Potential First Stage Blade Materials in Simulated Supercritical CO_2 99
4.1 Introduction 100
4.2 Experimental 102
4.2.1 The materials systems 102
4.2.2 Exposure procedure 103
4.3 Results and discussion 104
4.3.1 Average weight change 104
4.4 Conclusion 112
5 Paper 2 : Comparison of the Oxidation Behaviour of Wrought and Additively Manufactured Alloy 625 in a 113
5.1 Introduction 114
5.2 Materials and exposure procedure 119
5.2.1 Materials 119
5.2.2 Pre-exposure treatment of samples 120
5.2.3 High temperature exposure of samples 121
5.3 Effect of manufacturing technique on the oxidation behaviour 122
5.4 Effect of Heat Treatment on the Oxidation Behaviour 129
5.5 Conclusions 133
6 Paper 3 : Influencing Effect of Surface Roughness on the Oxidation and Carburization behaviour of Laser Powder Bed Fusion (LPBF) Alloy 625 in a Simulated High Temperature Allam Cycle Environment 135
6.1 Introduction 136
6.2 Experimental procedure 139
6.2.1 Material system 139
6.2.2 High temperature testing 141
6.2.3 Analysis 142
6.3 Results and discussion 142
6.3.1 Mass change results 142
6.3.2 Dimensional metrology 146
6.3.3 Analysis the effect of roughness on the Oxidation and carburization behaviour 147
6.4 Conclusion 153
7 Paper 4: Effect of Nitrogen and Sulphur on the oxidation of Rene 80 in a high temperature CO_2 environment. 154
7.1 Introduction 156
7.2 Materials and Methods 158

7.3 Results and discussion 160
7.3.1 Mass change 160
7.3.2 Dimensional metrology assessment of metal loss 162
7.3.3 Microstructural analysis 164
7.4 Conclusion 171
8 Discussion 173
9 Conclusion 185
9.1 Limitations and Future Work 187
References 189
Appendix A Ethical approval letter 226

List of Figures

Figure 1-1 - Electricity demand in selected regions from 1991 – 2025 [2] 17

Figure 1-2 - Global energy generation by source from 2014 – 2025 [2] 18

Figure 1-3 - Generation and demand of UK's electricity 2024 [4] 18

Figure 1-4 - Turbine inlet temperature vs thermal efficiency of various power conversions [12] 21

Figure 2-1 - Classification of thermodynamics 33

Figure 2-2 - Open cycle gas turbine [46] 36

Figure 2-3 - Closed Brayton cycle [46]. 37

Figure 2-4 - Schematic P-T phase diagram of CO_2 41

Figure 2-5 - Recuperated closed-loop Brayton cycle [61] 43

Figure 2-6 - Recuperated recompression closed-loop Brayton cycle [61] 44

Figure 2-7 - Semi-closed direct oxyfuel Brayton Cycle [61] 45

Figure 2-8 - Schematic of a commercial scale natural gas Allam cycle [17] 46

Figure 2-9 - Comparison of Echogne's 10MWe sCO_2 power turbine compared to a 10 MWe steam turbine [67] 49

Figure 2-10 - Categories of elements important to the constitution of nickel-based superalloys, and their relative positions in the periodic table[74] 58

Figure 2-11 - Approximate temperature time transformation diagram of Alloy 625 62

Figure 2-12 - ASTM classification of AM 64

Figure 2-13 - Processing steps of converting 3D CAD to 3D AM object 66

Figure 2-14 - Schematic of LPBF technique 67

Figure 2-15 - Failure analysis, the role of understanding a material's property [123] 70

Figure 2-16 - Schematic diagram of the cross-section of an oxide layer formed on the surface of an alloy 71

Figure 2-17 - Wagner's Model of Oxidation [110] 72

Figure 2-18 - Ellingham-Richardson diagram [110] 74

Figure 3-1 - Pre-exposure steps 87

Figure 3-2 - Photographs of samples after grinding and polishing LPBF Alloy 625 88

Figure 3-3 - Before exposure images of samples. 88

Figure 3-4 - schematic of furnace [154] 89

Figure 3-5 - Demonstration of dimension metrology [156] 92

Figure 3-6 - Cross-sectional dimension metrology of a metal sample after exposure 93

Figure 3-7 - Schematic of scanning electron microscope [158] 94

Figure 3-8 - X-ray generation process [159] 96

Figure 3-9 - Schematic of EPMA [163] 98

Figure 4-1- Principles of a power conversion system [61] 101

Figure 4-2 - Various power conversion efficiencies [61] 101

Figure 4-3 - Simple schematic of a furnace [154] 104

Figure 4-4 - Averaged weight change plot showing mass change vs exposure time for test 1 and 2;(a) Metal change for 800 ^{o}C /1 bar /CO_2 + 2.7 mol% H_2O +0.17 mol% O_2 and (b) Metal change for (b) 800 ^{o}C /1 bar /CO_2 + 1.43 mol% N_2 +0.17 mol% O_2 + 300 ppm SO_2 105

Figure 4-5 - Dimensional metrology for tests (a) 1 and (b) 2 106

Figure 4-6 - SEM micrographs of CM247. (1), (2) and (3) represent the unexposed samples of CM247, CM247+SC2464, and CM247+SC2464+8YSZ respectively. (a) and (b) CM247 at 1000h for test 1 and 2 respectively, (c) and (d) CM247+SC2464 at 1000h for test 1 and 2 respectively whilst (e) and (f) CM247+SC2464+8YSZ at 1000h for test 1 and 2 respectively 107

Figure 4-7- Backscattered and EDX maps for test 1 exposed for 1000h. (a) CM247, (b) CM247+SC2464, and (c) CM247+SC2464+8YSZ 109

Figure 4-8 - Backscattered and EDX maps for test 2 exposed for 1000h (a) CM247, (b) CM247+SC2464 and (c) CM247+SC2464+8YSZ 111

Figure 5-1 - Weldability diagram of nickel-based superalloys with IN625, an Alloy 625 variant, highlighted [191] 117

Figure 5-2 - Images of as-built (AB), solution heat treated (SH) and wrought manufactured (WM) samples before exposure 121

Figure 5-3 - Mass change plot of as-built (AB), solution heat treated (SH) AM and wrought manufactured (WM) Alloy 625 exposed at 800ºC for up to 1000h. Error bars indicate the maximum and minimum values from up to 5 samples. 122

Figure 5-4 - BSE SEM micrographs of polished (a) AM as-built (b) AM solution heated (c) Wrought Alloy 625 after 1000h exposure in CO_2 + 2.7mol% H_2O

+ 1.43mol% N_2 + 0.17mol% O_2 + 300ppm SO_2 at 800°C. Samples have been electrolytically etched in 10% oxalic acid at 4V for 4 seconds 124

Figure 5-5 - Wrought Manufactured Alloy 625 exposed after 1000h oxidation in CO_2 + 2.7mol% H_2O + 1.43mol% N_2 + 0.17mol% O_2 + 300ppm SO_2 at 800°C 126

Figure 5-6 - SEM/EDX maps of as-built AM Alloy 625 after 1000h oxidation in CO_2 + 2.7mol% H_2O + 1.43mol% N_2 + 0.17mol% O_2 + 300ppm SO_2 at 800°C 127

Figure 5-7 - Etched EDX image of solution heated AM Alloy 625 exposed for 1000h in CO_2 + 2.7mol% H_2O + 1.43mol% N_2 + 0.17mol% O_2 + 300ppm SO_2 at 800°C then electro-etched in 10% oxalic acid. 128

Figure 5-8 - SEM images of as-built and solution heat treated LPBF and wrought Alloy 625 after 1000h oxidation in CO_2 + 2.7mol% H_2O + 1.43mol% N_2 + 0.17mol% O_2 + 300ppm SO_2 at 800°C 129

Figure 5-9 - As-built LPBF Alloy 625 after 1000h exposure in CO_2 + 2.7mol% H_2O + 1.43mol% N_2 + 0.17mol% O_2 + 300ppm SO_2 at 800°C 131

Figure 6-1 - Schematic of furnance 142

Figure 6-2 - Mass change plot of Alloy 625 samples with 3 roughnesses exposed in CO_2 with contaminants for 1000h at 800°C..... 143

Figure 6-3 - Etched SEM images of Alloy 625 at x1500 magnification. Solution heat-treated LPBF (a) as-received (b) P600 grit (c) polished exposed in CO_2 + 2.7mol% H_2O + 1.43mol% N_2 + 0.17mol% O_2 + 300ppm SO_2 for 1000h at 800°C 145

Figure 6-4 - SEM images of Alloy 625 at x4500 magnification. Additive manufacturing of (a) as-received (b) P600 grit (c) polished exposed in CO_2 + 2.7mol% H_2O + 1.43mol% N_2 + 0.17mol% O_2 + 300ppm SO_2 for 200h at 800°C 145

Figure 6-5 - Dimensional metrology of (a) as-received (b) P600 grit (c) polished exposed in CO_2 + 2.7mol% H_2O + 1.43mol% N_2 + 0.17mol% O_2 + 300ppm SO_2 for 1000h at 800°C. 147

Figure 6-6 - SEM images of Additive manufacturing of (a) as-received (b) P600 grit (c) polished and exposed in CO_2 + 2.7mol% H_2O + 1.43mol% N_2 + 0.17mol% O_2 + 300ppm SO_2 for 1000h at 800°C. 148

Figure 6-7 - As-received depth profile of as-received Alloy 625 exposed in CO_2 + 2.7mol% H_2O + 1.43mol% N_2 + 0.17mol% O_2 + 300ppm SO_2 for 1000h at 800°C 149

Figure 6-8 - P600 profile of alloy 625 exposed in CO_2 + 2.7mol% H_2O + 1.43mol% N_2 + 0.17mol% O_2 + 300ppm SO_2 for 1000h at 800°C 150

Figure 6-9 - 6µm polished solution heat-treated alloy 625 Line scan exposed in CO2 + 2.7mol% H2O + 1.43mol% N2 + 0.17mol% O2 + 300ppm SO_2 for 1000h at 800°C..... 150

Figure 6-10 - EDX map of AM solution heat-treated as-received Alloy 625 exposed in CO_2 + 2.7mol% H_2O + 1.43mol% N2 + 0.17mol% O_2 + 300ppm SO_2 for 1000h at 800°C. 151

Figure 6-11 – EDX maps of AM solution heat-treated P600 grit alloy 625 exposed in CO_2 + 2.7mol% H_2O + 1.43mol% N_2 + 0.17mol% O_2 + 300ppm SO_2 for 1000h at 800°C..... 152

Figure 6-12 - EDX map of AM polished solution heat-treated Alloy 625 exposed in CO_2 + 2.7mol% H_2O + 1.43mol% N_2 + 0.17mol% O_2 + 300ppm SO_2 for 1000h at 800°C..... 152

Figure 7-1 - Schematics of vertical controlled-atmosphere furnace for oxidation testing..... 159

Figure 7-2 - Mass change plot of Rene 80 in test 1: 800°C/CO_2 + 2.7 mol% H_2O +0.17 mol% O_2 and test 2: 800°C/CO_2 + 1.43 mol% N_2 +0.17 mol% O_2 + 300 ppm SO_2. Error bars show the max and min value of mass change of samples in the same time interval..... 160

Figure 7-3 - Mass change vs square root of time showing the parabolic behaviour of Rene 80 exposed in test 1 and test 2 environment..... 161

Figure 7-4 - Rene 80 cumulative probability plot in test 1: 800°C/CO_2 + 2.7 mol% H_2O +0.17 mol% O_2..... 162

Figure 7-5 - BSE SEM images of Rene 80 in in test1: 800°C/CO_2 + 2.7 mol% H_2O +0.17 mol% O_2 and test 2: 800°C/CO_2 + 1.43 mol% N_2 +0.17 mol% O_2 + 300 ppm SO_2 + 2.7 mol% H_2O..... 165

Figure 7-6 – BSE and EDX map of Rene 80 after 1000h exposure in test 1 800°C/CO_2 + 2.7 mol% H_2O +0.17 mol% O_2 166

Figure 7-7 – EDX map of Rene 80 after 1000h exposure in t2: 800°C/CO_2 + 1.43 mol% N_2 +0.17 mol% O_2 + 300 ppm SO_2 + 2.7 mol% H_2O 167

Figure 7-8 - EPMA maps of Rene 80 after 400h exposure in test 1 800°C/CO_2 + 2.7 mol% H_2O +0.17 mol% O_2..... 167

Figure 7-9 - EPMA maps of Rene 80 after 400h exposure in test 2 800°C/CO_2 + 1.43 mol% N_2 +0.17 mol% O_2 + 300 ppm SO_2 + 2.7 mol% H_2O..... 168

Figure 7-10 - EPMA maps of Rene 80 after 1000h exposure in test 2 800°C/CO_2 + 1.43 mol% N_2 +0.17 mol% O_2 + 300 ppm SO_2 + 2.7 mol% H_2O 169

Figure 8-1 - Mass change plot of test 1, CO_2 + 2.7 mol% H_2O + 0.17 mol% O_2 173

Figure 8-2 - Mass change plot of test 2, 800°C/CO_2 + 1.43 mol% N_2 +0.17 mol% O_2 + 300 ppm SO_2 + 2.7 mol% H_2O 174

Figure 8-3 - BSE images of CM247, IN738, IN939, MARM247, PWA1480 exposed in test 1, CO_2 + 2.7 mol% H_2O + 0.17 mol% O_2 and test 2 environment and test 2 , 800°C/CO_2 + 1.43 mol% N_2 +0.17 mol% O_2 + 300 ppm SO_2 + 2.7 mol% H_2O 175

Figure 8-4 - Wrought IN625, additive manufactured (b) as-received, as built (c) 600-grit size as built (d) polished as-built (e) as-received, solution heated (f) 600-grit size solution heated (g) polished solution heated. 180

Figure 8-5 - Wrought Alloy 625 after 1000h exposure 183

List of Tables

Table 2-1 - Various samples and state processes [43] 34

Table 2-2 - Difference between open and closed cycle [47] 38

Table 2-3 - Properties of various fluids [49] 40

Table 2-4 - Applications for sCO_2 for power generation 50

Table 2-5 - Key components and challenges faced 54

Table 2-6 - Effect of addition of elements on Ni-based superalloys 56

Table 2-7 - Comparison of CM247 and MARM 247 elementary composition 59

Table 2-8 - Comparison of some AM technologies adopted from [96] 65

Table 3-1 - Nominal elementary composition using EDX (wt.%) 85

Table 3-2 - IN625 AM process specification 86

Table 3-3 - Nominal Composition of Alloy 625 87

Table 3-4 - Test design and materials investigated in this thesis. 90

Table 4-1 - Composition based on EDX outputs (wt.%) [173] 102

Table 4-2 - K_p Values where the exposure time was 1000h (Units are $mg^2/cm^{-4}.s^{-1}$) 106

Table 4-3 - EDX analysis composition of CM247exposed for 1000h in test environment 1(wt.%) (C excluded from analysis) 108

Table 4-4 - Elemental composition of CM247 in test environment 2 (wt.%). Note that this data has been corrected to exclude carbon from all spectra 110

Table 5-1 - Sample codes 119

Table 5-2 - Chemical composition of alloys, AM powder composition measured using LECO-ICM XP and WM composition obtained from SEM for Alloy 625 samples 120

Table 5-3 - K_p value of as-built, solution heat treated and wrought manufactured Alloy 625 over 1000h exposure 123

Table 5-4 - ASTM E112 grain size analysis 125

Table 5-5 - Point analysis of as-built LPBF Alloy 625 after 1000h exposure in CO_2 + 2.7mol% H_2O + 1.43mol% N_2 + 0.17mol% O_2 + 300ppm SO_2 at 800°C 132

Table 6-1 - Manufacturing specification of AM Alloy 625 139

Table 6-2 - Sample codes for AM Alloy 625 samples with various surface roughnesses as determined by laser profilometer. 140

Table 6-3 - Chemical composition of AM alloy 625, obtained using LECO – ICM. 141

Table 6-4 - Kp value of Alloy 625 with variation in surface roughnesses..... 144

Table 7-1 - Elementary composition of Rene 80 .wt%[247]..... 158

List of Equations

Equation 2-1 72
Equation 2-2 72
Equation 2-3 72
Equation 2-4 72
Equation 2-5 75
Equation 2-6 77

List of Abbreviations

AM	Additive Manufacturing
ASTM	American Society for Testing and Materials
BC	Bond Coat
TBC	Thermal Barrier Coating
CO_2	Carbon Dioxide
sCO_2	Supercritical Carbon Dioxide
SO_2	Sulphur Dioxide
N	Nitrogen
GHG	Greenhouse Gas (GHG)
CAD	Computer-Aided Design
SLS	Selective Laser Sintering
EBM	Electron Beam Melting
SLM	Selective Laser Melting
SLS	Selective Laser Sintering
LMD	Laser Metal Deposition
LPBF	Laser Powder Bed Fusion
WM	Wrought manufacturing
SR	As-received Solution Heated
SEM	Scanning Electron Microscope
EDX	Electron Dispersive X-ray
TGO	Thermally Grown Oxide
ODP	Ozone Depletion Potential
TP	Triple Point
STEP	Supercritical Transformation Electric Power
SWRI	Southwest Research Institute
RCBC	Recompression Brayton Cycle
HP	High Pressure
MP	Medium Pressure
LP	Low Pressure

TP	Triple Point
SCFs	Supercritical Fluids
SCBC	Simple Closed Brayton Cycle
CSP	Concentrated Solar Power
DS	Directionally Solidified
FCC	Face Centred Cubic

1 Introduction

Globally, the rise of industrialization has subsequently led to the production of electrical energy as the major driver of environmental pollution and the main cause of carbon dioxide emissions, as well as other greenhouse gases [1]. This is because fossil fuel combustion is still being extensively used to meet energy demand growth, especially in China and India, as seen in Figure 1-1, an important aspect of a productive economy.

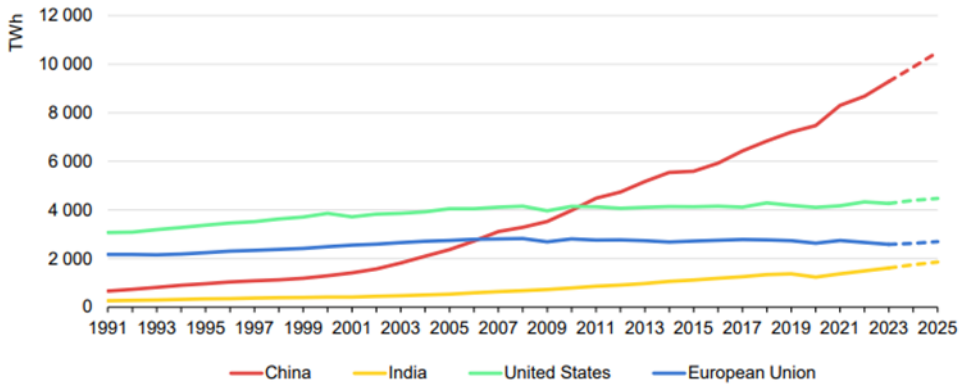


Figure 1-1 - Electricity demand in selected regions from 1991 – 2025 [2]

Since the surging growth in demand in countries such as China and India, burning of fossil fuels for generation also rose in 2024 to meet the demand. Figure 1-2 shows the global energy source by generation with 2024 and 2025 forecasts. Since 2020, the electricity demand has increased globally, and some parts of the world have relied more on the combustion of fossil fuels to meet this demand.

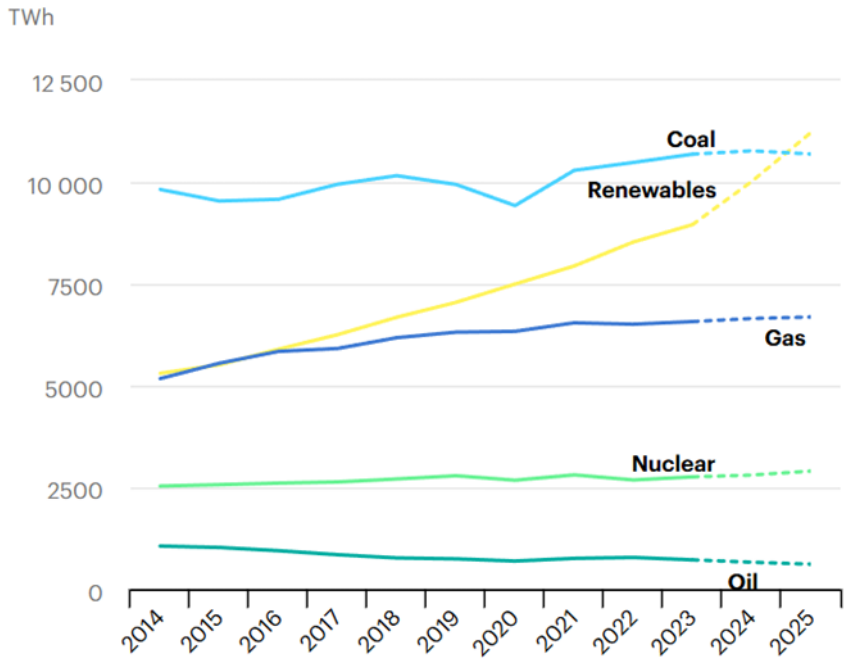


Figure 1-2 - Global energy generation by source from 2014 – 2025 [2]

Focusing on the UK generation of electricity shown in Figure 1-3, the burning of fossil fuel plays a major role of 28.9% in meeting demand. As turbine systems play a critical role in power generation, there has been a growing necessity to improve the efficiency to enhance overall plant performance. This drive is tied to reducing GHG emissions, lower operational costs, and overall improving plant efficiency [3].

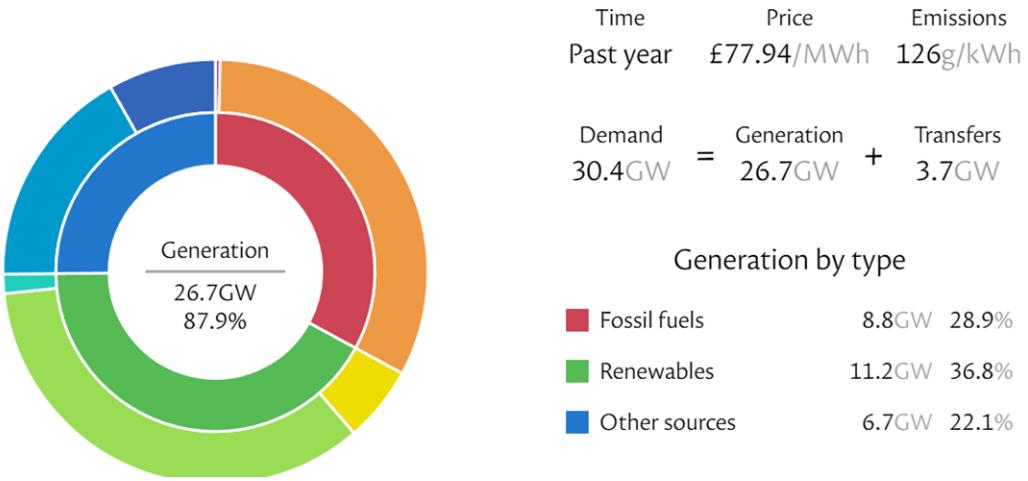


Figure 1-3 - Generation and demand of UK's electricity 2024 [4]

Increasing electricity demand has raised the importance of more sustainable energy sources. Minimizing environmental impacts while providing affordable, reliable, and sustainable energy services that support social and economic development is essential. This entails delivering energy in an environmentally friendly manner while maintaining security and affordability.

The present-day power generation challenges necessitate that specific objectives must be achieved in gas turbine development, including but not limited to:

1. Enhanced availability and durability.
2. Heightened overall efficiency.
3. Minimization of environmental impact
4. Reduced initial investment and maintenance cost.

One route towards improving gas turbine efficiency involves increases in the operating temperature and pressure. To achieve this, researchers and developers have postulated that supercritical carbon dioxide (sCO_2) can be used as the turbine working fluid. To this end, a demonstrator power plant using sCO_2 is currently being developed in Texas, USA.

sCO_2 power cycles offer an innovative way to improve the thermal efficiency of gas turbine systems, while potentially enhancing sustainability through the integration of carbon capture technology. The increase in thermal efficiency is estimated to be between 50% and 60% compared to conventional steam or gas cycles. Such improvements could be significant for the UK's goals to boost energy efficiency and meet climate targets [8,9]. However, the extreme operating conditions, i.e., high temperatures (up to 800°C), pressures (300 bar) [10], and a novel CO_2 working fluid, may accelerate material degradation in key components such as turbine blades, vanes, and heat exchangers, potentially shortening their lifespan [9]. This is critical, as the UK heavily depends on gas turbines to balance intermittent renewable energy sources [8]. The degradation behaviour also affects cost-effectiveness, since more frequent component failures would raise

maintenance costs and undermine the economic advantages of sCO_2 systems [9]. As the UK strives for net-zero emissions by 2050, understanding and mitigating degradation in sCO_2 systems is essential for developing sustainable and reliable energy solutions.

This research aims to investigate these challenges through the exploration of the degradation behaviour in CO_2 environments of both conventionally manufactured and AM-fabricated nickel-based superalloys. This thesis is composed of paper-based contributions presented in Chapters 4 through 8.

1.1 Background

Various modified conventional thermodynamic power cycles, as well as innovative alternative power cycles, have been proposed to achieve sustainable energy generation [5–7]. sCO_2 is currently being investigated as an alternative working fluid to conventional fluids in clean technologies as it achieves higher thermal efficiencies.

Numerous researchers have proposed the adaptation of sCO_2 Brayton cycle as a promising solution for power generation, offering various advantages across a range of applications, including fossil fuels, waste heat [8,9], solar [10], biomass [11], and nuclear energy. The advantages sCO_2 offers include higher cycle efficiencies, reducing emissions, compact turbomachinery (leading to a smaller plant footprint and quicker response to load changes), minimised water use, and heat source flexibility. These benefits make sCO_2 power cycles suitable for a wide range of power applications, including gas and coal-fired power plants, industrial waste heat recovery [9] ship propulsion and nuclear power [11].

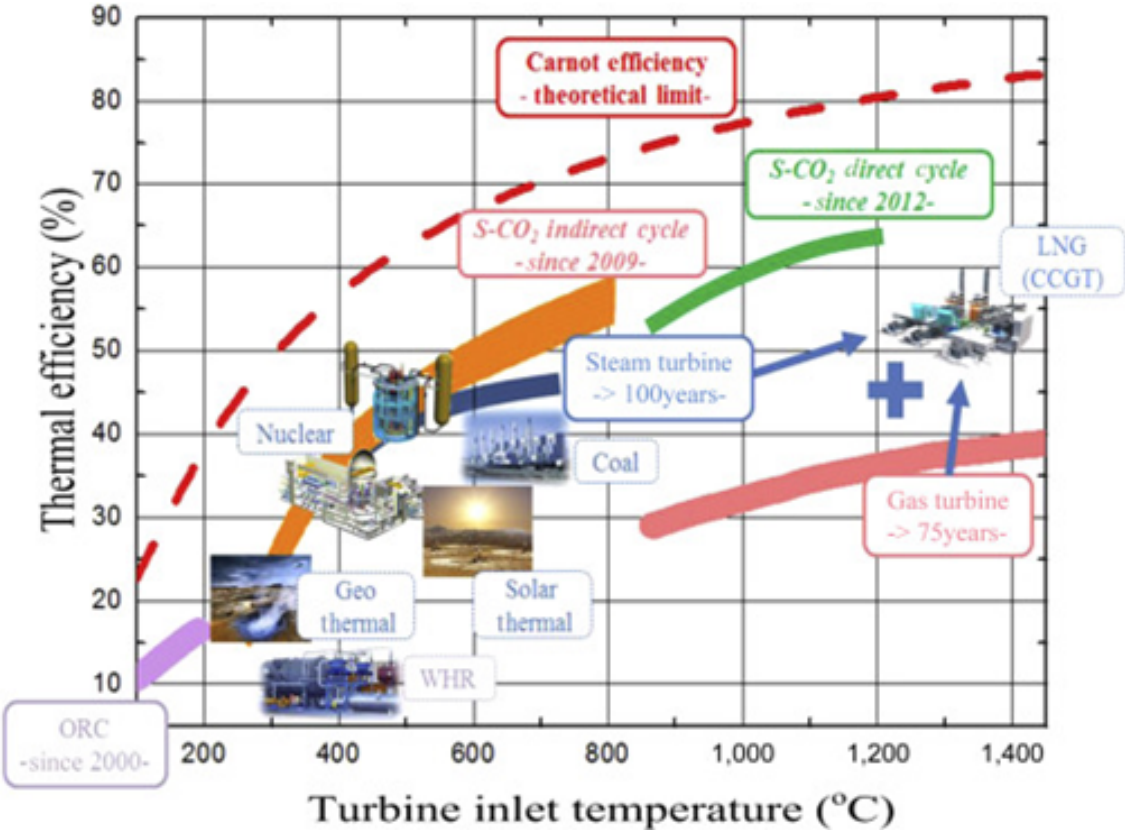


Figure 1-4 - Turbine inlet temperature vs thermal efficiency of various power conversions [12]

Traditional power cycles, including natural gas combined cycle (NGCC), supercritical coal-fired steam cycles [13], and combined cycle gas turbines combined cycles (CCGT), necessitate the use of costly equipment to capture and reduce emissions of CO_2 and other pollutants, often at the expense of efficiency shown in Figure 1-4. Studies on these cycles indicate that incorporating CO_2 removal systems can raise electricity production costs by 50% to 70%, while typically capturing around 90% of the CO_2 produced from burning hydrocarbon fuels. The Allam cycle has been postulated as a potential approach to minimising emissions through the employment of oxy-combustion and high-pressure supercritical CO_2 working fluid in a highly recuperated cycle [14]. This study centres on the Allam cycle, a process patented by Rodney Allam in 2013 [15], that offers a potential pathway to a sustainable energy future through improved efficiency and cleanly utilizing hydrocarbon energy resources while inherently capturing combustion-derived CO_2 for sequestration or reuse. This has a

significant advantage over traditional systems that do not capture high pressure CO_2. It achieves a 59% LHV efficiency, comparable to the best NGCC power plants, and offers much higher efficiencies than modern coal plants, which reach up to 51% LHV. The cycle operates with a single turbine which has an inlet pressure of approximately 300 bar and a pressure ratio of 10, with turbine operating above 700°C [16].

The Allam cycle can utilize a wide range of hydrocarbon fuels, such as natural gas, raw and sour natural gas streams with H_2S and CO_2, as well as gasified solid fuels such as coal, oil refining residues, and biomass [17]. These fuel sources typically have impurities such as H_2O, COS, CS_2, NH_3, H_2S, and HCN, which, when combusted, are converted to SO_2, NO, H_2O, and N_2.

Understanding material degradation in sCO_2 power cycles is essential for the energy sector, particularly in the shift towards efficient, low-carbon energy systems. This knowledge also plays a key role in facilitating the selection of suitable materials for these advanced systems. Materials selection for turbomachinery is a complex process that entails a careful balance of costs, material properties, fabrication ease, and availability [18]. Superalloys are a family of materials that have great mechanical strength, creep resistance, surface stability, and oxidation and corrosion resistance [19]. These characteristics make superalloys suitable to be in high-temperature applications [19,20]. Nickel-based superalloys are widely used in gas turbine engine components for land-based power production and aviation propulsion operating at elevated temperatures and pressures [21]. This widespread application is largely due to their exceptional resistance to harsh conditions, combined with excellent high-temperature mechanical strength and oxidation resistance.

Nevertheless, the need for complex geometries in components such as turbine blades presents manufacturing challenges for suitable alloys, such as nickel-based superalloys. Conventionally, these superalloys have been manufactured using processes such as casting, forging, and machining, which can limit design flexibility [22–24]. Recently, the use of Additive manufacturing (AM) has been explored for fabricating superalloys. According to ASTM standards, AM is the

process of joining materials to create objects from 3D model data, typically layer by layer as opposed to the traditional subtractive manufacturing methodology [25]. Compared to conventional manufacturing methods, AM offers distinct advantages in specific applications. These include design flexibility for complex geometries [26,27]. Recently, AM has made significant advancements in the energy and power sector, with Siemens incorporating 3D-printed gas turbine blades [28]. Amongst various AM technologies is laser powder bed fusion (LPBF), which has been applied for the fabrication of alloys such as Alloy 625 [29,30], Rene 80, and stainless steel [31]. LPBF has been studied for manufacturing superalloys, and the process produces a preferential grain orientation in the microstructure, resulting in anisotropy of mechanical properties. Common defects with LPBF process include balling [32], denudation [33], and surface roughness [34].

This thesis carries out an experimental analysis to evaluate the influence of contaminants such as SO_2, NO_X, H_2O, typically found in an Allam cycle plant, on the oxidation and carburization behaviour of commercially utilized nickel-based superalloys [17]. Further analyses were conducted to evaluate the effect of manufacturing technique and microstructural attributes, and its surface roughness, providing a deeper insight into how additive manufacturing impacts the oxidation resistance of Alloy 625. Assessing the oxidation and carburization behaviour of nickel-based superalloys and AM Alloy 625 at high temperatures helps provide in-depth information into its resistance and guides the postulation of a degradation pathway.

1.2 Research Challenges and current state of the art

Materials utilised for High-temperature applications are crucial for advancing sCO_2 power cycles, particularly those relating to turbines and heat exchangers. These components experience extreme thermal and mechanical stresses, necessitating the development of robust materials with superior oxidation, creep, corrosion, and carburization resistance.

This section discusses the current state of research, challenges in material performance, and the necessary experimental work to improve plant and material durability and efficiency in sCO_2 environments.

8 Rivers, alongside its lead inventor, Rodney Allam, has developed technologies, including the Allam-Fetvedt cycle, to meet global climate targets without increasing electricity costs. 8 Rivers Capital developed the first Allam cycle using coal. This first cycle is considered a syngas-fired power generation cycle. Another development is Net Power in La Porte, Texas, founded by 8 Rivers Capital, which has commercialised the natural gas application of the Allam cycle, starting with a 50MWth plant. The computational models and bench-scale testing have been completed and are exclusively licensed to NET Power. Another advancement is the STEP Demo Project, a $165.6 million initiative leading the way in sCO_2 power cycle technology. This project aims to demonstrate pathways to achieving net plant efficiencies greater than 50%, with operational turbine inlet temperatures exceeding 700°C in a 10 MWe power generation facility using a recompression Brayton cycle with sCO_2 as the working fluid [35].

1. Material Selection and Performance

Nickel-based superalloys such as Inconel 740, Alloy 625 and Haynes 282 have emerged as promising candidates for high-temperature sCO_2 applications [35]. However, challenges persist in optimizing these materials for long-term operation under sCO_2 conditions. Studies have shown that materials exposed to sCO_2 environments at temperatures exceeding 700°C experience accelerated degradation due to oxidation and carburization. Alloys such as 625 and 718 form protective oxide layers [36]; however, the long-term stability of these layers in sCO_2 environments remains a concern. Advanced coatings and surface modifications are also being investigated to enhance materials' longevity [37].

2. Fabrication and Welding

Ensuring the integrity of welds in high-temperature components is a challenging task. For instance, during the STEP project, 3% percentage of tube-to-tube butt

welds in the heater's 740H tube bundle failed during inspection due to stress relaxation cracking during post-weld heat treatments [38].

3. Oxidation and Creep Resistance

Materials operating above 500°C must resist degradation such as oxidation and creep. While alloys such as Inconel 740H, Alloy 625 and Haynes 282 are selected for their high-temperature capabilities, their long-term performance in sCO_2 environments is still under investigation. Oxidation can lead to material degradation, affecting the efficiency and component lifespan.

4. ***Heat Exchanger Durability and Efficiency***.

Scaling up heat exchangers to commercial-scale power cycles presents fabrication and design difficulties. The thermal expansion difference between hot and cold sections induces mechanical stresses potentially leading to failure. This adds complexity to the design and operation of heat exchangers in sCO_2 power cycles and highlights the need for further research into optimizing performance under a wide range of operating conditions [38].

5. Compressor Efficiency

The efficiency of compressors in sCO_2 systems is another area of concern. During the STEP project, the actual compressor performance was found to be significantly different from predicted values, resulting in a twofold reduction in turndown capability. Accurate measurement of compressor efficiency at high rotational speeds (up to 21,000 rpm) proved difficult with existing instrumentation, leading to the installation of a torque meter to improve measurement accuracy [38].

1.3 Aim and Objectives

This thesis presents results from experimental testing to understand the degradation mechanisms, i.e., carburization, sulphidation, nitridation, and oxidation, of nickel-based superalloys in baseline high-temperature CO_2 environments at 800°C, focusing on the effects of contaminants, heat treatments,

surface roughness, and manufacturing techniques, such as LPBF. The research has generated valuable insights into how these factors influence oxidation and carburization for future energy systems.

The following research objectives are outlined:

Objective 1: Investigate the Effects of Contaminants found in an Allam cycle, on Oxidation and Carburization in Nickel-Based Superalloys

This objective seeks to experimentally assess the influence of environmental contaminants, such as impurities in the working fluid, on the oxidation and carburization behaviour of nickel-based superalloys. The tests will replicate operational conditions found in the baseline Allam cycle, with the goal of determining how these impurities affect the material's long-term performance.

Objective 2: Evaluate the Influence of Surface Roughness on the Oxidation Behaviour of Additively Manufactured Alloy 625

This objective focuses on evaluating the role of surface roughness in the oxidation resistance of AM Alloy 625 under sCO_2 conditions. By comparing AM-produced components with varying surface finishes, this study aims to correlate surface roughness with accelerated degradation mechanisms, providing insights into how surface engineering techniques might mitigate these effects.

Objective 3: Analyse the Influence of Microstructural Attributes on Oxidation Behaviour in Additively Manufactured Alloy 625

The microstructure of materials produced via AM processes is often different from conventionally manufactured materials, with features such as grain orientation and porosity affecting the material's properties. This objective will investigate how microstructural attributes, including grain size and defects such as microcracks and pores, influence the oxidation and carburization behaviour of AM Alloy 625 in a CO_2 environment.

Objective 4: Develop a Degradation Pathway for First-Stage Blade Materials under Baseline Allam Cycle Conditions

Drawing upon the experimental findings from the previous objectives, this research aims to establish a comprehensive degradation pathway for nickel-based superalloys, including LPBF Alloy 625, under the baseline conditions of the Allam cycle. This pathway will map the progression of material failure from initial oxidation and carburization to eventual performance degradation, providing a detailed understanding of the mechanisms at play. The degradation pathway will serve as a critical tool for predicting material lifespan and identifying areas where further material improvement is necessary.

Objective 5: Propose Mitigation Strategies Based on the Developed Degradation Pathways

Based on the degradation pathways identified in Objective 5, this objective seeks to propose mitigation strategies to enhance the performance and longevity of turbine materials in high temperature CO_2 environments. These strategies These strategies may include recommendations for alloy composition modifications, optimized heat treatments, surface engineering techniques in additive manufacturing.

1.4 Scope of study

This thesis emphasizes the degradation behaviour of nickel-based superalloys, focusing on their oxidation and carburization resistance in high-temperature CO_2 environments, typically experienced in the Allam cycle. This research has been conducted to further expand the understanding of the impact of manufacturing techniques, such as conventional wrought and LPBF AM, on the oxidation and carburization resistance of nickel-based superalloys, especially Alloy 625.

The performance of conventional materials including Rene80, PWA1480, MARM48, IN738LC, IN939, and CM247 with and without plasma sprayed thermal barrier coating (TBC) or corrosion-resistant coatings was tested in high-temperature CO_2 and pressure of 1 bar. The exposure time was up to 1000 hours. In this work, the impact of contaminants typically found in an Allam cycle such as H_2O, NO_x and SO_2 on the degradation of pathways. The importance of

contaminants in the degradation processes is a significant part of the investigation and can accelerate oxidation and carburization.

This research is also aimed at expanding the understanding of the impact of manufacturing techniques such as conventional casting and additive manufacturing (AM), on the oxidation and carburization resistance of nickel-based superalloys specifically Alloy 625. This investigation is limited to laboratory-simulated environments.

1.5 Significance of research

Turbomachinery components, which are exposed to harsh environments such as high temperatures, carbon, and the presence of impurities, face the risk of failure if the materials are not optimised for such conditions. Consequently, research into material performance, particularly in CO_2-based environments, is vital for ensuring the reliability and efficiency of future power systems.

This research examines the impact of oxidation on materials such as CM247, Alloy 625, and other high-temperature alloys. Building on prior research systems that examine thermal barrier coating systems applied through plasma spray processes. Specifically, it examines how TBCs deposited via plasma spraying, along with their associated bond coats, serve as protective layers to mitigate material degradation in turbine blade applications. This research contributes to a growing body of knowledge on how TBCs influence the overall durability and performance of turbine blades in CO_2-rich environments. The investigation into the role of sulphur and nitrogen containing species in accelerating oxidation under these conditions adds a new depth to the understanding of degradation mechanisms.

Another key aspect of this research is the comparison between wrought and additive manufacturing fabricated materials, particularly focusing on Alloy 625. The findings reveal that while both wrought and AM Alloy 625 show promising oxidation resistance, the microstructure of AM-fabricated materials can significantly impact their performance.

The UK government has identified advanced power cycles, such as the Allam cycle, as a promising technology for reducing carbon emissions while maintaining high power generation efficiency [39]. The Allam cycle, which operates with sCO_2 as a working fluid, offers high thermal efficiency and inherent carbon capture capabilities, making it a strong candidate for next-generation power plants [15]. However, the successful implementation of sCO_2 power cycles in the UK energy infrastructure depends on the development and optimization of materials capable of withstanding the extreme thermal, mechanical, and chemical conditions present in these systems. High-temperature oxidation, carburization, and creep resistance are critical factors in ensuring the long-term reliability of key components such as turbines and heat exchangers [40,41]. By providing insights into the performance of both conventional and AM-fabricated materials in high-temperature CO_2 environments, this research offers valuable guidance for material selection in the UK's energy transition.

1.6 Contribution to knowledge

Throughout this PhD, my research has made significant contributions to the materials science world. To date, my research findings have been published and presented across international platforms and publications.

1.6.1 Conference presentation

- In August 2022, presented 'Corrosion of potential first-stage blade materials in simulated supercritical CO_2' at EUROCORR in Berlin.

- September 2022, 'Analysis of turbine blade materials exposed at 800°C simulating a supercritical Allam cycle' poster presentation at the Microscopy of Oxidation conference at Cranfield University.

- In August 2023, presented 'The comparison of the oxidation behaviour of wrought and additively manufactured Alloy 625' at the EUROCORR 23 conference in Belgium.

- In August 2024, presented 'Influencing effect of surface roughness on the oxidation and carburization behaviour of laser powder bed fusion (LPBF) Alloy

625 in a simulated high-temperature Allam cycle environment' at the EUROCORR 24 conference in Paris.

- In August 2024, presented 'The effects of nitrogen and sulphur on the oxidation behaviour of Rene 80' at the EUROCORR 24 conference in Paris.

1.6.2 Publications

Paper 1, titled 'Corrosion of potential first-stage blade materials in simulated supercritical CO_2', was published in High-Temperature Corrosion of Materials. Focuses on the effect of thermal barrier coatings and bonded coatings on bare alloy CM247 in a CO_2 environment with the presence of contaminants.

The rest include papers currently to be published:

Paper 2, titled 'Comparison of the oxidation behaviour of wrought and additively manufactured Alloy 625', to be published in High-Temperature Corrosion of Materials. Discusses the effect of manufacturing technique, i.e. conventional and laser powder bed fusion (LPBF) additive manufacturing of Alloy 625 in a simulated high-temperature CO_2 environment.

Paper 3, titled 'Influencing effect of surface roughness on the oxidation and carburization behaviour of laser powder bed fusion (LPBF) Alloy 625 in a simulated high-temperature Allam cycle environment', to be published in Materials Science and Engineering 2024. Discusses the influence of polished, as-received and 600 grit surfaces AM Alloy 625 on its oxidation and carburization behaviour.

Paper 4, titled 'Effect of N and S on the oxidation of Rene 80 in a high-temperature CO_2 environment to be published in high temperature corrosion of materials 2025. Analyses the effects contaminants such as nitrogen and sulphur could have on the oxidation and carburization behaviour. One of the key challenges in turbine materials operating under sCO_2 conditions is the presence of contaminants that can accelerate oxidation and carburization, leading to material degradation.

1.7 Thesis Structure

The remainder of the thesis is structured into 10 sections, aligning with the project aim. Chapter 2 presents the literature review, offering insights into material selection processes and identifying knowledge gaps. Chapter 3 explains the rationale for the experiments, detailing the procedures and techniques used for microstructural analysis. Chapter 4 contains Paper 1, titled “Corrosion of Potential First Stage Blade Materials in Simulated Supercritical CO_2,” which addresses Objective 1 and focuses on the impact of thermal barrier coatings on oxidation behaviour. Chapter 5 presents Paper 2, “Comparison of the Oxidation Behaviour of Wrought and Additively Manufactured Alloy 625,” linked to Objective 3. Chapter 6 features Paper 3, “Influence of Surface Roughness on the Oxidation and Carburization Behaviour of Laser Powder Bed Fusion (LPBF) Alloy 625 in a Simulated High-Temperature Allam Cycle Environment,” corresponding to Objective 2. Chapter 7 presents Paper 4 titled “Effect of N and S on the Oxidation of Rene 80 in a High-Temperature CO_2 Environment,” related to Objective 1. Chapter 8 summarises the findings and is tied to Objectives 4 and 5, while Chapter 9 concludes the thesis.

2 Literature Review

2.1 Introduction

The increasing demand for cleaner and more efficient energy sources is the main driver of advances in power cycle technology. Among these, supercritical carbon dioxide (sCO_2) cycles have emerged as a promising alternative to traditional steam and gas turbine cycles. This review aims to provide a detailed overview of the current state of sCO_2 power cycles, their configurations, materials used, and the challenges faced during implementation.

The review begins with an overview of various power cycles, including open and closed cycles, followed by a detailed discussion of the Brayton cycle and its advancements in utilising sCO_2 as a working fluid. The different configurations of CO_2-based power cycles are then examined, including the recuperated closed-loop and semi-closed oxyfuel Brayton cycles. These technologies are presented with an emphasis on their potential applications and benefits for power generation.

The review highlights the critical role of materials in the development of sCO_2 power cycles, with a focus on the use of superalloys in high-temperature environments. Various manufacturing methods, including conventional and additive manufacturing, are explored, along with the associated advantages and challenges. The review also discusses the failure mechanisms of materials in extreme conditions and the protective treatments necessary to ensure the long-term reliability of components.

Finally, the review highlights the current state of research, the challenges still to be addressed, and the prospects of sCO_2 power cycles, including their application in power generation systems. By providing a comprehensive understanding of these technologies, this literature review contributes to the ongoing development and optimization of sCO_2 power cycles.

2.2 Power cycles

Cengel and Boles [42] defined thermodynamic cycles as a series of thermodynamic processes transferring heat and work while varying temperature, pressure, and other state variables, with the system eventually returning to its initial state. Thermodynamic cycles are classified into two types, namely, power cycles and heat pump cycles (also known as refrigeration cycles). These are shown in Figure 2-1.

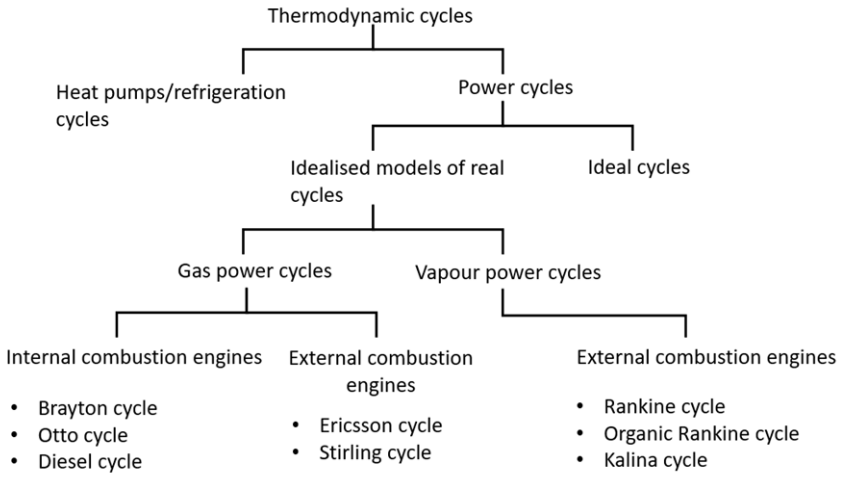


Figure 2-1 - Classification of thermodynamics

Pump cycles transfer heat from low to high temperature by utilising mechanical work as an input source. Power cycles are thermodynamic cycles in which the heat energy is absorbed to produce mechanical work, and so power cycles are the operational foundation of a heat engine. Power cycles are further divided into Ideal cycles and real cycles.

Table 2-1 - Various samples and state processes [43]

Cycle	Process 1-2 (Compression)	Process 2-3 (Heat Addition)	Process 3-4 (Expansion)	Process 4-1 (Heat Rejection)	Notes
Power cycles normally with external combustion - or heat pump cycles:					
Bell Coleman	adiabatic	isobaric	adiabatic	isobaric	A reversed Brayton cycle
Brayton	adiabatic	isobaric	adiabatic	isobaric	Jet engines aka first Ericsson cycle from 1833
Carnot	isentropic	isothermal	isentropic	isothermal	
Ericsson	isothermal	isobaric	isothermal	isobaric	the second Ericsson cycle from 1853
Scuderi	adiabatic	variable pressure and volume	adiabatic	isochoric	
Stirling	isothermal	isochoric	isothermal	isochoric	
Stoddard	adiabatic	isobaric	adiabatic	isobaric	
Power cycles normally with internal combustion:					
Diesel	adiabatic	isobaric	adiabatic	isochoric	
Lenoir	isobaric	isochoric	adiabatic	isobaric	Pulse jets (Note: 3 of the 4 processes are different)
Otto	adiabatic	isochoric	adiabatic	isochoric	Gasoline / petrol engines
Rankine	adiabatic	isobaric	adiabatic	isobaric	Steam engine

Internal combustion cycles, such as the Otto and Diesel cycles, along with the Brayton cycle, are well-known examples of engines that operate on the same fundamental principles as the gas cycle.

Table 2-1 illustrates the various cycles and their corresponding state processes. The Rankine cycle and Brayton cycle have the same state process. While there are different power cycles, the most frequently used for large-scale power generation are the Rankine, also known as the steam cycle, as well as the Brayton cycle. In both cycles, heat is added or ejected at constant pressure whilst a pump or compressor increases pressure before addition of heat. A turbine is responsible for extracting work from the cycle and reducing pressure.

Different researchers have classified gas turbines based on different criteria. Patel and Karamchandani [44] postulated that gas turbine plants can be classified based on six factors:

1. **Combustion**: continuous-combustion or constant-pressure gas turbine and explosive type combustion or constant-volume gas turbine.
2. **Gas power cycle (Thermodynamic cycle):** Brayton Cycle(constant pressure gas turbines), Atkinson cycle (constant volume gas turbines) and Ericsson cycle (constant pressure gas turbines with large degree of reheating and intercooling).
3. **Cycle of operation:** This explains open, semi-closed, and closed cycle gas turbines. Constant-pressure gas turbines (with continuous combustion) can operate in either a closed or open cycle, whereas constant-volume gas turbines work in an open cycle. An open-cycle gas turbine involves an internal combustion engine, whereas a closed-cycle gas turbine utilises an external combustion engine.
4. **Shafts Arrangement**
5. **Fuel**
6. **Application**: This focuses on stationary, automatic, locomotive, marine and aircraft gas turbine.

2.2.1 Brayton Cycle

The Brayton cycle is named after an American engineer, George Brayton, for his work on developing and building a two-stroke reciprocating engine in the 1800s. This development became an ideal model for gas turbine operations. The Brayton cycle is a thermodynamic cycle commonly used for electricity generation and propulsion (mechanically driven) systems. It is the air-standard thermodynamic cycle for gas turbine engines. An ideal air Brayton cycle consists of three main parts – isentropic compression of the working fluid, constant pressure in the combustion chamber, and isentropic expansion of the working fluid to produce mechanical work.

There are two types of Brayton cycles: the open cycle, which is heated directly using a combustor, and the closed cycle, which is heated indirectly through a heat exchange [45]. In the closed cycle, the working fluid circulates within a closed loop and is heated by an external source, similar to the steam Rankine cycle. Gas

turbines typically operate on an open cycle, where a fuel-air mixture enters the compressor, undergoes combustion, and exits as exhaust gases.

2.2.1.1 Open cycle gas turbine

Figure 2-3 highlights a simple open Brayton cycle and its key components. Fresh/ambient air is compressed from the atmosphere. This ambient air is compressed to high pressure and temperature. (2), the ambient air is drawn into the combustion chamber and further heated through burning, a fuel-air combination. (3) Expansion of gases occurs in the turbine either close to atmospheric pressure or the pressure required by the engine. The heated air and combustion gas mixture drives the turbine, the heated combustion products are expanded, producing sufficient energy to deliver shaft power to the mechanical process or generator and enough to also drive the compressor

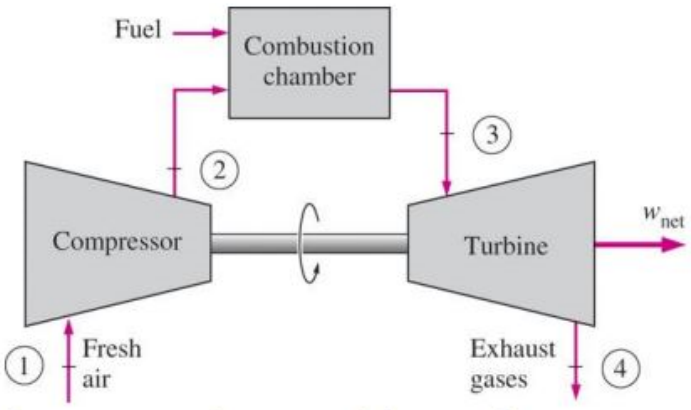


Figure 2-2 - Open cycle gas turbine [46]

As seen in Figure 2-2, open cycles have no pipe between the compressor and turbine stage after the expansion process in the turbine, instead of circulation through a cooler back into the compressor [42]. The absolute temperature of the working fluid passing through the system is proportional to the power produced by a turbine and consumed by a compressor, meaning that the work necessary to operate the compressor is extracted from the total working output of the turbine, and the remainder is available as the network output of the engine. Given that, at the beginning, ambient air enters the compressor, and exhaust is expelled at the end, this cycle is described as an open cycle.

2.2.1.2 Closed cycle gas turbine

In a closed cycle, the working fluid recirculates at the end of the cycle. As shown in Figure 2-3, the gas expelled at the expansion process (turbine) is reintroduced into the combustor, heat exchanger [46].

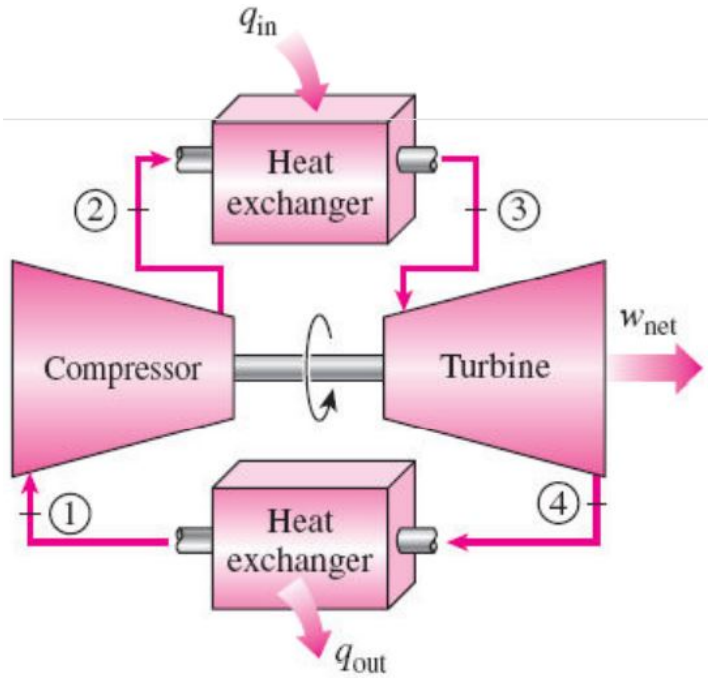


Figure 2-3 - Closed Brayton cycle [46]**.**

The closed cycle operates similarly to the operations of a steam Rankine cycle. In this report, the classification factor focused on is the cycle of Operation. The difference between the open cycle and closed cycle is simplified in Table 2-2.

Table 2-2 - Difference between open and closed cycle [47]

Closed Cycle Gas Turbine	Open Cycle Gas Turbine
1. The compressed air is heated in a heating chamber.	1. The compressed air is heated in the combustion chamber.
2. As the gas is heated by an external source, the amount of gas remains the same through the cycle.	2. The products of combustion are getting mixed up in the heated air, hence, the same gas doesn't remain in the cycle.
3. The gas after the turbine is passed into the cooling chamber.	3. The gas after the turbine is exhausted into the atmosphere.
4. The working fluid is circulated continuously	4. The working fluid is replaced continuously.
5. Any fluid with better thermodynamic properties can be used.	5. Only air is used as the working fluid.
6. The turbine blades do not wear away earlier, as the enclosed gas does not get contaminated while flowing through the heating chamber.	6. The turbine blades wear away earlier, as the air from the atmosphere gets contaminated while flowing through the combustion chamber.
7. The mass of installation per Kwatt is more.	7. The mass of installation per Kwatt is less.
8. High maintenance cost.	8. Maintenance cost is low.

A Brayton cycle's efficiency is a function of various factors, including turbine inlet air temperature, pressure ratio, turbine blade-cooling requirements, ambient air temperature, specific engineering design requirements, reheat, steam, inter-air cooling, intercooling, recuperator, and compressor energy use [48]. The aforementioned advancement leads to increased machinery costs, enhanced manufacturing efficiency, and higher value. The higher value signifies greater generated power, higher efficiency, which overall provides a net economic benefit [48]. Higher temperature/pressure ratios lead to a higher efficiency. Subsequently, it is advantageous for turbines to be operated at the highest feasible temperature whilst it being consistent with financially viable materials and intercooling technology and, at the compressor, the inlet air flow temperature operating at the lowest temperature possible. Hence, the direction of research has been towards gas turbines with higher temperatures and pressures.

The supercritical CO_2 (sCO_2) power cycle operates similarly to other turbine cycles, but utilises CO_2 as the working fluid.

2.2.2 Supercritical carbon dioxide (sCO_2) power cycles

The supercritical CO_2 Brayton cycle can be applied to direct-heating applications, offering the potential for high efficiency and capturing process water. This cycle also facilitates CO_2 capture from the combustion process. When its availability and low cost are factored in, no other substance is a more attractive working fluid for the supercritical Brayton cycle than carbon dioxide.

2.2.2.1 Supercritical fluids (SCFs)

Supercritical fluids (SCFs) are known to exhibit significant differences from conventional fluids. Supercritical fluids exist in a phase where temperature and pressure are above its critical point.

Table 2-3 - Properties of various fluids [49]

Fluid name	ASHRAE No.	Formula	Critical temp. (°C)	Critical press. (Bar)	ASHRAE Level for safety[6]	ODP rel. R11	GWP rel. CO_2
Carbon dioxide	R744	CO_2	30.98	73.8	A1	0	1
Water	R718	H_2O	373.89	22.10	A1	0	-
Hydroflorocarbon	R134a	CH_2FCF_3	101.1	40.7	A1	0	1300
Butane	R600	C_4H_{10}	152	37.9	A3	0	0
Isobutane	R600a	C_4H_{10}	134.7	36.4	A3	0	<20
Sulfur Dioxide	R764	SO_2	157.5	78.8	B1	0	-
Ammonia	R717	NH_3	132.89	112.8	B2	0	<1
Sulfur Hexafluoride	R-7146	SF_6	45.56	37.6	?	?	239000
Perfluoropropane	R218	C_3F_8	71.89	26.8	?	0	7000
Zeotropic mixture	R407C	R32/R125/R134a (23/25/52)	87.3	48.2	A1	0	1600
Azeotropic mixture	R500	R12 / R152a (73.8%26.2%)	102.1	41.7	A1	0.605	7870

Unlike real fluids, SCFs exist in a distinct "supercritical state," which is achieved when a substance exceeds its critical temperature (T_c) and critical pressure (P_c). Table 2-3 shows the T_c and P_c of various gases that can exist in supercritical state. Comparing the critical temperature and pressure, CO_2, has a high critical pressure and low critical temperature (7.38MPa and 31.1°C). These high critical pressure and low pressure are advantages due to high density and low specific volume. CO_2 is an important natural fluid widely utilised in various commercial and industrial applications. CO_2 as a working fluid is regarded as non-toxic, stable, and incombustible [50] and has numerous advantages and applications from a low-grade heat source. Although supercritical water (SCW) has also been considered for high efficiency power cycles, safety challenges – high pressure, high temperature, and intensive corrosion prevent its application in nuclear power generation [51].

Recently, supercritical CO_2 as a working fluid has gained traction in the scientific and energy industry as an alternative to the steam Rankine cycle [13,52]. Feher [53] postulated that CO_2 is the most suitable working fluid when it comes to factors like chemical stability, corrosion, and moderate temperature range. Ease of accessibility and abundance, as well as desirable features such as non-toxicity,

non-flammability, high-temperature stability, and zero ozone depletion potential (ODP), are attractive properties that promote CO_2 as an ideal selection as a working fluid in modern power cycles.

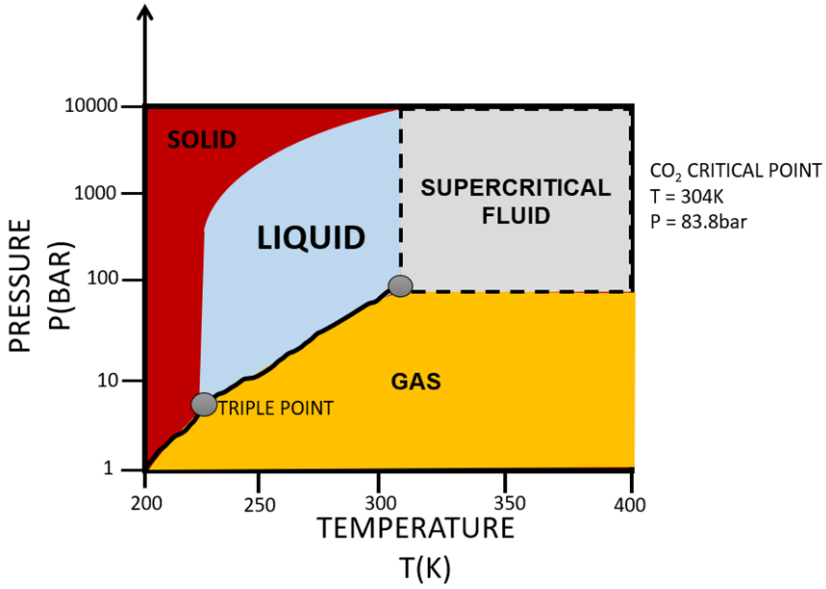


Figure 2-4 - Schematic P-T phase diagram of CO_2

Figure 2-4 depicts a P-T phase diagram of CO_2, which has 4 distinctive phases: solid, liquid, gas and a supercritical phase. Triple point (TP), the point where all phases are in equilibrium. Supercritical fluid can be attained by increasing either temperature/ pressure while the other remains constant. The transition phase to supercritical state occurs at a relatively low critical pressure and temperature of 7.38MPa and 31.1°C. As a result of this, supercritical CO_2 can be easily compressed directly to supercritical pressures and, without difficulty, be heated to supercritical state. Above C_p, increases in temperature and pressure does not further change the state of CO_2, the fluid exists in a supercritical phase.

SCFs can be applied in various industries, including the pharmaceutical and energy industries. SCFs in the pharmaceutical industries can be used to improve bioavailability of drugs through production of nano- and micro-sized drug particles [54]. In the energy and power industry, utilisation of sCO_2 facilitates energy-saving and reduction of emissions [55]. Zhu [56] reviewed the recent developments of S-CO_2 and discussed the technical challenges, including the

construction of turbomachinery, the design of low-cost and compact recuperators, and the development of oxycombustor.

Traditionally, power cycles – natural gas combine cycle, coal cycles, and integrated gasification combined cycle, necessitate adding expensive, efficiency-reduced equipment for the reduction of CO_2 and other pollutants. Analysis of these cycles has shown that an additional CO_2 removal system can increase electricity cost by 50-70% in comparison to a typical 90% of CO_2 generated from hydrocarbon fuel combustion [57]. Dostal et al. [58] emphasised the importance of sCO_2 as a potential working fluid in a power cycle. A sCO_2 cycle operates in a single phase, reducing the complexity of the system. Subsequently, sCO_2 power cycles could require lower capital investments, reduce operational and maintenance costs and consequently lead to cheaper electricity [59–61].

2.3 sCO_2 Brayton Cycle

Supercritical Brayton cycle in recent times has earned its attention as a result of its distinguishing features from compact and small turbomachinery, high efficiency, etc. sCO_2 Brayton cycle has gained consideration as a capable power conversion system for various power types – fuel cell, coal power, geothermal energy, solar energy etc [61]

Having mentioned that there are different cycles, Brayton Cycle etc, there are also variations to each of the different cycles. These variations are regarded as the Configuration of CO2 power cycles. The most suitable cycle is determined through various factors, including operational costs, installation costs, type of heat source (fuel type; directly fired cycles and grade of heat; Indirectly-fired cycles).

2.3.1 Configuration of CO_2 power cycles

The configuration of CO_2 power cycles plays a crucial role in determining their performance, efficiency, and suitability for various heat sources. Since the interest in sCO_2 cycles has grown, different configurations have been investigated. This section explores the different configurations commonly employed in CO_2-based power systems, including simple Brayton,

recompression, intercooling, and recuperated cycle layouts. Each configuration offers distinct thermodynamic and operational advantages tailored to specific applications such as nuclear, solar, and waste heat recovery.

2.3.1.1 Recuperated closed-loop Brayton cycle

The simple closed-loop Brayton Cycle (SCBC) is acknowledged as the recuperated closed Brayton cycle – the simplest sCO_2 design. Figure 2-5 depicts a simple closed-loop Brayton cycle, with an estimated maximum cycle efficiency of 34.5% [61]. In a recuperated closed Brayton cycle, the working fluid, CO_2 is indirectly heated through a heat exchanger. As the working fluid reaches the expansion chamber known as the turbine, energy is extracted from the working fluid as it moves through the turbine. The CO_2 exiting the turbine is then cooled down in a heat exchanger to a required inlet temperature of the compressor.

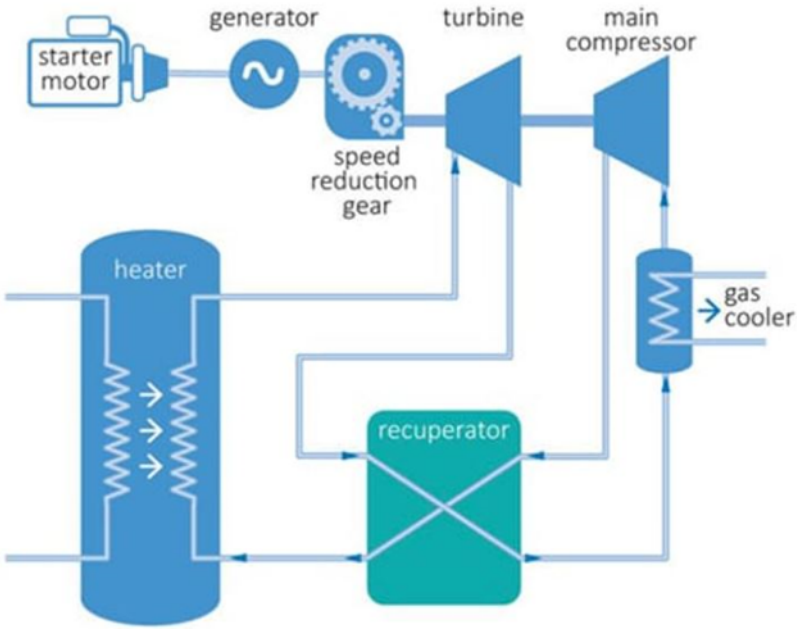


Figure 2-5 - Recuperated closed-loop Brayton cycle [61]

2.3.1.2 Recuperated recompression closed-loop Brayton cycle

Figure 2-6 shows a recuperated recompression closed-loop Brayton cycle. In this cycle the low-pressure CO_2 stream exiting from the recuperator is split in two. One portion is cooled in the cooler and compressed in the main compressor before being heated in the low-temperature recuperator, while the other bypasses

the cooler and is compressed in the re-compressor to maximum cycle pressure. The streams are then mixed before they pass through a high-temperature recuperator and the CO_2 heater. “With this cycle layout, the heat capacity between the hot and cold sides of the recuperator is better matched and hence, the overall efficiency of the recuperator is improved” more than 5% compared to the conventional Brayton cycle [61]. This improvement is due to the more balanced thermal load between the two streams, allowing the recuperator to recover more heat and reducing the need for external heating. As a result, less energy is required to heat the CO_2 stream, leading to a more efficient overall cycle performance and lower fuel consumption, enhancing the overall system efficiency and sustainability.

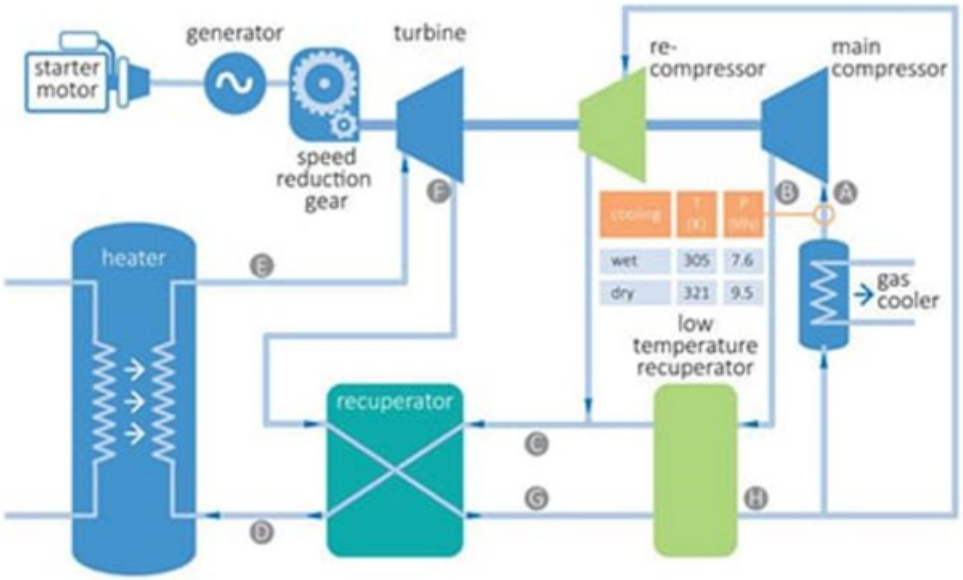


Figure 2-6 - Recuperated recompression closed-loop Brayton cycle [61]

The supercritical CO_2-based recompression Brayton cycle offers the opportunity to increase cycle efficiency compared to Rankine cycles and some other Brayton cycles and leads to power plants with higher process efficiency. Replacement of the heat source with a pressurised oxycombustor implies the working fluid is no longer high-purity CO_2, as such, the cycle efficiency reduces due to the decrease in CO_2 concentration [62].

2.3.1.3 Semi-closed direct oxyfuel Brayton cycle

Semi-closed direct oxyfuel Brayton cycles shown in Figure 2-7, the CO_2 heater is replaced with a pressurized oxy-fuel combustor. Inside the combustor, fuel is burned in relatively pure and near-stoichiometric oxygen, and the resulting stream (which contains mainly CO_2 and water) is used to drive the turbine. After remaining heat in the stream is recuperated, the stream is cooled to condense the water, leaving a high concentration of CO_2. One portion of this CO_2 is compressed before passing through the recuperator to be preheated and reused in the combustor (as a diluent), while the other portion is ready to be compressed for storage.

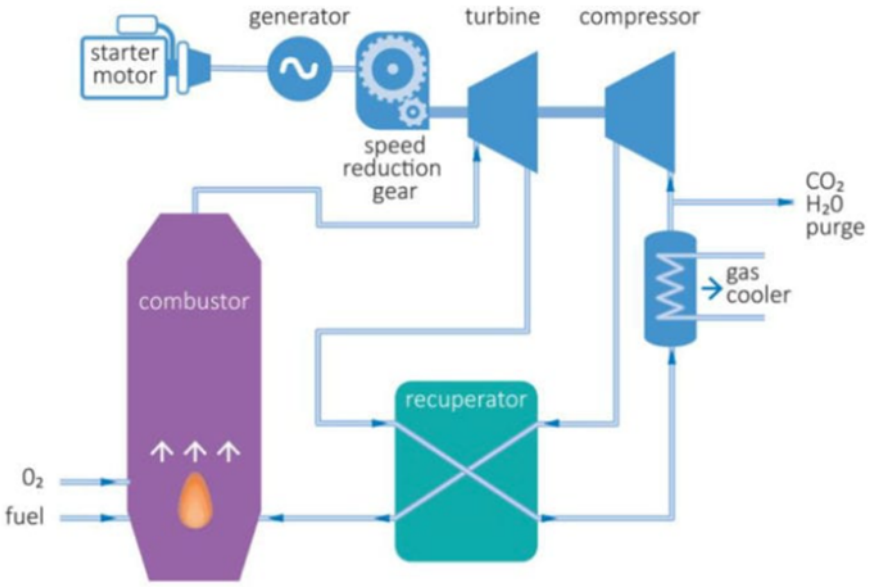


Figure 2-7 - Semi-closed direct oxyfuel Brayton Cycle [61]

2.3.1.3.1 Allam cycle

This study centres on the Allam cycle, a process patented by Rodney Allam in 2013 [15], which provides a pathway to a sustainable energy future by efficiently and cleanly utilizing hydrocarbon energy resources while inherently capturing combustion-derived CO_2 for sequestration or reuse. The Allam Cycle takes a novel approach to reducing emissions by employing oxy-combustion and a high-pressure supercritical CO_2 working fluid in a highly recuperated cycle [15]. The Allam cycle can utilize a wide range of hydrocarbon fuels, such as natural gas,

raw and sour natural gas streams with H_2S and CO2, as well as gasified solid fuels like coal, oil refining residues, and biomass [17]. This results in power cycles with significant advantages over traditional systems that do not capture high pressure CO_2. It achieves a 59% LHV efficiency, comparable to the best NGCC power plants, and offers much higher efficiencies than modern coal plants, which reach up to 51% LHV. The cycle operates with a single turbine which has an inlet pressure of approximately 300 bar and pressure ratio of 10 [16].

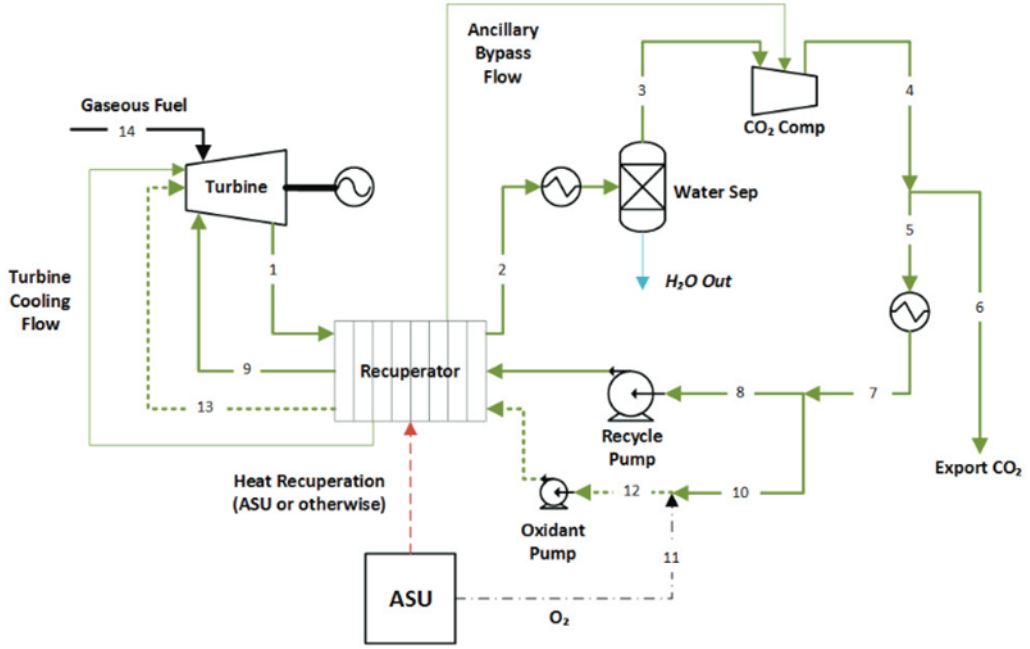


Figure 2-8 - Schematic of a commercial scale natural gas Allam cycle [17]

A simplified diagram of the cycle using natural gas as fuel is shown in Figure 2-8 These values represent a simplified version of a commercial-scale plant, without considering the additional optimization details for heat exchangers, compressors, and turbines. In this cycle, pressurized gaseous fuel (14) is combusted with a mixture of CO_2 and nearly pure oxygen (13), provided by a co-located Air Separation Unit (ASU), and a hot CO_2 diluent recycle stream (9), at around 300 bar under lean combustion conditions. The resulting exhaust from the combustor is expanded through a turbine to about 30 bar, with the temperature decreasing to above 700°C (1). After expansion, the exhaust gas enters a heat exchanger, where heat is transferred from the hot exhaust to the high-pressure CO_2 recycle

stream. This stream acts as a diluent, cooling the combustion products and lowering the turbine inlet temperature to an acceptable 1150°C. Additionally, the oxidant flow is used to supply oxygen to the combustor's flame zone.

The turbine exhaust is then cooled to near ambient temperature and water from combustion is separated (3). The remaining CO_2-rich fluid stream is recompressed (4), cooled (7), and pressurized back to approximately 300 bar before re-entering the cold end of the heat exchanger. Before entering the heat exchanger, a portion of the recycled CO_2 (10) is mixed with oxygen (11) to form an oxidant mixture (12), which is fed separately to the heat exchanger and turbine. Inside the main process heat exchanger, the recycle flows are reheated by the hot turbine exhaust before returning to the combustor at temperatures greater than 700°C. To maintain mass balance in the semi-closed cycle, a portion of the high-purity CO_2 process gas is exported during the recompression phase to a high-pressure CO_2 pipeline for either sequestration or utilization.

2.4 Current state of the art of sCO_2 cycle

Researchers have been working on the development of sCO_2 cycles for power generation. Recently, headway has been made regarding research and development as well as demonstrating the Allam cycle. This includes the supercritical Transformation Electric Power (STEP) project in collaboration with GTI energy, Southwest research Institute (SWRI) and General Electric vernova advanced research (GEV-AR) funded by the United States department of energy (DOE) and National energy technology laboratory (NETL). The STEP project is the largest indirect-fired sCO_2 plant in the world at 10Mwe, and its main objective is to operate both a Recuperated closed-loop Brayton cycle, the simple cycle and a recompression Brayton cycle (RCBC) configurations with a turbine inlet temperature of 500°C and 715°C for RCBC. The cycle is aimed to demonstrate 50% efficiency at a larger commercial scale applicable for low/zero emission heat sources such as concentrated solar, waste heat, biomass, and carbon capture plants [37].

Recently, the STEP project successfully demonstrated a 1 MW loop, named SunShot, of the sCO_2 turbine under operating conditions of 715°C at 250 bar. The STEP initiative has accomplished three significant achievements since 2022. These include completing the mechanical assembly of the world's most extensive indirect-fired supercritical CO_2 power facility, successfully bringing the compressor circuit online, and conducting the inaugural full-scale system demonstration [37].

The mechanical assembly phase concluded in October 2023, marking the culmination of seven years of development efforts aimed at creating a functional facility. This phase involved the complete installation and acceptance testing of all plant equipment, along with individual component commissioning activities where feasible, to prepare the installation for comprehensive system validation.

The second achievement involved successfully activating the compressor circuit, which validated the proper functioning of the primary compressor unit and its related subsystem components while meeting specified performance targets at the intended operating conditions. This subsystem validation process was finalized in November 2023.

The third milestone was achieved in January 2024, when the complete system underwent its first operational test under heated conditions. This represents an unprecedented achievement, as no indirect-fired supercritical CO_2 system had previously been operated at such a magnitude [37].

2.5 Application and advantages of sCO_2 cycles

Sulzer in 1950 [63], first patented a CO_2 closed Brayton cycle, which was later explored further in the 1960s. Feher [53,64], Angelino [64,65] were among the first to investigate sCO_2 power cycles. Feher established CO_2 as an appropriate working fluid due to its unique properties such as low critical pressure, good thermal stability at high temperatures, Inertness, non-toxicity, affordability, and availability [53]. However, the properties of CO_2 at its critical point significantly increase its density. sCO_2 cycles capitalize on this enhanced density by operating the compressor inlet near the critical point, which reduces the required

compression work. This reduction in compression work enables the achievement of high thermodynamic efficiency. Ma and Turchi [66] outlined the potential advantages of sCO_2 in power cycles, including heat transfer medium in a solar tower. Persichilli et al [67] highlighted the space-saving advantages of recuperators in sCO_2 power cycles by comparing the size of conventional shell-and-tube heat exchangers with more compact alternatives. The favourable chemical and thermophysical characteristics, single-phase operation, reduced capital costs, and enhanced efficiency, combined with a simpler plant design, strongly support the adoption of sCO_2 in power cycles. The next generation of sCO_2 technology holds significant potential for large-scale power generation. An example is the sCO_2 power turbine developed by Echogne, which is shown in Figure 2-9. sCO_2 power cycles have attractive benefits over the traditional superheated/supercritical Rankine cycles [10].

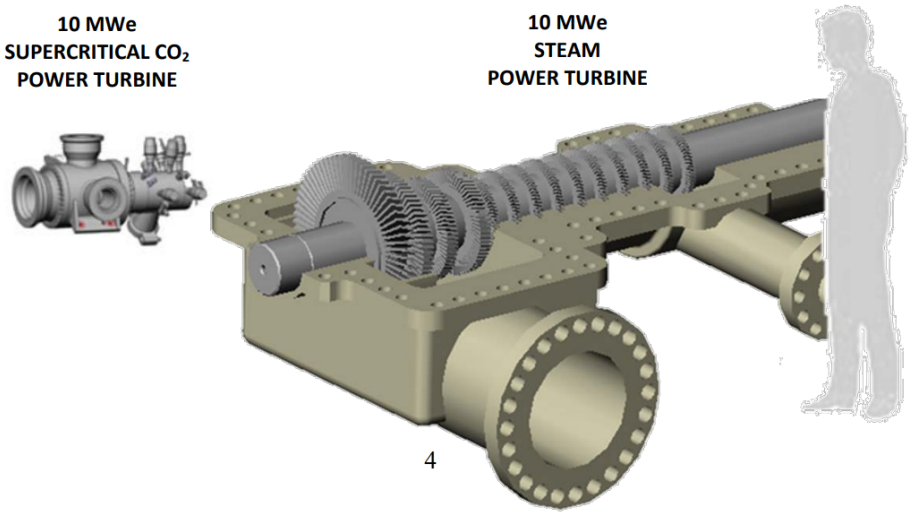


Figure 2-9 - Comparison of Echogne's 10MWe sCO_2 power turbine compared to a 10 MWe steam turbine [67]

Supercritical CO_2 turbines are compact and highly efficient, featuring a simpler design with a single casing. In contrast, steam turbines typically require multiple stages, including high-pressure (HP), medium-pressure (MP), and low-pressure (LP), each with its casing. This multi-stage setup adds complexity to system packaging because of the need for additional inlet and outlet piping for each stage [53,64].

The design advantage of supercritical CO_2 turbines arises from the unique properties of CO_2 in its supercritical state. Operating at pressures typically between 20–25 MPa, sCO_2 systems handle much higher pressures than conventional steam cycles, which generally operate at pressures between 10–18 MPa for supercritical steam [68]. These elevated pressures, combined with the high density of CO_2 near its critical point, allow for compact and efficient turbomachinery design.

For example, the power turbine in the large-scale Echogen supercritical CO_2 heat engine employs a turbine impeller measuring just 0.24 meters (9.5 inches) in diameter. Despite its small size, this turbine is capable of generating sufficient electricity to power approximately 8,000 homes, demonstrating the efficiency and scalability of sCO_2 technology.

Table 2-4 - Applications for sCO_2 for power generation

Application	Cycle Type	Size [Mwe]	Temperature (C)	Pressure
Fossil Fuel (Syngas etc)	Direct sCO_2	300 - 600	350 – 700	35
Geothermal	Indirect sCO_2	1 – 50	550 – 900	15
Wate Heat Recovery	Indirect sCO_2	1 – 10	< 230- 650	15 – 35
Shipboard House Power	Indirect sCO_2	< 1- 10	230 – 650	15 -35
Fossil Fuel (Coal, Cfb)	Indirect sCO_2	300 – 600	550 – 900	15 -35
Solar Power	Indirect sCO_2	10 -100	500 - 1000	35
Nuclear Power	Indirect sCO_2	10 – 300	350 – 700	20 -35

Table 2-4 shows that sCO_2 power cycles can be adopted for various applications, including fossil fuel, geothermal, waste heat recovery, shipboard house power, solar, and nuclear energy. sCO_2 power cycles have gained significant attention in recent years due to its higher efficiency, compactness, and environmental benefits. The increasing interest in sCO_2 cycles across various sectors is fuelled by the ability of these cycles to operate efficiently at a wide range of temperature and pressure conditions, making them highly versatile and adaptable to different energy sources.

For fossil fuel-based power plants, including those utilizing syngas or coal, the direct sCO_2 cycle has shown potential in large-scale applications ranging from 300 to 600 MWe. These plants typically operate at temperatures between 350°C and 700°C, with pressures reaching up to 35 MPa. The direct sCO_2 cycle is particularly advantageous for fossil fuel plants because it eliminates the need for steam boilers, turbines, and condensers, which are large, complex, and require substantial amounts of water for cooling [56,69]. The supercritical CO_2 working fluid can directly extract heat from combustion processes, leading to more compact systems, lower maintenance costs, and improved overall efficiency. Additionally, the high temperatures and pressures of the cycle enable better thermal energy extraction and more efficient power generation. These attributes make direct sCO_2 cycles highly suitable for large-scale power plants in regions with access to fossil fuels, such as coal and natural gas.

Geothermal power plants, which harness the Earth's internal heat for generating electricity, can also benefit greatly from sCO_2 cycles. Usually ranging in size from 1 to 50 MWe, these plants operate at temperatures between 550°C and 900°C and at pressures around 15 MPa. Geothermal energy has long been recognised for its sustainability and low environmental impact; however, conventional geothermal plants often encounter limitations related to efficiency, especially when using lower temperature geothermal resources [70,71].

Waste heat recovery systems, which employ excess thermal energy from industrial processes or exhaust gases, are another area where sCO_2 cycles have demonstrated advantages. Typically ranging from 1 to 10 MWe in size, operate

at temperatures below 230°C to 650°C and pressures around 15 to 35 MPa [8,9]. Recovering waste heat has always been a challenge due to the low temperature differentials between the exhaust gases and the surrounding environment. However, with an indirect sCO_2 cycle, waste heat recovery can be achieved more efficiently, as supercritical CO_2 is highly effective at absorbing and transferring heat even at moderate temperature differences. This leads to increased energy recovery, improved efficiency, and reduced environmental impact, making it a compelling solution for industries such as steel production, cement manufacturing, and petrochemicals, where large amounts of waste heat are generated.

For solar power applications, sCO_2 cycles are increasingly regarded as a viable option to improve the performance of concentrated solar power (CSP) systems. Solar power plants typically operate within the range of 10 to 100 MWe, with temperatures between 500°C and 1000°c. These plants depend on the ability of concentrated solar energy to produce high-temperature heat, which is then converted into electricity through thermodynamic cycles. The use of an indirect sCO_2 cycle in CSP plants offers several key advantages. The supercritical CO_2 working fluid can effectively absorb and transfer concentrated solar heat, allowing for higher efficiencies than traditional steam Rankine cycles [60].

Utilising sCO_2 as a working fluid in both open and closed cycle systems poses material challenges due to the high temperature environment. These challenges are discussed below.

2.5.1 Challenges

Despite the operational advantages, there are significant material related technical challenges that must be addressed to ensure the reliability and longevity of sCO_2 systems. These challenges stem from the extreme operating conditions of sCO_2 power plants – high pressure, high temperatures, and impurities that impacts material performance over time. The major issues include fabrication of the STEP turbine rotor and blades which was fabricated with Nimonic 105, a wrought nickel, cobalt and chromium-based alloy. Manufacturing difficulties with specialized nickel-based components have resulted in substantial cost overruns

and schedule delays, particularly when working with alloys like Inconel 740H and Haynes 282 [37]. These materials, while essential for extreme service conditions exceeding 700°C and 250 bar pressure, present unique fabrication challenges such as weldability challenges that traditional manufacturing approaches struggle to address effectively.

While some existing materials have been identified as suitable for major components, gaps remain in material qualification, long-term performance data, and component reliability. Several materials with appropriate mechanical properties are available for use in sCO_2 systems, particularly for primary components such as piping, valves, and turbomachinery. The challenges faced with key components and suitable materials are shown in Table 2-5.

One of the main challenges is the durability of the heat exchanger. Microchannel heat exchangers, which are essential components in the compact design of sCO_2 systems, are prone to erosion, fouling, and blockage over time. Thermal fatigue is another concern, as temperature fluctuations in heat exchangers can lead to material fatigue and ultimately result in failure. The combination of high temperatures, high pressures, and rapid temperature cycling makes it vital to select materials that can endure these conditions without significant deterioration.

Table 2-5 - Key components and challenges faced

	Component	Material Type	risks
Heat	Heat exchangers >1000F	Ni-Cr alloys, solid solution strengthened alloys i.e. Inconel625, Hastealloy C-276	Sco_2 oxidation, weldability, moderate strength
Turbomachinery	Turbine Housing	Ni-based casting alloys	Low (technology readiness level) TRL
	Turbine Disk	Ni-based superalloys	Shorter life, sCO_2 oxidation, creep, high cycle fatigue (HCF)
	Turbine Blade	High Cr, Ni-base superalloys, Ni-based superalloy +Pt+Al	Shorter life, sCO_2 oxidation, creep, HCF

Despite the numerous technical challenges to overcome for the successful integration of supercritical cycle technology, the utilization of sCO_2 is acknowledged as highly efficient and sustainable, a high-efficiency power cycle considering the triple bottom line – environment, social and economic, as the driving advantage. The corrosive behaviour due to its high working temperature has emphasized the material challenges. Thus, suitable material is critical for the establishment of the power system. The aforementioned advancement causes increase in machinery cost, manufacturing ease, and higher value, the higher value signifies greater generated power, higher efficiency which overall provides a net economic benefit [48].

2.6 Materials in high temperature sCO_2

Many systems operate at high-temperature sCO_2 environments – Heat exchangers, power generation systems, turbomachinery, aerospace and propulsion systems, and carbon capture and utilisation (CCU). Over the decades,

high-temperature materials such as superalloys have been optimised to provide high temperature resistance.

2.6.1 Superalloys

There is no strict or universal definition used to describe a superalloy, also known as a high-performance alloy. Nonetheless, several researchers have postulated different definitions. In this research, the utilized definition of alloy is ‘an alloy developed for elevated temperature service, typically based on groups 8-10 / VIIIB elements, where relatively severe mechanical stressing is encountered, and where high surface stability is frequently required [20]. In this research, the alloys are classified as alloys based off group VIII elements – nickel, cobalt, or iron, with a high percentage of nickel [72].

Superalloys are known for its’ great mechanical strength, creep resistance, high surface stability, and oxidation and corrosion resistance [19]. Thus, employed in high-temperature applications, especially as thermal protection system front panels [19,20]. Space components, turbine blades and vanes, rocket engines, submarines, nuclear reactors, chemical processing vessels, and heat exchangers are also manufactured using superalloys.

Superalloys are commonly classified following its predominant matrix element – nickel, cobalt and or iron, and based on casting and forging methods, superalloys can be classified as – polycrystalline equiaxed, polycrystalline directionally solidified, and single crystals. Nickel-based superalloys, iron-based superalloys, and cobalt-based superalloys are the three main types of superalloys. Metals that are nickel-based superalloys have an unmatched combination of high temperature strength, hardness and resistance to oxidative or corrosive deterioration to high temperature environments [21].

2.6.1.1 Nickel based superalloys

Nickel-based superalloys are widely used in gas turbine engine components for land-based power production and aviation propulsion. Turbines, for example, operate at elevated temperatures and pressures, creating a hostile environment for materials [21]. In a power generation system, each component of the turbine

has its own set of requirements. For example, turbine blades and vanes are positioned in areas with the highest temperature and, therefore, the highest stress, necessitating the use of nickel-based materials that are specifically designed for this application [21].

To enhance the performance and efficiency of aircraft and power-generating gas turbines, single-crystal nickel-based superalloys, which exhibit higher creep strength than traditionally cast and directionally solidified superalloys, are utilised for these components [20]. Nickel-based superalloys are employed in the hot structural components of aviation engines, which can reach temperatures of up to 1500ºC. These temperatures are close to or above these alloys' melting points. Metals usually lose their mechanical characteristics when heated. Precipitation hardened nickel-based superalloys have outstanding creep strength, thermomechanical fatigue characteristics, and oxidation and corrosion resistance throughout service.

As it is apparent from Table 2-6, although face-centred cubic (FCC) nickel is the major constituent of superalloys, many alloys contain up to 40 wt% of a combination of five to ten other elements. The elements typically alloyed with nickel to form a superalloy are highlighted in Figure 2-10. The nickel–aluminium system is the binary basis for superalloy compositions. As the level of aluminium added to γ-nickel increases, a second precipitate phase forms. This phase has a nominal composition of Ni_3Al, is designated the γ’ phase, and has an ordered intermetallic L12 crystal structure. Formation of the γ’ phase occurs in the solid state as the supersaturated solid solution of γ -nickel.

The presence of a high-volume fraction of the γ phase is crucial for strengthening [73]. All Ni-based superalloys have an austenitic face-centred cubic (FCC) matrix (γ), with additions to enhance strength through solid-solution strengthening. Additional Strengthening can be derived from carbides, mainly precipitated at the grain boundaries. in polycrystalline superalloys. Coherent or semi-coherent, as well as intermetallic phases – gamma prime (γ’) and gamma gamma prime (γ").

Table 2-6 - Effect of addition of elements on Ni-based superalloys

Effect	*Element*
Solid-solution strengtheners	Co, Cr, Fe, Mo, W, Ta, Re
Grain-boundary refiners	B, C,Zr, Hf
Carbide forms:	
MC	W,Ta, Ti, Mo. Nb, Hf
M_7C_3	Cr
$M_{23}C_6$	Cr, Mo, W
M_6C	Mo, W, Nb
Carbonitrides (MCN)	C, N
Hardening precipitates and/or intermetallic	Al, Ti, Nb
Dispersoid formers	Y,Al,O
Oxidation resistance	Al,Cr,Y,La,Ce
Improve hot corrosion resistance	La,Th
Sulphidation resistance	Cr,Co,Si
Raise solvus temperature	Co
Improve creep properties	B, Ta
Increase rupture strength	B
Retards coarsening	Re

The presence of a high-volume fraction of the γ phase is key to strengthening [73]. All Ni-based superalloys have an austenitic FCC matrix (γ), with additions to improve strength through solid-solution strengthening. Additional strengthening can be obtained from carbides, mainly precipitated at the grain boundaries in

polycrystalline superalloys. Coherent or semi-coherent, as well as intermetallic phases – gamma prime (γ') and gamma gamma prime (γ") can strengthen Ni superalloys.

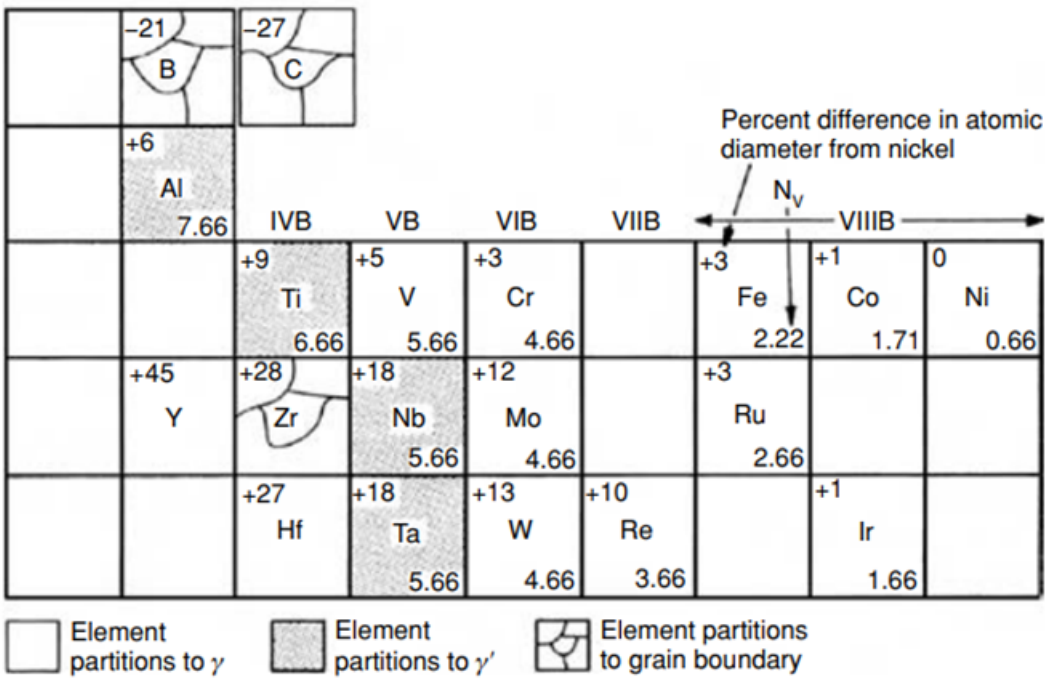


Figure 2-10 - Categories of elements important to the constitution of nickel-based superalloys, and their relative positions in the periodic table[74]

Figure 2-10 presents a modified periodic table that categorizes elements based on their partitioning behaviour in a nickel-based alloy. Elements in the white boxes prefer to dissolve to γ phase. Elements like Nb, Ti, Al, and Ta partition into ordered γ' precipitate phase. Elements like Zr, C and B tend to segregate at the grain boundaries, which could influence grain boundary improvement or embrittlement.

Microstructure of a superalloy typically consists of different phases. These phases are:

The Gamma phase (γ): This has an FCC structure and almost always forms a continuous, matrix phase where other phases are located**.** Elementary concentration includes cobalt, chromium, molybdenum, ruthenium, and rhenium.

The Gamma prime precipitate (γ'): This is a precipitate phase that typically forms in coherence. γ-matrix and contains high concentration of elements like aluminium, titanium, and tantalum. In nickel–iron superalloys and alloys rich in niobium, a similar ordered phase, γ′, is favoured over γ″.

Carbides and borides: Carbon typically found at concentrations of up to 0.2 wt%, reacts with elements like titanium, tantalum, and hafnium to form MC carbides. During processing or service, these carbides may decompose into other forms, such as $M_{23}C_6$ and M_6C, which tend to accumulate along γ-grain boundaries and are enriched with chromium, molybdenum, and tungsten. Boron in combination with elements such as chromium or molybdenum forming borides residing on the γ-grain boundaries.

In certain superalloys, especially after prolonged service, additional phases may form, such as topologically close-packed (TCP) phases like μ, σ, and laves. However, superalloy compositions are specifically designed to minimize the formation of these phases rather than encourage their development.

2.6.1.1 CM247

CM247 is a directionally solidified (DS) cast Ni-base superalloy made with a modified low carbon concentration from the MARM 247 composition used in gas turbine blades and vanes applications [75]. Table 2-7 compares CM247 and MARM 247.

Table 2-7 - Comparison of CM247 and MARM 247 elementary composition

Sample	Ni	C	Co	Cr	Al	Mo	W	Ta	Ti	Zr	Hf	B
CM247	Bal	0.07	9.5	8	5.6	0.5	9.5	3.2	0.7	0.01	1.4	0.015
MARM247	Bal	0.07	9	8	5.45	0.4	9.3	3.1	0.6	-	1.2	0.01

CM247 consists of a γ matric with a 62% volume of γ' as intermetallic phase ($Ni_3(Al,Ti)$) precipitates which is distributed within the γ -nickel matrix [76]. Jalowicka et al.[77] investigated the oxidation behaviour of CM247 in synthetic air with and without 2 vol.% SO_2 at 1050°C, and CM247 formed Al-rich oxide

scale with local intrusions due to the alloy's microstructure deteriorating its resistance to internal sulphidation.

2.6.1.2 Rene 80

Rene 80 is a polycrystalline Ni-based cast superalloy with excellent mechanical properties, including high tensile strength, creep, and fatigue resistance at elevated temperatures. For example, at 870°C, it has a rupture stress of 350 MPa for 100 hours and 240 MPa for 1000 hours; at 980°C, the rupture stress is 160 MPa for 1000 hours [78] It is a precipitation-strengthened alloy widely used to produce blades and vanes in aero-engines and gas turbines for power generation, designed to withstand service temperatures of up to 980°C [79]. The microstructure of Rene 80 consists of a γ matrix and γ' precipitates. Mallikarjuna et al. [80] investigated Rene80 at 900°C and results show Rene 80 forms Cr_2O_3 rich oxide layer and TiO_2 as well as severe spallation in air.

2.6.1.3 Inconel 939

Inconel 939, known as IN939, is a precipitation-hardened Ni-Cr-Co superalloy developed through the modification of Waspaloy. It has an operating temperature of up to 850°C. It is mainly used for manufacturing of gas turbine blades, vanes, as well as turbine casing and burner nozzles. Aside from its high Cr content, IN939 has a high Co content, which prevents formation of *η* phase during heat treatments or hot working [81]. Murata et al. [82] established that the Ti/Al weight ratio of 2 improves the corrosion resistance of IN939. The alloy's strength results from the synergy between the dendritic gamma (γ) solid solution matrix and the dispersed gamma-prime (γ′) precipitates, which work together to improve its mechanical properties[83]. The presence of γ and γ′ phases in the alloy's microstructure enhances its strength, primarily due to the optimal concentrations of tungsten (W), tantalum (Ta), and niobium (Nb) [22]. The manufacturing process of wrought alloys yields suitable strength and creep properties due to the presence of these elements. The alloy has a high titanium content. This element plays a crucial role in forming γ′ precipitates, which contribute to enhanced strength at elevated temperatures [20]. A High number of carbide-forming elements – Ti, Nb and Ta are present with no Mo. MC carbides, which are known

to be free from Mo, can improve the fatigue life of the alloy [22]. Its high temperature resistance is achieved through a combination of dispersion hardening, precipitation hardening, and solid solution strengthening.

2.6.1.4 Inconel 738

IN738 is a cast Ni-base superalloy utilised for turbine blades in high temperature gas turbines and turbojet engines [84]. IN738 is a precipitation-strengthened alloy with an operating temperature of up to 980°C. This high service temperature comes from the precipitation of the ordered $L1_2$ intermetallic $Ni_3(Al,Ti)$ γ′ phase within the FCC γ matrix [22,85]. At high temperature, the superalloys have properties such as high creep rupture resistance, elevated yield strength, and enhanced resistance to hot corrosion, oxidation, and sulphidation [86]. Solid solution strengthening of the γ phase is achieved through the addition of Cr, Co, and refractory metals such as Nb, Ta, Mo, and W. Meanwhile, grain boundary strengthening is enhanced by the presence of Zr, borides, and carbides [22,87], It is widely recognized that superalloys with high γ′ content, such as IN738, are considered ‘non-weldable’ due to their significant aluminium and titanium levels. These elements contribute to poor castability and weldability, making the alloy highly susceptible to solidification cracking, liquation, and strain-age cracking [88,89].

2.6.1.5 Alloy 625

Alloy 625 was first patented in 1962, registered under Inconel 625 on the basic Ni-Cr-Mo-Nb alloy system. Alloy 625 is a solid solution-strengthened alloy which precipitates γ". Alloy 625, which is widely used in high-temperature applications, has been employed in the turbine casing of the Allam cycle pilot plant in Texas [90].

Alloy 625 is widely used due to its exceptional combination of high strength, resistance to pitting and stress-corrosion cracking, excellent fatigue performance, and remarkable weldability. Additionally, it performs efficiently across a broad temperature range, from cryogenic conditions to elevated temperatures up to 900°C. Applications of Alloy 625 span various fields, including steam-line systems, aerospace components (such as rocket nozzles, aircraft ducting, and turbine seals), nuclear technology, naval and marine environments (e.g., submarine parts), and the chemical industry (reaction vessels, distillation columns, and valves). It is also employed in dissimilar welding [91]

Alloy 625 is considered in advanced turbine components, including turbine casing. The alloy is known for its high creep strength and good oxidation resistance at elevated temperatures; however, studies have shown that Alloy 625 exhibits microstructural changes when exposed at high temperatures for a prolonged period [92,93]. Suave et al.[94] studied the thermal ageing of Alloy 625 at 550 - 900°C for up to 2000h. Alloy 625 ageing (550–900 °C, up to 2000 h) shows γ″ precipitation (550–750 °C) and δ phase formation (650–900 °C). γ″ coarsens per Lifshitz–Slyozov–Wagner (LSW) theory. Grain growth starts at 900 °C due to M_6C carbide dissolution. Shear spinning enhances δ precipitation, slowing γ″ formation, consistent with ageing under load.

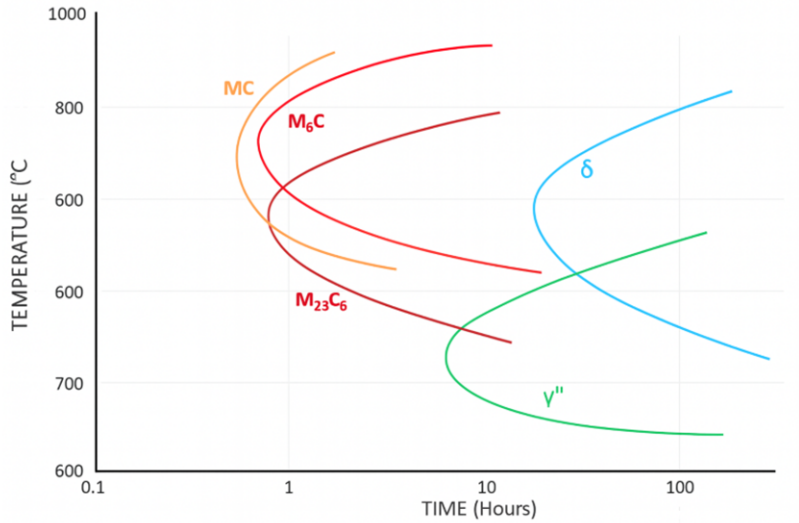


Figure 2-11 - Approximate temperature time transformation diagram of Alloy 625

Different carbides as well as intermetallic phases can precipitate depending on the temperature and exposure duration. Figure 2-11 shows the types of carbides that form at elevated temperatures.

$Ni_3(Nb,Al,Ti)$ γ" and δ-Ni_3Nb phases are observed on the microstructure depending on the temperature. The γ″ phase is a coherently ordered A_3B compound, with the δ-phase representing its equilibrium intermetallic state. The latter, being an incoherent Orthorhombic phase precipitates in a needle-like form. δ phase can form directly or through the transformation of the metastable γ″ phase [95].

2.6.2 Additive Manufacturing

This wide-cut application of superalloys is essentially due to its exceptional resistance in harsh environments whilst maintaining high mechanical and oxidation properties. Nevertheless, these elevated properties in a high temperature environment makes it challenging manufacturing these types of alloys i.e. nickel-based superalloys.

Additive manufacturing also known as rapid prototyping or 3D printing, as defined by ASTM International [25] as the ‘process of joining materials to make parts from 3D model data, typically joined layer by layer’. This is opposed to subtractive or formative manufacturing methods. AM has recently gained more attention and has shown great promise for manufacturing complex parts whilst minimizing material waste in addition to a reduced production time. This technique has evolved into a range of processes utilising diverse materials, including metals, polymers, and ceramics. AM differs from traditional and subtractive methods due to its ability to offer the aforementioned advantages, making it suitable for prototypes and small production runs. Despite these advantages, AM faces challenges in aspects including limitations in material variety, part size, and post-processing requirements, possibly leading to anisotropic mechanical properties [96].

ASTM, ASTM F42-Additive manufacturing classified AM techniques into seven broad sets shown in Figure 2-12.

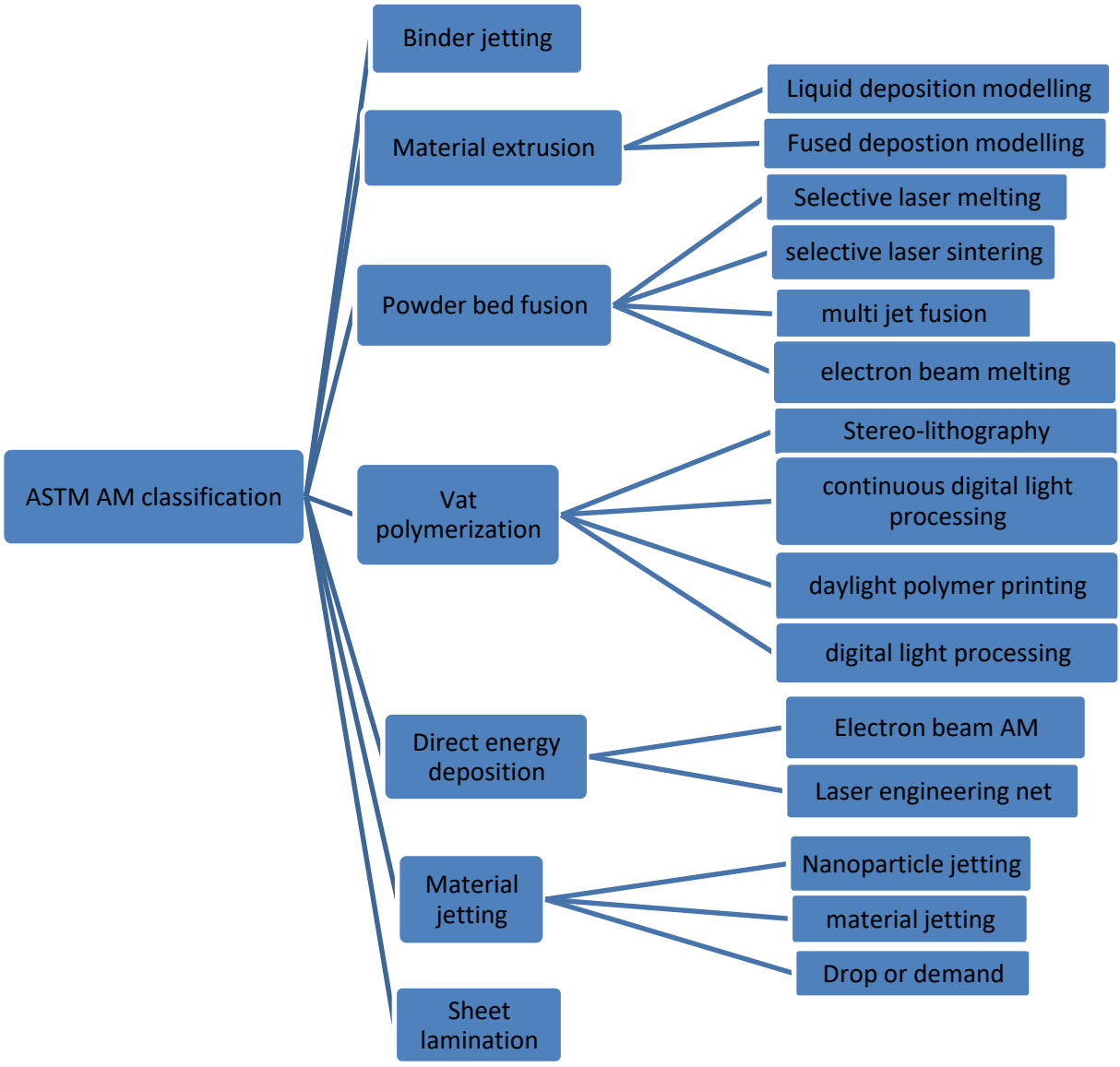


Figure 2-12 - ASTM classification of AM

Table 2-8 compares some AM technologies, including their limitations and the common materials used.

Table 2-8 - Comparison of some AM technologies adopted from [96]

AM Technology	Advantages	Limitations	Common Materials
Fused deposition modelling (FDM)	Low price Speed efficiency Low maintenance	Requires high temperatures Requires supports Inability for certain geometries	Polylactic acid Polyethylene terephthalate glycol
VAT polymerization (VP)	Exceptional details and surface ideal for intricate features	Limited build volume Shrinkage & warping Toxicity & environmental concerns	Photocurable resins Waxes Ceramics
Material jetting (MJ)	Exceptional resolutions &details Multi-material and full-colour Wide array of materials	High costs Restricted build volume Low printing speed	Photopolymers Thermoplastic polymers Metal powders
Binder jetting (BJ)	Full-colour Various materials	Low-density parts Labor-intensive Complex post-processing	Polyvinyl pyrrolidone Polyvinyl alcohol Polyacrylic acid
Selective laser sintering (SLS)	Support free Isotropic final products Complex geometries	Porosity, shrinkage, and impurities Poor surface quality Post-processing for final appearance	Plastics Composites Ceramics
Selective laser melting (SLM)	Binder-free Often faster than SLS High powder recyclability	High costs Less material flexibility Support structures and inert gas	Titanium alloys Stainless steels Aluminium alloys
Direct metal laser sintering (DMLS)	Support-free Various materials of metal alloy High power recyclability	High costs High porosity Limited build volume	Stainless steels Aluminium Titanium
Multi-jet fusion (MJF)	High speed & efficiency Less post-processing Multiple colours High ductility	Material limitations Specific use cases	Polyamides Thermoplastic Polyurethanes Polypropylene
Direct energy deposition (DED)	Minimizes waste Part repair and modification Efficiency for larger components	Post-processing for a smooth finish Low precision	Stainless steel Titanium alloys Nickel-based alloys

Break throughs have occurred in the energy and power sector due to AM offering freedom of design. AM has shown advancements and continues to advance in the energy and power sector in applications such as 3D printed gas turbine blades [28], In geothermal applications, permits the development of heat exchangers with improved thermal conductivity [97]. Solar panels, more efficient and cost-effective solar cells [98]. Wind turbine blade Molds and nacelle components [99]. In the nuclear sector, developing complex nuclear reactor components with improved performance and safety features.

The process of transformation of 3D model data to a 3D physical part in various techniques are technically the same thus processing steps are performed using different mechanisms depending on the energy employed. The overall process is demonstrated in Figure 2-13.

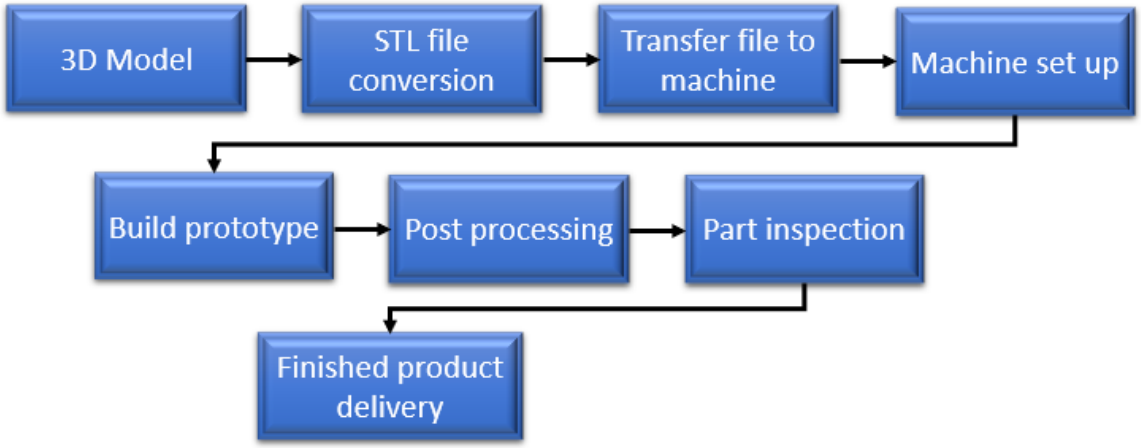


Figure 2-13 - Processing steps of converting 3D CAD to 3D AM object

Utilizing the procedural methodologies depicted in Figure 2-13, the advancement of innovative, and progressive additive manufacturing technologies has substantially enhanced, leading to a proliferation of applications within an industrial sector.

2.6.2.1 Laser powder bed fusion

Laser power bed fusion (LPBF), also known as selective laser melting (SLM), is an AM technique that involves melting and fusing the material powder layer after layer [25]. Figure 2-14 illustrates the LPBF process. Using the LPBF, the powder

bed is placed in an inert atmosphere or partial vacuum to protect the molten metal. Typically, an energy source, in this case, a laser, is employed to scan the spread powder layer after layer to selectively melt the powder material according to the 3D CAD model [100]. After a layer is scanned, the build platform goes downwards, and the powder dispenser piston goes upwards by the defined layer thickness. The recoater blade deposes powder across the powder dispenser chamber where it is subsequently scanned again by the energy source. This is repeated continuously layer-by-layer until part is completed.

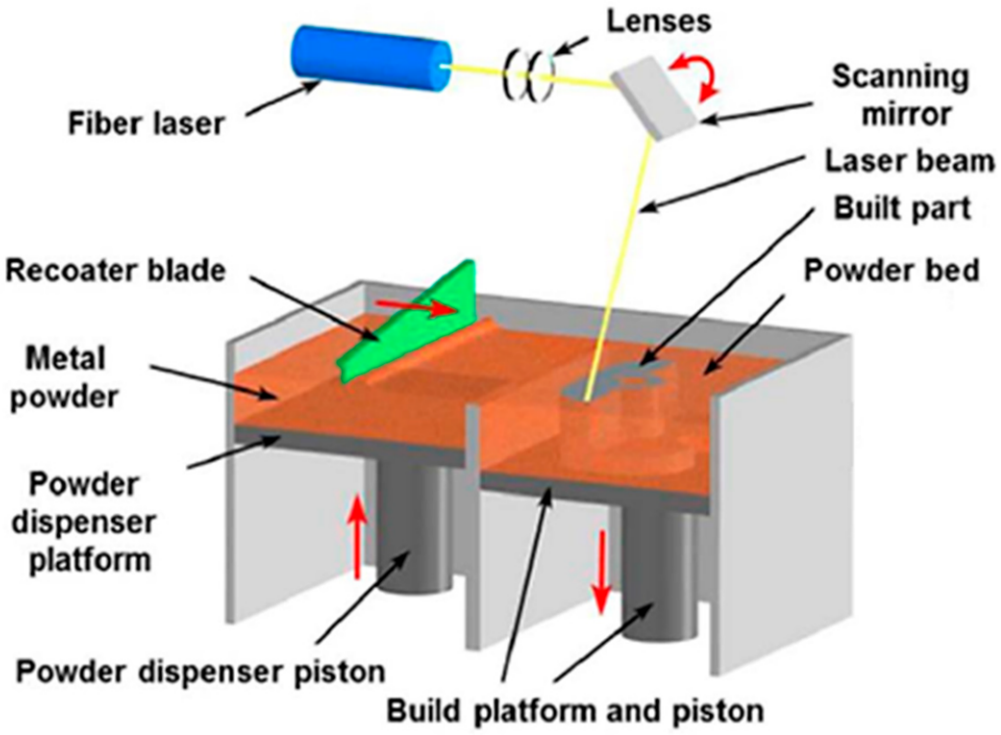


Figure 2-14 - Schematic of LPBF technique

2.6.2.2 Advantages and Limitations of LPBF

LPBF, like other AM techniques, benefits from a shorter build time compared to traditional manufacturing processes. LPBF has various advantages, including high forming accuracy, high precision with tolerance of around ±0.1 to ±0.3% of feature dimension [101], and ability to fabricate complex geometries. Unlike sintering-based methods, LPBF fully melts and fuses metal powder, producing denser parts, parts with up to 99.9% density and maximizing tensile strength [96].

Hager et al. [102] were able to print LPBF AF9628 steel with density >99.5% with two samples being 99.9% dense.

Despite the ability to produce dense, near-neat shape parts, this technique still struggles with limitations. One major limitation is the higher energy cost; the technique relies on extremely high energy to fully melt and fuse the material [68]. Due to this energy cost, LPBF has been found to be less energy efficient than SLS. LPBF also experiences defects which are most often related to the higher temperature. Some defects include balling [32], denudation [33], surface roughness [34], porosities (lack-of-fusion, keyhole, and gas porosity) [32,103,104], cracking (solidification [105] and liquation) and delamination [106]. Lack of fusion porosity is often linked to the balling effect, where a high scan speed combined with low laser power results in insufficient melting time for the powder [107]. The unique thermal conditions inherent to LPBF processes significantly influence the microstructure and, subsequently, the oxidation behaviour of the components [108,109] The oxidation behaviour of nickel-based superalloys is governed by the formation of protective oxide scales primarily chromia (Cr_2O_3) and alumina (Al_2O_3) acting as a diffusion barrier to prevent further oxidation [110,111]. The effectiveness of the protective layers depends on various factors including alloy composition, microstructure, surface condition, and environmental conditions i.e. temperature, oxygen partial pressure, and presence of reactive species like CO_2 [112]

LPBF processing involves extreme thermal conditions due to the rapid heating and cooling cycles, with cooling rates typically ranging from 10^3 to 10^6 K/s [113,114]. Resulting in non-equilibrium solidification and unique microstructural features distinguishing it from conventionally manufactured. According to Korner et al [115], the interaction between the laser and the material creates localized melt pools with steep temperature gradients leading to columnar grain growth along the build direction. LPBF manufactured nickel-based superalloys exhibits distinctive microstructural features that influence oxidation behaviour. The conditions of rapid solidification promote the formation of fine, columnar grain growth along the build direction, can influence the diffusion pathways for oxidation

and affect the protective oxide scale formation [116]. Amato et al. [117] established that the non-equilibrium can alter or suppress the precipitation of strengthening phases such as γ' (Ni_3Al) and carbides, affecting not only mechanical properties but also the distribution of elements critical for oxidation resistance.

LPBF processing of Alloy 625 results in several microstructural modifications that influence oxidation behaviour. LPBF Alloy 625 typically exhibits a fine, columnar grain structure with grains oriented along the build direction, generally finer than conventionally processed material due to rapid cooling rates [117,118]. The rapid solidification can lead to micro segregation of alloying elements, particularly niobium and molybdenum, which can affect local oxidation behaviour [119]. The rapid cooling suppresses the precipitation of secondary phases such as δ-phase (Ni_3Nb) and carbides, resulting in a more homogeneous matrix composition [120].

Research has been conducted on the oxidation behaviour of LPBF processed Alloy 625. The high surface roughness and defects in as-built LPBF Alloy 625 could lead to accelerated initial oxidation compared to conventionally processed material with increased surface area and presence of surface defects which provides additional sites for oxidation initiation [120]. LPBF Alloy 625 typically forms chromia protective scales similar to the conventional material, but the scale morphology may differ due to unique microstructural features, with the fine grain structure influencing the nucleation and growth of oxide scales [118].

Tucho et al. [121] Investigated the microstructural evolution of LPBF Inconel 718 solution heat treated to 1100°C or 1250°C to examine the dissolution of macro and micro-segregated precipitates. < 1100°C, the laves and segregated phases were not dissolved, while at 1250°C, the sub-grains, including precipitates and dislocation networks along the sub-grain boundaries, were entirely dissolved, but micro segregated precipitates and carbides were not.

During high-temperature exposure, changes were observed in precipitation behaviour that could influence oxidation resistance. The study found that prolonged exposure at elevated temperatures led to the formation of secondary phases that affected the distribution of chromium and other oxidation-resistant

elements. Criales et al. [122] conducted investigations on LPBF processing parameters for Alloy 625 and their effects on microstructure and structural integrity. The study investigated the effects of process parameters and scan strategy on the melt pool size, shape and relative density.

2.6.3 Failure mechanisms in extreme conditions

Failure analysis is crucial as it provides a thorough understanding of a material's role and properties, which are critical to ensuring it is 'fit for purpose' in specific industrial processes and applications. The importance of failure analysis is shown in Figure 2-15.

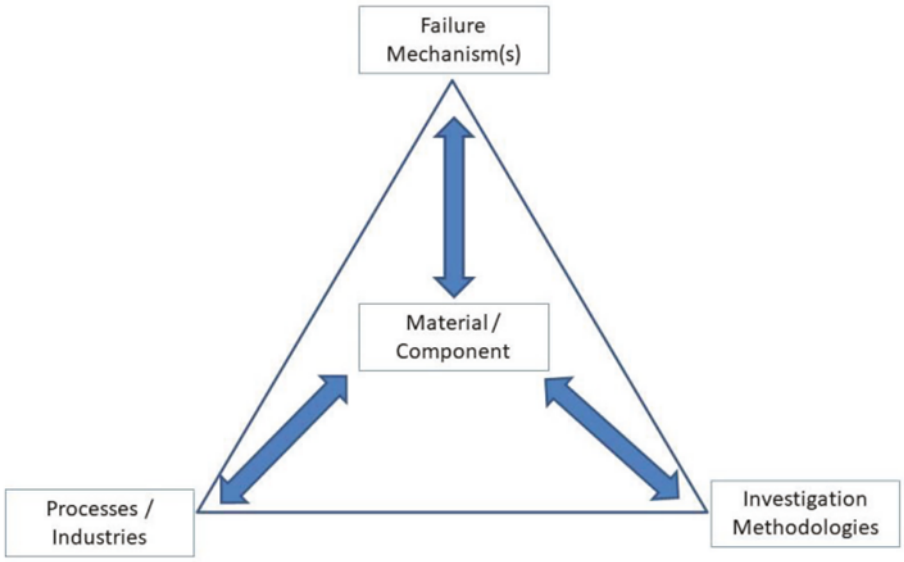


Figure 2-15 - Failure analysis, the role of understanding a material's property [123]

Increasing efficiency requires an increase in the turbine inlet temperature (TIT) of gas turbine engines. This increase in temperature presents material challenges due to the extreme conditions. Nickel-based superalloys are susceptible to degradation as temperatures are elevated, leading to failure.

The failure mechanisms range from instantaneous, caused by overload or static failure, to more gradual or delayed modes, such as creep and creep fatigue, fatigue from cyclic loading, corrosion, environmentally assisted cracking, as well

as wear and surface degradation. The service life of high-temperature and high-pressure components, such as gas-turbine blades and heat exchangers, is primarily influenced by the deterioration of material properties resulting from mechanical and thermal loading, as well as high-temperature corrosion.

2.6.3.1 Oxidation

When a metal surface is exposed to an oxidizing environment, the initial interaction begins at the gas-solid interface. Oxygen molecules from the gas environment are adsorbed onto the metal surface. The molecules dissociate into atoms and accept electrons from the underlying metal. This electron transfer facilitates the chemical reaction between the oxygen and the metal atoms, resulting in the formation of a thin oxide film, as shown in Figure 2-16.

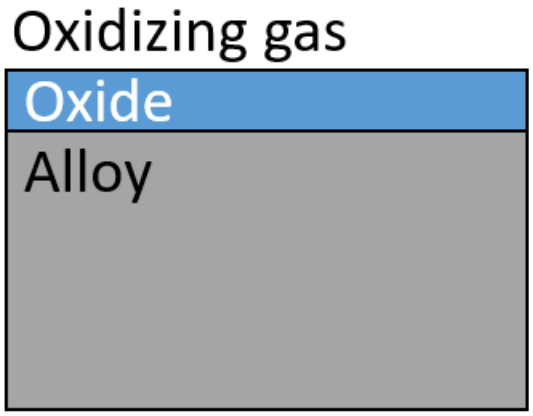


Figure 2-16 - Schematic diagram of the cross-section of an oxide layer formed on the surface of an alloy

As oxidation progresses, the growth of the oxide layer becomes governed by the transportation of atoms through the existing oxide scale. This transportation occurs through diffusion, driven by the difference in chemical potential across the oxide layer.

Based off the Fick's law, the flux of metal species B through the oxide layer is proportional to the gradient of the chemical potential $\Delta\mu_B$ across the oxide scale of thickness X_{BO}

$$j_B = -D_B \frac{\Delta\mu_B}{X_{BO}}$$ Equation 2-1

The scaling rate being proportional to the ion flux flowing through the scale

$$\frac{dX_{BO}}{dt} = j_B \cdot V_{BO}$$ Equation 2-2

Where V_{BO} is the molar volume of oxide BO, combining Equations (2-3) and (2-4) and then integrating, the relationship describing the parabolic growth of the oxide layer thickness is obtained.

$$X_{BO}^2 = 2k_p + C$$ Equation 2-3

When C = 0, k_p value is the by-product

$$k_p = D_B V_{BO} \Delta\mu_B$$ Equation 2-4

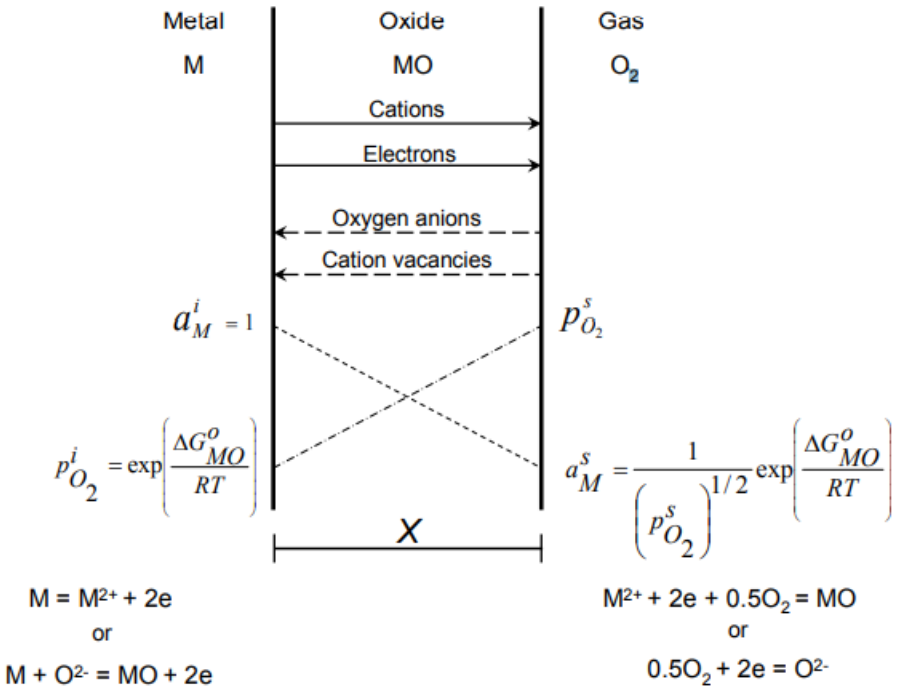


Figure 2-17 - Wagner's Model of Oxidation [110]

Wagner's parabolic oxidation rate prediction is frequently observed experimentally in high-temperature oxidation processes. However, as previously

mentioned, this theory relies on several assumptions that are not always fully met. Various independent factors can influence overall oxidation kinetics, such as increased metal consumption due to oxide spallation followed by scale healing [110] or the reactive evaporation of the oxide layer [110]. Another key simplification in Wagner's theory is its exclusive focus on lattice diffusion within the oxide, without accounting for short-circuit diffusion along grain boundaries. In oxides with very few lattice defects, such as Al_2O_3, oxygen diffusion along grain boundaries often becomes the dominant transport mechanism, leading to sub parabolic oxidation kinetics [110]

Nickel based superalloys employed in high-temperature applications depend on formation of slow, dense, good adherent chromia or alumina scale [110,111]. Commonly, binary nickel alloys with low percentages of less noble alloying elements, such as Al or Cr, are subject to internal oxidation when exposed to an oxidising atmosphere at high temperatures [110,111]. However, when the mole fraction of the less noble component in binary nickel alloys is increased to exceed a certain critical amount, the nickel alloy no longer oxidizes internally but rather forms a protective and compact layer of the external single-oxide (alumina or chromia) scale on the alloy surface [110]

Chromia (Cr_2O_3) is the most stable form of chromium oxide at high temperatures. It's structure consisting of a hexagonal close packed sublattice of anions with 2/3 octahedral sites occupied by Cr [110]. Cr_2O_3 is stable when the oxygen partial pressure in the environment is more than the oxide's equilibrium partial pressure also regarded as 'dissociation pressure'.

$$2Cr + \frac{3}{2}O_2 = Cr_2O_3$$

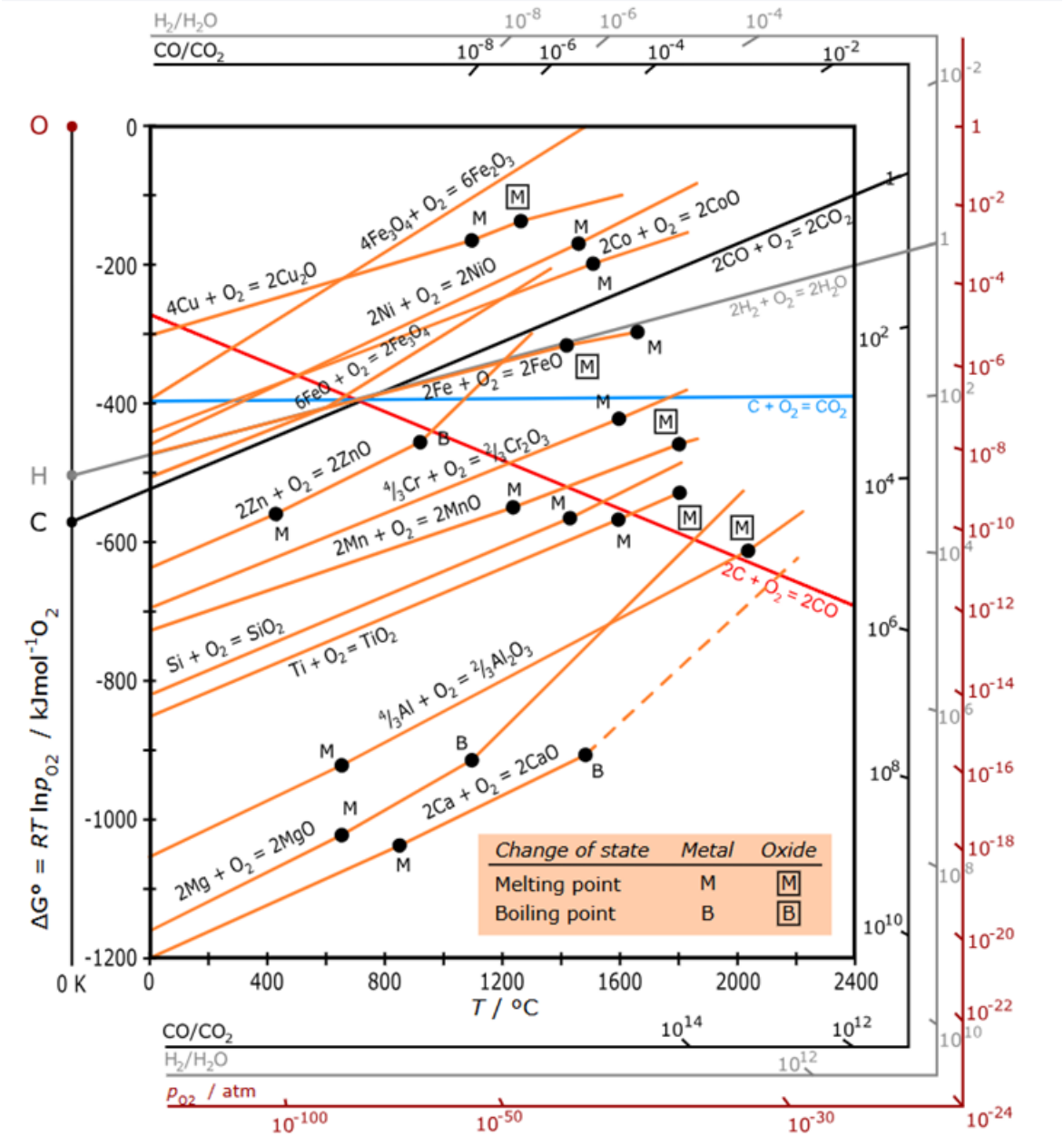


Figure 2-18 - Ellingham-Richardson diagram [110]

Figure 2-18 displays the Ellingham-Richardson diagram, which shows the standard free energy of oxide formation as a function of temperature and equilibrium oxygen partial pressure [34,35]. This shows metals reacting with oxygen and the lower a line is on the diagram, the more stable the oxide it represents.

According to Wagner's oxidation theory, the mass transport of anions and cations across the oxide scale is governed by two primary driving forces: the electric field and the chemical potential gradient across the oxide layer. Wagner established a relationship between the parabolic rate constant and the diffusion rate of ionic species in the oxide scale, expressed by the equation below:

$$\mathbf{K} = \frac{6V}{D}(C_1 - C_2) \qquad \text{Equation 2-5}$$

where V represents the oxide volume per unit quantity of diffusing species, D denotes the diffusion coefficient, and C_1 and C_2 are the concentrations of the diffusing species at the metal-scale and scale-gas interfaces, respectively [45]. However, Wagner's theory models an idealized situation, which relies on the following assumptions [46]:

a. The oxide scale is adherent and dense.
b. The ionic (or electronic) diffusion across the scale is the rate-determining step.
c. Thermodynamic equilibrium is maintained throughout the scale and at both the metal-oxide and oxide-gas interfaces.
d. The solubility of oxygen in the metal is negligible.
e. The metallic substrate is assumed to be pure.

2.6.3.2 Carburization

Carburization occurs in various industrial processes where alloys are exposed to carbon-rich atmospheres at high temperatures. During this process, carbon from the surrounding environment diffuses into the matrix, leading to the formation of internal carbides [124]. The carburization process involves two primary stages. Initially, the carbon-containing gas penetrates the oxide layer on the alloy's surface. Then, a portion of the carbon reacts with alloying elements to form carbide precipitates. At the same time, the remaining carbon creates an amorphous layer at the interface between the oxide layer and the matrix [125]. This phenomenon is relevant in environments containing CO_2, which could dissociate at high temperatures to provide a source of carbon [111]. Carburization can significantly alter the microstructure and mechanical properties of

superalloys, potentially leading to premature failure in critical applications. The carburization of nickel-based superalloys in CO_2 environments begins with the dissociation of CO_2 molecules at the gas-metal interface. This process can occur through several reactions, with the Boudouard reaction being particularly significant at elevated temperatures [126]:

$$2CO \longrightarrow C + CO_2$$

CO_2 can react directly with the metal surface:

$$CO_2 + M \longrightarrow MO + CO$$

The generated CO can react further to deposit carbon:

$$CO_2 + H_2 \longrightarrow C + H_2O$$

These reactions can subsequently lead to carbon deposition on the metal surface or carbon diffusing into the alloy resulting in carburization. This is relevant at high temperatures and under low oxygen partial pressures, where carbon becomes more thermodynamically stable than certain metal oxides. The thermodynamic driving force for these reactions depends on temperature, pressure, and the composition of the gas phase.

The Ellingham helps to visualise this transition. At elevated temperatures, the line for carbon oxidation ($C + O_2 \rightarrow CO$ or CO_2) intersects the stability lines of various metal oxides. When the oxygen partial pressure is sufficiently low—such as in high-purity CO_2 or CO-rich environments—carbon becomes more stable than some metal oxides (e.g., NiO or FeO), enabling carburization instead of oxidation.

Chromium is the most important alloying element for carburization resistance in nickel-based superalloys. It forms a protective Cr_2O_3 scale that acts as a barrier to carbon ingress [127]. Additionally, chromium has a high affinity for carbon, forming stable $Cr_{23}C_6$ carbides that can trap carbon near the surface, preventing deeper penetration.

The effectiveness of chromium depends on its concentration, with a minimum of about 20% being necessary for significant carburization resistance. The

relationship between chromium content and carburization rate can be approximated by:

$\log(kp) = A - B(\%Cr)$ (13) Equation 2-6

where kp is the parabolic rate constant for carburization, %Cr is the chromium content in weight percent, and A and B are temperature-dependent constants [111].

Aluminium and silicon can enhance carburization resistance by promoting the formation of protective oxide scales (Al_2O3 and SiO_2) that have low carbon permeability [128]. Yang et al. [129] reported that a due to rapid diffusion of Mn in the chromia layer, the Mn-Cr spinels oxides grew slower than the single chromia slowing down the consumption of Cr. However, Pint and keiser [130] alumina forming alloys such as Alloy 216 which formed thin alumina layer improved the corrosion resistance in sCO_2 at 750 °C/20 MPa. Carburization at oxide/metal interface were observed in chromia forming alloys but not observed in alumina forming nickel-based alloy, hence alumina layer shows a better barrier against carburization than the chromia layer [131,132].

2.6.3.3 Sulphidation

The supercritical CO_2 (sCO_2) Brayton cycle can operate in either an open or closed configuration. In closed systems, air ingress may occur through leaks or degassing, introducing external contaminants. In contrast, open systems generate CO_2 through oxy-fuel combustion of coal, which also produces various byproduct gases [129].

SO_2 gas similar to CO_2 can diffuse through the chromia scale. The formula would be

$$SO_2\,(g) = ½\ S_2\,(g) + O_2\,(g)$$

The thermodynamics of sulphidation can be analysed using the Ellingham diagram, where sulphides typically lie above the line, indicating greater stability at lower oxygen partial pressures and high sulphur activity. Sulphur diffuses preferentially along the grain boundaries as shown by Beckmann and Woodford [133], their study on Ni-270 showed sulphur penetrated deeply into the alloy at partial pressures as low as 6×10−86 \times 10^{-8}6×10−8 atm, especially when temperatures were increased from 450°C to 800°C.

Sulphur and other sulphur species such as H_2S could diffuse through oxide scales or alloy grain boundaries and react internally with alloying elements.

Lee et al. [134] showed that sulphur reduces the adhesion of oxide scales through segregation to the metal/scale interface and to oxide rain boundaries, promoting scale spallation and decreasing the protectiveness of oxides such as Cr_2O_3 and Al_2O_3. Huczkowski et al. [135] investigated the corrosion behaviour of P92, Super S304HCu, and Alloy 617 in simulated oxyfuel combustion gases with and without SO_2 at 550–700 °C. P92 was unaffected by SO_2, while SO_2 improved oxidation resistance in S304HCu by promoting Cr-rich oxide formation. In contrast, Alloy 617 experienced increased corrosion at lower temperatures due to SO_2 but formed stable chromia at 700 °C. Olaksak et al. [136] investigated various steels – Low Cr, High Cr steels exposed to 95 % CO_2, 4 % H_2O, 1 % O_2 with/without 0.1 % SO_2 at 550 °C and 1 atm. In SO_2-free conditions, high-Cr steels formed protective Cr-rich oxides, while low-Cr steels developed thicker Fe-rich oxides. Adding SO_2 had minimal effect on low-Cr steels but degraded high-Cr steels by incorporating sulphur into chromia, causing scale breakdown and Fe-rich nodule formation.

2.6.3.4 Nitridation

Nitrogen-rich atmospheres combined with high temperatures are encountered in power plants, including the Allam cycle. Although the Allam cycle uses pure O_2, which results in very low NO_X formation, trace NO_X will be generated from fuel-derived N_2 in the natural gas. Nitridation is regarded as a significant failure mechanism that can compromise component integrity and overall service life.

Nitridation occurs when nitrogen from the operating environment interacts with the substrate alloy, leading to the formation of nitrides through chemical reactions with reactive alloying elements. Unlike oxidation that can form protective scales, nitridation typically results in internal precipitation phenomena that can severely compromise the mechanical properties and accelerate component failure [137].

The nitridation process in nickel-based superalloys is primarily driven by thermodynamic forces that promote nitride formation. At high temperatures, nitrogen molecules split at the alloy surface, and atomic nitrogen then dissolves into the metal substrate.

The standard free energy of formation ($\Delta G°$) of nitrides provides insight into which elements preferentially form nitrides. In decreasing order of stability, titanium, aluminium,

chromium, and niobium form thermodynamically favourable nitrides in typical superalloy compositions [138]. This results in the formation of various nitrides such as:

1. Titanium nitrides (TiN)
2. Aluminium nitrides (AlN)
3. Chromium nitrides (Cr_2N, CrN) : precipitates that form predominantly along grain boundaries.
4. Niobium nitrides (NbN)

The internal nitride precipitates mainly form beneath the alloy surface, creating a nitride precipitation zone whose depth is proportional to the square root of exposure time [129,130]. As nitride-forming elements (notably Al and Ti) are depleted, the local concentration of these elements drops below the critical levels needed to sustain the γ' strengthening phase. This causes the γ' phase to dissolve in these regions, forming depletion zones with significantly reduced mechanical properties [131]. Furthermore, in environments containing carbon, simultaneous carburisation and nitridation can occur, resulting in complex carbonitride precipitates with distinct morphologies and properties [132].

The formation of internal nitrides and associated depletion zones significantly influences the mechanical performance of superalloys. Nitride precipitation along grain boundaries can cause considerable embrittlement and diminished ductility. This effect is particularly pronounced at elevated temperatures where grain boundary sliding becomes a significant degradation mechanism [139,140]. The hard, brittle nitride particles act as stress concentrators, facilitating the initiation and propagation of cracks under tensile loading. The consumption of γ'-forming elements (Al, Ti) during nitridation results in the dissolution of these strengthening precipitates in affected regions. This microstructural degradation significantly reduces creep resistance, a critical property for power plant components operating at high temperatures under sustained loading [141]. The presence of brittle nitrides and element-depleted zones creates preferential sites for fatigue crack initiation. Under cyclic loading conditions typical in power plant operations, these microstructural features accelerate both crack initiation and propagation, reducing component fatigue life [142].

Several approaches can mitigate nitridation in nickel-based superalloys. Modified superalloy compositions with reduced concentrations of highly reactive elements like Ti and Al, or increased levels of nitridation-resistant elements, represent one approach. For instance, increasing Cr content above 25 wt% can promote the formation of a protective

chromia layer that impedes nitrogen ingress [143]. Surface coatings provide an effective barrier against nitrogen penetration.

2.6.4 Protective treatments

Increasing turbine inlet temperature (TIT) results in an increment of turbine efficiency thus improving energy saving. Ni-based superalloys are prone to Oxidation after prolonged exposure to high temperatures, this exposure causes turbomachinery to fail earlier than expected resulting in loss of millions of pounds. For protection of materials applied in high-temperature conditions, surface treatments can be used to the component, acting as a protective cover, to improve its lifetime. These protective coatings could be bond coat/ environmental barrier coats or Thermal barrier coatings (TBC).

Such protective coatings have high resistance to oxidation, excellent microstructural and thermal stability, and crack resistance. The ongoing demand for enhanced efficiency in turbine engines continues to propel the development of advanced coating systems for protecting superalloys operating at higher temperatures [144]. TBC has been utilised in turbine plants for improved performance and longevity. A TBC is consists of an inner layer of metallic bond coat (MCrAlY), and an outer layer of ceramic top coating (8wt% yttria stabilised zirconia (YSZ)) [145].

Bond coat is the oxidation resistant intermediate layer between the ceramic topcoat and the substrate. The primary role is to protect the substrate alloy from oxidation and corrosion. While BCs are primarily made of metallic materials, intermetallic phases significantly influence their behaviour and effectiveness. The two main types of high-temperature coatings widely used for resistance to oxidation and hot corrosion are diffusion aluminide coatings and MCrAlY coatings, where the M stands for Ni, Co, Fe, or a combination. Its primary function is to shield the underlying superalloy from oxidation and hot corrosion. In addition to this protective role, the bond coat, characterized by a thermal expansion coefficient of approximately 13–14 $mm \cdot m^{-1}$ in the 1100–1300 K [146] temperature range, helps to mediate the thermal expansion disparity between the substrate (13–13.5 $mm \cdot m^{-1}$) and top coat (9–10 $mm \cdot m^{-1}$) [147]. This mismatch

arises due to the inherent differences in their respective coefficients of thermal expansion [148,149] . Wu et al. [150] established that the TBC system is primarily driven by oxidation of the bond coat, along with residual stress from thermal expansion mismatch. This stress is intensified by the “pegging effect,” where oxides protruding from the bond coat grow into radial cracks within the topcoat. Marm247 coated with ZrO_2 8 wt% Y_2O_3/Ni-22Cr-10Al-1Y duplex thermal barrier coatings were tested under various operating conditions within the temperature range from 1000 to 1150°C, it reported the presence of NiO and $Ni(Cr,Al)_2O_4$ on both the underside of the spalled ceramic topcoat and the external surface of the oxide scale on the MCrAlY bond coat after topcoat spallation was observed in all tested specimens. Maier et al. [151] demonstrated that the oxidation of components within both the YSZ topcoat and the MCrAlY bond coat compromises the bond coat's protective effectiveness during thermal ageing. They also observed significant degradation of the bond coat, along with substantial formation of nickel oxide. This nickel oxide was found to grow outward into the thermal barrier layer, leading to increased stress within the coating system and contributing to failure near the interface between the YSZ topcoat and the MCrAlY bond coat.

3 Experimental procedures and microstructural analysis

Understanding the degradation mechanisms of first-stage blade and heat exchanger materials in high-temperature supercritical CO_2 environments requires controlled laboratory testing, including long-term experiments and detailed microstructural analysis. This chapter outlines the methodology of oxidation /carburization investigations. The experimental procedures were designed to replicate realistic operating conditions while controlling variables for precise analysis. Isothermal oxidation testing is an approach used to investigate the oxide growth rate of metals during exposure at high temperatures. It entails keeping the material at a constant temperature while exposed to an oxygen-containing environment. Isothermal testing aids this precision by maintaining preparations and operating conditions whilst controlling variables for precise analysis.

The chapter is divided into three main parts:

Section 3.1: Experimental approach, the rationale behind designing the experiments.

Section 3.2: Experimental preparation and testing procedures, which include pre-exposure preparation, testing protocols, and post-exposure handling.

Section 3.3: Experimental analysis, the characterization techniques used to analyse the microstructural and compositional changes for a comprehensive understanding of the degradation mechanisms.

3.1 Experimental approach

The experimental approach was designed to address critical gaps in understanding high-temperature material degradation in a sCO_2 environment. The methodology's rationale is rooted in the need to assess oxidation, carburization, sulphidation, and nitridation mechanisms that affect the performance of turbine blade and heat exchanger materials.

3.1.1 Rationale and significance of the testing approach

The effect of how carbon, sulphur and nitrogen in one test environment influences the oxidation behaviour of already employed nickel-based superalloys has not been fully explored. Various tests have been conducted to examine the effects of carburization, sulphidation, and nitridation individually, and it has been established that they accelerate the oxidation behaviour. One of the key aspects of this experiment is to analyse the degradation mechanisms and identify the types of oxide scales and internal degradation that occur.

The development of the Allam cycle places demanding requirements on materials used for turbomachinery and hot gas path components, where high temperatures, CO_2-rich environments, and impurities such as H_2O, SO_2 and O_2 can significantly influence long-term degradation. Some of these material challenges include fabrication concerns, cost of materials, and long-term degradation. Regarding fabrication concerns, LPBF is being explored as a potential solution capable of producing complex geometries. The oxidation and carburization behaviour of LPBF Alloy 625 is therefore compared directly with that of wrought Alloy 625 to evaluate whether the additively manufactured material can deliver equivalent or improved high-temperature performance.

To fully assess how LPBF processing influences environmental degradation, samples were tested in six conditions defined by microstructure (as-built LPBF and solution-treated LPBF) and surface finish (as-received, 600-grit ground, and polished). As-received refers to the high-roughness surface produced directly by the LPBF process, while “as-built” refers to the LPBF microstructure before heat treatment. Among the six experimental conditions, the one most representative of real turbine service is the solution-treated LPBF material with a ground or polished surface, as turbine casings are typically heat-treated and finished to low roughness before operation.

However, the rationale for this study extends beyond LPBF alone. Advanced CO_2 power cycles rely on CO_2-based working fluids, and there is a broad need to understand how these environments interact with Ni-based superalloys used in turbomachinery. Alloys such as Rene 80, IN738, IN939, MAR-M247, PWA1480,

ECY768 and CM247 with and without TBC have all been investigated under similar CO_2-rich environments because they form the material baseline for turbine blades, vanes, combustor components and casings. Therefore, assessing Alloy 625 under controlled CO_2-based gas mixtures contributes both to the evaluation of the LPBF route and to the wider effort to establish degradation mechanisms for Ni-based alloys in sCO_2 cycles.

The selected test environments and temperatures replicate the high temperature, high CO_2 conditions expected in sCO_2 power cycles. A test temperature of 800°C was selected because it aligns with the operational conditions in sCO_2-based turbines and heat exchangers. All exposures were carried out for 1000 h, providing an accelerated but meaningful representation of long-term behaviour. This is short compared to the multi-year service life of turbine components, but sufficient to identify the oxidation and carburization trends.

- **Environment 1: 800°C/1 bar/CO_2 + 2.7 mol% H_2O +0.17 mol% O_2**
  This condition simulates oxidizing environments with water vapour content, leading to potential oxide scale formation and accelerated material degradation, which is a known contaminant in the Allam cycle [14,17]
- **Environment 2: 800°C/1 bar/CO_2 + 2.7 mol% H_2O + 1.43 mol% N_2 +0.17 mol% O_2 + 300 ppm SO_2**
  This is a sulphur and nitrogen-containing environment, and the presence of 300ppm SO_2 and N_2 simulates exposure in an Allam cycle. It is important this is investigated as sulphur-containing impurities can induce sulphide formation, potentially weakening grain boundaries and accelerating material failure.

Using isothermal oxidation with 200-hour intervals helps to analyse oxide formation over time and monitor oxidation kinetics. In power plant operations, turbine blades experience repeated heating and cooling cycles, which can exceed 80 cycles per year. This may cause oxide spallation, stress buildup, and microstructural changes. Cyclic testing enables an accurate assessment of these mechanisms [111].

3.2 Experimental Procedures

Before sample preparations were carried out, materials were selected, and the materials chosen were already employed alloys in the energy industry.

3.2.1 Material selection

The process begins with the selection of materials based on factors such as resistance to high temperature, potential resistance to carbon in the atmosphere etc. The key components in a CO_2 open system regarding concern for material selection are the turbine blades, turbine combustors, turbine expanders, and heat exchangers, all of which operate at high temperatures and pressures [152] . Materials systems selected for this experiment are already utilised in the power industry for power generation. However, the lack of a comprehensive understanding regarding its performance and degradation mechanisms under extreme conditions experienced in Allam cycle power generation systems make this experiment relevant.

Two manufacturing techniques were selected: wrought manufacturing and Alloy 625 AM. For all experiments, the materials were cylindrical samples between 10-14Ømm with a length of 10mm. The nominal composition of superalloys is listed in the table below

Table 3-1 - Nominal elementary composition using EDX (wt.%)

Sample	Ni	C	Co	Cr	Al	Mo	W	Ta	Ti	
CM247	Bal	0.07	9.5	8	5.6	0.5	9.5	3.2	0.7	Zr (0.01), B (0.015)
SC2464 (BC)	Bal	-	26	18	11	-	-	-	-	Re (1.8), Y (0.4)
8YZS (TBC)	-	-	-	-	-	-	-	-	-	Zr (68), Y (13)
Rene80	Bal	0.17	9.5	14	3	4	4	-	5	Zr (0.03), B (0.015
ECY768	10	0.6	54	23.5	0.15		7	3.5	0.2	Fe (1), Zr (0.05), B (0.01)
IN939	Bal	0.15	19	22.5	1.9	-	2	1.4	3.7	Zr (0.09), B (0.009)
IN738	Bal	0.17	8.5	16	3.5	1.7	-	-	3.5	Zr (0.1), B (0.01), Nb (0.8)
MARM247	Bal	0.07	9	8	5.45	0.4	9.3	3.1	0.6	Hf (1.2), B (0.01)
PWA1480	Bal	-	5	10	5	-	4	12	1.5	

Table 3-1 is a combination of superalloys- nickel based and nickel-chromium based superalloys. The SC2464 bond coat was deposited onto the CM247 alloy using a thermal spray process to provide an oxidation-resistant intermediate layer. For the TBC system, an 8YSZ (8 mol% yttria-stabilised zirconia) ceramic coating was subsequently applied over the SC2464 bond coat. Thus, the study included two surface conditions: (i) CM247 with a thermally sprayed SC2464 bond coat, and (ii) CM247 with an SC2464 bond coat plus an 8YSZ TBC. The samples were prepared in accordance with the industrial standards and was provided by SIEMENS.

3.2.1.1 AM samples

The Second type of experiment conducted focused on wrought manufactured and additive manufactured Alloy 625 samples. To adequately analyse the microstructure, two manufacturing techniques, AM in as-built and solution heat-treated. The LPBF AM manufactured samples were manufactured by the University of Birmingham, and Alleima supplied wrought samples. The AM cylindrical rods had dimensions of the cylindrical samples ranging from ø 10-14mm X 10-11mm. All samples were built in a vertical (Z) build orientation, meaning the main axis of each sample is parallel to the build direction. The LPBF Alloy 625 powder and the process parameters for are shown in Table 3-2.

Table 3-2 - IN625 AM process specification

AM Sample specification	
Material	IN625
Process	LPBF
Machine	EOS M280 (400W)
Powder size range	15 – 45 µm
Parameters	Proprietary
Build orientation	Vertical (Z)

The Chemical composition presented in Table 3-3 is the composition of the Alloy 625 powder, on the other hand, Sanicro 625, which is Sandvik's designation of Alloy 625, the composition was obtained from [153].

Table 3-3 - Nominal Composition of Alloy 625

	Ni	C	Cr	Co	Al	Ti	Mo	Nb	Fe	S	Si	P	Mn
LPBF	Bal	-	21.27	0.04	0.11	0.1	9.02	3.65	3.66	-	0.07	<0.01	
Wrought	62	<.025	21	<1	<0.4	0.2	8.7	3.5	4	≤0.015	0.2	<0.015	<0.5

3.2.2 Preparation Prior to Exposure

Pre-exposure of the samples preparation is a critical step in ensuring consistent and accurate results. The preparation of samples of testing is a vital part to maximise accuracy in oxidation testing. Figure 3-1 shows a flowchart outlining the pre-exposure preparation phase for high temperature testing.

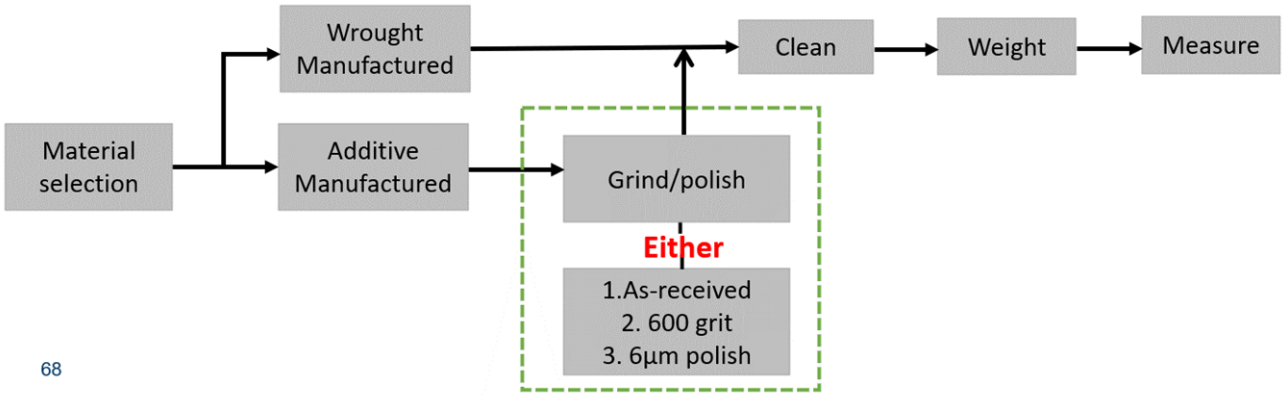


Figure 3-1 - Pre-exposure steps

Figure 3-1 illustrates a flowchart outlining the pre-exposure preparation phase for high-temperature testing.

1. Before samples were cleaned, AM LPBF Alloy 625 samples were ground to control surface finish to understand the influence of surface finish on oxidation behaviour. The AM samples had two variables, the as-built and the solution heat treated variable. The surface conditions were:
    1. As received (no additional treatment)
    2. 600-grit grinding (moderate surface smoothing)
    3. 6µm polishing (fine surface finish for improved uniformity).

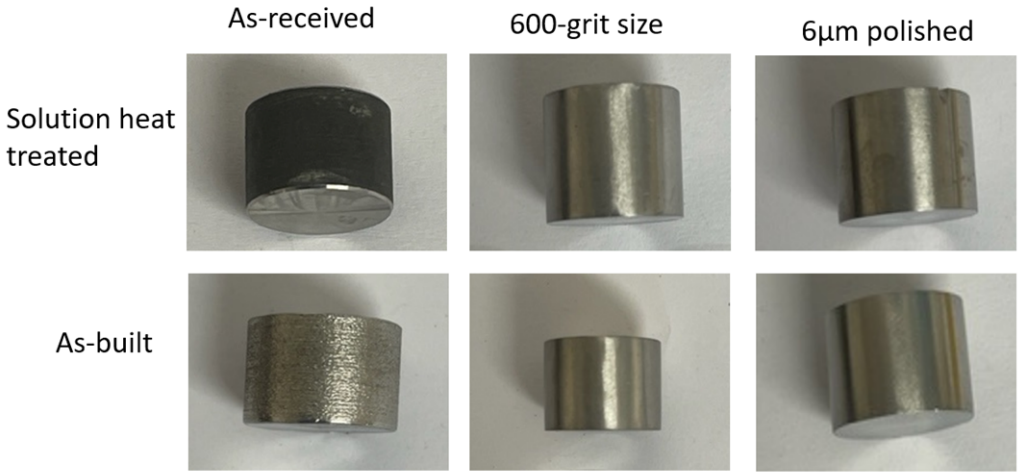


Figure 3-2 - Photographs of samples after grinding and polishing LPBF Alloy 625

2. **Cleaning**: Samples are cleaned in an ultrasonic bath using isopropanol and acetone to remove dirt or debris as well as grease to avoid acceleration of oxidation during cyclic oxidation affecting the overall test results.
3. **Weight and Measure**: After cleaning the samples, the initial weight of samples is recorded to track changes to oxidation or material loss during high temperature exposure. The dimensions are measured around the sample to monitor dimensional metrology. Figure 3-3 shows examples of some of the samples, and each sample was measured using a micrometre, with diameters ranging from 7-10mm

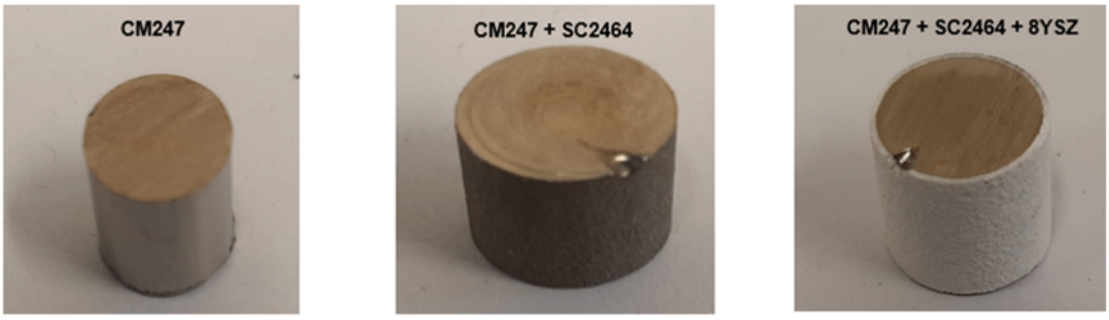


Figure 3-3 - Before exposure images of samples.

3.2.3 Testing

This phase uses the controlled atmosphere furnace to simulate a corrosive sCO_2 environment.

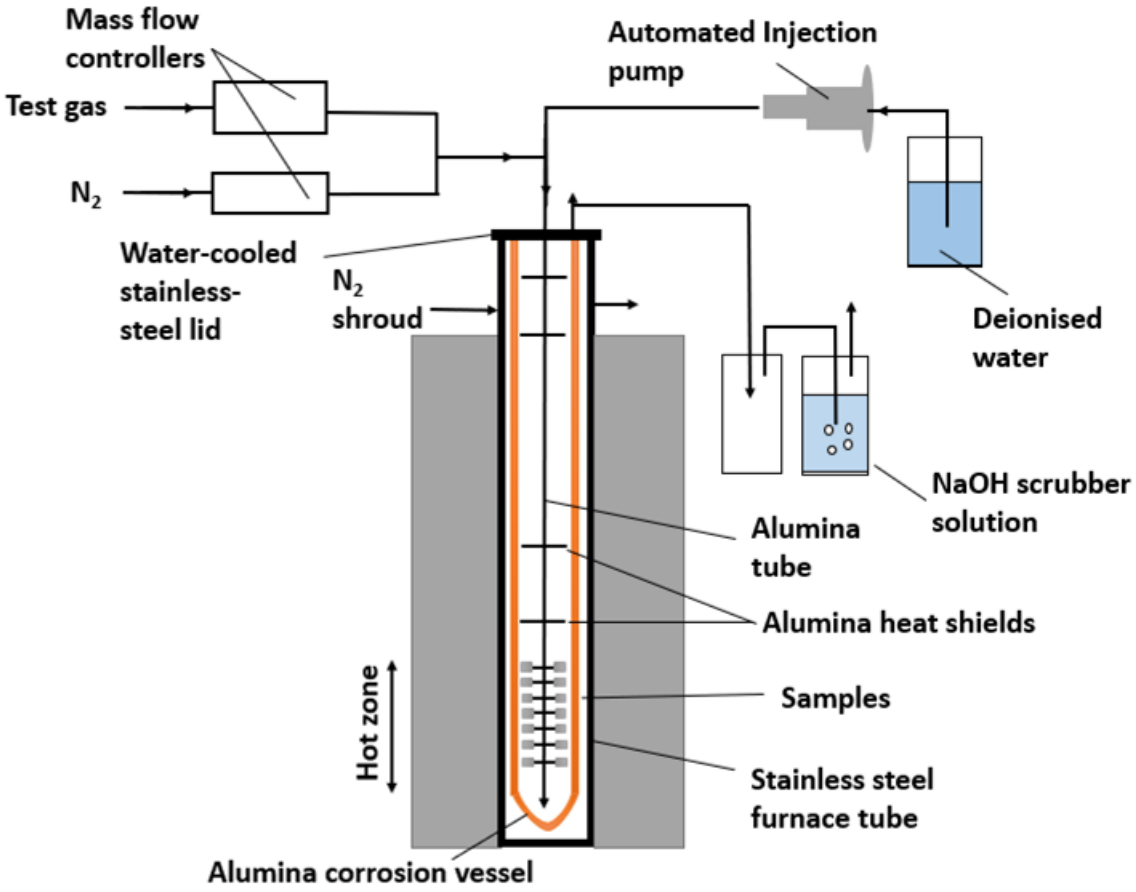


Figure 3-4 - schematic of furnace [154]

The gas flow rate for all experiments was set at 88.74cc/min using the mass flow controller. 88.74 cc/min was selected to ensure delivery of gas composition and consistent gas distribution in the furnace during the 800°C exposure. This gas flows into the alumina corrosion vessel and out of the furnace into a NaOH scrubber solution. An automated injection system was used to inject deionised water into the furnace at a concentration of 2.7 mol% at a rate of 0.002 ml/min. The two gas environments investigated in this thesis were:

Gas 1:CO_2 + 2.7 mol% H_2O +0.17 mol% O_2

Gas 2: CO_2 + 1.43 mol% N_2 +0.17 mol% O_2 + 300 ppm SO_2 + 2.7 mol% H_2O

Each test carried out was exposed for up to 1000h, with each cycle lasting 200h. After which, samples are allowed to cool, weight measurements taken of samples with and without the crucible and put back into the furnace, and the procedure is repeated 5 times. Three tests were conducted during this PhD, and Table 3-4 shows each test design.

Table 3-4 - Test design and materials investigated in this thesis.

Test	Environment	Test conditions	Material systems	Manufacturing technique	Use
1	Gas 1	800°C, 1 bar	CM247,CM247+SC2464,CM247+SC2464+8YZS, Rene80,In738, In939, Marm247, Ecy768, PWA1480	Wrought	Turbine blades, vanes, and hot section components in gas turbines
2	Gas 2	800°C, 1 bar	CM247,CM247+SC2464,CM247+SC2464+8YZS, Rene80,In738, In939, Marm247, Ecy768, PWA1480	Wrought	Turbine blades, vanes, and hot section components in gas turbines
3	Gas 2	800°C, 1 bar	LPBF AM Alloy 625 and conventional Alloy 625	Wrought and additive manufactured.	Heat exchangers, turbine casing, and sCO_2 pipes.

Test 3 was not performed in Gas 1 because impurities are typical in Allam-cycle environments, and the purpose of this test was to evaluate whether AM Alloy 625 can match the performance of its wrought counterpart under more realistic impurity-containing conditions.

3.2.4 Post-exposure

The post-exposure analysis procedure involves two main stages: the monitoring phase, which is the initial part of post-exposure analysis, and the microstructural analysis phase, which involves characterization techniques. These stages are

vital for understanding material behaviour and degradation mechanisms under different exposure conditions.

- Monitoring Phase: The monitoring phase involves systematic documentation and measurements of samples at predetermined intervals of 200h. To track the growth of oxide layer over time. Mass change analysis entails measuring the sample mass after each cycle completion, providing insights into material loss and assessing the condition of the crucible after each cycle for spallation inspection. These samples are weighed using a high-precision analytical balance with an accuracy of ±0.01 mg. Documentation requires recording of mass change after each cycle in comparison to the initial mass change analysis. Another aspect of monitoring involves taking sample photographs after testing to track the samples' surface appearance, mounting, cutting, and polishing. The experiment used five samples per alloy. After each 200-hour cycle, one sample was removed to capture the microstructural state at that exposure time. This means separate samples were used for each interval rather than repeatedly analyzing a single specimen.

Following the monitoring phase, samples undergo thorough preparations for detailed microstructural analysis. This sequence includes:

a. Mounting: Samples are cold-mounted in epoxy to preserve surface integrity and prevent damage during subsequent preparation steps. In this process, low-shrinkage epoxy resin with ballotini glass spheres in a 60:40 ratio in a mounting mould and allowed to cure at room temperature. Cold mounting is preferred to avoid cracking and spalling. To minimise spallation, the samples were handled carefully during placement, and the epoxy was poured slowly and vacuumed to avoid trapping air bubbles that could create localized stresses.
b. Cutting: Cross-sections are obtained using a precision automated cutting machine. Cutting is performed under continuous flow of lubricant to minimize heat generation.
c. Grinding and Polishing: For all samples, a sequence was followed.
    a. For the grinding with SiC paper (120, 240, 600, 1200 grit)

b. Polishing (6µm, 1µm)

Each grinding and polishing step is carried out with a consistent force of 35N and a rotation speed of 140rpm. The force applied varies depending on the number of samples being polished. To avoid any risk of dissolving water-soluble phases, all grinding and polishing steps were performed using oil-based lubricant instead of water.

After the final polishing, the samples were further cleaned with isopropanol to remove any debris and grease that resulted from grinding and polishing. All phases followed the ISO standard in accordance with ISO 26146: 2012 [155].

3.3 Characterization Techniques

3.3.1 Optical microscopy

Optical microscopy was the initial technique used to characterize the surface morphology and cross-section features. Using a calibrated stage optical microscope, a dimensional metrology plot can be created, as demonstrated in Figure 3-5.

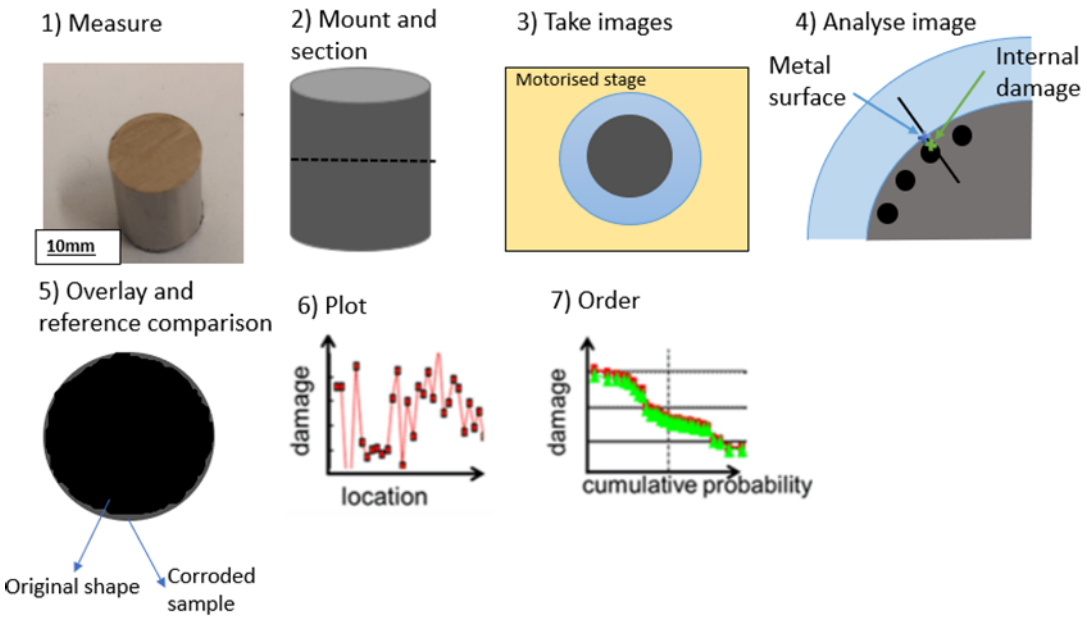


Figure 3-5 - Demonstration of dimension metrology [156]

1), The initial dimensions of each metal sample (diameter and height) are measured using a micrometre to establish a baseline for comparison with post-exposure measurements. 2) After oxidation, the samples are mounted in epoxy and cross-sectioned to enable internal examination. 3) Cross-sectional images are then acquired using a motorised-stage microscope to document the extent of damage. 4) These images are analysed by selecting X–Y coordinates along the metal surface and the internal damage front for both the reference (unexposed) and exposed samples. The reference sample is processed first to extract its X–Y data into Excel, where the gradient and positional shift are calculated. The same procedure is then applied to the exposed samples, using the reference gradient and shift for alignment. This allows direct comparison between the original and oxidised geometries, as illustrated in Figure 3-5, and enables quantification of sound metal loss as a measure of damage.

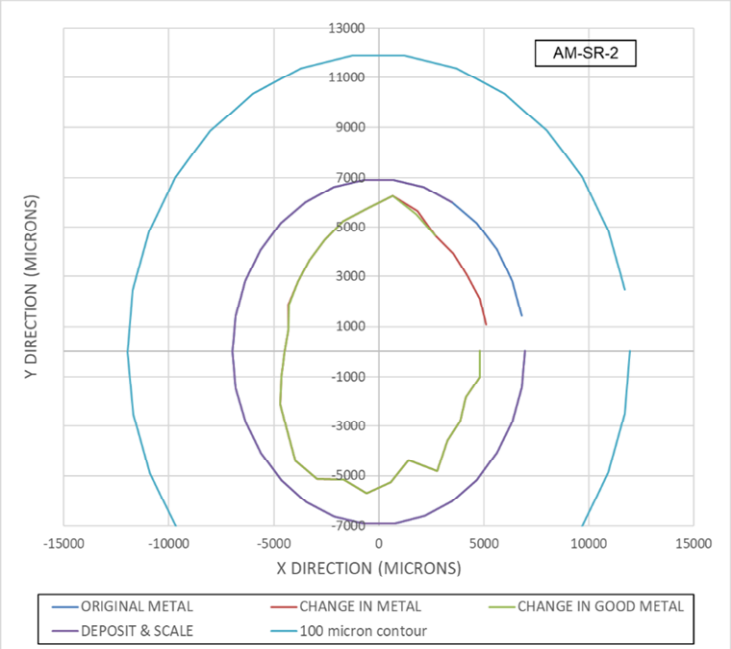


Figure 3-6 - Cross-sectional dimension metrology of a metal sample after exposure

Figure 3-6 shows the X and Y directions showing change in geometry through comparison with original metal (reference). The change in good metal, in relation to its location, was plotted cumulatively to create a cumulative probability plot.

3.3.2 Scanning Electron Microscopy (SEM) & Energy Dispersive X-ray Spectroscopy (EDX)

The main characterisation technique is the SEM and EDX, and the technology used for analysis is a Tescan VEGA LSEM with an EDX detector. SEM offers high-resolution imaging to study the surface morphology and microstructural features of each sample. Before this technique is used, samples are coated with gold because the samples are mounted in non-conductive epoxy. A thin layer of gold is necessary to prevent charging of the surface and promote the emission of secondary emissions. Materials other than gold can also be used to coat specimens, including silver, carbon and platinum. However, gold is commonly used as a conductive metal on SEM images because it reduces static electric charge from the non-conductive epoxy, providing clearer images, and also had high secondary electron yields, that makes imaging easier due to the emission of more electrons when struck by the electron beam [157].

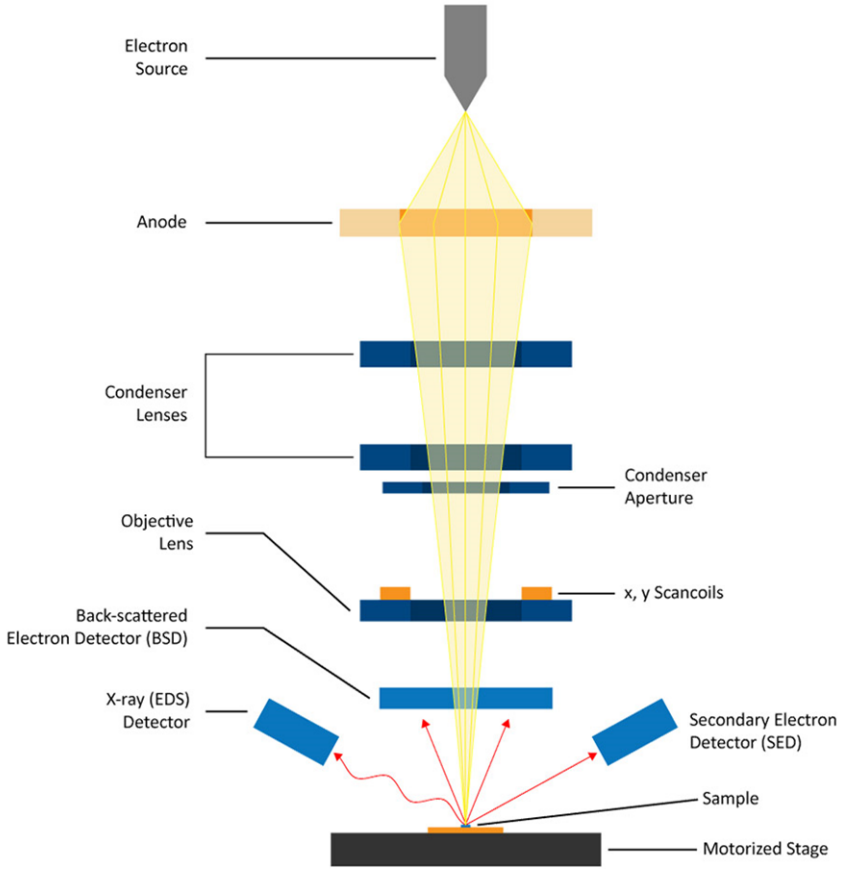


Figure 3-7 - Schematic of scanning electron microscope [158]

Figure 3-7 shows a schematic of the SEM and explains how it works by scanning the sample with electron beams. An electron gun at the top fires these beams, which are then accelerated at a specified voltage (1 KeV – 30 Kev) down the column to the sample. For this analysis, all images were taken at 20 Kev, at this accelerating voltage, the images are clear and stable because of the high signal-to-noise ratio and better backscattered electron contrast. The electron beams scan the mounted sample, which is on a motorised stage, in a raster pattern across the surface. The position of the electron beam is controlled by scan coils located above the objective lens. When electrons interact with the atoms, they produce signals such as secondary electrons, backscattered electrons, and X-rays, which are characteristic of the sample. These signals are detected by suitable detectors for imaging. The images used in this thesis were obtained from backscattered electrons (BSE), which create images with contrast that reflects differences in atomic number, as opposed to secondary electrons (SE), which provide topographic information [159].

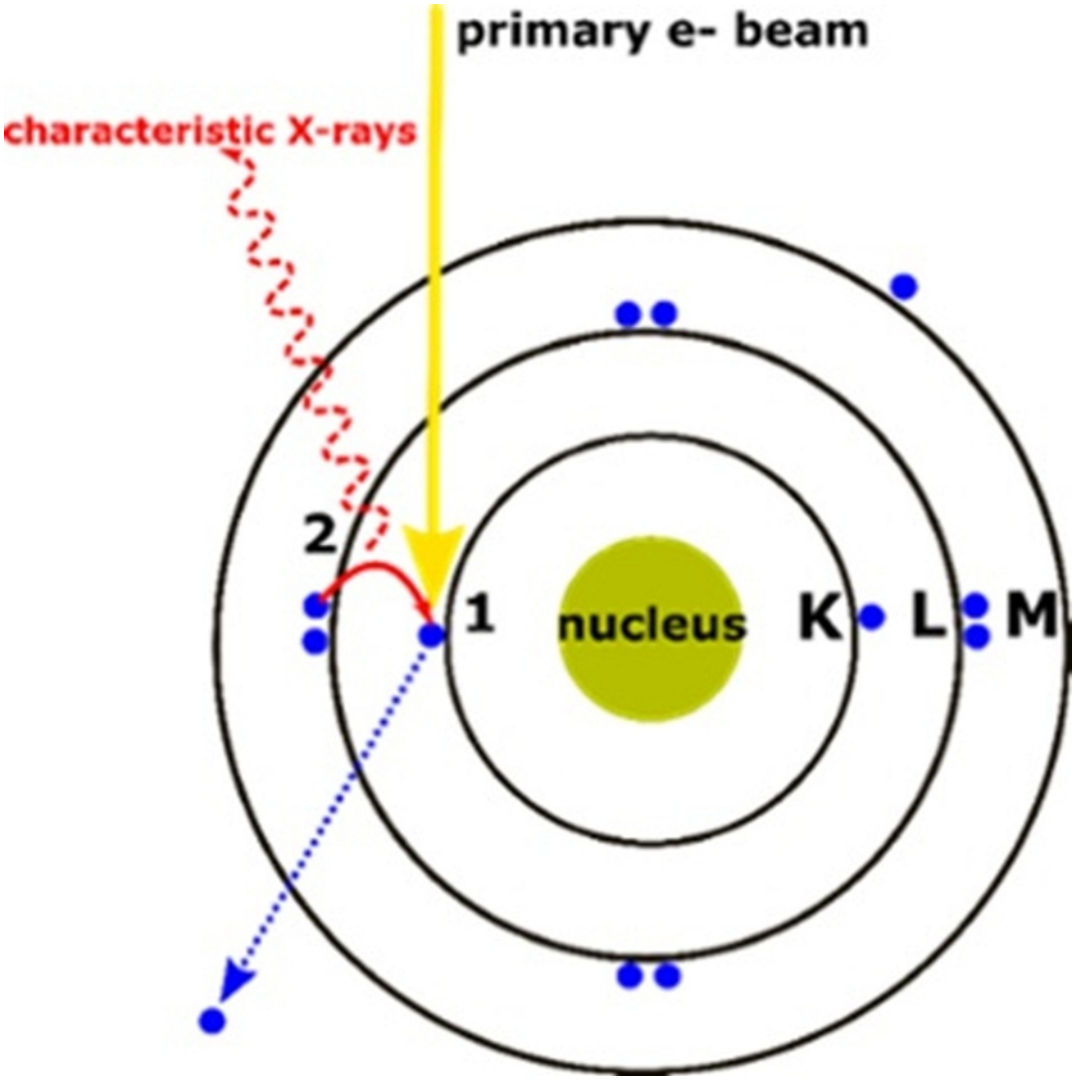


Figure 3-8 - X-ray generation process [159]

EDX is then used for elemental analysis, oxide compositions, reaction products and heavier element constituents; however, carbon quantification is limited for carbide composition due to detection limitations of the technique. All atoms possess a different number of electrons in a particular position under normal conditions, with each position belonging to a specific shell, having different and separate energies. There are two steps for X-ray creation as illustrated in Figure 3-8:

1. The electron beam first strikes the sample, transferring energy to the atoms. This energy allows electrons to move to higher energy shells or be ejected from the atom, leaving a hole behind if the latter happens.

2. Next, the positively charged vacancies in the inner electron shells attract electrons from higher-energy shells. When an electron from a higher shell fill one of these vacancies, the energy difference is emitted as an X-ray.

The energy of the X-ray depends on the atomic number, a unique property of each element, and reflects the energy difference between the two shells. This makes X-rays a "fingerprint" for each element, allowing them to be used to identify the elements present in a sample [159].

Unlike SE, and BSE, X-rays are electromagnetic radiation, similar to light, and consist of photons. A detector, typically silicon-drift, is used to detect the X-rays. These detectors are positioned at an angle, very close to the sample, and can measure the energy of incoming X-ray photons [159]. EDX can be used for both qualitative analysis (identifying the types of elements) and quantitative analysis (determining the concentration percentage of individual elements in the sample). Also detect oxide compositions, reaction products and carbide composition [98].

However, EDX analysis has limitations, including elemental detection limit, especially light elements such as nitrogen, carbon and sulphur [160]. This impacts the research, as a large part of the research involved investigating the formation of carbides, the diffusion of carbon, and the effects of nitrogen and sulphur. Therefore, further analysis was carried out using techniques with high sensitivity to these light elements, such as Atom probe tomography (APT) and electron probe micro-analyser (EPMA).

3.3.3 Electron probe microanalysis (EPMA)

EPMA is another analytical technique used to further locate of sulphur and nitrogen in the sample, this is based on a more precise quantitative elementary analysis than EDX using wavelength dispersive spectroscopy (WDS).

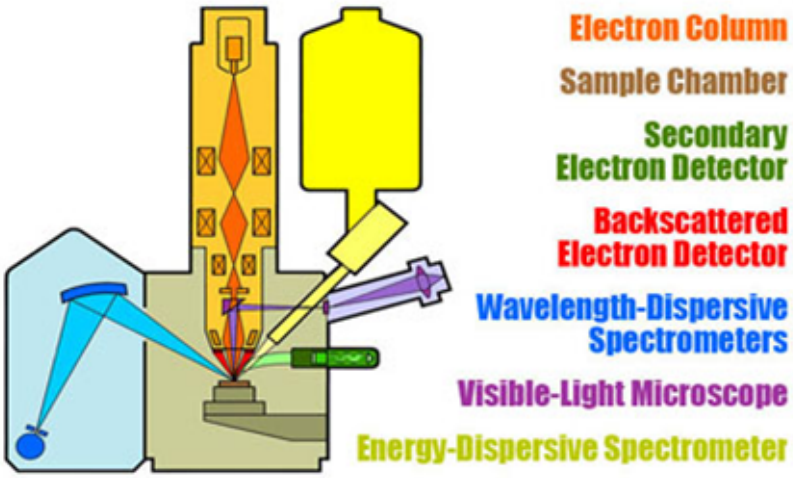


Figure 3-9 - Schematic of EPMA [163]

Figure 3-11 shows the schematic of a typical microprobe, where a sample is bombarded by an accelerated and focused electron beam, resulting in separation of atom and energy from the sample. This excitement as the result leads to emission of characteristic X-rays which are unique to each element allowing precise identification.

The difference between EPMA and EDX is EPMA uses a wavelength-dispersive X-ray spectroscopy for detection which has a higher energy resolution, measures the X-ray wavelengths (energies) with higher precision. While the EDX uses a solid-state detector to measure the energy of the X-rays direction.

4 Paper 1: Corrosion of Potential First Stage Blade Materials in Simulated Supercritical CO_2

Phoebe Norman, Cranfield University, Cranfield, United Kingdom
Hisham Al Baroudi, Cranfield University, Cranfield, United Kingdom
Andrew Potter, Cranfield University, Cranfield, United Kingdom
Stefano Mori, Cranfield University, Cranfield, United Kingdom
Nigel Simms, Cranfield University, Cranfield, United Kingdom
Anand Kulkarni, Siemens Corporation, Charlotte, United States of America
Joy Sumner, Cranfield University, Cranfield, United Kingdom

Abstract

Global power consumption is predicted to double by 2050, notably driven by the transportation and energy sectors necessitating limitations of emissions. Due to its compact turbomachinery, better thermal efficiency, and simpler layout, supercritical-CO_2 cycles have received attention, with numerous variations proposed (either indirect-fired/closed cycles or direct-fired-open cycles). One technical challenge is degradation pathway quantification of turbine materials in sCO_2 as selection is crucial to successfully and economically operate new plants. This requires degradation assessment in representative environments simulating the Allam cycle. Laboratory tests were conducted on a first stage turbine blade alloy, CM247, with either an environmentally resistant coating or bond coat/thermal barrier coat at one atmosphere and 800°C, with potential exposure including (O_2, H_2O, N_2, SO_2) for up to 1000 h. Weight change and metallographic measurements tracked scale development. Scanning electron microscopy/energy dispersive X-ray spectroscopy studied scales and internal precipitates. Locations of contaminant elements in the CO_2-rich environment were investigated.

4.1 Introduction

The energy industry has acknowledged the need for cleaner, and more sustainable energy as the increase in population and economic activities over the past two decades has driven global energy demand subsequently resulting in environmental concerns. According to the Department of Business, Energy and Industrial Strategy, the UK's energy demand has increased by 3.2 mega tonnes (oil equivalent) since 2020 with the UK's electricity demand in 2021 approximately 334 terawatt-hours[164]. Improving power generation efficiency whilst considering its environmental impact can be achieved through three areas – increasing the percentage of energy from the heat source that can be collected for use in the thermal power cycle; enhancing the thermal power cycle's inherent efficiency; and minimising the parasitic power demand for plant balance[165].

Existing power conversion cycles, as shown in Figure 4-1, include the Rankine cycle and Brayton cycle which generally utilize water or combustion gases as their working fluids. However, with the necessity of attaining higher thermal efficiencies, alternative working fluids are being brought to the limelight. Over the years, the interest in carbon dioxide as working fluid for power generation has grown. Utilization of supercritical carbon dioxide, sCO_2 has the potential to improve cycle efficiency in comparison to the steam-based Rankine cycle [62]. To achieve higher thermal efficiency, the sCO_2 Brayton cycle has been postulated as a novel power conversion cycle, with a thermal efficiency reaching over 50%.

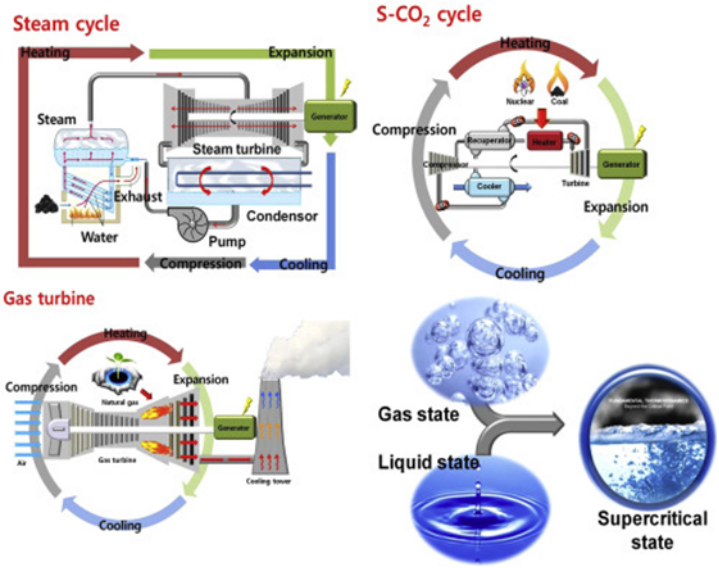


Figure 4-1- Principles of a power conversion system [61]

CO_2 has a critical temperature and pressure of 31°C and 73.78 bar respectively and its unique features (stable supercritical fluid, non-toxic, low cost, and low critical point) have made it an ideal working fluid. sCO_2 power cycles have been postulated as novel cycles, however, with high thermal efficiencies and turbine inlet temperatures > 350° [166]. There are material challenges especially for the heat exchangers and turbine blades, as both experience the hottest region of the cycle. Exposure of materials at high temperatures and pressures over long periods, results in degradation of the metal.

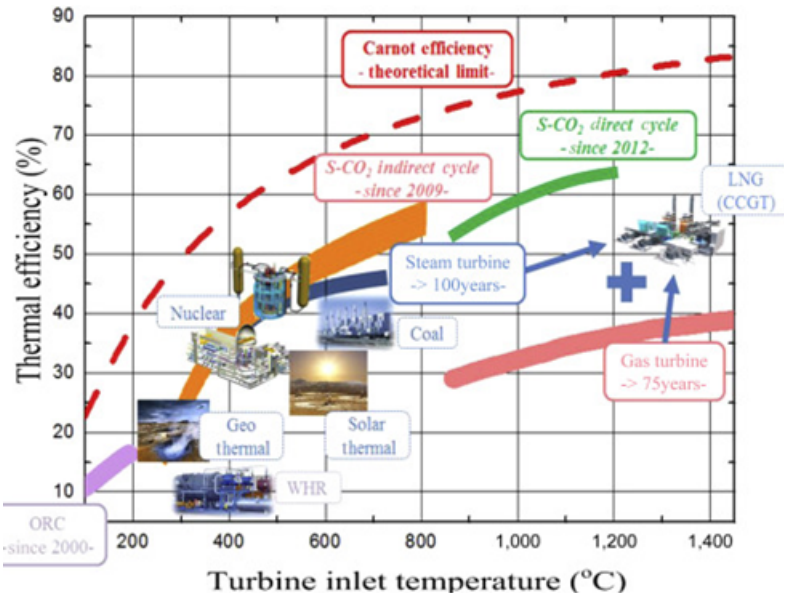


Figure 4-2 - Various power conversion efficiencies [61]

Figure 4-2 shows the thermal efficiency vs turbine inlet temperature of the different power generation systems for sCO_2 cycles with different heat sources – nuclear, solar thermal, coal etc. Figure 4-2 shows that power conversions utilizing sCO_2 have a high thermal efficiency in comparison to the power generation means.

Angelino explored the practicality of utilising CO_2 as a working fluid for power generation, with further work considering supercritical cycles applied to different cycle layouts[64,65,167]. CO_2 gas has been applied widely for commercial and

industrial use, refrigerator, and air conditioning systems [168], heat pumps[169], and in its supercritical state, supercritical Brayton cycle [59] etc. Utilization of supercritical CO_2 has been investigated for different applications – nuclear, geothermal [70], and concentrated solar [170].

Turbine blades play a critical role in power plants and typically operate in harsh conditions – high pressure, high temperature, and complex dynamic loading conditions. As a result, the demand for high-efficiency power conversion systems has driven the need for improvements in materials selection. Turbine blade failure can occur due to different factors. Life-limiting mechanisms include high temperature oxidation, hot corrosion, and creep, while other degradation factors include fatigue, erosion, and or foreign object damage [171]. The failure of turbine blades results in unexpected and economic repercussions, so suitable alloys are necessary. Nickel-based alloys are extensively used for severe environments in turbine engines, processing plants and nuclear power [172]. This paper focuses on illustrating the failure mechanisms anticipated in first-stage blade materials in a direct fired sCO_2 power cycle. So far, research and development for materials reliability of a sCO_2 power cycle has not been fully explored thus the high temperature corrosion behaviour, oxidation behaviour and carburization of nickel-based alloys are addressed.

4.2 Experimental

Experimental exposures were carried out at high temperature to study the chemical properties i.e., oxidation behaviour as well as the carburization behaviour.

4.2.1 The materials systems

In this study, one nickel-based alloy, CM247 was exposed. This was used bare or with a bond coat with and without a thermal barrier coating. Such material systems are used for current power generation because of their high oxidation and corrosion resistance. The nominal compositions of the alloy and coatings are shown in Table 1 along with chemical composition of coating layers.

Table 4-1 - Composition based on EDX outputs (wt.%) [173]

Wt%	Ni	C	Co	O	W	Ta	Cr	Ti	Al	Zr	Y	Hf
CM247	57	0.07	8.1	-	9.5	3.2	6.4	0.7	5.6	-	-	-
SC2464 ERC/ BC		-	16.1	4.1	-	-	10.9		6.4	-	-	-
8YZS TBC		-	-	-	-	-	-	-	-	54.7	0.3	-

4.2.2 Exposure procedure

The four stages include pre-exposure, testing and monitoring and analysis phase. The pre-exposure stage involves separating the samples, which were machined from alloy rods into cylinders between 8-10.9mm long, with a diameter of 7.9 - 10.9 mm. After this, the samples were ultrasonically cleaned in acetone and isopropanol before the preliminary dimensional and mass measurements were taken.

In the testing phase, a high-temperature corrosion test chamber has been utilized to simulate a sCO_2 corrosive environment. The schematic diagram is shown in Figure 4-3 with the main parts being the alumina corrosion vessel, a water pump and mass flow controllers. The gas input was CO_2 with a vertical upward flow through the vessel with working temperature and pressure, 800°C and 1 bar, respectively. The gas flowrate was set at using the mass flow controller with deionised water automatically injected into the furnace at 0.002ml/min. The gas composition for tests 1 and 2 were CO_2 + 2.7 mol% H_2O + 0.17 mol% O_2 and CO_2 + 1.43 mol% N_2 + 0.17 mol% O_2 + 300 ppm SO_2, respectively. The samples were exposed for up to 1000h, each cycle lasting 200h. As a real operating scenario contains contaminants, H_2O, N_2, O_2 and SO_2. Tests 1 and 2 can thus be

compared to illustrate the effects of contaminants and protective treatments on material corrosion.

In the monitoring and exposure stage, mass measurements were taken between each cycle. After completing their exposure time, samples were mounted in resin and sections, cut, ground, and polished for analysis. In the last phase, the analysis stage, the acquired mass change data was plotted. An optical microscope analysed the sample surface to study the metal loss across the sample surface – Dimensional metallurgy. The last step of the analysis phase was using the SEM/EDX to investigate the surface morphology and oxide scale on the sample.

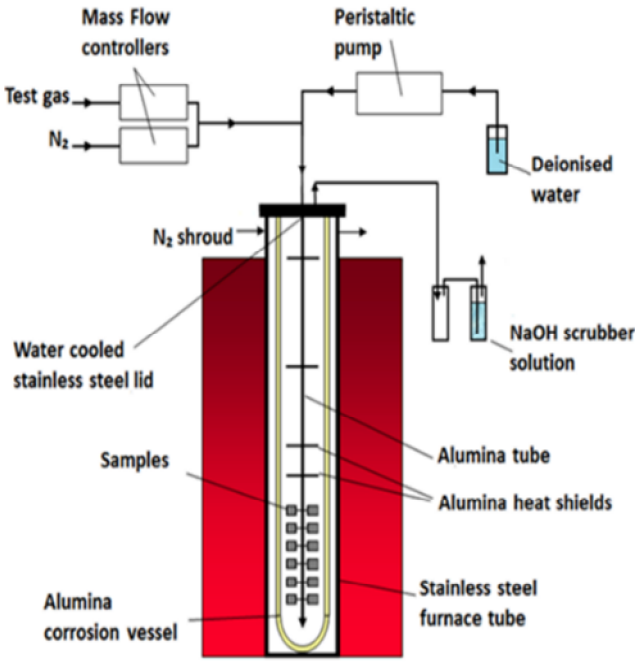


Figure 4-3 - Simple schematic of a furnace [154]

4.3 Results and discussion

4.3.1 Average weight change

The average weight change data for samples exposed in both environments are shown in Figure 4-4. All test samples exhibit an increase in average mass over the exposure period. Figure 4-4a shows that after 1000h of exposure in test 1, CM247+ SC2464 + 8YSZ exhibited the highest average mass change of 0.618mg/cm^2, whilst CM247 exhibited the lowest average mass change of 0.168mg/cm^2. This can be compared with the data obtained after exposure in test 2 where CM247 had an average mass change of 0.4921 mg/cm^2 whilst CM247+SC2464 and CM247+SC2464+8YSZ had 0.494mg/cm^2 and 0.497mg/cm^2 respectively. These

datasets, indicate that the uncoated samples are affected by the SO_2 present in the test 2 environment whereas the coated samples were not influenced. The observed increase in masses suggests the formation of corrosion products, which are likely carbides or oxides.

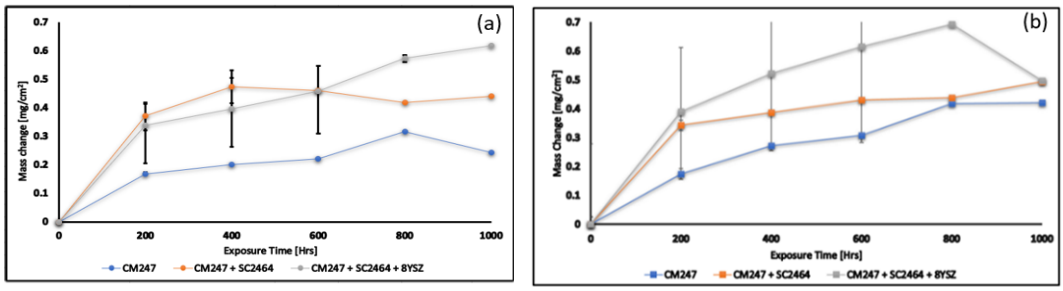


Figure 4-4 - Averaged weight change plot showing mass change vs exposure time for test 1 and 2;(a) Metal change for 800 ºC /1 bar /CO_2 + 2.7 mol% H_2O +0.17 mol% O_2 and (b) Metal change for (b) 800 ºC /1 bar /CO_2 + 1.43 mol% N_2 +0.17 mol% O_2 + 300 ppm SO_2

Dimensional change in metal data presented in terms of cumulative probability of metal loss exceedance is shown in Figure 4-5. Figure 4-5a (test 1) shows that, after a 1000h exposure time, CM247 had a good metal loss of approximately 9µm at the lowest level of probability, while in Figure 4-5b (test 2) CM247 for the same exposure time had approximately 14 µm of good metal loss. Although there has been a loss of good metal from the samples, the chart shows that the rate at which metal was lost is small. Figure 4-5 also indicates that results from the dimensional metrology show that the second testing environment, although not a highly damaging environment does accelerate corrosion. This indicates that the presence of contaminants does not influence the rate at which corrosion progresses.

Despite there being a significant but small metal loss across 1000h, corrosion rate could be fitted using equation, $X^2 = K_p t + C$**.** The K_p values were calculated and shown in Table 4-2.

Table 4-2 - K_p Values where the exposure time was 1000h (Units are $mg^2/cm^{-4}.s^{-1}$)

$X^2 = K_pt + C$	CM247	CM247+ SC2464	CM247+ SC2464+8YSZ
Test 1	0.004	0.00004	0.0001
Test 2	0.0003	0.0002	0.0002

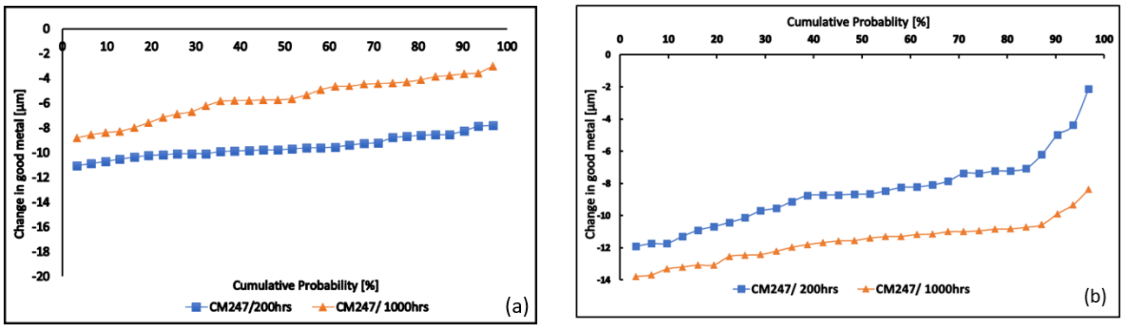


Figure 4-5 - Dimensional metrology for tests (a) 1 and (b) 2

Figure 4-6 shows the backscattered micrographs of the coated and uncoated CM247 alloys under the two experimental conditions as well as unexposed reference samples. Figure 4-6a shows that after exposure in test environment 1, a continuous scale is formed on the surface of the sample. This is a Cr rich oxide scale shown in Figure 4-7. Figure 6b shows a continuous scale on the surface has also formed after exposure in test environment 2. However, there is also evidence of oxides within the alloy matrix adjacent to the surface. These phases are further examined in Figure 4-8.

Figure 4-6c and 4-6d show BSE images of CM247+SC2464 after 1000h exposure in test environments 1 and 2 respectively. In comparison with the unexposed reference sample in Figure 46(2), both samples show little to no change in surface morphology. Figures 4-6c, and 4-6d exhibit a thin (approximately 2µm) oxide layer, shown to be rich in Cr and Al based on the EDX

analysis shown in Figure 7. The formation of this oxide layer may explain the increase in mass observed in Figure 4.

Figure 4-6e and 4-6f depict the BSE images of CM247+SC2464+8YSZ after 1000h exposure in test environments 1 and 2 respectively. These images show little change in morphology in either environment.

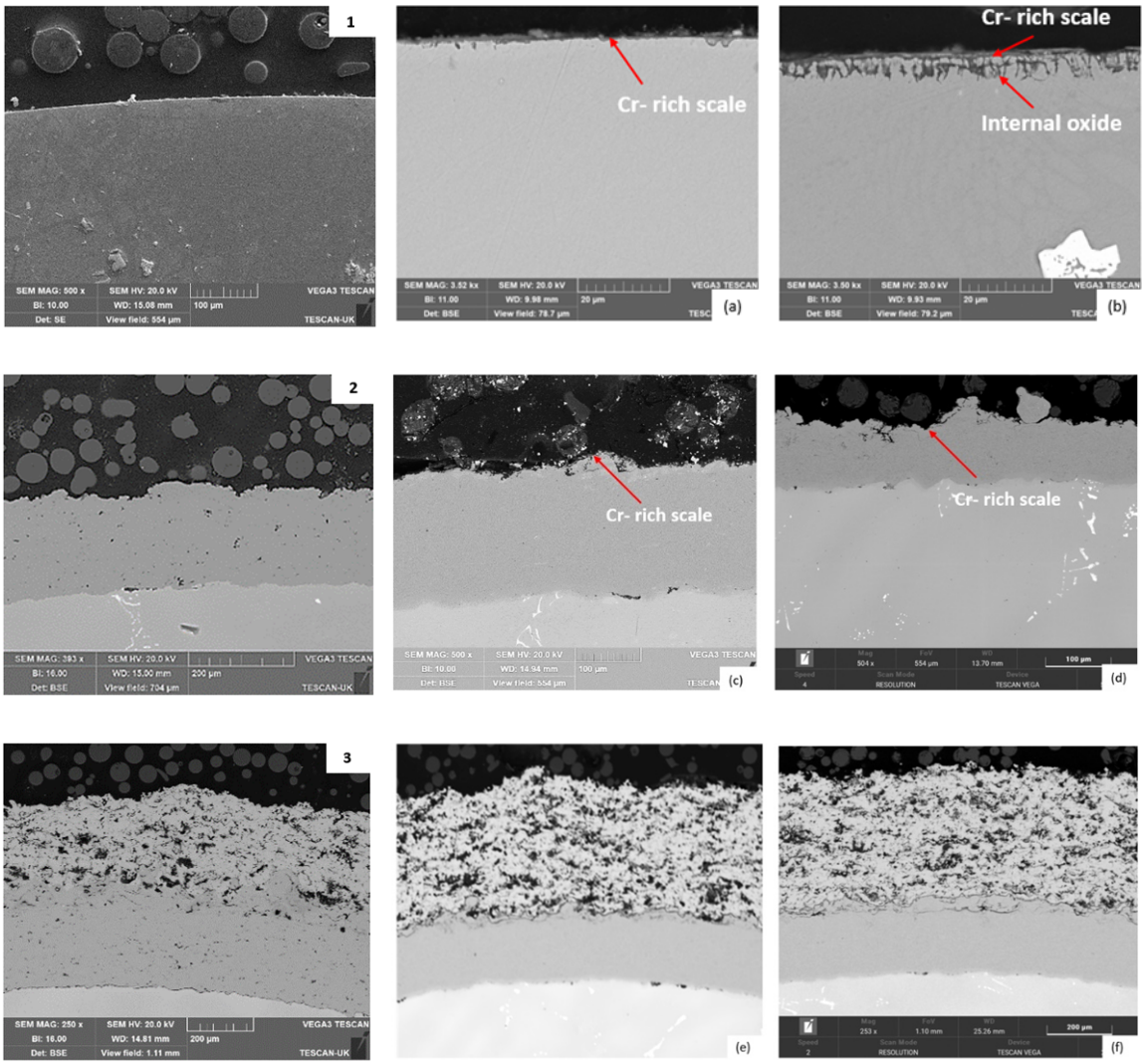


Figure 4-6 - SEM micrographs of CM247. (1), (2) and (3) represent the unexposed samples of CM247, CM247+SC2464, and CM247+SC2464+8YSZ respectively. (a) and (b) CM247 at 1000h for test 1 and 2 respectively, (c) and (d) CM247+SC2464 at 1000h for test 1 and 2 respectively whilst (e) and (f) CM247+SC2464+8YSZ at 1000h for test 1 and 2 respectively

Figure 4-7 presents the EDX maps and point analysis of the tested materials exposed for 1000h in test environment 1. Figure 4-7a shows the element distribution of CM247 revealing the formation of a continuous oxide scale rich in Cr and Al. The point analysis in Table 4-3, indicate a higher wt.% of Al, O, Cr and depletion in the Ti, Ta and Ni content at the surface (point 5). The EDX analysis also indicates that the carbide phase (point 6) is rich in Ta and Ti.

Table 4-3 - EDX analysis composition of CM247exposed for 1000h in test environment 1(wt.%) (C excluded from analysis)

CM247	Ni	Cr	Al	O	Co	Ti	W	Ta
Point 1	61.8	9.1	5.3	0.9	9.9	0.6	9.0	3.4
2	64.9	6.2	6.1	1.2	7.7	0.9	8.4	4.5
3	61.8	8.9	5.3	1.2	9.7	0.7	9.4	3.0
4	62.4	8.1	5.1	1.7	9.6	0.6	9.1	3.3
5	46.1	9.2	13.4	13.6	8.6	0.2	6.9	2.0
6	2.5	0.6	-	3.4	0.3	8.0	11.6	73.5

Figure 4-7b, relating to CM247+SC2464, also shows the formation of an oxide scale rich in Al and Co at the surface of the coating. This indicates the formation of a scale on the surface.

Figure 4-7c, relating to CM247+SC2464+8YSZ, does not show any significant changes in the composition of the ceramic coating through its thickness. However, the maps indicate the formation of an Al-rich layer at the interface of the SC2464 bond coat and 8YSZ TBC. This Al-rich layer, while in the location expected for a thermally grown oxide, does not appear to contain oxygen. This could be due to the presence of oxygen in the TBC affecting the EDX map scale.

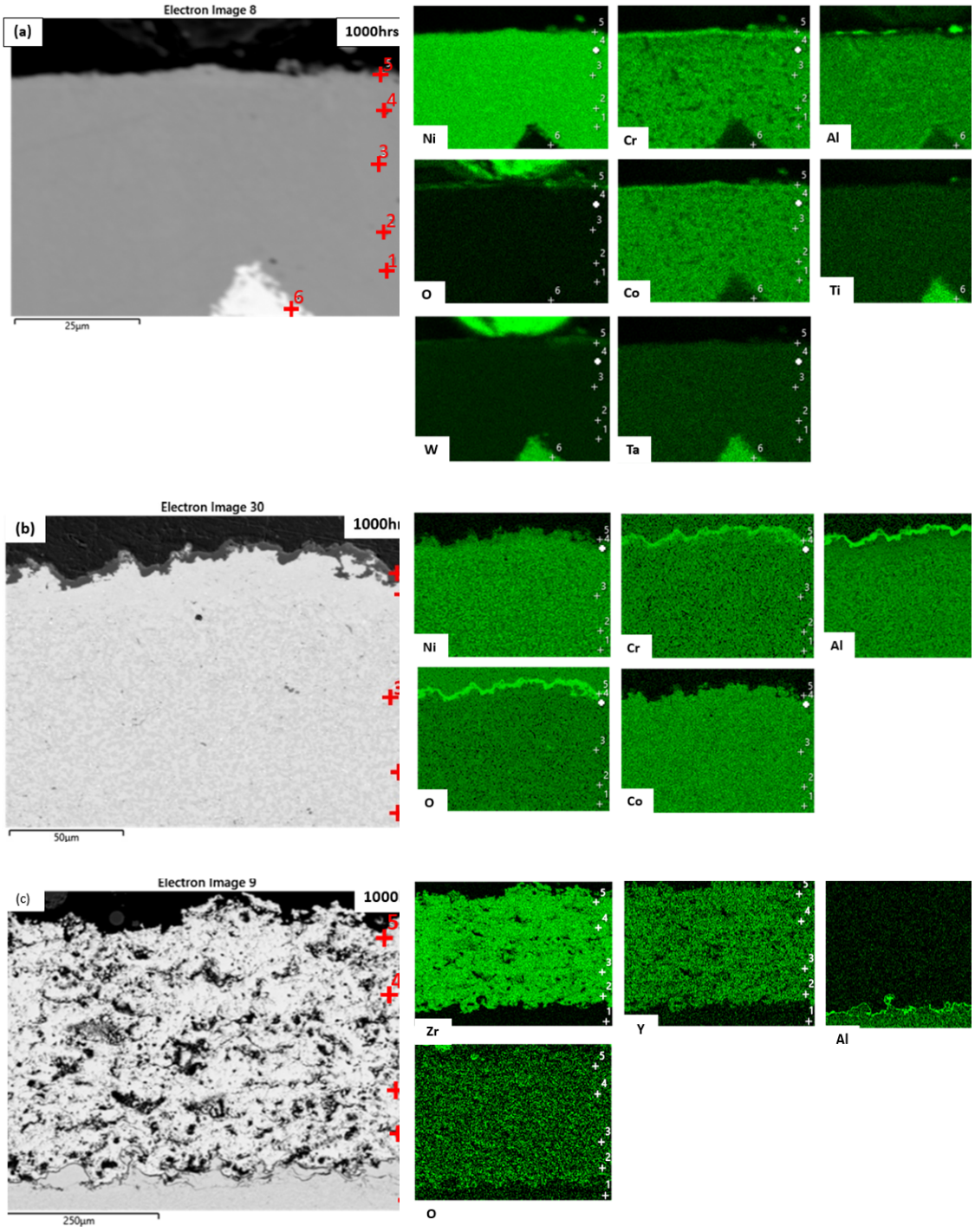


Figure 4-7- Backscattered and EDX maps for test 1 exposed for 1000h. (a) CM247, (b) CM247+SC2464, and (c) CM247+SC2464+8YSZ

Figure 4-8 presents the EDX maps and point analysis of the exposed materials after 1000h in environment 2. Figure 4-8a shows the elemental distribution of alloy CM247, revealing the formation of an oxide scale rich in Cr and Al (thicker

than that in Figure 4-7a). The maps also indicate the formation of internal oxides which are also rich in Al. The point analysis, Table 4-4. The EDX maps also indicate that the alloy below the oxide scales is depleted of Al, Ti and Ta, leaving a Ni-rich zone. The depletion of oxide-forming metals is believed to be a result of the protective scale being formed. Comparing the composition with Figure 4-7a and 4-8a, it can be postulated that exposing CM247 in environment 2 results in a more depleted alloy, with a thicker oxide scale. Based on the SEM analysis of these uncoated samples, the effect of oxidation is more pronounced in environment 2, indicating the importance of the change in contaminants; this is supported by the average weight change data.

Table 4-4 - Elemental composition of CM247 in test environment 2 (wt.%). Note that this data has been corrected to exclude carbon from all spectra

CM247	Ni	Cr	Al	O	Co	Ti	W	Ta
Point 1	60.3	9.7	5.4	0.5	10.3	0.6	10.3	2.9
2	64.0	7.3	5.4	0.4	10.1	0.6	9.5	2.7
3	64.4	7.7	5.9	0.4	9.7	0.7	8.1	3.1
4	59.1	7.9	7.7	8.5	8.5	0.8	6.1	1.5
5	31.8	6.8	18.4	25.2	4.7	1.4	5.6	6.1

Figure 4-8b, relating to CM247+SC2464, also shows the formation of an oxide scale rich in Al (and with a slight Cr enrichment) at the surface of the coating. However, this layer does not appear continuous, which may account for the higher weight change as compared to the bare alloy. This effect may be exacerbated by the relatively rougher surface (and hence greater surface area) of the coating, compared to the bare alloy.

Figure 4-8c, relating to CM247+SC2464+8YSZ, does not show the significant change to the TBC's composition. (Similar to environment 1; Figure 4-7c). However, the maps do indicate the formation of an Al- and O-rich layer at the

interface of the SC2464 bond coat and 8YSZ TBC. This Al-rich layer appears to contain oxygen unlike Figure 4-7c.

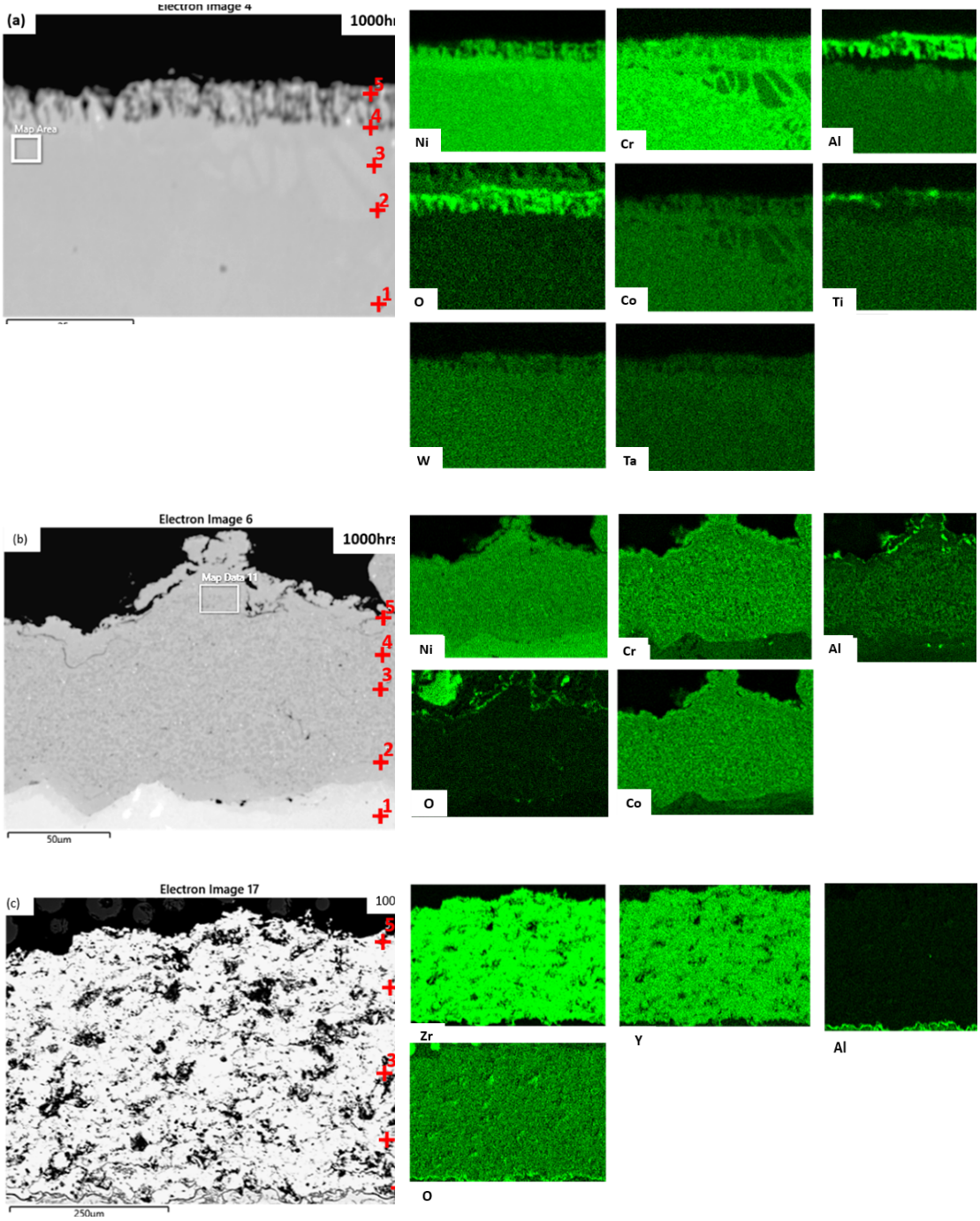


Figure 4-8 - Backscattered and EDX maps for test 2 exposed for 1000h (a) CM247, (b) CM247+SC2464 and (c) CM247+SC2464+8YSZ

4.4 Conclusion

In this study, a nickel-based superalloy, CM247, either bare or with two different coating systems (an environmentally resistant coating or a bond coat/thermal barrier coating system), was tested, simulating a sCO_2 cycle for a power plant scenario. Testing was carried out at 800°C and 1 atmosphere. Samples were studied to investigate the effects of contaminants on the oxidation/carburisation processes, finding that adding contaminants such as SO_2 and N_2 to the gas lead to a more rapid oxidation process in the bare alloy, although neither S not N has been detected in the substrate alloy using EDX. Coatings did not result in a lower rate of oxidation (as observed from weight change measurements); this may be due to the greater surface area of the coating compared to the bare alloy.

5 Paper 2: Comparison of the Oxidation Behaviour of Wrought and Additively Manufactured Alloy 625 in a

Boma Phoebe Norman[a*], Andrew Potter[a], Nigel Simms[a], Emily Rose Lewis[b], Nick Cruchley[c,d], Sam Cruchley[b], and Joy Sumner[a]

[a]Center for Energy Engineering, Cranfield University, Cranfield, UK; [b]Oxford Sigma, Oxford, UK; [c]Manufacturing Technology Centre, Coventry, UK. [d]Rolls-Royce, Goodwood, UK

Abstract

In pursuit of cleaner and more sustainable power generation, supercritical carbon dioxide (sCO_2) has emerged as a power plant working fluid option to help meet emissions targets. The Allam cycle achieves emission reduction through the use of high-pressure sCO_2 in an oxy-combusted, highly recuperated cycle, operating at 300 bar and up to 800°C. Alloy 625, known for its high corrosion resistance, is used for high-temperature components, including heat exchangers, which can be manufactured either traditionally or via additive manufacturing (AM) techniques, such as laser powder bed fusion (LPBF).

This study investigates the impact of Alloy 625's microstructure on resistance to simulated Allam cycle conditions; comparing as-built and solution-heated LPBF AM samples to conventionally manufactured wrought ones. Isothermal oxidation tests were conducted at 800^0C for 1000h in a CO_2 rich environment (CO_2 + 2.7mol% H_2O + 1.43mol% N_2 + 0.17mol% O_2 + 300ppm SO_2). Results indicate that wrought Alloy 625 demonstrated the lowest oxidation rate, attributed to its homogenized microstructure and fine grain size. In contrast, solution heat-treated AM samples exhibited a continuous oxide layer due to grain boundary changes enhancing oxide scale formation. The K_p values of as-built, solution heat treated and wrought manufactured Alloy 625 samples were 4.8 x 10^{-5}, 5.3×10^{-5}, and 4.0×10^{-5} mg^2/cm^4 respectively.

Microstructural analysis revealed that grain morphology and heat treatment influenced oxidation behaviour. As-built samples showed the formation of ridges

on the oxide scale and void formation beneath the oxide scale, while wrought samples displayed uniform oxide layers without subsurface voids. These findings highlight the importance of manufacturing techniques and post-processing on the high-temperature performance of Alloy 625 and its application for turbine casing and heat exchangers in a baseline Allam cycle environment.

Keywords: supercritical carbon dioxide, oxidation kinetics, additive manufacturing, as-built microstructure, solution microstructure, Alloy 625.

5.1 Introduction

The global push towards cleaner and more sustainable power generation aims to reduce greenhouse gas emissions by at least 55% by 2030 [1]. Utilizing supercritical carbon dioxide (sCO_2) as a working fluid in power plant cycles is a potential strategy for the energy industry to enhance turbine efficiency and overall plant performance [2]. The Allam cycle employs high-pressure sCO_2 in an oxy-combustion, highly recuperative cycle with a turbine inlet temperature of up to 800°C and pressures of up to 300 bar [3]. As well as being highly efficient and having a small turbomachinery footprint, this cycle addresses emission reduction objectives by integrating CO_2 capture [3]. However, the unique characteristics of sCO_2 introduce new challenges for turbomachinery components such as heat exchanges, requiring materials that balance cost, mechanical performance, and manufacturability [4].

In high temperature and pressure working conditions, nickel-based superalloys such as Alloy 625 have been used for manufacturing turbomachinery such as turbine casing, heat exchangers etc [5].

Alloy 625 is typically utilized in a gas turbine for components such as swirlers in combustion systems [6], heat exchangers and for turbine casing. Alloy 625 (see Table 5-2 for composition) is a Ni-based superalloy known for its excellent corrosion resistance at temperatures up to 980ºC. Alloy 625 is a chromia-former, which is strengthened by both precipitation hardening [7], and also by solid-solution hardening from the Nb and Mo in the Ni-Cr matrix [8]. Precipitation hardening of Alloy 625 is typically dependent on to the formation of a number of

phases to help minimise creep at high temperatures. These include a δ-Ni_3Nb strengthening phase, gamma double prime (- Ni_3Nb) and various carbides ($M_{23}C_6$, M_6C, MC) [9,10]. The dominant form of MC in Alloy 625 is niobium carbide (NbC). However, with exposure to high temperatures, NbC may decompose, leading to the formation of secondary carbides such as M_6C (Mo, W and Nb rich) and $M_{23}C_6$ (Cr-rich). This formation of secondary carbides can be beneficial or detrimental, depending on their distribution and morphology. Finely dispersed and located along grain boundaries can improve creep strength through prevention of grain boundary sliding, however, the formation of continuous films at the grain boundaries can be detrimental for ductility [11,12]. The heat required for such phase transformation may be introduced during standard processing or post-treatment, however, this is important to consider when exploring newer manufacturing routes such as additive manufacturing (AM). In addition to phases that benefit performance, Ni-based superalloys can form undesirable phases such as laves, μ, and δ phases; after prolonged exposures to high temperatures [13]. As such, Alloy 625's manufacturing methods are important when considering high temperature applications.

Conventional processing techniques include casting, forging and machining, but additive manufacturing (AM) enables the production of complex geometries, faster production time, autonomous production capabilities, the creation of lightweight structures, and topology optimization [14,15]. AM is the process of building up materials to create objects from 3D model data, typically layer by layer, as opposed to conventional subtractive manufacturing methodologies [16]. Despite challenges such as cost of 3D machines and materials, and extensive post-processing to meet industrial standards increases the cost and manufacturing time [17].

Among AM techniques, Laser Powder Bed Fusion (LPBF) offers fine microstructural control, high density, and near-net-shape capability, making it promising for components like heat exchangers [18]. However, due to the energy used, these techniques result in components with complex thermal histories,

which contribute to producing components with unique microstructure & performance characteristics [19–22], including for Alloy 625.

Indeed, research into Alloy 625 indicates that the following microstructural variations may exist as a result of AM:

- The segregation of Nb, Mo and other alloying elements [23], which accumulate in interdendritic regions forms laves phases (Nb-rich) and δ phases (Ni_3Nb) [24,25].
- The as-built microstructure in AM has been found to be more prone to forming laves (Nb-rich) and δ (Ni_3Nb) phases due to the rapid cooling and repeated remelting associated with powder processing.
- The residual stresses and microstructural exposure to high temperature contribute to laves and δ phases formation. Post-build heat treatments help reduce these internal stresses, as well as homogenize the microstructure.

However, Alloy 625 is less susceptible than many other alloys to the formation of ‘hot cracks’ when produced by AM. As an indication, Figure 5-1 shows a weldability diagram (with weldability being a good indicator of suitability for AM production) of various Ni-based superalloys, indicating the ease of fabrication of nickel-based superalloys as a function of their Ti and Al contents. Alloys above the red line have high Ti and Al contents, and present manufacturing challenges for AM fabrication. Alloy 625, with its low levels of 0.10% Ti and 0.11% Al and higher Nb, 3.65% content compared to other Inconel alloys, has been noted to impede rapid age hardening post-welding. Additionally, weld cracking is prevented by inducing chromium carbide precipitation at grain boundaries [26].

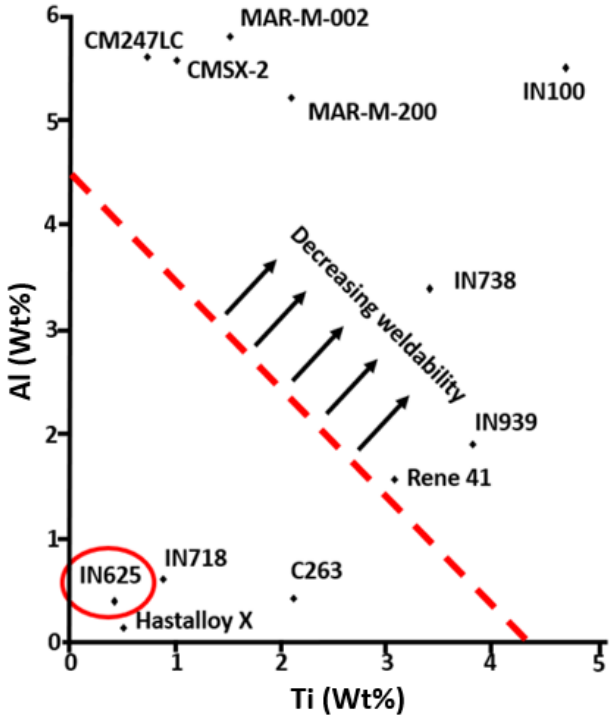


Figure 5-1 - Weldability diagram of nickel-based superalloys with IN625, an Alloy 625 variant, highlighted [191]**.**

LPBF is widely utilised across industries including automotive, energy, and medical sectors [28–30]. Ni-based superalloys produced by LPBF such as Haynes 230 [31], Alloy 718 [32] and Alloy 625 [33–35] have been studied for their mechanical strength and oxidation behaviour at elevated temperatures. However, LPBF components can exhibit defects influenced by process parameters and the material's thermophysical properties such as balling [19], denudation [36], surface roughness [37], porosities (lack-of-fusion, keyhole, and gas porosity) [19,38,39], cracking (solidification [40] and liquation) and delamination [41]. Minimisation of defects through adjusting process parameters has been attempted, for example, Chowdury et al. [43], found that surface roughness can be reduced by increasing energy density, using higher laser power at lower scan speeds, and optimizing hatch spacing. Despite potential defects, LPBF offers advantages over other AM technologies due to its high precision (±0.1 - 0.3%) [44], ability to fabricate complex geometries, and full melting of metal powders resulting into 99.9% density and maximizing tensile strength [17]. Hager et al. [45] were able to print LPBF AF9628 steel with density >99.5%.

Studies have been conducted on LPBF Alloy 625, including microstructural changes [46], manufacturing techniques [47], mechanical properties and surface morphology on oxidation behaviour**.** One area which still needs study is the influence of the Allam cycle's working fluid (sCO_2) on the AM Alloy 625. In particular, as the cycle is a direct-fired system, the working fluid may contain contaminants such as nitrogen and sulphur. For high-temperature oxidation, sulphur can influence the formation of alumina on Ni-based alloys and consequently increase oxidation kinetics as the sulphur content increases [49]. As such, the impact of these in trace levels on the long-term performance of any AM components must be understood

While the oxidation behaviour of traditional wrought Alloy 625 in environments such as air and CO_2 is well documented, the microstructural characteristics of AM material, such as dendritic structure, columnar grains, and fine grain sizes, can influence oxidation resistance. Ramenatte et al. [13] highlights that laser beam manufacturing (LBM) Alloy 625 exhibits lower oxidation resistance than its wrought counterpart, despite identical compositions, primarily due to the difference in microstructure and surface quality. Edwards & Ramulu [50], identifies residual stress microstructure, porosity, and surface finish as key factors influencing fatigue performance and subsequently oxidation behaviour.

This study investigates the role of grain size, phase distribution, and precipitate formation in influencing the oxidation resistance of AM Alloy 625. To address current knowledge gaps, this work examines the oxidation and carburization behaviour of LPBF Alloy 625 in a simulated baseline Allam cycle environment (800°C) in comparison to the wrought samples. Additionally, it provides an in-depth analysis of the oxidation resistance of both as-built and solution heat-treated (1177°C, 1 hr, water-quenched) AM microstructures after 1000h exposure. Metallic AM components may exhibit microstructure and properties distinct conventionally manufactured counterparts, which must be fully understood to build industrial confidence.

As the Allam cycle's sCO_2 working fluid typically contains impurities such as H_2O, COS, NH_3, and HCN, which when combusted, are converted to SO_2, NO, H_2O,

and N_2, AM Alloy 625's performance in this test atmosphere is also studied and compared to conventional manufacturing routes.

5.2 Materials and exposure procedure

5.2.1 Materials

As-received wrought Alloy 625 supplied by Alleima, and LPBF AM manufactured material supplied by the University of Birmingham [46] manufactured by the Manufacturing Technology Centre, have been compared (Table 1). Wrought manufactured (WM) Alloy 625 was machined into cylindrical rods. The dimensions of the cylindrical samples were ∅ 14mm x 10-11mm. The chemical composition of the wrought material is presented in (Table 5-1). WM samples underwent no heat treatment.

The chemical composition of the powder used for AM, given in Table 5-2, was determined using a combination of LECO ICP-MS and XRF. The powder has a size range of 15 – 45 µm and was manufactured into cylindrical samples using the laser-powder bed fusion process in an EOS M280 machine with proprietary parameters. The cylindrical rods produced were 14 mm in diameter x 125 mm in length. To adequately analyse the AM samples' final microstructures, two post-printing procedures were followed. The AM samples were either exposed in an as-built format or underwent solution heat treatment, as shown in Table 5-1. Both WM and AM samples were polished before exposure.

Table 5-1 - Sample codes

Code	**Manufacturing Process**	**Heat Treatment**
As-built (AB)	LPBF AM	None (as-built)
Solution heat treated (SH)		1177°C, 1hr, water quenched (Solution heat treated)

Wrought manufactured (WM)	Wrought	None

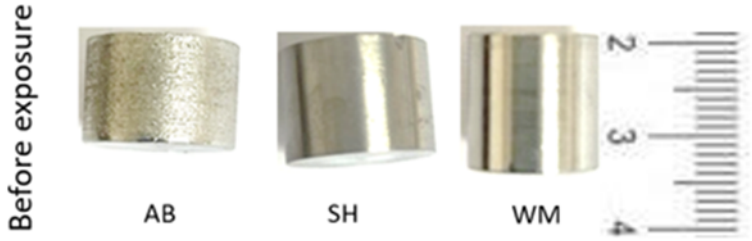
Table 5-2 - Chemical composition of alloys, AM powder composition measured using LECO-ICM XP and WM composition obtained from SEM for Alloy 625 samples

Alloy 625	**Elemental composition (%$_{wt.}$)**												
	C	Mn	Si	P	S	Cr	Co	Mo	Nb	Ti	Al	Fe	Ni
AM	-	<0.01	0.07	<0.01	0	21.27	0.04	9.02	3.65	0.10	0.11	3.66	B
WM	0.025	0.15	0.2	≤0.015	≤0.015	21.5	-	8.7	3.5	-	-	4	61

5.2.2 Pre-exposure treatment of samples

The samples were cleaned with isopropanol and acetone in an ultrasonic bath for 15 mins each to remove any surface contamination. Figure 2 shows the samples before exposure. Dimensions of the cylindrical samples were measured using a digital micrometre with a 0.001mm resolution, and mass was recorded for comparison after the oxidation test (with a 0.01 mg resolution). After each

exposure cycle's completion, sample masses were taken to create a mass change plot.



.

Figure 5-2 - Images of as-built (AB), solution heat treated (SH) and wrought manufactured (WM) samples before exposure

5.2.3 High temperature exposure of samples

Isothermal oxidation tests were performed in a vertical controlled atmosphere furnace at 800°C, for up to 1000h in CO_2 + 2.7mol% H_2O + 1.43mol% N_2 + 0.17mol% O_2 + 300ppm SO_2. The gas flow rate was set at 88.78cc/min using a mass flow controller, and automated injection was used to inject deionised water at a rate of 0.003ml/min into the furnace. This was conducted in 5 cycles, each with a 200h cyclic period.

5.2.3.1 Post-exposure treatment of samples

Samples were mounted in a low-shrinkage epoxy resin with ballotini glass spheres in a 60:40 and cross-sectioned in the XY plane perpendicular to the Z-axis of LPBF build or the cylindrical axis for WM. Samples were ground to 1200 grit size using SiC paper and then polished to 1µm using oil-based diamond polishing medium.

5.2.3.1.1 Microstructural analysis

A VEGA L scanning electron microscope (SEM) was used to capture backscattered electron (BSE) images of cross-sectioned samples and the chemical composition of the oxide scale on alloy was ascertained using elemental dispersive X-ray spectroscopy (EDX). The combination of electron microscopy and EDX techniques was used to provide a comprehensive analysis of the sample's microstructure and oxide scale composition. Samples were electrolytically etched in 10% oxalic acid at 4V for 4 seconds to reveal grain boundary carbides.

5.3 Effect of manufacturing technique on the oxidation behaviour

Parameters including heat treatment and microstructural characteristics, influence the oxidation behaviour of LPBF Alloy 625. To assess the impact of manufacturing solution-treated and as-built LPBF samples were compared with wrought Alloy 625 to evaluate how factors like solution treatment influence phase formation, grain structure, and oxide formation.

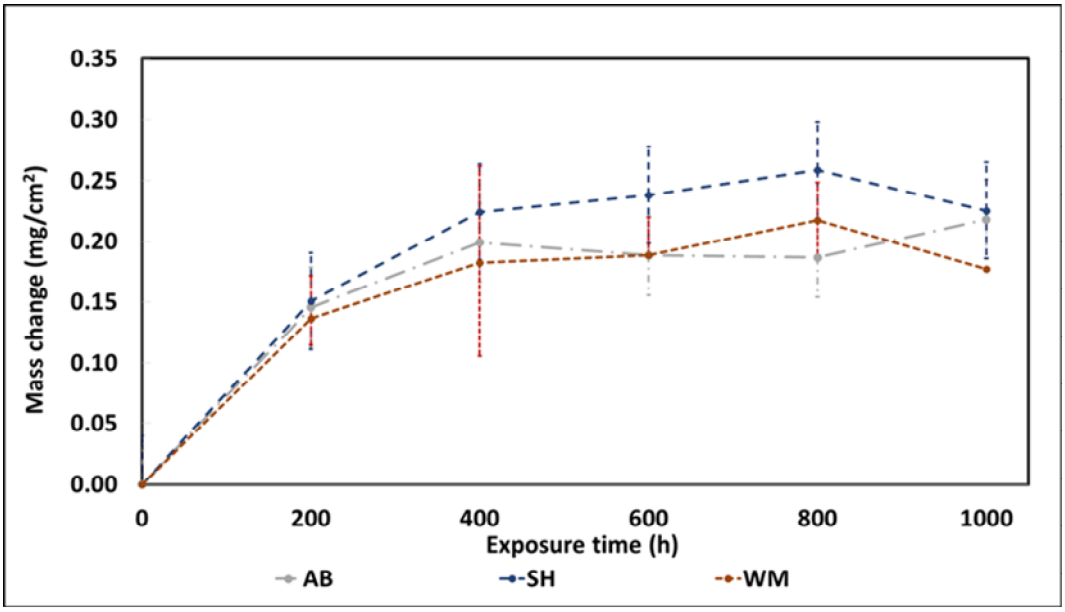


Figure 5-3 - Mass change plot of as-built (AB), solution heat treated (SH) AM and wrought manufactured (WM) Alloy 625 exposed at 800ºC for up to 1000h. Error bars indicate the maximum and minimum values from up to 5 samples.

Figure 5-3 shows the mass change data for Alloy 625. All samples demonstrated less than <1.3g/cm^2 mass gain following 1000h exposure time. The low mass gain indicates Alloy 625 exhibits low oxidation rates in the tested exposure condition. At 1000h, the wrought (WM) solution heat-treated (SH), and as-built (AB) samples show no significant difference in change in mass. Given the overlapping error bars, no significant differences in oxidation behaviour can be concluded between the manufacturing conditions. Noticeably, the mass fluctuations ie, the decreases at 800h points, indicate spallation, which was noticeable in the crucible, which should be considered in interpreting the plot [49]. The three production variants showed little difference in mass change, notably, solution heat-treated LPBF has shown the highest mass gain, 0.26 mg.cm^2/hr while the wrought has shown the least mass gain, 0.18 mg.cm^2/hr.

Table 5-3 - K_p value of as-built, solution heat treated and wrought manufactured Alloy 625 over 1000h exposure

Time (h)	K_p(mg^2/cm^{4}hr)	Error (mg^2/cm^{4}hr)
AB	48.4 x 10^{-6}	8.8 x 10^{-6}
SH	52.9 x 10^{-6}	9.2 x 10^{-6}
WM	40 x 10^{-6}	8 x 10^{-6}

The parabolic oxidation behaviour of as-built LPBF, solution heat-treated LPBF and wrought manufactured Alloy 625 was quantified based on mass change per unit area $\Delta m^2 = K_p t$. Where K_p is the parabolic rate constant, Δm is mass change and t is the exposure time.

The parabolic rate constants (K_p) exhibited similar oxidation resistance across the variations in manufacturing techniques as seen in Table 5-3.

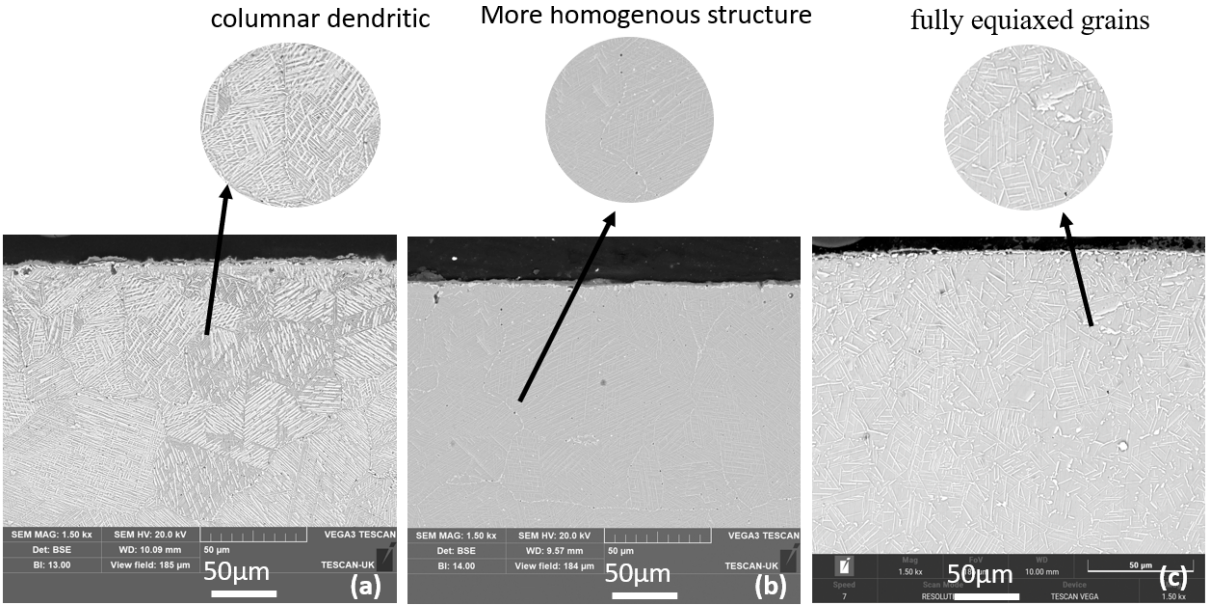


Figure 5-4 - BSE SEM micrographs of polished (a) AM as-built (b) AM solution heated (c) Wrought Alloy 625 after 1000h exposure in CO_2 + 2.7mol% H_2O + 1.43mol% N_2 + 0.17mol% O_2 + 300ppm SO_2 at 800°C. Samples have been electrolytically etched in 10% oxalic acid at 4V for 4 seconds

The as-built microstructure, Figure 4a shows fine grain structure which Emily et al. [46] EBSD analysis shows this as-built structure was a fine columnar dendrites which extended parallel to the build direction, typically due to rapid solidification. The EBSD also showed very few twin grain boundaries (TGBs). LPBF typically produces components with preferential <001> crystallographic orientation, resulting in columnar grains aligned with the building direction [56]. The solution heat-treated sample shown in Figure 4b, shows a more homogenized grain structure and EBSD in Emily et al. [46], shows 30% more TGBs. The wrought sample shows microstructure with fully equiaxed grains, EBSD maps of alloy 625 seen in Chyrkin et al. [51]. As-built AM samples typically demonstrate more pronounced crystallographic texture and grain distribution [52,53]. However, studies like Qi et al. [54] postulate that the grain orientation and texture are controlled by the direction of heat flow and temperature gradient, which depend on process parameters.

Grain size data from the BSE images in Figure 4 were analyzed using the ASTM E112 intercept method in Image J, and the results summarized in Table 5. This intercept line was taken in the horizontal direction, and this reveals a significant difference in grain size as a result of processing.

Table 5-4 - ASTM E112 grain size analysis

Sample Name	**Average Grain Size (μm)**	**Standard deviation Error (μm)**
AB	33.5	9.3
SH	26.1	4.9
WM	13.7	1.9

The relationship between grain characteristics and oxidation behaviour was evident in this study. Microstructural analysis of the as-built (AB), solution heat-treated (SH) LPBF and wrought manufactured (WM) Alloy 625 samples revealed notable differences in grain morphology and size, which correlated with oxidation performance.

The WM samples exhibit the finest average size of 13.7 μm and thus promoting accelerated oxidation as the higher grain boundary density acts as an enhanced diffusion path, which is evident in the BSE images in Figure 5-5. While the AB samples show considerably coarser grains averaging 33.5 μm. The SH samples display an intermediate grain of 26.1 μm due to partial recrystallization. Previous research indicates grain sizes could be important to oxidation behaviour, higher mass gain exhibited in LPBF samples in comparison to wrought samples has been associated with the grain size [55].

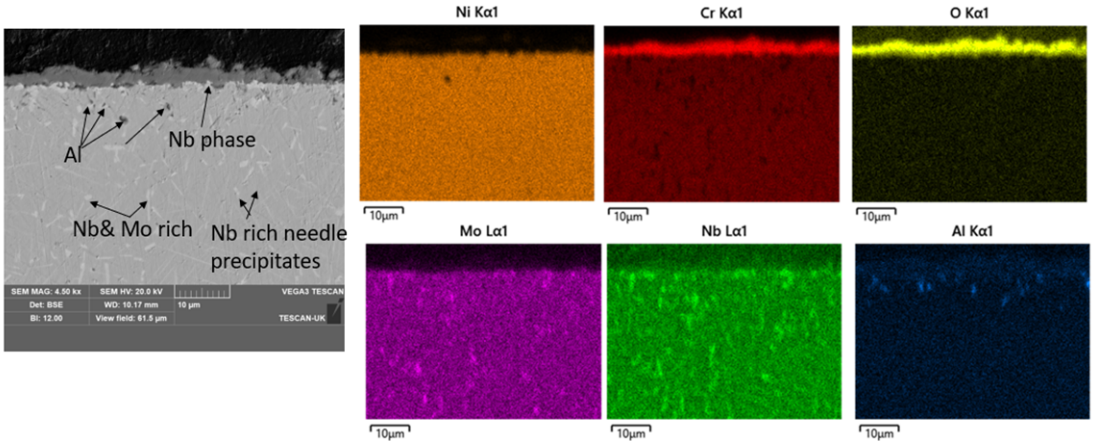


Figure 5-5 - Wrought Manufactured Alloy 625 exposed after 1000h oxidation in CO_2 + 2.7mol% H_2O + 1.43mol% N_2 + 0.17mol% O_2 + 300ppm SO_2 at 800°C

The finer-grained WM samples in Figure 5 developed a thicker continuous oxide layer, indicative of good oxidation resistance. The dense grain boundary network enhanced Cr diffusion, enabling the rapid formation of a continuous and adherent Chromia scale. This promotes efficient selective oxidation of chromium while minimising internal oxidation and maintaining stable oxide/metal interfaces. Such behaviour is consistent with previous studies on chromia-forming alloys manufactured via laser beam processes, including Alloy 718 [57], Alloy 625 [58] and Hastelloy X [59], which also all exhibit parabolic oxidation kinetics. These experimental observations are consistent with previous findings linking grain boundary characteristics to oxidation kinetics in chromia-forming alloys in Sanviemvongsak et al. [60], and Ramenatte et al. [61] works. These results confirm that the refined microstructure of WM Alloy 625 facilitates a more effective selective oxidation of Cr. The improved oxidation resistance observed in wrought specimens can be attributed to their refined grain structure, which shows through multiple protective mechanisms. The finer grain size of WM (13.7 µm) promotes more efficient chromium diffusion to the surface through shortened diffusion pathways and an enhanced grain boundary network, facilitating the rapid formation of a protective chromia layer.

The presence of voids and surface ridges in the oxidized as-built LPBF samples shown in Figure 5-6 indicates the development of stress and non-uniform scale growth. In contrast, the absence of such features in the WM and solution heat-

treated LPBF samples supports the more stable oxide/metal interface and improved scale adherence

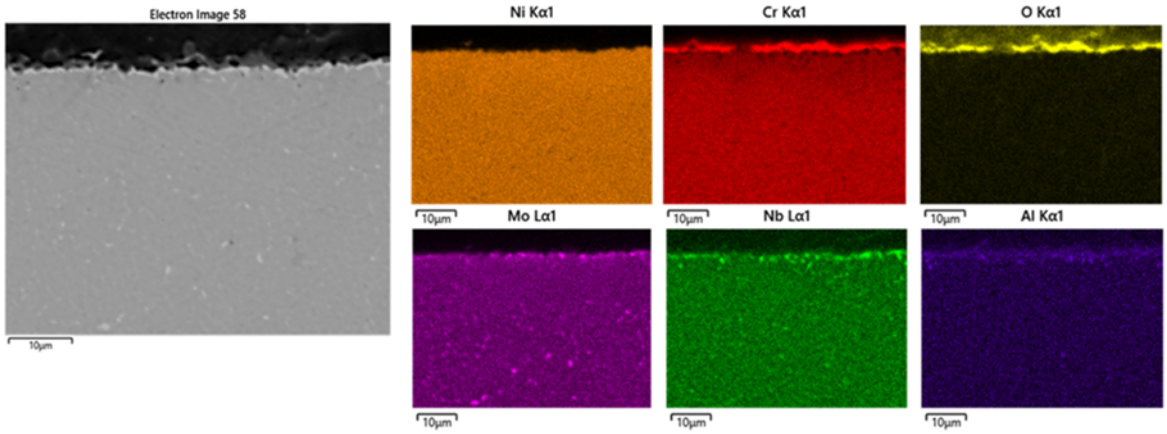


Figure 5-6 - SEM/EDX maps of as-built AM Alloy 625 after 1000h oxidation in CO_2 + 2.7mol% H_2O + 1.43mol% N_2 + 0.17mol% O_2 + 300ppm SO_2 at 800°C

The EDX maps as-built sample shows the formation of an almost continuous chromia rich layer, the Al signals have a very low intensity and do not show any significant alumina looking at the O maps as well in Figure 5-6. Mo and Nb show enrichment near the oxide/substrate interface which indicates the formation of Nb and Mo rich phase. The oxide layer in the as-built appears less uniform than in the wrought counterpart, displaying localised thickening and areas of spallation. This suggests less efficient chromium transportation and delayed chromia formation. The coarser and columnar grains provide few grain boundary diffusion paths compared with the finer grain wrought microstructure, leading to less efficient chromia diffusion towards the surface. Sanviemvongsak et al. [60] identified a microstructural feature in as-built samples: the absence of special grain boundaries with specific crystallographically aligned features that typically enhance oxidation resistance. The absence of such boundaries also combined with higher residual stresses and elementary segregation, leads to discontinuous chromia formation and reduced oxide adhesion. These microstructural features explain the less protective and more irregular oxide scale observed in the as-built Alloy 625 samples compared to the uniform and adherent chromia layer of the wrought.

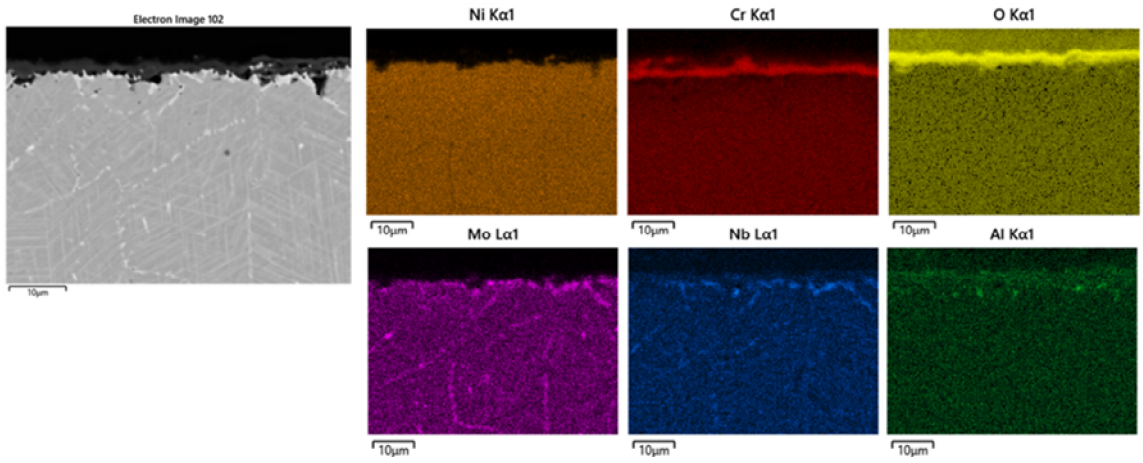


Figure 5-7 - Etched EDX image of solution heated AM Alloy 625 exposed for 1000h in CO_2 + 2.7mol% H_2O + 1.43mol% N_2 + 0.17mol% O_2 + 300ppm SO_2 at 800°C then electro-etched in 10% oxalic acid.

The solution heat treated sample in Figure 5-7 shows a more continuous chromia layer. Ni-Cr alloys like Alloy 625 form duplex oxide structure characterized by a Ni rich δ phase near the metal-oxide and Cr_2O_3 layer near the oxide-alloy interface. These findings align with Parozia et al. [62], who investigated LPBF Alloy 625, comparing solution annealed (2h at 1150°C) and as-built at 900°C up to 100h**.** Their investigation revealed higher mass gain in heat-treated samples attributed to the formation of $NiCr_2O_4$ and Nb_2O_5 clusters inside the oxide scale.

In the as-built AM sample (Figure 5-6), a duplex oxide structure comprising Ni and Cr oxides is observed at the oxide-alloy interface. In contrast, the solution heat-treated sample (Figure 5-7), subjected to oxidation at 800°C for 1000 hours after being heat-treated at 1100°C for 1 hour and water-quenched, exhibits a well-developed and continuous chromia layer. Beneath the chromia layer, an intermetallic Ni and Nb rich phase, expected to be δ-Ni_3Nb phase, was detected in both the as-built and solution heat-treated samples.

5.4 Effect of Heat Treatment on the Oxidation Behaviour.

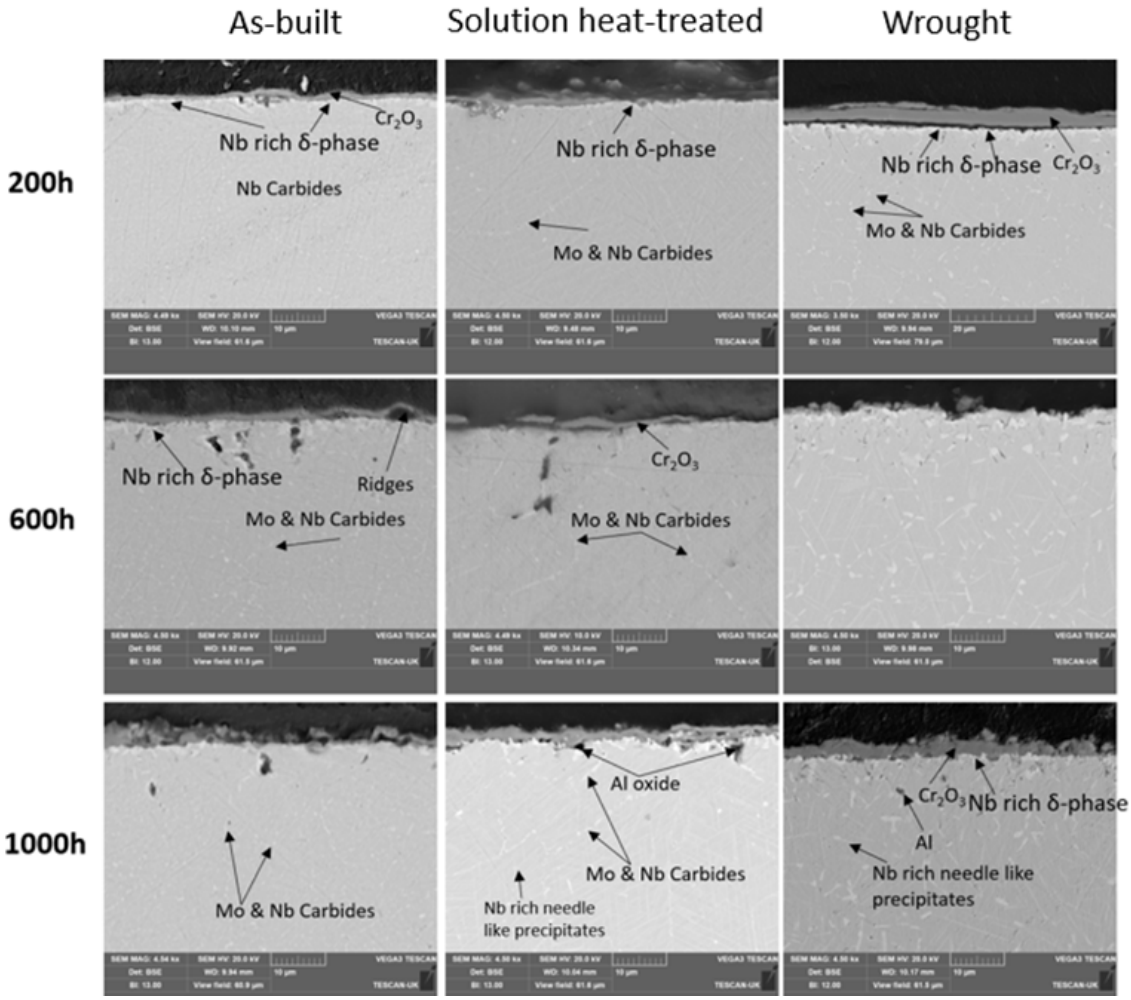


Figure 5-8 - SEM images of as-built and solution heat treated LPBF and wrought Alloy 625 after 1000h oxidation in CO_2 + 2.7mol% H_2O + 1.43mol% N_2 + 0.17mol% O_2 + 300ppm SO_2 at 800°C

Figure 5-8 illustrates cross-sectional SEM images of LPBF as-built, solution heat-treated and wrought manufactured Alloy 625 samples after exposure to CO_2 + 2.7mol% H_2O + 1.43mol% N_2 + 0.17mol% O_2 + 300ppm SO_2 for 200, 600, and 1000h. Cross-sectional SEM analysis after 200h of exposure demonstrates the initial formation of a chromia, likely Cr_2O_3, protective layer in all conditions, accompanied by Nb-rich δ-phase and Nb carbides, though the protective oxide layer is thin, suggesting the initial stage of oxide formation. The solution heat-treated samples exhibited enhanced precipitate structure visibility even at this early stage. Compared to both LPBF samples, the wrought Alloy 625 has a

denser, more continuous oxide layer and a thinner Nb-rich δ-phase below the oxide layer.

As exposure time increased to 600 hours, both microstructures developed thicker oxide scales while maintaining the presence of possible Nb-rich phase and carbides. The as-built sample uniquely developed characteristic ridge formations, marking a divergence in oxidation behaviour between the as-built and solution heat-treated samples. Furthermore, void formation in the subsurface region is noticed in the as-built microstructure after 600h and 1000h. The void formation can be attributed to vacancy injection or internal oxidation of carbon, a phenomenon consistent with the Kirkendall effect. As proposed by Bricknell et al. [63], the outward diffusion of metal cations during oxidation must be balanced by an inward flux of metal vacancies. These vacancies migrate to grain boundaries, where they agglomerate, resulting in the formation of voids and grain boundary deterioration.

The as-built also formed ridges may be linked to the stress concentration in the sample, which could lead to acceleration of spallation [64]. The most substantial differences emerged after 1000 hours of exposure, where solution heat-treated samples demonstrated superior oxidation resistance through the formation of a thick, continuous oxide scale and the presence of internal Al. These samples also developed needle-like δ-phase precipitates throughout the bulk material, while both conditions showed Mo- and Nb-rich precipitate formation along grain boundaries, confirmed through EDX mapping, possibly a Ni_3Nb_2 δ-phase.

These findings have direct industrial applications in gas turbine manufacturing, chemical processing equipment, and advanced manufacturing protocols. The better resistance in terms of formation of ridge void, lesser spallation, and denser oxide layer of solution heat-treated samples (as seen in Figure 5-7) suggests that post-processing heat treatments for AM samples could eliminate the formation of ridges and reduction in spallation, which could improve component durability in high-temperature CO_2-rich environments. Spallation was observed in LPBF materials, with the as-built exhibiting more pronounced spallation after exposure. The absence of Ridge-Void (RV) formations in wrought samples, as noted by

Chyrkin et al. [64] indicates that RV morphology is not inherently linked to AM processing and appears independent of reaction conditions. This independence from processing method suggests that RV formation is a fundamental material response to environmental conditions rather than a manufacturing artifact when the as-built and solution heat-treated micrographs in Figure 5-7 are compared. The formation of RV on the as-built can act as stress concentration sites, which can influence surface degradation. The increased spallation in as-built samples may be linked to higher residual stresses, or microstructural heterogeneities specific to the LPBF process.

The absence of RV morphology could benefit component performance through improved mechanical integrity, enhanced oxidation resistance due to more uniform oxide layer formation, and potentially extended component lifetime through reduced degradation mechanisms. Further investigation of the relationship between precipitation kinetics and oxidation behaviour could yield valuable insights for optimizing industrial applications of AM-manufactured Alloy 625 components.

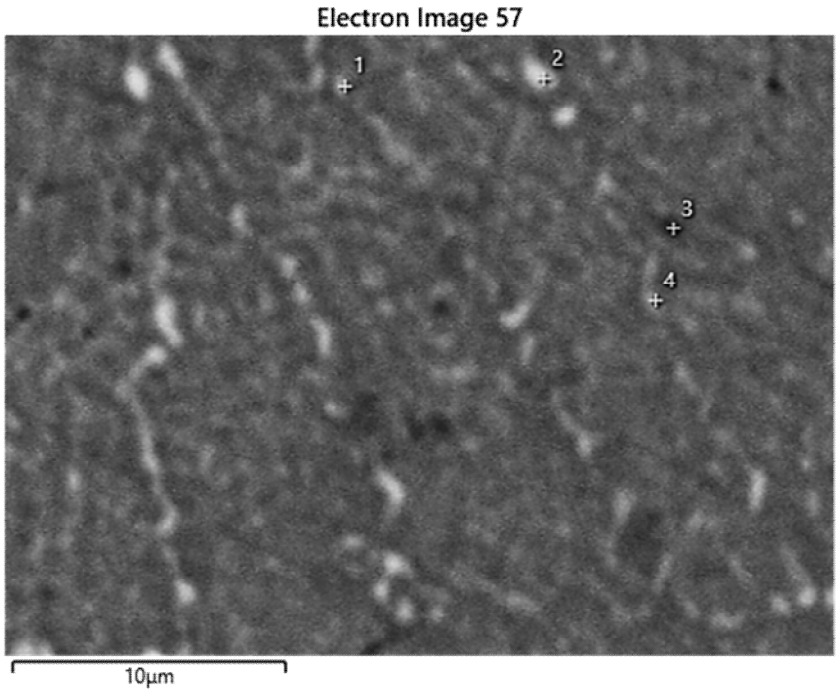


Figure 5-9 - As-built LPBF Alloy 625 after 1000h exposure in CO_2 + 2.7mol% H_2O + 1.43mol% N_2 + 0.17mol% O_2 + 300ppm SO_2 at 800°C

Figure 5-9 shows the locations corresponding to the points analysed in Table 5-5 for As-built LPBF Alloy 625, where precipitates were observed along grain boundaries to identify the precipitates that formed.

Table 5-5 - Point analysis of as-built LPBF Alloy 625 after 1000h exposure in CO_2 + 2.7mol% H_2O + 1.43mol% N_2 + 0.17mol% O_2 + 300ppm SO_2 at 800°C

Point(wt%)	Ni	Cr	Mo	Nb	Fe	Si	S
1	53.6	21.1	15.9	4.6	3.6	0.4	0.3
2	45.7	25.1	19.8	4.7	3.2	0.6	0.6
3	58.5	21.3	7.9	5.4	3.8	-	-
4	58	20	9.5	7.8	3.4	0.2	-

The point analysis of precipitates after 1000h oxidation reveals the formation of Nb- rich and Cr- rich carbides. The elevated Nb concentrations at Points 3 (5.4wt%) and 4 (7.8wt%), suggest the formation of niobium carbides (NbC), consistent with the known carbide-forming tendency of Nb in Ni-based superalloys under thermal exposure [65]. The Cr enrichment at point 2 (25.1wt%) suggests the presence of $Cr_{23}C_6$ carbides, which are thermodynamically favoured in high-Cr alloys under oxidizing conditions [66]. The significant Mo levels (up to 19.8% at Point 2) suggest the potential for complex mixed-metal carbides (e.g., M_6C, where M = Ni, Mo, Cr). Variations in elemental distribution reflect localized phase formation and diffusion induced segregation during oxidation. Additionally, Xuebing et al. [67] observed that $M_{23}C_6$ was not found in the as-cast specimen, suggesting that $M_{23}C_6$ was exclusively formed during the solution heat treatment process. The presence of carbon in the environment during high-temperature oxidation potentially accelerates carbide formation through carbon diffusion into the alloy surface, leading to enhanced precipitation. Notably, despite the presence of sulphur and nitrogen in the testing environment, these elements were not detected during point analysis, suggesting potential limited interaction with

the alloy surface or delocalised distribution. These findings have significant implications for industrial applications, particularly in component lifetime prediction in high-temperature environments and the optimization of heat treatment protocols for desired carbide distributions, while also enhancing our understanding of degradation mechanisms in service conditions. The comprehensive understanding of microstructural evolution in additively manufactured superalloys under oxidizing conditions provided by this analysis suggests that further investigation of the carbon environment's role in precipitation behaviour would be valuable for optimizing material performance in industrial applications, particularly in high-temperature and oxidizing environments where carbide stability plays a crucial role in component longevity. The absence of detectable sulphur and nitrogen indicates favourable environmental conditions for oxide scale formation and stability, contributing to the overall oxidation resistance of the alloy.

5.5 Conclusions

This study investigates the oxidation behaviour of LPBF in comparison with wrought Alloy 625, highlighting the influence of manufacturing parameters such as heat treatment, and microstructural characteristics on its high-temperature oxidation resistance. Heat treatment of LPBF, particularly solution heat treatment, influenced oxidation resistance by promoting a microstructure which was demonstrated to support the development of a protective chromium oxide layer. The study demonstrates that solution heat treatment forms adherent chromia layer which is important for high temperature exposures. Careful consideration must be given to managing microstructural defects such as voids and ridges that can compromise long-term stability. These defects highlight spallation noticeable during cyclic oxidation and the need for post-processing optimization to mitigate the impact of these microstructural flaws. The study examines the role of microstructure, and grain boundary in the formation of a protective oxide layer. Wrought Alloy 625, with its fine and uniform grain structure, demonstrated a thicker protective oxide layer, indicating better oxidation resistance compared to the LPBF variants, both as-built and solution heat-treated. Despite this, both

LPBF variants also developed Cr oxide layers, indicating baseline suitability for high temperature applications. Notably, the solution heat treated LPBF sample displayed a thicker continuous oxide layer with the absence of ridge like features when compared to as-built. By 1000 h, the wrought alloy had already formed a much thicker oxide layer, suggesting that prolonged exposure may lead to the depletion of protective elements such as Al, Cr. In contrast, the solution-treated LPBF sample is expected to continue developing its oxide layer at a more gradual rate, reducing the risk of significant alloy degradation or alloy strength during extended service. The findings hold particular relevance for Allam cycle power plants operating in supercritical CO_2 environments, where component durability under extreme conditions directly impacts system reliability and efficiency.

Future work should focus on extended cyclic oxidation studies beyond 1000 hours, and investigation of combined high-pressure and temperature effects on oxidation behaviour. Additional research directions include exploring modified alloy compositions and understanding the impact of thermal and pressure cycling on oxide scale adherence. These investigations would further enhance our understanding of material behaviour in supercritical CO_2 environments and contribute to the advancement of Allam cycle technology.

Funding Acknowledgement

The Authors would like to thank EPSRC for funding, also thank Alleima in Germany for the provision of the Alloy 625 wrought samples and the University of Birmingham, United Kingdom, for providing the LPBF samples made by the Manufacturing Technology Centre.

6 Paper 3 : Influencing Effect of Surface Roughness on the Oxidation and Carburization behaviour of Laser Powder Bed Fusion (LPBF) Alloy 625 in a Simulated High Temperature Allam Cycle Environment

Boma Phoebe Norman[a*], Joy Sumner[b], Stefano Mori[a], Nigel Simms[a], Emily Rose Lewis[c], Nick Cruchley[d], Sam Cruchley[e] and Andrew Potter[a]

[a]Centre for Energy Engineering, Cranfield University, Cranfield, UK; [b]Centre of Energy, Swinburne University of Technology, Victoria, AU; [c]Oxford Sigma, Oxford, UK; [d]Rolls- Royce, Derby, UK; [e]School of Metallurgy and Materials, University of Birmingham

Abstract

The Allam cycle, a novel climate-friendly power generation method, minimizes greenhouse gas emissions by using highly thermally efficient supercritical CO_2 as its working fluid. However, its extreme operating conditions challenge material selection and manufacturing for turbomachinery. Additive manufacturing (AM) techniques, including Laser Powder Bed Fusion (LPBF), promise low-wastage component production with complex geometries but have high as-produced surface roughness, potentially affecting performance. This study explores surface roughness effects on the cyclic oxidation and carburization of LPBF Alloy 625 under representative Allam cycle conditions for 1000h at 800^0C in CO_2 + 2.7mol% H_2O + 1.43mol% N_2 + 0.17mol% O_2 + 300ppm SO_2. Three surface finish variations (P600 UK grit size, 6 µm polished, and as-received) were tested and compared to wrought manufactured results. Findings show polished surfaces exhibit lower oxidation kinetics and thinner oxide scales compared to rough ones, highlighting the importance of surface quality in performance enhancement.

Keywords: CO_2, oxidation, carburization, Allam cycle, additive manufacturing, LPBF, surface roughness, Alloy 625.

6.1 Introduction

Potential solutions to significantly reduce current greenhouse gas emissions are currently being implemented in the energy sector. However, this must be carried out whilst ensuring efficiency and cost effectiveness of the plant. The Allam Cycle offers a promising pathway towards a sustainable energy future by enabling the clean and economical utilization of hydrocarbon energy reserves. The Allam cycle is a novel solution that employs oxy-combustion and high-pressure supercritical CO_2 (sCO_2) working fluid in a highly recuperated cycle [15] operating at a temperature of up to 1100°C and pressures of up to 300 bar. This process also captures CO_2 generated during combustion, making it available for sequestration or reuse, thereby addressing the environmental concerns associated with traditional means of power generation [17]. sCO_2 power cycles can significantly increase cycle efficiencies in comparison to conventional steam cycles. Higher efficiency results in lower fuel costs and reduced greenhouse gas (GHG) emissions; moreover, the high operating pressure throughout the cycle leads to higher density, enabling smaller equipment size and a smaller plant footprint, consequently lowering capital costs [218].

Oxidation and carburization of component materials at high temperature and pressure CO_2 is a major issue in Allam cycle systems. Allam cycle power systems require alloys that will be exposed to high temperatures (>650°C) for components like the heat exchangers. For these sections to withstand the operating conditions, superalloys are typically used due to their high temperature strength coupled with oxidation and corrosion resistance. Oxidation as well as carburization of suitable materials in high temperature sCO_2 has been investigated at various temperatures [35,219–221].

Alloy 625 is one of the Ni-based superalloys widely used in high-temperature environments in various industries. Alloy 625 has good corrosive environment resistance enabling it to be used in industrial applications such as turbine casing and heat exchangers. Alloy 625's strength is primarily derived from solid solution strengthening via alloying with Cr (20-23wt%), Mo (8-10wt%) and Nb+Ta (3.15-4.15wt%) [222]. Furthermore, Alloy 625 forms carbides such as $M_{23}C_6$, M_6C or

even MC, where $M_{23}C_6$ is Cr-rich carbide, M_6C is Ni, Nb and Mo rich and MC is Nb rich [223]. γ″ and δ phases are observed to develop in traditional solid solution strengthened Alloy 625 when subjected to prolonged periods of elevated temperatures, typically ranging from hundreds to thousands of hours [223]. Casting and forging of Alloy 625 are difficult, especially when manufacturing complex geometries parts thus using new technologies would be beneficial.

Additive manufacturing (AM) has gained significant adoption over the past few years and has since been applied to various sectors such as the power and energy industry, medical, aeronautics, etc. AM following ASTM [25], is the 'process of joining materials to make objects from Computer Aided Design (CAD) model data, usually layer upon layer' as opposed to a conventional manufacturing technique. AM is a disruptive technology [224], enabling engineers to produce complex geometry power plant parts, which can drive advancement in the energy industry. By generating, for example, shaped film cooling [184]. AM technology can be categorized in accordance with the material state; solid-based, powder-based, and liquid-based. Powder-based includes selective laser sintering (SLS), electron beam melting (EBM), selective laser melting (SLM), and fused metal deposition (LMD). SLM is also called laser powder bed fusion (LPBF) and uses a high-density laser energy source, melting and fusing selective regions of powder, layer by layer. Amongst currently employed alloys for additive manufacturing are Ni- based alloys such as Alloy 718 and 625. Oak Ridge National Laboratory has produced turbine blades via EBM from Inconel 738 potentially improving the efficiency of the turbine through incorporating complex internal cooling channels, allowing turbines to run hotter [225].

Several factors have an effect on the oxidation and carburisation behaviour of LPBF alloys. To understand the impact of LPBF on resulting components, the two major defect formation mechanisms associated with Ni–based superalloys, cracking and porosity, must be known. Cater et al. [226] studied Ni-based superalloys and established that, to determine cracking and porosity, multiple processing parameters from the AM system could be combined into a single parameter; energy density. This is useful for controlling the porosity thus tailoring

mechanical properties of the alloy**.** Surface preparation is another influencing factor affecting AM component performance in a high-temperature environment. The surface finish of a component before being utilized influences the density of subsurface dislocations that may persist at low and intermediate temperatures [227].

Sudbrack et al. [227] investigated the surface variation of two turbine blade materials, LDS-1101 HF and CMSX-4, and postulated a correlation between the surface preparation and the oxide scale formed. Results show surface roughness influences the type of oxidation mechanism that forms at 815°C, with rough finishes promoting the formation of thin, stable Al_2O_3 external scales, and smooth finishes resulting in thicker, less protective NiO external scales with a complex internal oxide structure**.** A rough surface accelerates the transformation of ε-Al_2O_3 to α–Al_2O_3 through increment of density of alpha-alumina nuclei whilst a polished surface delays the transformation. The growth rate of α–Al_2O_3 grains is influenced by the surface finish with a rough surface promoting faster growth [228].

Similarly, Uran et al. [229] studied Fe-Cr-Al alloys and observed that residual stresses are higher in polished samples with 3μm surface roughness. The scale composition also had higher Fe concentration on rougher surfaces, with almost no Fe on polished samples indicating that roughness influences scale growth rate and also scale phase type. Whilst establishing a correlation between composition changes, residual stresses, and scale thickness and roughness, this study does not conclusively determine the driving mechanism behind these effects.

The responses of these alloys are important when considering what materials to use in industrial applications. For example, the supercritical CO_2 transformational electric power (STEP) pilot plant is a demonstration plant in San Antonio, Texas, USA. The 10MWe pilot is the largest test facility for indirect-fired supercritical carbon dioxide technology. Major challenges in manufacturing components for the plant include the technological challenges arising from Alloy 625 fabrication, scheduling factors as a result of the COVID era well as alloy 625 weld problems. Hence, this paper investigates the effect of surface preparation of LPBF Alloy 625 after 1000h oxidation and hypothesizes that rougher surface preparation

techniques lead to higher point defects into the alloy and increased oxidation. To test this hypothesis, the influence of surface roughness on alternative techniques of metal manufacturing in a simulated baseline Allam cycle working condition is examined.

6.2 Experimental procedure

6.2.1 Material system

Cylindrical as-built and solution heat-treated AM alloy 625 samples were manufactured using the LPBF process, specifically with an EOS M280 (400W) machine from the University of Birmingham was used [201]. The manufacturing specifications of this process are in Table 6-1. The build orientation is vertical (Z) aligned perpendicular to the build plate, and layers are deposited upwards along the Z-axis.

Table 6-1 - Manufacturing specification of AM Alloy 625.

AM Sample specification	
Material	Alloy 625
Process	LPBF
Machine	EOS M280 (400W)
Powder size range	15 – 45 μm
Parameters	Proprietary
Sample shape	Cylindrical
Build orientation	Vertical (Z)

The as-built alloy 625 was solution heat-treated at 1172°C for 1 hour and water quenched to produce the solution heat-treated samples used for this experiment. Samples were cut to a diameter of 12mm and length of 10mm for this experiment.

1.1. Surface Preparation

Three surface finishes of solution heat-treated samples were investigated to study the influence of oxidation behaviour. The external body of the solution heat-treated sample finishes were:

1. As received.
2. Ground with P600 SiC paper for 2 mins.
3. Ground with P600 SiC paper and polished with 6µm diamond for 96s.

For 2&3, these preparations were carried out using an automated grinding/polishing machine at a load of 35N. The sample codes are summarized in table 6-2.

Table 6-2 - Sample codes for AM Alloy 625 samples with various surface roughnesses as determined by laser profilometer.

Sample code	Sample Overview	Surface roughness (R_a) (µm)
6µm	Polished AM solution heat-treated microstructure	0.28
P600	600 UK grit solution heat-treated microstructure	0.21
SR	As-received solution heat-treated microstructure	2.62

The surface roughness of the alloy samples was measured using a laser profilometer, and this was done in the Y direction. The average value of 3 measurements was recorded. The chemical composition of the powder was determined using LECO ICP–MS and XRF techniques. The chemical composition of AM alloy 625 is presented in Table 6-3.

Table 6-3 - Chemical composition of AM alloy 625, obtained using LECO – ICM.

Alloy 625	**Chemical composition (%wt.)**											
	C	Mn	Si	P	Cr	Co	Mo	Nb	Ti	Al	Fe	Ni
AM	-	<0.01	0.07	<0.01	21.27	0.04	9.02	3.65	0.10	0.11	3.66	B

6.2.2 High temperature testing

Isothermal testing was performed at 800°C for up to 1000h in a CO_2 environment with contaminants such as N_2 and S typically found in an Allam cycle**.** Each cycle lasting up to 200h. Testing was carried out in a controlled atmosphere, vertical furnace and the test chamber schematic is given in Figure 1. The test gas used for the experiment is CO_2 + 2.7mol% H_2O + 1.43mol% N_2 + 0.17mol% O_2 + 300ppm SO_2 with a flow rate of 88.74cm/min and Deionised water was introduced into the furnace at 0.002ml/min.

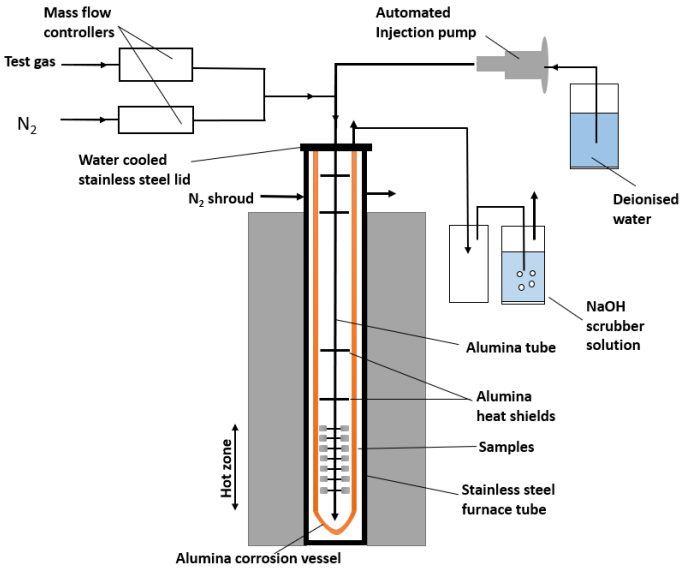


Figure 6-1 - Schematic of furnance

Before exposure, samples were cut and cleaned with isopropanol. Dimensional measurements were taken round the sample using a digital micrometre with a ±1 ± 2 µm accuracy. After mass measurements were taken, which had a measurement accuracy of ± 0.1-0.2 mg. Weight measurement was also recorded after each cycle to monitor mass change.

6.2.3 Analysis

The microstructure of the samples was examined using an optical microscope to gather information on the extent of metal loss. The X and Y coordinates of the metal loss were analysed for dimensional measurements and a cumulative probability vs change in good metal plot is made. Subsequently, a VEGA L scanning electron microscope was employed to capture backscattered electron (BSE) images of cross-sectioned samples. At the same time, energy-dispersive X-ray spectroscopy (EDX) was utilized to determine the chemical composition of the oxide scale. Samples were electro etched in 10% oxalic acid at 4 volts for 4s before SEM analysis to capture the grain boundary of the sample. The etching is done to make the crystalline structure visible with a microscope.

6.3 Results and discussion

6.3.1 Mass change results

Figure 6-2 shows the mass change plot for 3 samples: (i) polished (ii) P600, and as-received samples in solution heat-treated samples. Surfaces with a higher surface roughness have a larger surface area for diffusion. As-received samples at 600hrs experienced a gain in mass of 0.078mg/cm^{2,} and 6µm polished samples

gained 0.238mg/cm^2. Interestingly, the as-received sample, which had the roughest surface, showed the least change in mass with respect to time. However. spallation was observed with the alloys, especially with the as-received samples. Different factors can influence the mass change of a sample; Sudbrack et al. [227] observed that surface treatment processes on single-crystal superalloys, LDS-1101+Hf and CMSX-4+Y can influence grain refinement and thus increase the number of grain boundaries, subsequently changing the alloy's mass gain during oxidation. A study by Leistikow et al. [230] on Alloy 800 found that introducing higher grain boundary density through cold working led to smaller mass gains, while decreasing the grain boundary density increased the mass gain. The grain boundaries made for easy diffusion paths for the Cr and Mn in the oxide/alloy interface. The investigations demonstrate that mechanical pretreatment significantly benefits the formation of oxide scale on an austenitic Fe-Ni-Cr alloy. Techniques such as cold work, grinding, polishing, sand blasting, and shot peening create easy pathways for rapid Cr diffusion to the surface, ensuring an ample supply of Cr to develop a protective oxide layer.

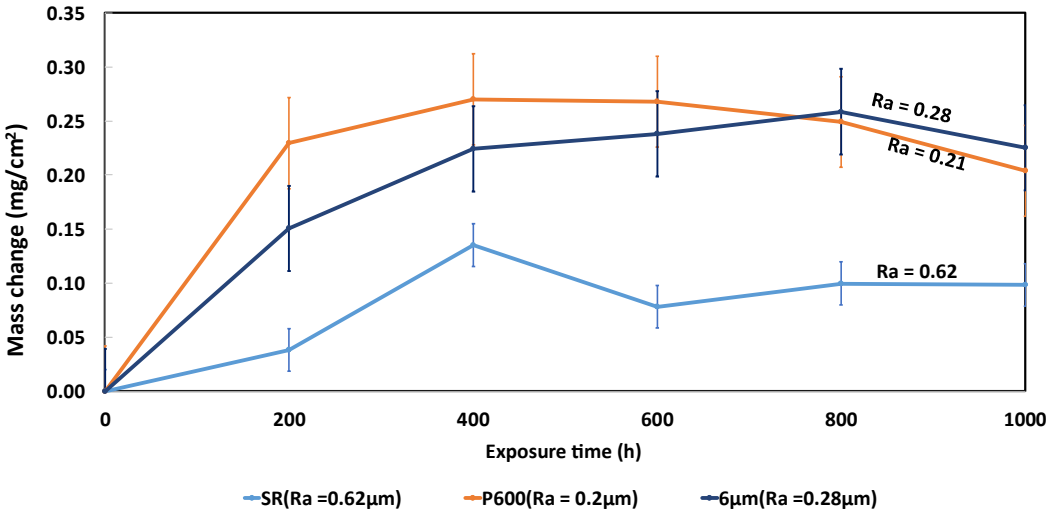


Figure 6-2 - Mass change plot of Alloy 625 samples with 3 roughnesses exposed in CO_2 with contaminants for 1000h at 800°C

The plot indicates the samples followed a parabolic rate, which is calculated using Pilling and Bedworth equation; $(\frac{\Delta W}{A})^2 = K_p * t + C$. Where $\frac{\Delta W}{A}$ is weight gain per

unit surface area (mg/cm^2), t is exposure time (h), C is a constant and K_p is the parabolic rate constant ($(mg/cm^2)^2$ /h) .

Table 6-4 - Kp value of Alloy 625 with variation in surface roughnesses

Sample Code	Kp Values ($mg^2/cm^4.h^{-1}$)
SR	0.0032
P600	0.0334
6µm	0.0132

K_p is highest for P600 and lowest for polished 6 µm. The results in Table 6-4 show that the average parabolic rate obtained for a polished sample is 0.0132 $mg^2/cm^4.h^{-1}$ whilst the ground is 0.0334 $mg^2/cm^4.h^{-1}$ and as-received is 0.0032 $mg^2/cm^4.h^{-1}$. The ground samples (P600) displayed higher and very similar oxidation rates. However, the as-received (SR) sample, despite having the highest surface roughness, exhibited the lowest mass gain and Kp. This counterintuitive behaviour may be due to oxide spallation, which is very noticeable in the crucible. Rougher surfaces generally develop thicker, more stressed oxides that are prone to cracking and detachment during cooling. Spallation would reduce the net measured mass gain, giving the appearance of slower oxidation. Therefore, the SR result is most likely influenced by spallation effects rather than roughness alone.

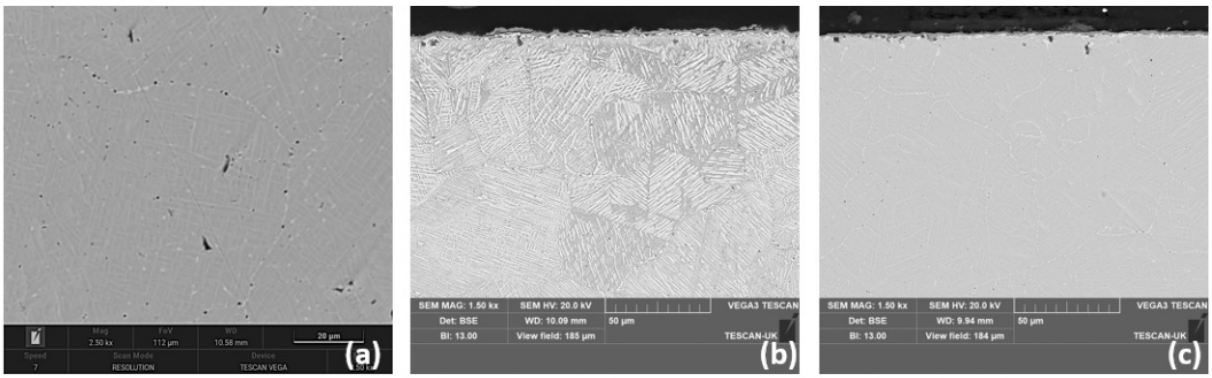


Figure 6-3 - Etched SEM images of Alloy 625 at x1500 magnification. Solution heat-treated LPBF (a) as-received (b) P600 grit (c) polished exposed in CO_2 + 2.7mol% H_2O + 1.43mol% N_2 + 0.17mol% O_2 + 300ppm SO_2 for 1000h at 800°C

Figure 6-3 shows the microstructure of various AM finishes of Alloy 625. The microstructure shows the needle-like precipitates form below the oxide scale and are heterogeneously distributed in the bulk material. It can be observed in Figure 6-3 that the rougher the surface, the more prominent the needle-like precipitates. Figure 6-3b displays P600 grit microstructure, and higher density needle-like precipitates can be noticed. Figure 6-3c shows the polished counterpart, after etching, shows a relatively more uniform grain size and less prominent needle-like precipitates. All the samples were electrolytically etched in the same oxaylic acid for 4 secs each to ensure the extent to which the samples were etched is the same. The polished surface reduces the sites for carbon diffusion, thus resulting in a more uniform carbon diffusion across the surface from the environment.

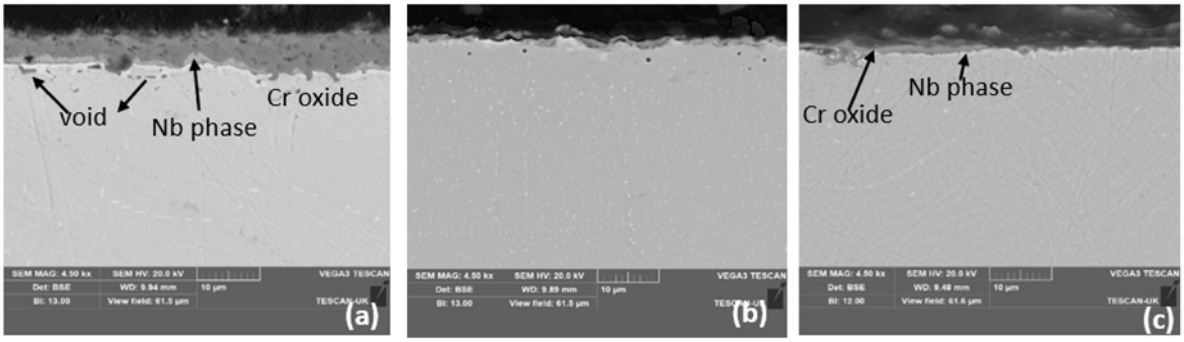


Figure 6-4 - SEM images of Alloy 625 at x4500 magnification. Additive manufacturing of (a) as-received (b) P600 grit (c) polished exposed in CO_2 + 2.7mol% H_2O + 1.43mol% N_2 + 0.17mol% O_2 + 300ppm SO_2 for 200h at 800°C

The formation of precipitates was observed as early as 200hrs, as seen in Figure 6-4, and the density of precipitates was dependent on the surface roughness. The P600 ground alloy formed more prominent precipitates than in polished indicating that the surface roughness exposes more nucleation sites for oxide

development subsequent Nb-rich phase formation. The prominence of Niobium-rich needle-like precipitates in ground AM than in polished can be attributed to the surface conditions. The ground AM alloy 625 potentially exposes more nucleation sites for formation of precipitates. The increased surface area in ground alloy can provide more sites for diffusion of alloying elements and nucleation of precipitates, thus a higher density of precipitates compared to the polished surface.

Figures 6-4(a–c) show that the polished sample developed a shallower oxide–alloy interaction zone, as expected for a surface with low roughness and fewer nucleation features. In contrast, the P600-ground and as-received sample demonstrates a thicker near-surface reaction zone with more numerous voids beneath the Cr-rich oxide. The Nb-rich phase observed directly beneath the oxide scale is characteristic of Alloy 625 and is commonly associated with niobium segregation during high-temperature exposure.

6.3.2 Dimensional metrology

Figure 6-5 displays the cumulative probability plots of the 3 different surface finish samples with respect to their change in good metal. The plots show the rate at which metal is lost with respect to the whole sample. P600 data indicates that at the 50% probability of metal loss shows about 8μm or more metal is lost, and relatively about the same amount of good metal is lost or more with the as received sample. The P600 samples also showed spallation which should be taken into account. The 6μm sample exhibited the least change in good metal; about 5μm or more metal loss occurred for the median probability. These results correlate with current literature about polished surfaces experiencing the least oxidation in comparison to the rougher surfaces [231]. The dimensional metrology shows that both samples lose a similar amount of metal, despite their very different mass-change curves. This confirms that the low mass gain in the as-received sample is not due to slower oxidation, but is instead consistent with extensive oxide spallation, which hides the true mass increase. This analysis considers spallation and is thus a more accurate method for analysing loss of

metal as it measures the direct geometric change i.e., diameter and thickness, than weight change, which measures the change in total mass.

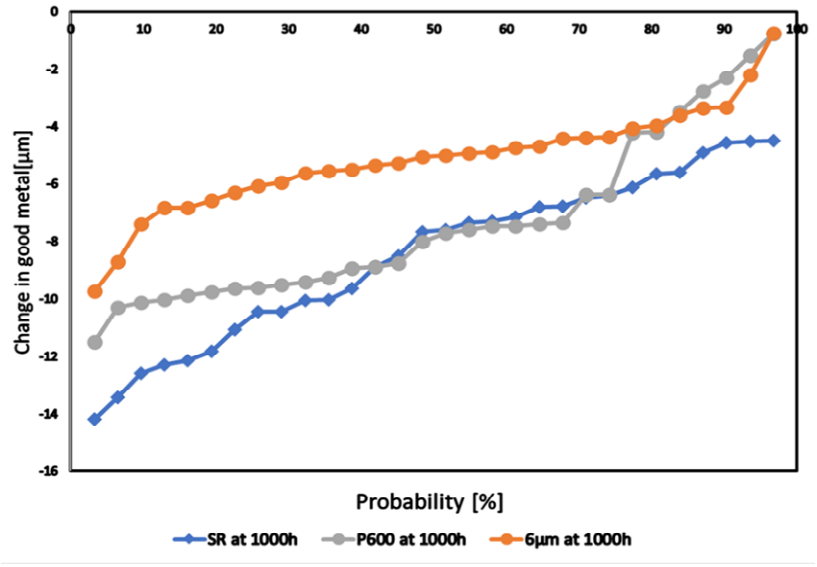


Figure 6-5 - Dimensional metrology of (a) as-received (b) P600 grit (c) polished exposed in CO_2 + 2.7mol% H_2O + 1.43mol% N_2 + 0.17mol% O_2 + 300ppm SO_2 for 1000h at 800°C.

6.3.3 Analysis the effect of roughness on the Oxidation and carburization behaviour

The cross-sectioned micrographs of SR, P600, 6µm up to 1000h are displayed in Figure 6-6a, b, and c, respectively. It can be noticed that a thicker oxide scale formed on the as-received sample than on the P600 ground sample. This is consistent with previous studies demonstrating that surface roughness significantly influences oxide scaler formation and thickness in nickel-based superalloys. The SEM analysis Figure 6-6a shows the formation of an external Cr oxide scale rich in Mn and the presence of noticeable internal Al oxide , which is the expected protective oxide layers that form on Ni-Cr based alloys during high-temperature exposure.

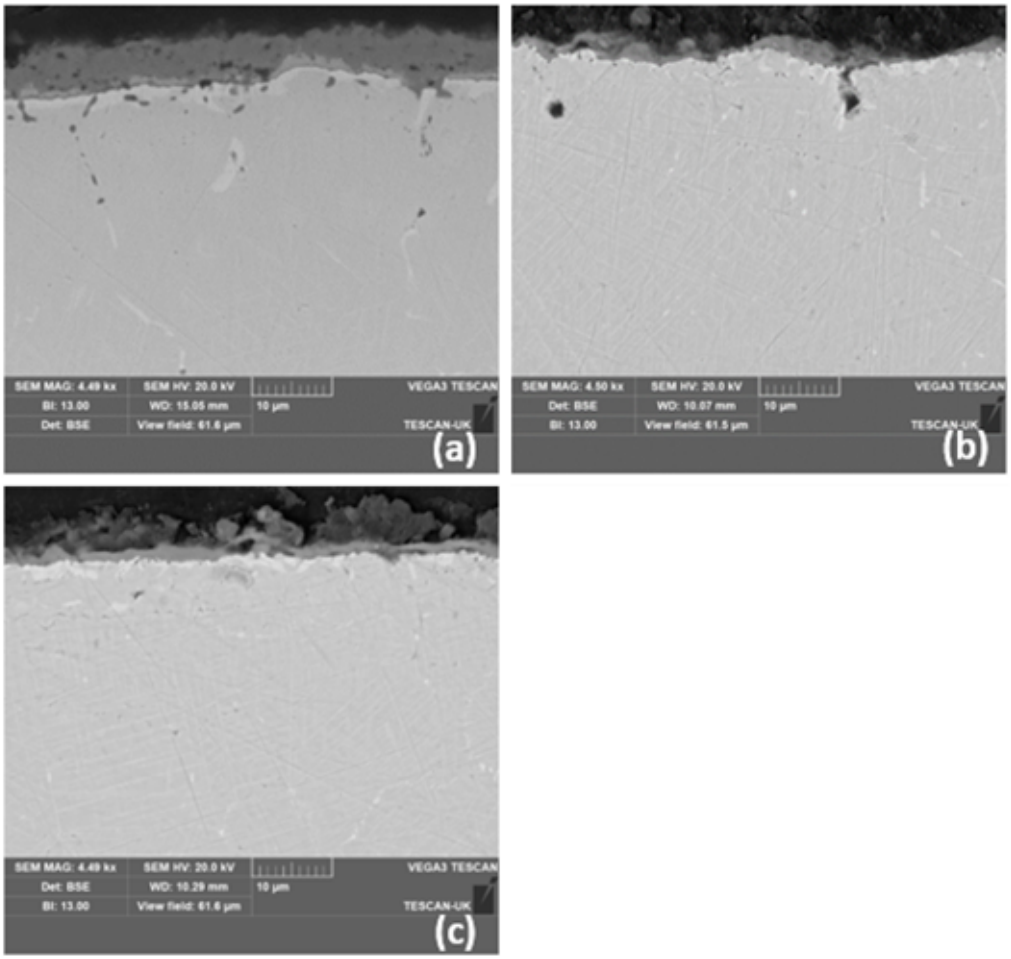


Figure 6-6 - SEM images of Additive manufacturing of (a) as-received (b) P600 grit (c) polished and exposed in CO_2 + 2.7mol% H_2O + 1.43mol% N_2 + 0.17mol% O_2 + 300ppm SO_2 for 1000h at 800°C.

The images in Figure 6-6 were cross-sectioned perpendicular to the Z build. The P600 sample shows the formation of ridges displayed in (Figure 6-6c), and a thinner Cr oxide scale formed with respect to the as-received sample with a rougher finish. This aligns with the established phenomenon that smoother surfaces provide fewer nucleation sites for oxide formation, resulting in more uniform and thinner oxide layers. P600 alloy formed a heterogeneous oxide scale with Al oxide scale and a void.

Depth profiles of samples were carried out through EDX to further investigate the depletion of Cr into the sample, as studies indicate that a more depleted Cr

subsequently increases oxidation. Line scans were acquired using EDX to show the elemental concentration of as-received, P600, polished LPBF alloy 625 after 1000 oxidation. Figures 6-7, 8, & 9 respectively. The line scans display a wt.% vs the position (depth into the alloy). The Line scans show the thickness and scale composition, and the selectively oxidised elements below the oxide scale.

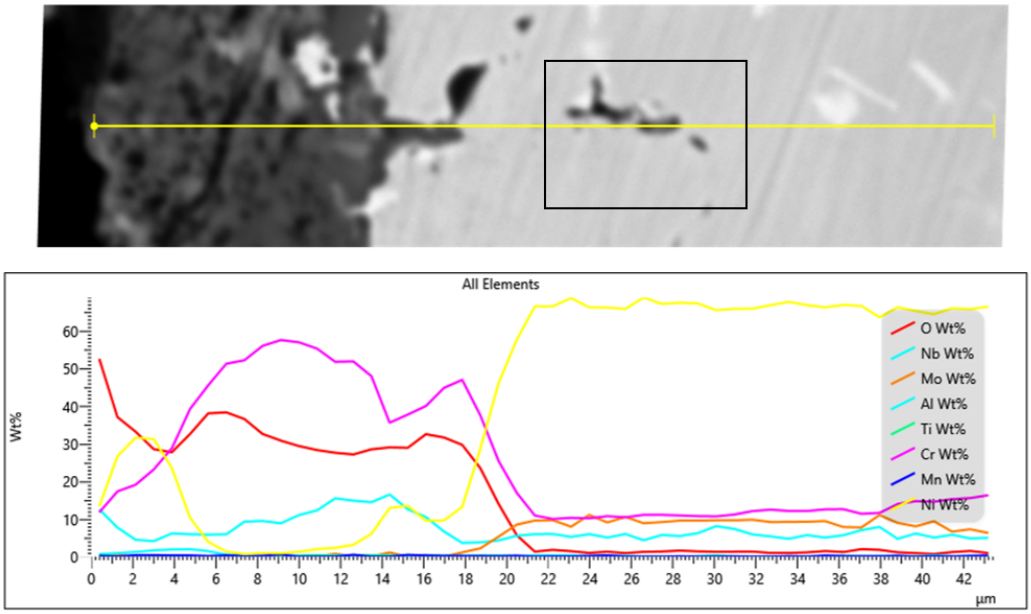


Figure 6-7 - As-received depth profile of as-received Alloy 625 exposed in CO_2 + 2.7mol% H_2O + 1.43mol% N_2 + 0.17mol% O_2 + 300ppm SO_2 for 1000h at 800°C

Figure 6-7 indicates the enrichment of Cr in the oxide scale after oxidation in as-received Alloy 625, depletion of Cr below the oxide scale. There also seems to be voids shown in the black box as there's no Al, O enrichment on the line scan. The enrichment of Nb can also be seen beneath the oxide scale and Mo enrichment extending into the alloy. In the external oxide scale, there's high O and Cr and further into the sample at a depth of 12 µm, the Nb content increases after which the Mo content results subsequently O content reduction. The formation of Nb-rich phases beneath the oxide scale is consistent with the precipitation behaviour of γ'' and δ phases in Alloy 625 during high-temperature exposures.

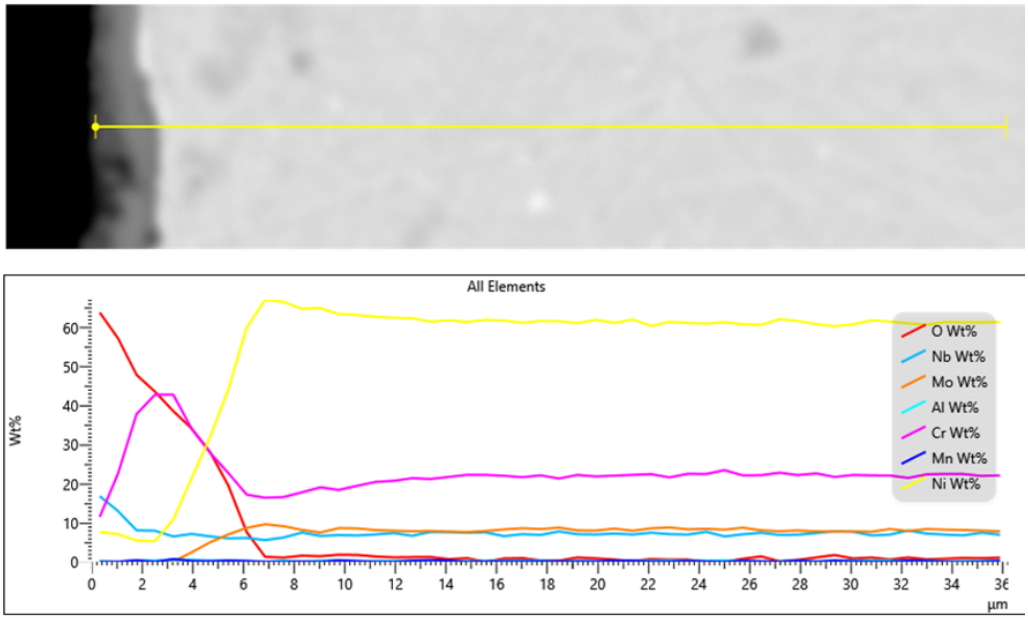


Figure 6-8 - P600 profile of alloy 625 exposed in CO_2 + 2.7mol% H_2O + 1.43mol% N_2 + 0.17mol% O_2 + 300ppm SO_2 for 1000h at 800°C

Figure 6-8 shows the profile depth of P600, indicating the enrichment of Cr in the oxide scale after oxidation and the depletion of Cr and Mn beneath the oxide scale. Whereas in the as-received, the Mn content remains similar.

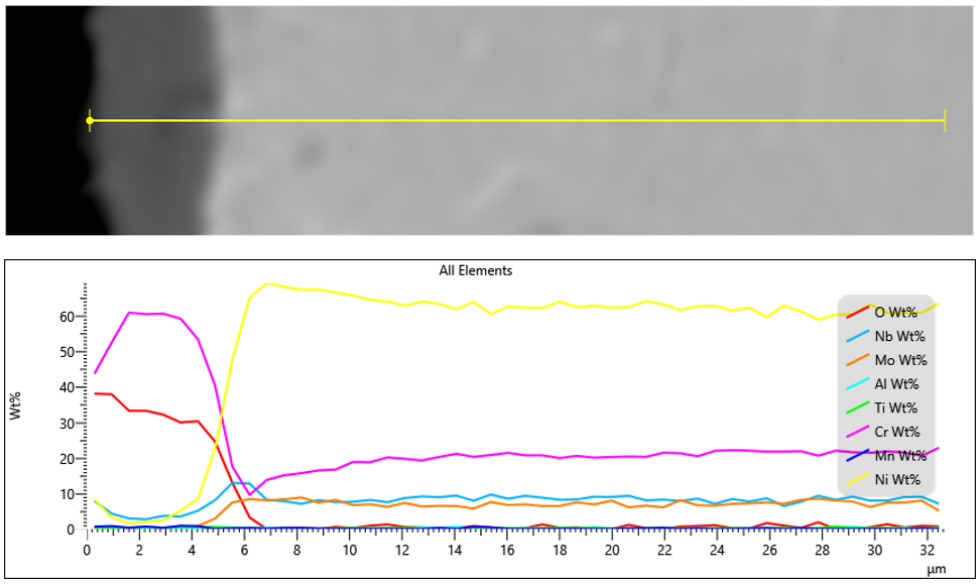


Figure 6-9 - 6µm polished solution heat-treated alloy 625 Line scan exposed in CO2 + 2.7mol% H2O + 1.43mol% N2 + 0.17mol% O2 + 300ppm SO_2 for 1000h at 800°C

Figure 6-9 shows the 6 µm depth profile, it can be seen that the external oxide scale is a Cr rich oxide, with no Mn and Ti increment or depletion. Beneath the oxide scale, the Nb and Mo enrichment can be observed and Cr depletion.

When the depth profiles of the as-received samples are compared, there's a high O and Cr content. By 5 µm, the O content drops at the end of the oxide layer, while Nb increases, as does a similar increment in Mo. It can be noticed that the Al content changes in the external oxide scale, implying that there was no internal oxide, which is present in the as-received and P600 alloy, evident in the EDX maps.

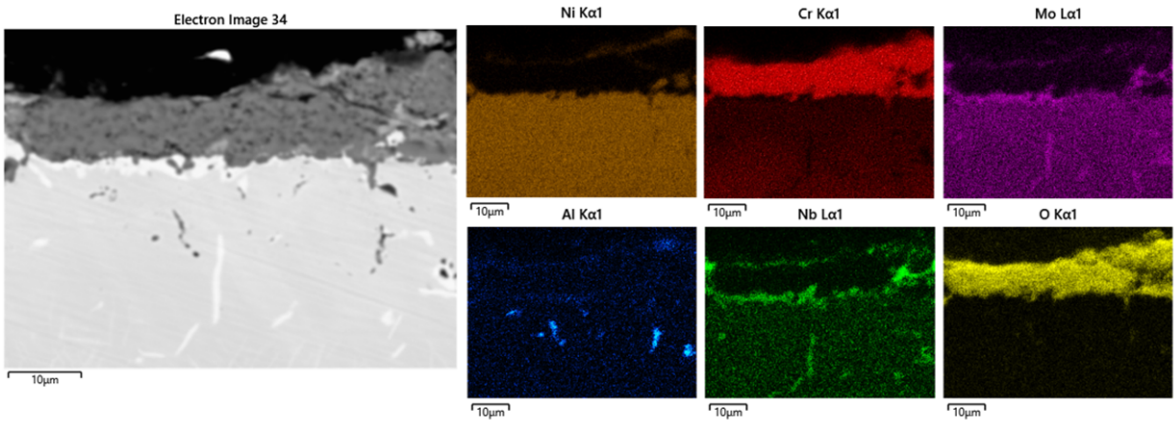


Figure 6-10 - EDX map of AM solution heat-treated as-received Alloy 625 exposed in CO_2 + 2.7mol% H_2O + 1.43mol% N2 + 0.17mol% O_2 + 300ppm SO_2 for 1000h at 800°C.

Figure 6-10 depicts the EDX maps of a 1000h exposed as-received sample, with a thick oxide scale of up to 15µm formed on the surface. The oxide was a Cr oxide scale similar to polished and P600 samples. A noticeable Nb- and Mo-rich phase can be observed below the oxide scale, indicating the formation of a Ni_3Nb (γ″) and Mo-rich zone.

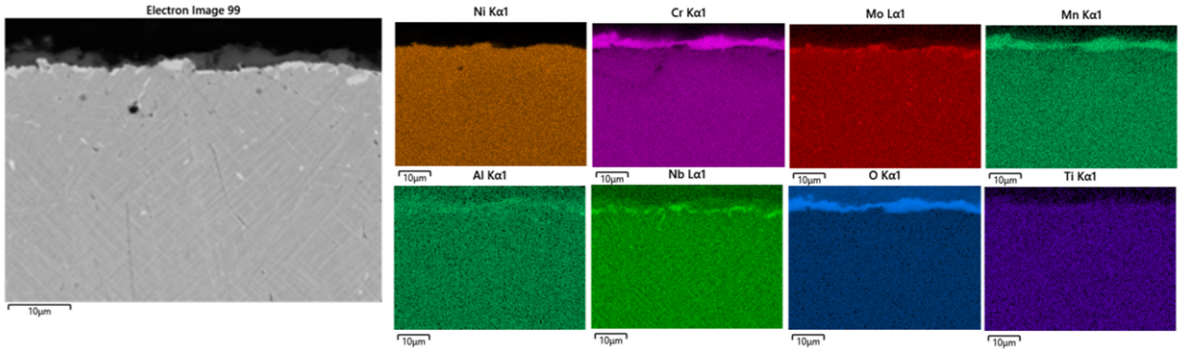


Figure 6-11 – EDX maps of AM solution heat-treated P600 grit alloy 625 exposed in CO_2 + 2.7mol% H_2O + 1.43mol% N_2 + 0.17mol% O_2 + 300ppm SO_2 for 1000h at 800°C

Figure 6-11 shows the EDX maps of the P600 sample after exposure. The formation of chromia and alumina can be observed. Beneath the oxide layer, the maps show enrichment of Nb and Mo-rich phases at the oxide-substrate interface. A small dark region in the BSE micrographs appears to be a pore created during the oxidation process.

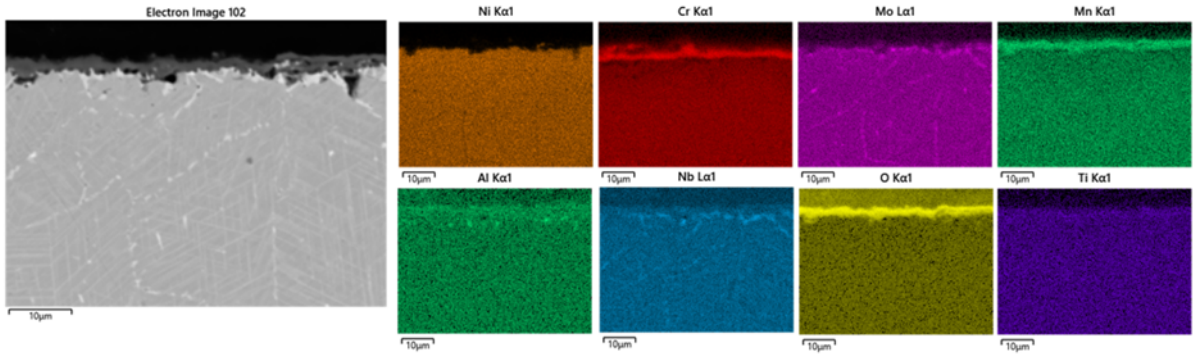


Figure 6-12 - EDX map of AM polished solution heat-treated Alloy 625 exposed in CO_2 + 2.7mol% H_2O + 1.43mol% N_2 + 0.17mol% O_2 + 300ppm SO_2 for 1000h at 800°C

Figure 6-12 shows that the polished Alloy 625 exhibits noticeable Mo and Nb enrichment below the oxide layer and more prominent Mo and Nb precipitates compared to Figures 6-10 and 6-11. Oxygen is not noticeable below the oxide scale, indicating minimal internal oxidation, which is confirmed by the line scan illustrating lower levels of O beneath the oxide layer. There is no apparent influence of SO_2 and N penetration into the alloy or on the oxide.

6.4 Conclusion

This study examines the influence of surface condition as well as the microstructural changes on high temperature oxidation behaviour of LPBF Alloy 625 under simulated baseline Allam cycle conditions. The results revealed that surface conditions play a significant role in the oxidation kinetics, and oxide scale morphology. The results demonstrate that the initial surface state affects not only oxidation kinetics but also oxide scale morphology, precipitate formation and element distribution during exposure.

Polished samples exhibited the lowest oxidation rate and thinnest oxide scale, showcasing a protective oxide layer in the CO_2 environment. In comparison, the P600 ground samples, though smoother than the as-received condition, showed higher oxidation kinetics. Interestingly, the as-received samples showed the lowest mass gain. Microstructural analysis confirms that surface roughness influenced the precipitate density, oxide scale uniformity and the depth of Cr diffusion. The presence of Nb-rich and Mo-rich precipitate was more prominent in rougher surfaces, suggesting an enhanced nucleation site for carbide formation. These observations indicate that surface preparation alters the near-surface microstructure, which subsequently affects element diffusion and oxide initiation.

Overall, the findings underscore that optimisation of surface preparation for additively manufactured Alloy 625 components operating in high-temperature CO_2 environments requires careful consideration of both surface roughness and the microstructural alterations introduced during surface finishing.

7 Paper 4: Effect of Nitrogen and Sulphur on the oxidation of Rene 80 in a high temperature CO_2 environment.

Boma Phoebe Norman, Cranfield University, Cranfield, UK

Andrew Potter, Cranfield University, Cranfield, UK

Mathias Galetz, Dechema, Frankfurt, Germany

Gerald Schmidt, Dechema, Frankfurt, Germany

Nigel Simms, Cranfield University, Cranfield, UK

Joy Sumner, Cranfield University, Cranfield, UK

Abstract

The Allam cycle with carbon capture storage offers a climate-friendly power generation cycle. The utilisation of CO_2 as its working fluid provides improved thermal efficiency whilst minimising CO_2 emissions, thus contributing to climate change goals**.** The Allam cycle operates at temperatures of up to 800 ºC and a pressure of 300 bar. In addition to these high temperatures and pressures, contaminants found in air separation units (ASU) oxygen and in the fuel, such as N_2 and SO_2 can be deleterious for the turbine components. These extreme operating conditions pose challenges for the material selection for turbomachinery. Rene 80 is a superalloy designed for gas turbine blades that could be a candidate for use in the Allam cycle and is investigated in this paper.

This paper evaluates the influence of sulphur and nitrogen species on the oxidation and carburisation performance of Rene 80 at 800 ºC for up to 1000 h in an Allam cycle atmosphere at ambient pressure. This research compares degradation in two distinctive environments: CO_2 + 2.7 mol% H_2O + 0.17 mol% O_2 with and without 300 ppm SO_2 + 1.43 mol% N_2. These are realistic post-combustion conditions that turbine blades and heat exchangers would face.

Analysis was carried out using dimensional metrology, scanning electron microscopy (SEM) equipped with energy dispersive X-ray spectroscopy (EDX), and electron probe micro analyzer (EPMA)

A thicker external Cr-Ti oxide scale and extensive internal alumina precipitation (24.4 μm) along grain boundaries were observed after exposure when sulphur and nitrogen contaminants were present. It is observed that the aluminium oxide forming along the grain boundary (GB) regions facilitated nitridation also along the GB. Results show that along the GB indicates the localisation of nitrogen, possibly due to the formation of TiN, influencing nitrogen diffusion; however, sulphidation potentially occurs in a non-uniform manner across the GB. The EPMA results suggest nitridation with Ti and Al-rich oxides.

Keywords: Rene 80, CO_2, oxidation, carburization, Allam cycle, EPMA.

7.1 Introduction

Increasing efficiency is an essential goal in the research and development of industrial gas turbines. Studies have shown that supercritical carbon dioxide (sCO_2) power cycles have the potential to achieve significantly higher cycle efficiency than a conventional steam Rankine cycle [56,233–236]. Enhancing cycle efficiency inherently reduces fuel consumption, water utilization, and, in scenarios involving fossil fuels, greenhouse gas (GHG) emissions. sCO_2 cycles maintain high pressures of up to 300 bar and temperatures of up to 800°C throughout the cycle, yielding a high-density working fluid due to the thermophysical properties of CO_2. The properties of the working fluid results in compact equipment sizes, a smaller plant footprint, and consequently, lower capital [237].

Material selection is a key aspect of gas turbine design. This is particularly true for turbine blades and vanes that need to operate under high mechanical forces at high temperatures while exposed to corrosive elements in the gas phase. Within sCO_2 cycles, materials are exposed to the CO_2 supercritical phase with contaminants such as H_2O, S, and N_2 [237]. The presence of these contaminants along with CO_2 accelerates degradation subsequently complicating material selection at elevated temperatures.

Nickel-based superalloys are widely used to produce turbine blades and vanes in gas turbine engines due to their high-temperature strength, hot-corrosion resistance and improved stability [19,20]. In this study, the nickel-based superalloy Rene 80 is investigated due to its widespread application in high temperature environments such as turbine blades [238] and combustor components in gas turbines.

Rene 80 is a polycrystalline material consisting of a solid solution matrix primary γ matrix reinforced within its strengthening mechanism achieved through the precipitation of the γ' phase. This precipitation strengthened alloy is designed to withstand service temperatures of up to 980°C [239]. Rene 80 exhibits notable resistance to high-temperature creep and low-cycle fatigue conditions.

Contaminants such as H_2O, S and N_2 have different effects on the oxidation behaviour of nickel-based superalloys. The effects of oxygen and carbon dioxide on Ni-based superalloys are well understood. Research such as Pint and Keiser [240], studied the impacts of impurities, O_2 and H_2O in sCO_2 at 750 °c at 1 bar and 300 bar, finding no significant changes in mass gain or oxide scale composition compared to impurity-free CO_2. Austenitic Fe steels, Ni-base chromia-forming alloys, and Ni-base alumina-forming alloys were examined, and minimal effects of pressure were observed, with no indication of C ingress. Previous studies have investigated the individual effects of sulphur and nitrogen impurities on high-temperature oxidation of superalloys. Sulphur has been shown to promote embrittlement and degrade mechanical properties by segregating at grain boundaries, oxide/alloy interfaces, and oxide grain boundaries. This segregation can weaken grain boundary cohesion, resulting in reduced tensile ductility, increased crack propagation, and lower impact resistance [111,241,242]. Sulphur also disrupts oxide scale adhesion, leading to scale spallation, as demonstrated by Ikeda et al [243] , in US304 stainless steel, who suggested that extensive exfoliation during cooling was due to surface segregation of sulphur. Lee [134] exclusively proposed that sulphur segregates not only to the scale/alloy interface, affecting adhesion, but also to oxide grain boundaries, influencing the oxide growth mechanism. These effects are critical for components exposed to extreme thermal and mechanical loading, such as turbine blade edges [244], where pores, cracks, or mechanical damage can facilitate penetration of N and S through the protective oxide layers.

Nitrogen has also been shown to influence the oxidation behaviour. Krupp and Christ [137] reported that nitrogen attack tends to be strongly localized, and thus penetration depth of zone of nitride precipitation is extremely heterogenous – not evenly distributed throughout the alloy. Nitrogen. This makes the material more susceptible to localized cracking under thermal cycling or stress. Non-mental elements such as nitrogen and carbon can promote the nucleation of Cr_2O_3 by co-segregation wit chromium at the alloy surface during early stages of oxidation. Whilst sulphur impedes the formation of chromia [245].

Beckman and Woodford [241], investigated the effect of S in a Ni 270 at temperatures between 450°C and 800°C with sulphur partial pressures between 10^{-8} to 10^{-4} atm. Results showed that sulphur penetrated from the environment down the GBs during pre-exposures at temperatures above 450C with significant embrittlement observed at higher temperatures, even under constant sulphur partial pressure. Suggesting temperature dependent acceleration of sulphur degradation which raises concerns with high temperature operations for extended periods.

The presence of CO_2 particularly in environment where sulphur, nitrogen, and water vapor are found presents complexity. The interactions between these impurities and CO_2 have not been fully understood. Although Oleksak et al. [246] examined the oxidation behaviour of Ni-based superalloys like H_2O and SO_2, their work does not include sulphur and nitrogen. Despite their work focused on chromia-forming alloys, it does not evaluate γ′-strengthened superalloys, i.e. Rene 80, which is used for gas turbine blades.

This study addresses these gaps by examining high temperature oxidation behaviour of Rene 80 in CO_2 environment with amounts of sulphur, nitrogen and water vapour. This study evaluates the oxide scale formation, and impurity penetration under baseline CO_2 conditions.

7.2 Materials and Methods

Commercially available Ni-base superalloy Rene 980 was selected for this experiment; the nominal composition is presented in Table 7-1.

Table 7-1 - Elementary composition of Rene 80 .wt%[247]

Elements

Ni	Cr	Co	Mo	W	Ti	Al	Fe	C	Nb	Zr	V	S
Bal	14.06	9.49	3.59	3.84	4.65	3.06	0.171	0.173	0.048	0.043	0.039	0.007

All samples were cut from a bar into 10mm x Ø14mm cylinders before being ultrasonically cleaned in acetone and isopropanol. Before exposure, the samples were weighed and the dimensions measured using a micrometre. All samples were polished.

Isothermal testing was performed in a vertical furnace with a controlled environment for up to 1000 h, schematic shown in Figure 7-1. The test gas flow for both experiments was set to 88.74 cc/min using a mass flow controller.

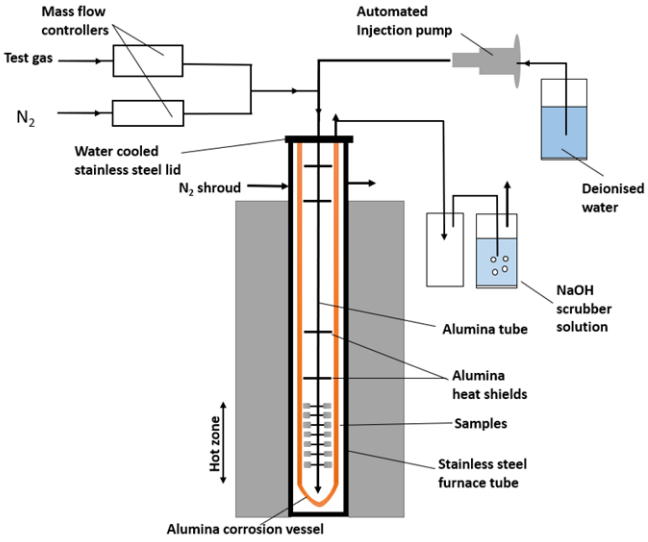


Figure 7-1 - Schematics of vertical controlled-atmosphere furnace for oxidation testing

To fully understand the effect of contaminants, two different gas compositions were explored. The turbine inlet of the gas turbine in an Allam cycle operates at up to 760°C, and as such, a high temperature of 800°C was used to investigate the failure mechanisms

Test 1: 800°C/1 bar/CO_2 + 2.7 mol% H_2O +0.17 mol% O_2

Test 2: 800°C/1 bar/CO_2 + 1.43 mol% N_2 +0.17 mol% O_2 + 300 ppm SO_2 + 2.7 mol% H_2O

300ppm SO_2 and N_2 as well as H_2O and O_2 are impurities present in an Allam cycle power plant. Mass change measurements were recorded before and after each cycle to generate a weight change plot, from which oxidation kinetics were

derived. Dimensional metal loss data was obtained using an optical microscope, with the corresponding dimensional metrology plot providing valuable insights into the sample's dimensional changes over the testing period. Oxide scale formation and microstructural changes were further characterized using scanning electron microscopy (SEM), coupled with energy dispersive X-ray spectroscopy (EDX) for elemental analysis. Electron probe micro analyser (EPMA) is another material characterisation technique used; to further locate sulphur and nitrogen in the sample. This is based on a more precise quantitative elementary analysis than EDX using wavelength dispersive spectroscopy (WDS). These methods together facilitated a comprehensive understanding of the material's behaviour under high-temperature oxidative conditions and provided critical data for assessing the impact of contaminants on alloy performance.

7.3 Results and discussion

7.3.1 Mass change

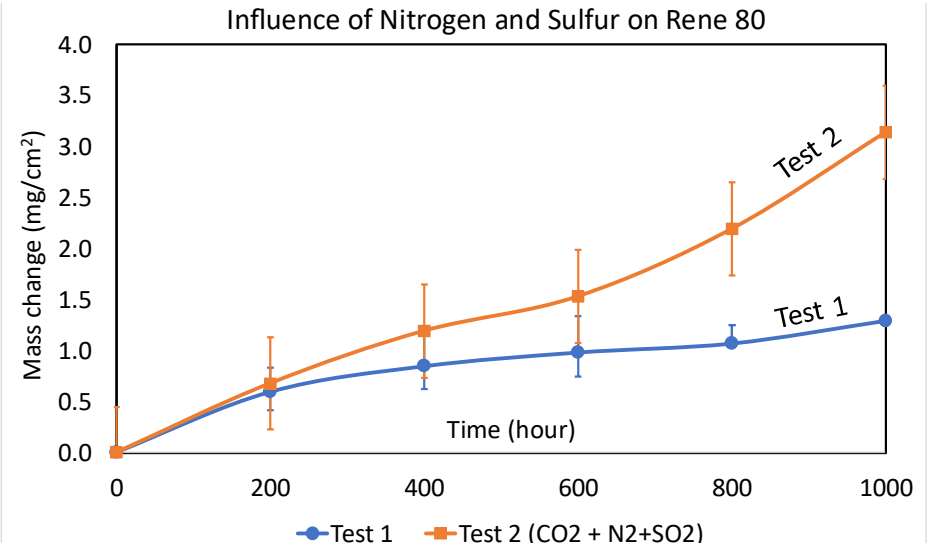


Figure 7-2 - Mass change plot of Rene 80 in test 1: 800°C/CO_2 + 2.7 mol% H_2O +0.17 mol% O_2 and test 2: 800°C/CO_2 + 1.43 mol% N_2 +0.17 mol% O_2 + 300 ppm SO_2. Error bars show the max and min value of mass change of samples in the same time interval

Figure 7-2 shows the average weight change of Rene 80 vs time exposed in two conditions. Rene 80 is one more of the commonly used nickel-based alloy employed in the industry, and the detrimental effects noticed even without the presence of impurities were interesting to see and needed further investigations. The mass change plot pertains to Rene 80 exposed in environments with and without contaminants. It can be observed that in Test 1 without impurities, mass change increases gradually with time showcasing a parabolic behaviour which is confirmed in Figure 7-3. Test 2 shows a greater increase in mass overtime suggesting higher material degradation compared to test 1. This more rapid mass gain suggests either a non-protective oxide growth or the formation of internal sulphides and nitrides. The error bar signifies the average mass change of samples in the same time interval.

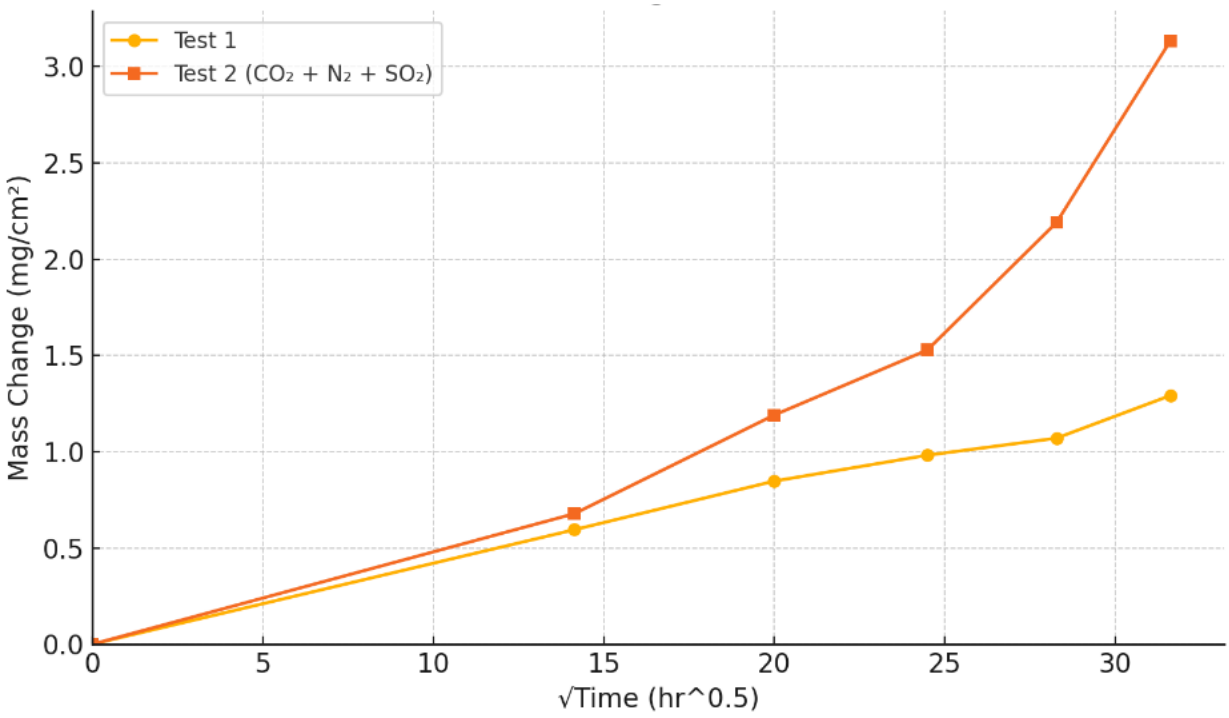


Figure 7-3 - Mass change vs square root of time showing the parabolic behaviour of Rene 80 exposed in test 1 and test 2 environment

Rene 80 samples in Test 1 show a linear line, suggesting a parabolic rate and slight deviation after about 600hrs. Both lines initially increase linearly indicating a parabolic oxidation in early stages.

7.3.2 Dimensional metrology assessment of metal loss

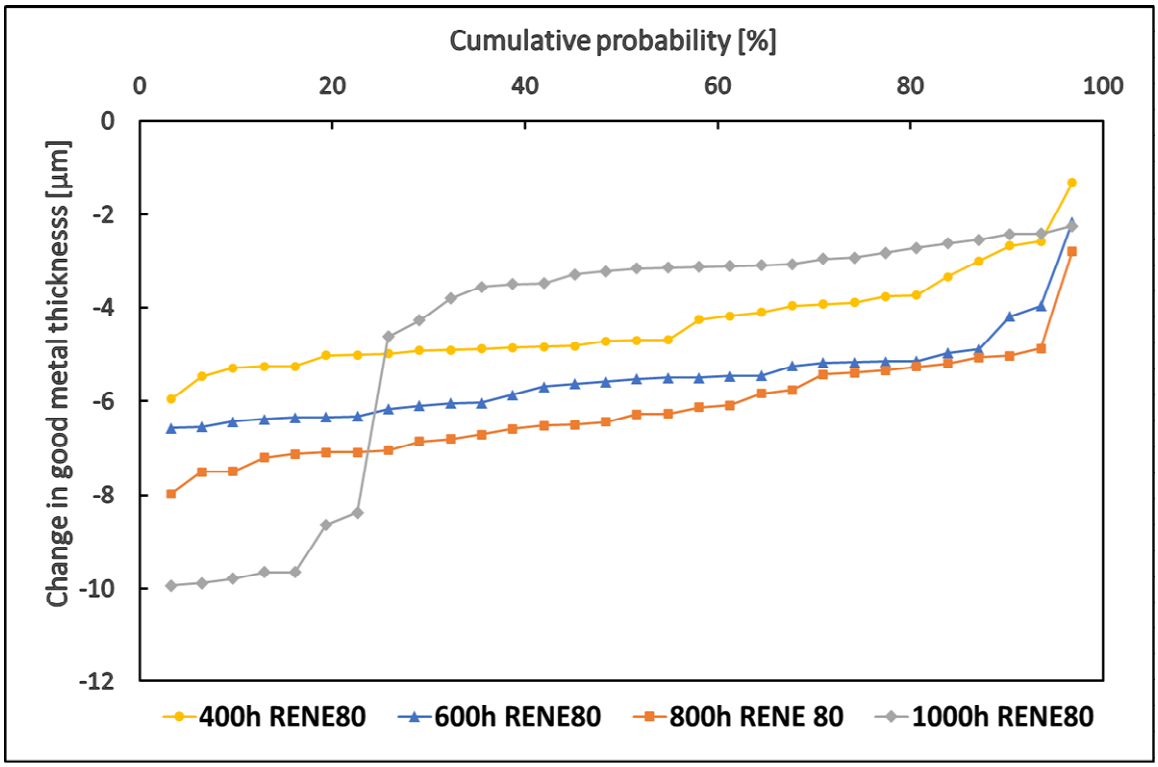


Figure 7-4 - Rene 80 cumulative probability plot in test 1: 800°C/CO_2 + 2.7 mol% H_2O +0.17 mol% O_2

Figure 7-4 shows the cumulative probability distribution of metal loss exceedance for Rene 80 exposed in Test 1. The plot compares results after 600, 800 and 1000h. The 400, 600 and 800h line show a shallow gradient which corresponds to a uniform distribution of metal loss. This indicates a consistent oxide scale formation across the Rene 80 sample. In contrast, after 1000h of exposure, the data exhibit an increase in metal loss exceedance below approximately 20% probability. This indicates that the metal loss is not entirely uniform, although the error margin is relatively small (approximately 5 or 6 microns).

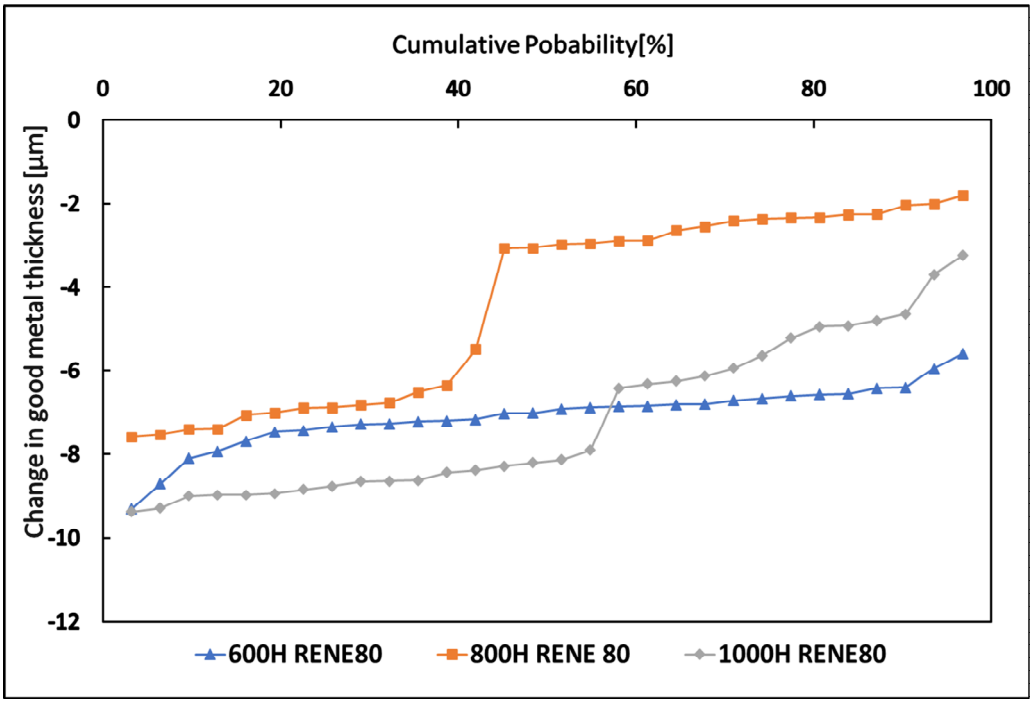


Figure 7-5 - Rene 80 cumulative probability plot in test 2: 800°C/CO_2 + 1.43 mol% N_2 +0.17 mol% O_2 + 300 ppm SO_2 + 2.7 mol% H_2O

Figure 7-5 illustrates the cumulative probability of metal loss exceedance for Rene 80 after exposure in the sulphur and nitrogen containing gas mixture. Overall, the dimensional metrology data indicate progressive metal loss with increasing exposure time, but with noticeable differences in the shape and steepness of the distribution curves. After 1000 h, the median loss is approximately 8.8 µm in the Test 2 environment, compared to roughly 3.8 µm for equivalent exposure in Test 1. This difference suggests that Test 1 promotes the development of a thicker external oxide scale, which may mask or reduce measurable loss of good metal, while the sulphur- and nitrogen-containing atmosphere in Test 2 encourages more direct metal recession and internal attack. However, it is important to recognise the ±5 µm measurement uncertainty, which means differences of similar magnitude should be interpreted cautiously.

The 800 h curve, in particular, exhibits a pronounced step increase around the 35–40% cumulative probability mark. This abrupt rise reflects the presence of several specimens with substantially higher metal loss, indicating a shift to more aggressive attack modes. Such discontinuities are consistent with the onset of

localised sulphur-induced or nitrogen-induced degradation mechanisms, such as accelerated internal sulfidation, internal nitridation or even breakdown of protective oxide phases on certain areas of the alloy surface. The absence of a similar feature in the 600 h data suggests that these damage processes become active only after extended exposure.

The curves in Figure 7-5 reinforce that the mixed CO_2–N_2–O_2–SO_2–H_2O atmosphere produces not only higher median metal loss but also a greater chance of an increase in damage severity. This behaviour differs from the smoother, more gradual distributions observed in the water-vapour-dominated environment of Figure 7-6, highlighting the more aggressive degradation in sulphur- and nitrogen-bearing conditions

7.3.3 Microstructural analysis

Figure 7-6 presents backscattered electron (BSE) micrographs showcasing the progressive degradation of Rene 80 after exposure in test 1 without contaminants and with test 2 over time. The micrographs show a significant difference in oxide scale morphology and internal attack between both conditions. In test 1, after 200h of exposure, a thin, relatively uniform oxide layer with minimal internal damage had formed. After longer exposures of 800h and 1000h, the oxide scale thickened, and more substantial internal oxidation was observed. After 1000h, it appears that these internal oxides appear to trace the outline of a grain boundary.

Test 2 Rene 80 samples demonstrated accelerated degradation behaviour across all time intervals. Even at 200h, compared to test 1, a slightly thicker oxide scale formed with deeper internal oxidation features. Across the exposure time, an increase in internal oxide penetration is noticed with internal oxidation forming along the grain boundaries. At 1000h, more severe internal degradation can be observed, and the internal oxidation has penetrated further into the substrate. While the external scale thickness is equivalent to 800h which was about 4.5 µm, the oxide layer was still a continuous oxide layer. The accelerated degradation in test 2 can be attributed to several mechanisms. Giggins and Pettit [248] established that sulphur can penetrate protective chromia scales, facilitating internal sulphidation and compromising alloy’s protective capacity. The presence

of nitrogen in the environment may further increase degradation by Hancock [249] where nitrogen can react with elements such as Cr, Ti and Al in the alloy, reducing their availability for beneficial effects on scale growth and adhesion. To locate if sulphidation and or nitridation occurred, EDX maps were analysed.

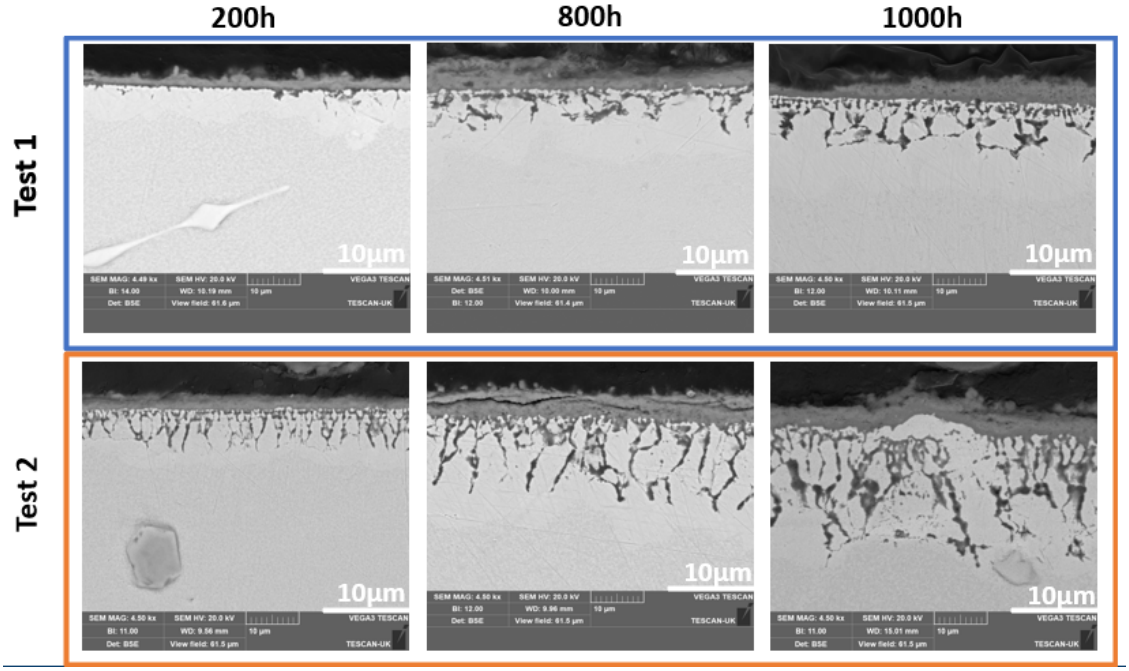


Figure 7-6 - BSE SEM images of Rene 80 in in test1: 800°C/CO_2 + 2.7 mol% H_2O +0.17 mol% O_2 and test 2: 800°C/CO_2 + 1.43 mol% N_2 +0.17 mol% O_2 + 300 ppm SO_2 + 2.7 mol% H_2O

The elementary distribution map of Rene 80 after 1000h exposed in test 1 environment in Figure 7-7, shows the formation of a continuous chromium rich oxide layer; also, Ti rich, and internal Alumina oxidation can be observed. The Cr and Ti rich oxide layer was about 5.83µm, and the Alumina was 11.70µm. With noticeable depletion of Cr, Al and Ti below the oxide layer. The maps also indicate the formation of a Ti and N rich oxide layer. The S maps signals are low and are overlapping with the Mo maps and as such, further analysis were carried out using EPMA.

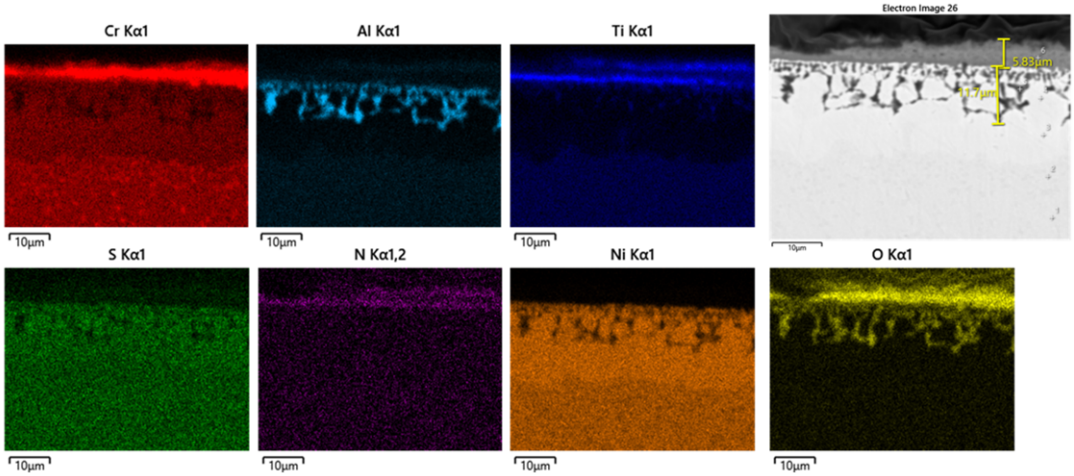


Figure 7-7 – BSE and EDX map of Rene 80 after 1000h exposure in test 1 800°C/CO_2 + 2.7 mol% H_2O +0.17 mol% O_2

Figure 7-8 shows the Rene 80 maps after 1000h exposure in test 2 with SO_2 and N. The BSE image shows a deeper internal oxide up to 24.4µm Al and Ti rich with an oxide layer of 4.55 µm rich in Ti and Cr oxide. The formation of a two-layer Ti and Cr rich oxide can be observed, which is common in Rene 80 alloys [250] . While both conditions produce internal oxidation and layer oxide scale, the extent and depth differ.

The distribution of Cr near the surface region shows more in-depth depletion in Figure 7-8 than in Figure 7-7. The increased depth of oxygen in Figure 7-8 suggests a less protective chromia in this environment, leading to enhanced internal oxidation. This formation of deeper oxygen ingression, enhancing oxidation, is noticeable as early as 200h, seen in Figure 5-7.

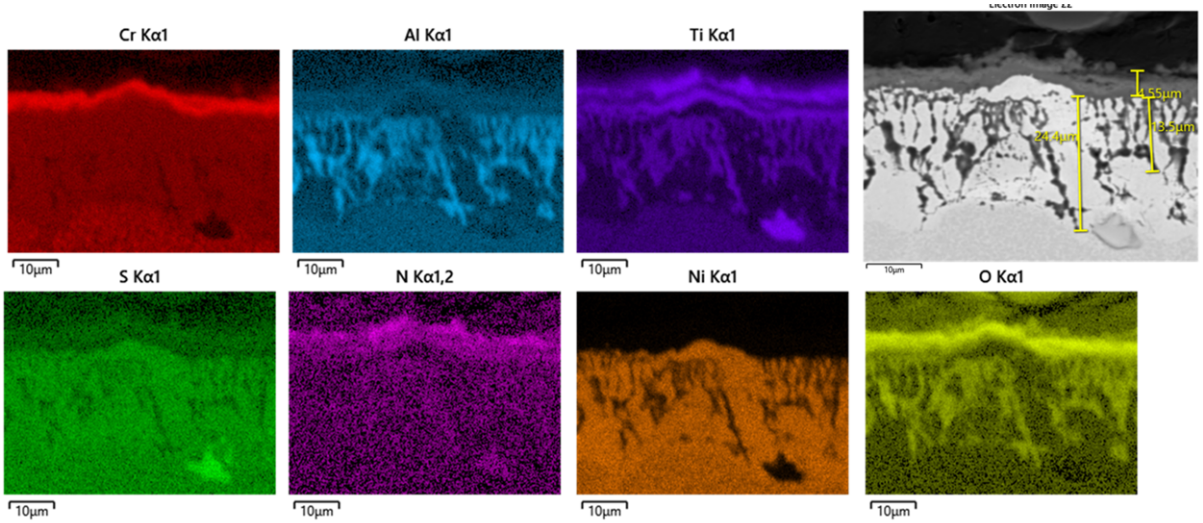


Figure 7-8 – EDX map of Rene 80 after 1000h exposure in t2: 800°C/CO_2 + 1.43 mol% N_2 +0.17 mol% O_2 + 300 ppm SO_2 + 2.7 mol% H_2O

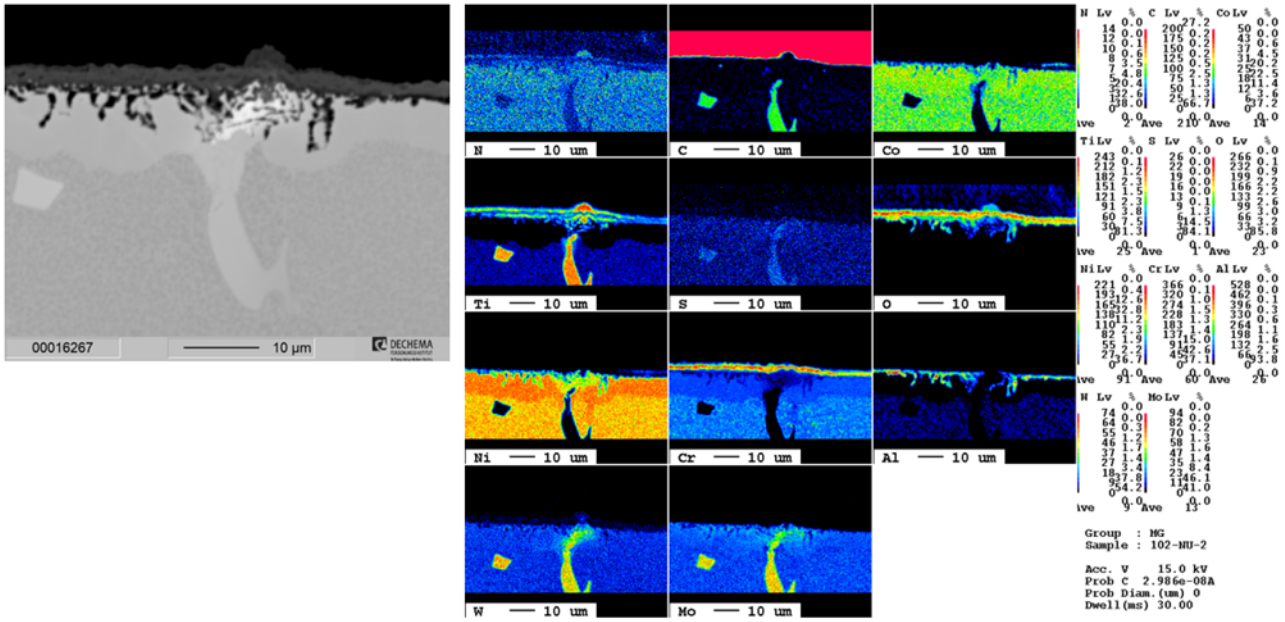


Figure 7-9 - EPMA maps of Rene 80 after 400h exposure in test 1 800°C/CO_2 + 2.7 mol% H_2O +0.17 mol% O_2

Figure 7-9 shows the EPMA maps of Rene 80 after 400h exposure in test environment 1, confirming the formation of a continuous, protective oxide layer

that is rich in Cr, with a sublayer enriched in Ti oxides and the presence of Ti oxide spinels on the surface. Carbides are also observed, rich in W, Mo, Ti, and C.

Figure 7-10 presents the EPMA elemental maps after 400 hours of exposure in the presence of impurities. The maps reveal near-surface depletion of Ti, C, and Al. The observed depletion of Ti and Al suggests their preferential oxidation and subsequent inward diffusion, contributing to the formation of an internal oxide zone enriched in titanium and aluminium along the grain boundary. Ni maps also indicate surface depletion, likely due to outward diffusion. While the S signals are not particularly strong, light signals can be seen, suggesting sulphur diffusion from the atmosphere. At the 400-hour mark, the data indicate that the protective scale is not as protective as deeper internal degradation is occurring, driven by the presence of the N and S. This is assumed, as when compared with Figure 7-9 without impurities, the internal oxidation is not as severe.

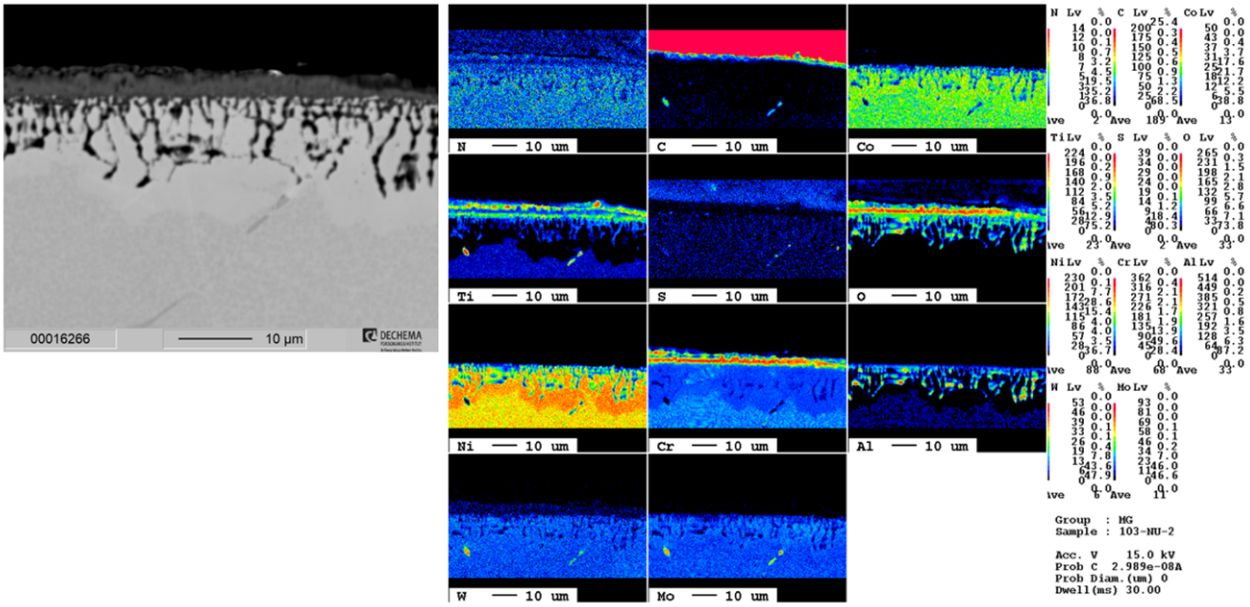


Figure 7-10 - EPMA maps of Rene 80 after 400h exposure in test 2 800°C/CO_2 + 1.43 mol% N_2 +0.17 mol% O_2 + 300 ppm SO_2 + 2.7 mol% H_2O

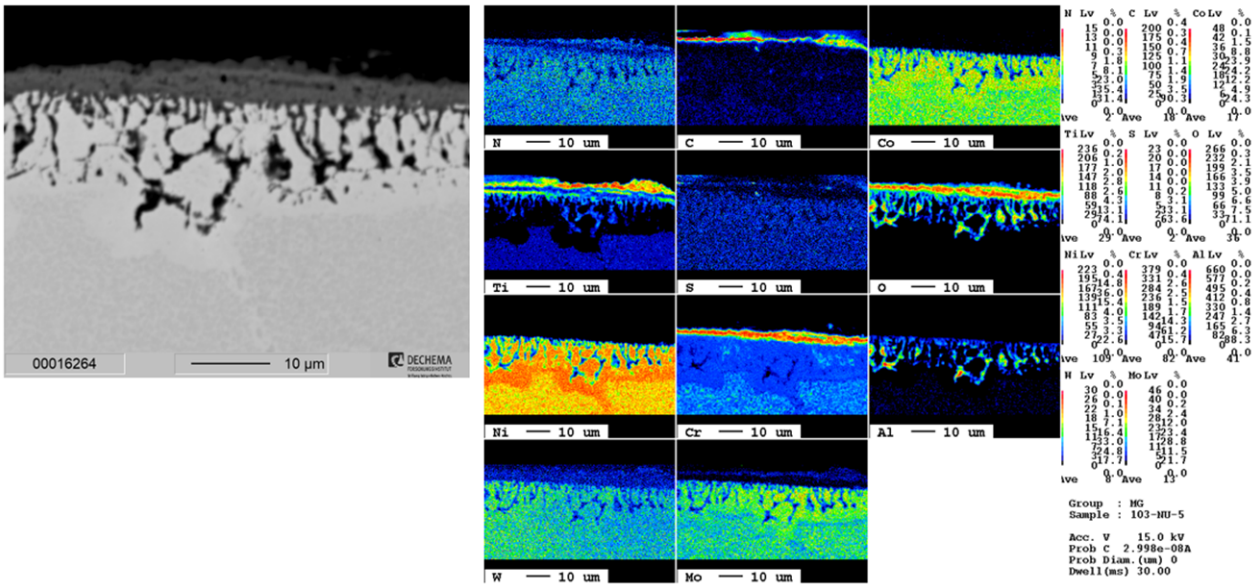


Figure 7-11 - EPMA maps of Rene 80 after 1000h exposure in test 2 800°C/CO_2 + 1.43 mol% N_2 +0.17 mol% O_2 + 300 ppm SO_2 + 2.7 mol% H_2O

Figure 7-11 presents the EPMA maps after 1000 hours of exposure in the presence of impurities. The sulphur signal is very low in intensity, appearing only in small, localized regions; these coincide with areas enriched in Mo, indicating that sulphur is segregating at the metal/oxide interface rather than forming distinct sulphide phases. The presence of sulphur is notable, as the maps clearly show a deeper internal oxidation zone and a thinner, less protective oxide scale compared to samples exposed without sulphur and nitrogen. The external oxide scale measured an average thickness of ~4.42 µm, with a maximum of 5.45 µm (Figures 7-9 and 7-10).

The element maps reveal strong internal oxidation dominated by Al- and Ti-rich oxides, consistent with the oxidation seen in the BSE micrograph. Al shows extensive internal oxide formation beneath the surface, and ti is concentrated both in the surface scale and within the internal oxidation zone. Although nitrogen is detected near the surface, its distribution is weak and diffuse, lacking the concentrated precipitate-like morphology expected for TiN formation. Instead, the nitrogen signal aligns with regions already rich in oxides, indicating that nitrogen is being adsorbed at or near the surface rather than forming internal nitrides. This behaviour is consistent with the strong preferential formation of alumina and Ti

oxide phases under these highly oxidising CO_2–H_2O–O_2 conditions, which thermodynamically suppress nitridation. Thus, the internal features observed are best interpreted as internal oxidation rather than internal nitridation.

The Ti depletion profile further supports this interpretation that Ti is consumed primarily through oxidation, forming Ti-rich surface oxides and mixed Al–Ti internal oxides, rather than forming discrete TiN precipitates. This contrasts with the Kofstad–Norell nitridation model [251], where nitrogen infiltration produces deep TiN needles; no such features are present here. Similarly, the findings reported by Krupp and Christ for nitridation of Ni–Cr alloys do not apply in this case. Krupp and Christ [251] investigation of Ni-Cr alloys at 1000°C showed that more Cr, 17wt.% is needed to see significant nitridation due to chromium nitrides being less stable than titanium nitrides. However, when the titanium content is high enough (2-6.wt%), a protective TiN scale forms on the surface slowing down further nitridation. Rene 80 contains sufficient Ti to form TiN under nitrogen-rich, low-oxygen conditions, but the oxygen-rich surface environment in this study prevents TiN scale development and instead possibly stabilises the Ti oxide and Cr-containing oxides. Consequently, the results indicate that oxidation and possible sulphidation are the dominant degradation mechanisms, despite the presence of nitrogen in the test gas.

Compared to the 400-hour exposure, more pronounced depletion of Ti, Al, and C is evident, reflecting progressive consumption of γ′-forming elements (Ti and Al) and carbide-formers (C). The loss of Ti and Al near the surface is particularly detrimental, as it compromises the γ′ volume fraction, reducing creep strength and hardness in critical surface regions. Likewise, carbon depletion reduces grain boundary carbide populations, increasing susceptibility to intergranular cracking.

In samples without S and N (test 1), chromium forms a comparatively stable and continuous chromia-rich scale, limiting internal attack. Cr competes with Ti and Al for oxygen, Cr dominance led to less Ti and Al oxidizing at the surface. Hence why the depletion of Ti and Al in test 1 is not deep into the substrate. Ti readily forms TiO2 contributing to oxide layer which was evident in test 1 and 2. However, in the sulphur-containing environment (test 2), even small amounts of sulphur

disrupt the chromia layer, reducing its continuity and promoting internal oxidation. The weakened scale allows deeper oxygen penetration, leading to extensive internal Al–Ti oxidation. The nitrogen present in test 2 does not form nitrides but may contribute to the destabilisation of the surface oxide, enhancing inward diffusion pathways.

Further depletion of Ti, C and Al was observed compared to the 400-hour exposure. Over time, this depletion near the surface can negatively affect Rene 80's performance under Allam cycle conditions. Ti and Al are essential for the formation of the γ′ phase, which strengthens the alloy at high temperatures, its' loss results in reduced creep resistance and hardness near the surface [250]. Carbon depletion leads to fewer carbides along grain boundaries, making Rene 80 more susceptible to intergranular cracking.

The formation of Ti and Al rich internal oxides accelerates degradation and could lead to component failure. As the protective oxide scale loses its integrity, the rate of internal oxidation is likely to increase. Eventually, the depletion of Ti, Al, and C may reach a critical threshold i.e the point where the loss of key elements severely compromises the mechanical properties. This is particularly concerning for turbine blades subjected to extreme mechanical stresses in Allam cycle environments.

7.4 Conclusion

The results confirm that turbine components particularly turbine blades fabricated from superalloys such as Rene 80 undergo significant material degradation when exposed to contaminants at elevated temperatures. In Test 1, which 800°C/1 bar/CO_2 +0.17 mol% O_2 a protective oxide scale formed, accompanied by moderate internal oxidation over time. In contrast, Test 2, 800°C/1 bar/CO_2 + 1.43 mol% N_2 +0.17 mol% O_2 + 300 ppm SO_2 led to markedly accelerated degradation. This was characterized by the formation of a non-protective oxide scale, deeper internal oxidation, and nitridation along grain boundaries.

While the dimensional metrology and oxide scale thickness did not show a significant difference between the two conditions, clear microstructural changes

even after 200 h showed progressive internal degradation in impurity environment. Internal oxidation and elemental depletion of Ti, Cr were visible as early as 200 h in test 2 indicating that sulphur and nitrogen accelerate degradation mechanisms. EPMA elemental maps showed that sulphides did not form, However, localised near -surface depletion of titanium, aluminium and carbon with Ti and Cr rich internal oxide along the Gb was observed.

8 Discussion

The demanding conditions of an sCO_2 power plant, including high temperatures and pressures, require stricter material properties, such as high oxidation resistance, carburization resistance, and excellent creep rupture strength. Various factors influence the oxidation and carburization behaviour of nickel-based superalloys, including temperature, pressure, impurities in the Allam cycle environment, and manufacturing techniques. These factors were examined in the previous chapters to understand their impact on industry-used alloys. The papers focused on investigating how these factors affect oxidation behaviour in a baseline CO_2 environment containing N, S, H_2O, and O_2. This section discusses how each finding in the paper relates together.

The influence of both nitrogen and sulphur in the environment is a critical gap in CO_2 power generation**.** Comparing the test results of both environments, with and without the addition of 300ppm SO_2 and 1.43mol%N_2 showed that the second test environment negatively influences the degradation behaviour of multiple nickel-based alloys.

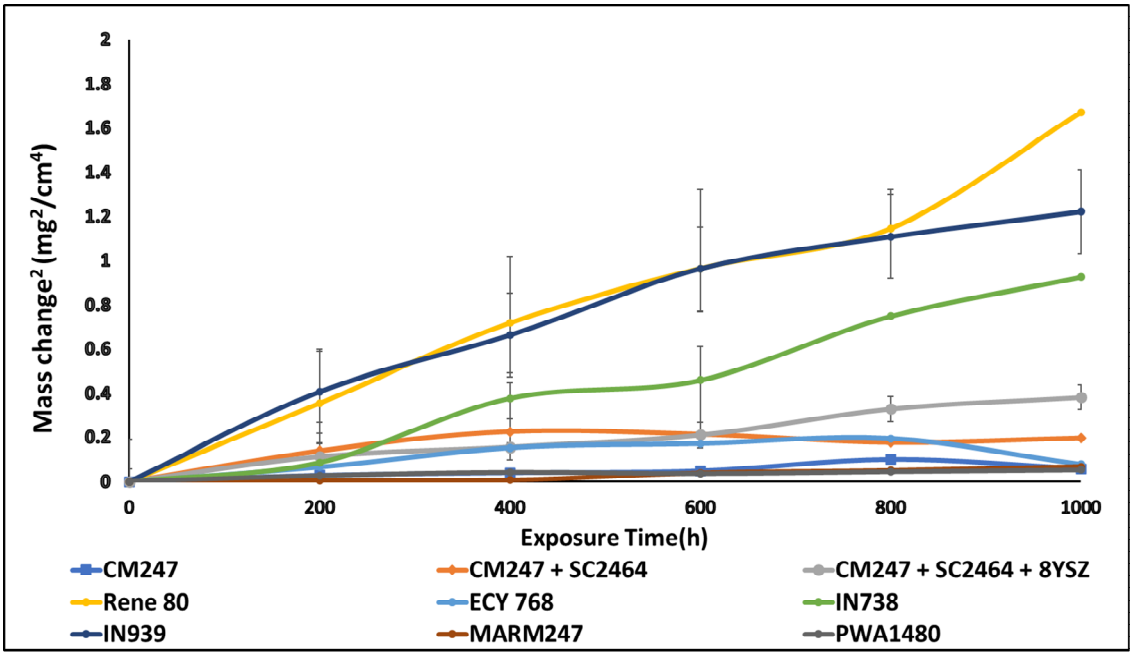


Figure 8-1 - Mass change plot of test 1, CO_2 + 2.7 mol% H_2O + 0.17 mol% O_2

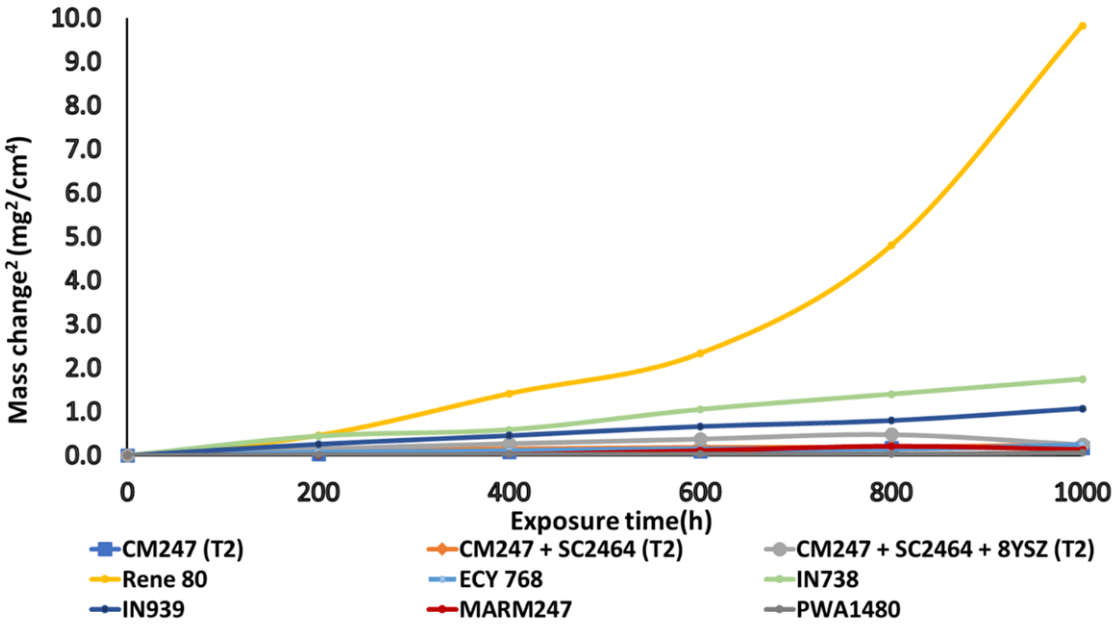


Figure 8-2 - Mass change plot of test 2, 800°C/CO_2 + 1.43 mol% N_2 +0.17 mol% O_2 + 300 ppm SO_2 + 2.7 mol% H_2O

Comparing the mass change plot squared of both Figure 8-1 and 8-2, the presence of impurities such as N and SO_2 leads to a higher mass change. Most of the samples in Figure 8-1 followed a parabolic rate, with exceptions to alloys like IN738 and Rene 80, which was investigated in Paper 4: Effect of Nitrogen and Sulphur on the oxidation of Rene 80 in a high temperature CO2 environment. Alloys such as IN738, IN939, Rene 80 and ECY768, which typically perform well in environments without contaminants, exhibited substantial mass gains, thick and continuous chromia oxide scales, and deeper internal oxidation under these aggressive test conditions shown in Figure 8-2.

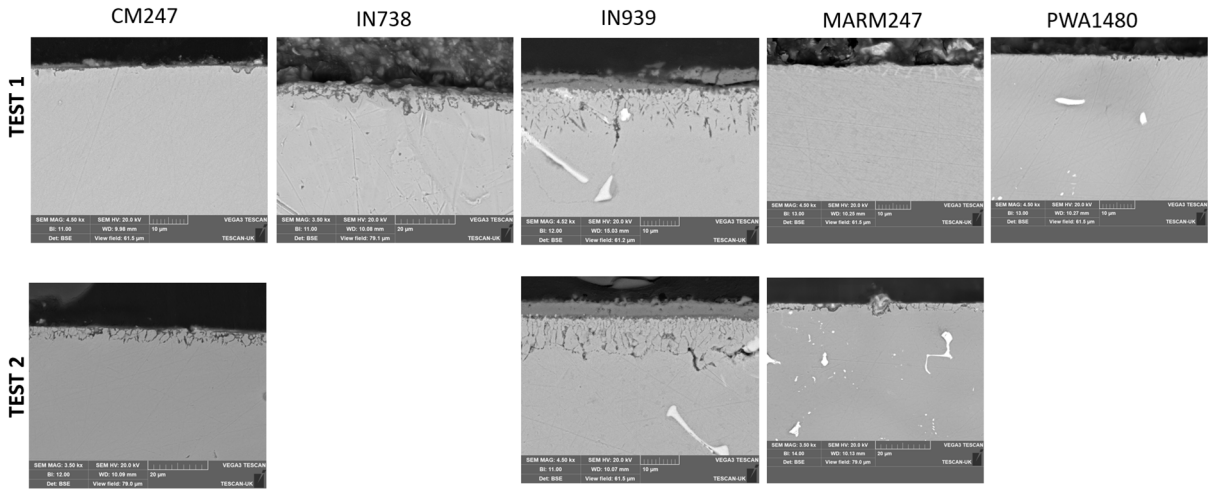


Figure 8-3 - BSE images of CM247, IN738, IN939, MARM247, PWA1480 exposed in test 1, CO_2 + 2.7 mol% H_2O + 0.17 mol% O_2 and test 2 environment and test 2 , 800°C/CO_2 + 1.43 mol% N_2 +0.17 mol% O_2 + 300 ppm SO_2 + 2.7 mol% H_2O

This degradation was not limited to surface oxidation but extended into grain boundaries. Alumina-forming alloys, such as CM247 and Marm247, were significantly more resilient in the presence of impurities linked to their high Al and low Ti content, which favors alumina formation, a slow-growing [112], protective oxide layer that was less prone to N and S disruption. Marm247 and PWA1480 have levels of 1 - 1.5% Ti compared to the others, which have about 3.5 - 5%. The reduced titanium contents limit the extent to which internal nitridation can occur whilst still providing enough for γ′ strengthening and grain boundary strengthening through carbide formation. With lower chromium content, there is reduced competition between Al and Cr for the available oxygen, thus allowing Al to easily form a protective scale. These alloys benefit from the high Al content and the low Ti levels, possibly minimizing nitride formation. Oleksak et al.[246] investigated Ni alloys exposed to 95%CO_2-4%H_2O-1%O_2, with/without 0.1% SO_2, at 750 °C and 1 atm and established that no sign of carburization was found and the formation of protective chromia layers was observed. This was also observed with Rene 80 samples with EPMA results, and the carbon maps did not indicate carburization however Ti rich carbides were formed.

This reinforces literature findings that Al_2O_3 scales are more stable at high temperatures and exhibit lower oxygen diffusivity than chromia, the slowest growing oxide due to the lowest oxygen diffusivity [112]. Moreover, the low Ti content in CM247 limits nitride formation, which in turn prevents the embrittlement and porosity commonly observed in high-Ti alloys. Nitrogen has a low solubility in Ni-based superalloys [252], and being in the environment leads to the formation of nitrides and carbonitrides, and these microstructural defects can compromise the mechanical properties, including ductility, fatigue life, and creep resistance [253].

The introduction of thermal barrier coatings and heat treatments is two ways of improving the lifespan of nickel-based alloys in a harsh CO_2 environment in this study. Paper 1: Corrosion of Potential First Stage Blade Materials in Simulated Supercritical CO2, The usefulness of TBCs applied to CM247 for turbine blades was investigated and reinforced, supporting the current work that highlights the use of a multi-layered TBC system – a thermal barrier coating (ceramic topcoat, 8YSZ) and a bond coat (SC2464) (BC) before the bare alloy CM247. The novelty lies in the direct comparison of three material configurations, bare CM247, CM247 with a bond coat (SC2464), and CM247 with both a bond coat and a thermal barrier coating (8YSZ), across two CO_2 corrosive gas environments. This work is amongst the few that study the behaviour of TBC systems in a CO_2-rich environment that simulates a baseline modern sCO_2 power cycle and the impact of impurities such as SO_2, H_2O, N_2 and O_2. The study highlights that while the weight gain due to oxidation in TBC-coated samples is not drastically lower than un-coated or bond coated CM247, the protective function of the coatings is evident in microstructural analysis.

Although the average weight gain of the coated samples was not significantly lower than that of the bare alloys, as seen in *Figure 4-4*. It was evident that coatings, specifically the 8YSZ ceramic topcoats, served as a diffusion barrier preventing ingress of oxidizing species, i.e., C, N, O, and S, into the substrate. Research shows that the failure of TBCs is associated with the BC oxidation [112] as Zirconia (Zr) is known as a fast-ion oxygen conductor, and as such, the BC

must be able to form a protective, stable, and slow-growing oxide to prevent oxidative attack on the alloy [254]. Figure 4-8 shows the SEM of the bare CM247 with BC and TBC. The BC form alumina on exposure with and without contaminants at high temperature, which is vital as Al_2O_3 is a compatible phase with YSZ, ensuring the long-term thermodynamic stability of the coating [254]. The presence of stable Al-rich TGO at the interface between the BC and TBC systems supports the TBC mechanisms described in earlier work [254]. SO_2 and N exposed to uncoated CM247, led to internal oxidation and depletion of strengthening elements such as Ti and Ta, coated samples experienced minimal internal oxidation, implying that TBCs can suppress the formation of sulphides and nitrides. The BSE micrographs and EDX maps in Figure 4-7 and Figure 4-8 show that the oxidation behaviour of CM247 improved by the application of both SC2464 bond coats and YSZ topcoats.

Alloys such as CM247, and MARM247, especially when coated, are promising candidates for turbine blades and hot-section applications in CO_2 power plants. The results strongly suggest that contaminants such as SO_2 and N_2 need to be accounted for during material selection and life prediction modelling, as evidently even small quantities can cause significant degradation with high-performing nickel-based alloys. High Cr alloys, which are traditionally selected for oxidation resistance, may not be optimal in sCO_2 environments due to the formation of thick, fast-growing chromia scale susceptible to internal nitridation.

Building on the benefits of TBCs in extending alloys' longevity at high temperatures, this could be essential for the chromia-forming alloys, which form a fast-growing chromia oxide layer and form sulphides and possible TiN when nitrogen is present. The introduction of thermal barrier coatings and heat treatments is two ways of improving the lifespan of nickel-based alloys. The application of thermal barrier coatings (TBCs) has been one of the effective strategies for enhancing material longevity in high-temperature corrosive environments. The usefulness of TBCs in a bare alloy of CM247 for turbine blades was investigated in Paper 1: Corrosion of Potential First Stage Blade Materials in Simulated Supercritical CO2. This study reinforced the current work

that supports the use of a multi-layered TBC system – thermal barrier coating (ceramic topcoat - 8YSZ) and then bond coat (SC2464) before the bare alloy CM247. Although the average weight gain of the coated samples was not significantly lower than that of the bare alloys, as seen in Figure *4-4*. It was evident that coatings, specifically the 8YSZ ceramic topcoats, served as a diffusion barrier preventing ingress of oxidizing species, i.e., C, N, O, and S, into the substrate. Research shows that the failure of TBCs is associated with the BC oxidation [112] as Zirconia (Zr) is known as a fast-ion oxygen conductor, and as such, the BC must be able to form a protective, stable, and slow-growing oxide to prevent oxidative attack on the alloy [254].

Figure 4-8 shows the SEM of the bare CM247 with BC and TBC. The BC form alumina on exposure with and without contaminants at high temperature, which is vital as Al_2O_3 is a compatible phase with YSZ which ensuring the long-term thermodynamic stability of the coating [254]. Alumina is known to be the slowest-growing oxide due to the lowest oxygen diffusivity [112]. The presence of stable Al-rich TGO at the interface between the BC and TBC coated systems supports the TBC mechanisms described in earlier work. While SO_2 and N are exposed to uncoated CM247, leading to internal oxidation and depletion of strengthening elements such as Ti and Ta, coated samples experienced minimal internal oxidation, implying that TBCs can suppress the formation of sulphides and nitrides. The BSE micrographs and EDX maps show that the oxidation behaviour of CM247 improved by the application of both SC2464 bond coats and YSZ topcoats. In summary, this investigation has demonstrated that TBC systems can withstand a CO_2 harsh environment with impurities. The microstructural and chemical analyses clearly indicate that TBCs maintain the structural and chemical integrity of superalloy substrates.

Building on the advantages of TBCs in enhancing substrate alloy lifespan at high temperatures, another crucial factor is the manufacturing method. After analysing the underlying substrate material and its behaviour, it was also vital to assess the manufacturing process, as additive manufacturing is gaining increasing popularity in the energy sector.

These results were investigated in Paper 2: Comparison of the Oxidation Behaviour of Wrought and Additively Manufactured Alloy 625 in a high temperature CO_2 environment and Paper 3: Influencing effect of surface roughness on the oxidation and carburization behaviour of laser powder bed fusion (LPBF) Alloy 625 in a simulated high temperature Allam cycle environment. The shift toward additive manufacturing technologies, such as LPBF, introduces new opportunities and challenges. As shown in earlier studies, alloys like IN738, IN939, and Rene80 were susceptible to accelerated oxidation and internal possible sulphidaton and nitridation in CO_2 + SO_2 + N_2 environments. These behaviours were especially related to the low solubility of nitrogen in Ni-based systems and the formation of internal TiN precipitates, which embrittle grain boundaries. Similarly, LPBF-produced Alloy 625 as-built samples, as seen in Figure 5-4, exhibits microstructural features such as grain boundary sizes, voids, and phases etc. that could increase such degradation pathways under similar exposure conditions. The potential of LPBF as a replacement for wrought materials lies in its ability to reduce material waste and enable complex geometries with near-net-shape fabrication. Life cycle assessments, including Faludi et al. [255] demonstrated that LPBF can reduce material consumption by up to 90% for complex geometries, an important consideration in high-cost as well as high-performing applications like heat exchangers in sCO_2 power cycles. The comparative analysis of wrought manufactured and LPBF Alloy 625, solution treated (SH), and as-built (AB) Alloy 625. There's an obvious complex relationship between the nickel-based alloy and its manufacturing processes, microstructural characteristics, and oxidation behaviour in CO_2-rich environments. Oxidation behaviour in LPBF materials differs from the wrought counterparts due to various factors such as surface morphology, porosity, which influence the ingression of oxides which is unacceptable in high-stakes environments like the STEP plant, where reliability directly influences energy security and economic viability. As shown in paper 3, surface conditions directly correlate with the diffusion of reactive species, and rougher surfaces in LPBF Alloy 625 lead to thicker Cr oxide layers, and greater mass gains, mirroring the behaviours seen in chromia-forming alloys under SO_2 + N environments.

Paper 3 : Influencing Effect of Surface Roughness on the Oxidation and Carburization behaviour of Laser Powder Bed Fusion (LPBF) Alloy 625 in a Simulated High Temperature Allam Cycle Environment, indicates that surface roughness influences the diffusion rates of reactive species and the stability of the oxide-metal interface. From the study, it is evident that even minor differences in surface preparation caused significant variations in oxidation behaviour and metal loss. For example, the as-received LPBF samples showed a thicker oxide scale and greater Cr depletion, which are associated with faster degradation rates. These microstructural degradations, such as carbide formation and void development, can weaken the component both structurally and chemically, reducing its effectiveness as a heat exchanger. Concerns arise from increased oxide scale thickness, uneven heat transfer, and structural loss due to rapid Cr depletion and localized void formation. Therefore, understanding and controlling surface variation in LPBF Alloy 625 is not merely of academic interest, but a fundamental requirement for ensuring the safety, efficiency, and economic viability of future sCO_2 power systems.

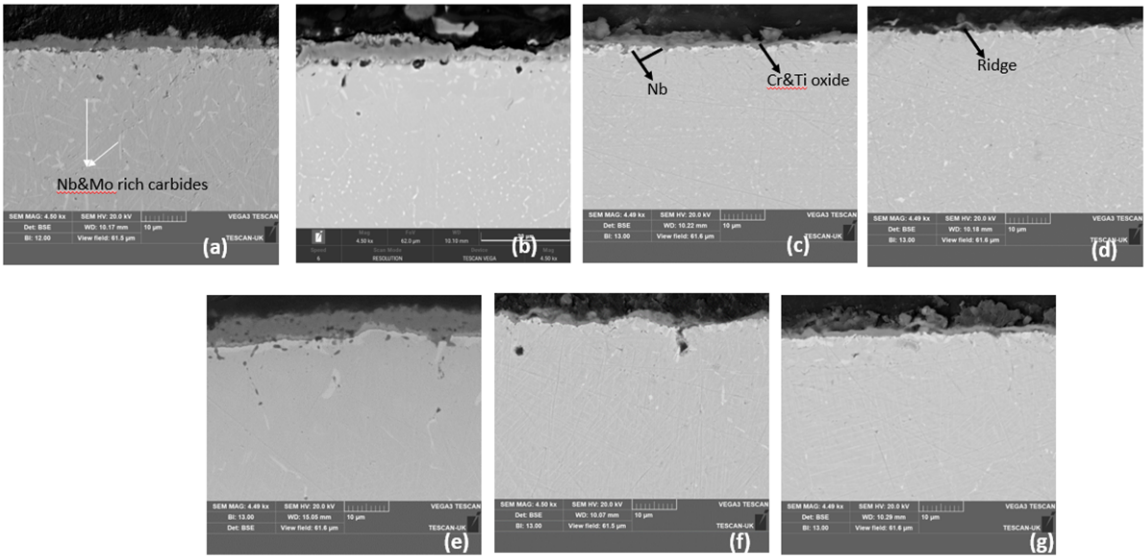


Figure 8-4 - Wrought IN625, additive manufactured (b) as-received, as built (c) 600-grit size as built (d) polished as-built (e) as-received, solution heated (f) 600-grit size solution heated (g) polished solution heated.

As seen in Figure 8-4, the formation of needle-like precipitates, particularly Nb-rich and Mo-rich phases, beneath the oxide scale is an emergent concern in rougher surfaces. P600 ground solution heated samples, though rougher than polished, offer acceptable performance in terms of oxidation and microstructural stability, making them a viable industrial compromise. Whilst the polished surface offers the best oxidation resistance, it does so at the cost of more time. Future improvements can be made through coating systems etc.

As seen in Figure 6-12, the polished samples formed thinner and more uniform chromia scales, which are considered to be protective under CO_2 exposure. However, the presence of SO_2 and H_2O in the Allam cycle working fluid alters this behaviour, as Cr_2O_3 becomes volatile (forming CrO_3) under such conditions. Here, the polished samples still maintained lower Cr depletion zones than their rougher counterparts, possibly due to less surface area for vapor-phase reactions or fewer nucleation sites for volatilization. This volatility may exaggerate Cr loss in laboratory tests compared with real components, where surface conditions and are carefully polished to minimise surface area for oxidation. Interestingly, the P600 and as-received samples exhibited internal alumina formation, which may imply deeper oxygen ingress due to poor Cr scale continuity. Alumina, though thermodynamically stable, is not as readily formed in Alloy 625 due to its lower Al content. Its presence, therefore, suggests selective internal oxidation. Also, the Nb-rich and Mo-rich precipitates were prominent in the rougher surfaces, these phases, particularly δ and γ'' in Alloy 625, affect mechanical integrity over time, and their nucleation appears sensitive to initial surface finish.

By addressing surface condition as a core factor, engineers and materials scientists can better align AM process parameters with the functional demands of high-efficiency, low-emissions power generation systems. The results of this investigation offer both a warning and a pathway: that without attention to surface preparation, even high-performance Alloy 625 may fail to deliver in transformative energy applications, but when considered, it can help in reliability, and sustainability.

Building on the discussion regarding the dependence on surface roughness on the oxidation behaviour in LPBF manufactured Alloy 625, the focus moves toward the performance of polished samples when compared to two fabrications, as-built and solution heat-treated conditions. In particular, the discussion addresses the comparative oxidation resistance observed between the polished LPBF samples and those that underwent solution heat treatment, as well as wrought counterparts. The underlying goal remains to understand how these findings translate into material selection and process design for key components within sCO_2 power systems, with the STEP pilot plant serving as a representative operational framework.

Paper 2: Comparison of the Oxidation Behaviour of Wrought and Additively Manufactured Alloy 625 in a , demonstrated a comparable oxidation resistance with mass gains below 1/3 g/cm^2 after 1000h of exposure. The parabolic rate constants (Kp) obtained from this study (AB: 48.4 × 10^{-6} mg²/cm⁴hr, SH: 52.9 × 10^{-6} mg²/cm⁴hr, WM: 40 × 10^{-6} mg²/cm⁴hr) are consistent with previous investigations on chromia-forming alloys. Marchese et al. [256] reported similar oxidation kinetics for LPBF Alloy 625, noting that the protective chromia scale formation mechanism remains fundamentally unchanged despite processing route variations. Paper 2 discussed in this thesis showed that wrought samples exhibited the finest average grain size (13.7μm), followed by solution heat-treated LPBF (26.1μm) and as-built LPBF (33.5μm). The grain size correlates with the observed oxidation behaviour, with the refined grain structure in wrought enhancing chromium diffusion through shortened diffusion pathways, facilitating rapid formation of protective chromia layers.

Figure 6-9 shows the line scan of solution heat-treated (SH) LPBF after 1000h exposure. Noticeable depletion of Cr near the surface, alongside a decrease in O within the first 6.8μm. The O penetration depth is comparable and suggests the formation of a continuous and adherent oxide scale. Under harsh environments, the formed oxide layer on SH samples is protective and effective at hindering oxygen ingression and diffusion.

An important factor distinguishing SH-LPBF from wrought material is the influence of microstructure on oxidation behaviour. Wrought Alloy 625, with its homogenized, small grain structure, allows for predictable oxidation pathways. These microstructural attributes can act as fast diffusion pathways during oxidation but also serve as nucleation sites for the rapid formation of protective oxides. Post-process heat treatment improves residual stresses and refines the grain structure as seen in Paper 2, yet the distribution of Cr and Mo remains non-homogeneous to a degree, which can localize oxidation and potentially slow its progression by forming more protective oxide scales at boundaries.

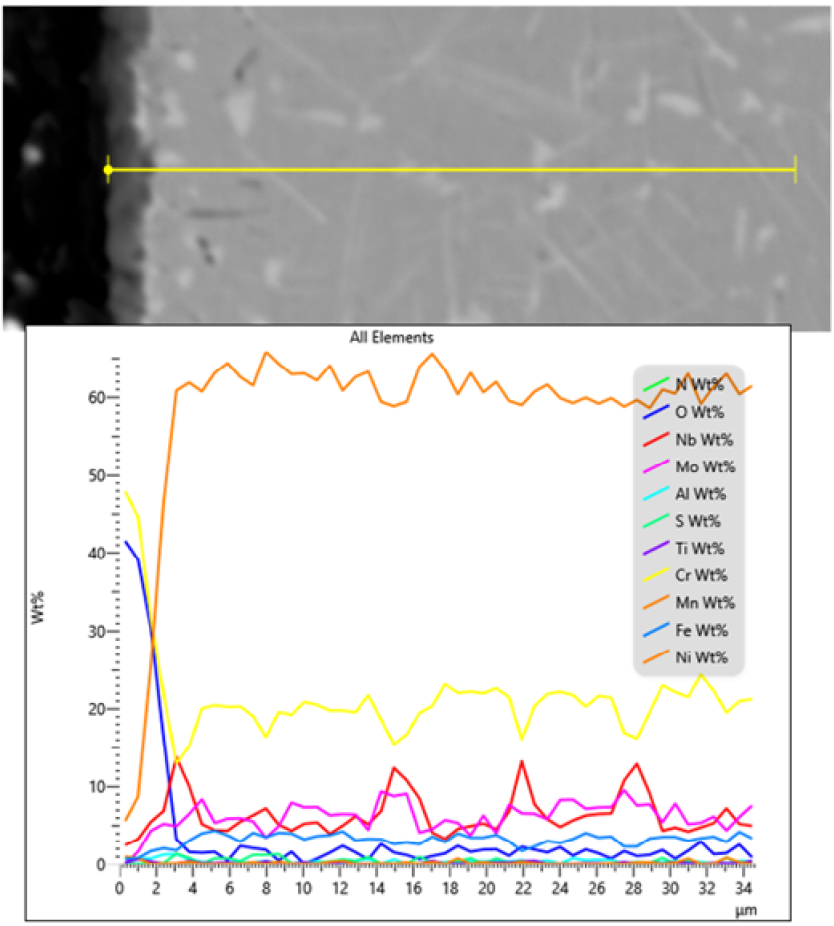


Figure 8-5 - Wrought Alloy 625 after 1000h exposure

Figure 8-5 shows the elementary line scans across the oxidized surface of wrought Alloy 625 after 1000h exposure. The Line scan shows that wrought exhibited a sharper drop in Cr near the surface compared to the solution-heated LPBF. The Cr content dropped within the first 4µm, also confirming the formation of a chromia scale, and the significant drop in O after 4µm as well indicates the scale was protective and prevented further oxygen ingress. This more oxygen ingression was also noted in Kopec et al. [257] the oxidation behaviour of wrought and direct metal laser sintered Haynes 282 was compared at 1000°C in air. Results showed that the oxidation was more progressive for the AM material due to the growth of titanium oxides due to the low structural stability of AM Haynes 282, and higher oxygen intake.

In contrast, the SH LPBF Alloy 625 showed more Cr depletion at the surface of the samples near the surface but allowed oxygen penetration up to 6µm.

However, a protective chromia layer also formed with SH LPBF alloy, as O ingress was not noticed further into the alloy. Interestingly, as a Chromia forming alloy, when compared to the other chromia forming alloys exposed to the impurity containing environment, the penetration of Nitrides below the oxide scale were not seen and the formation of TiN were not observed from SEM/EDX.

The wrought Alloy625 outperforms both variants of LPBF – as built and solution heat treated due to its fine grain structure, uniform oxide formation. However, the inclusion of heat treatments significantly improved LPBF Alloy 625 by enhancing microstructure and oxide adherence. Although currently, the Wrought has a better performance but the solution heated formed a protective oxide scale and possibly further studies and investigations into the various heat treatment techniques would further improve the performance for adoption. For sCO_2 cycles, which cycle between high and low temperature/pressure points daily, the oxidation scale stability and overall creep resistance of components like recuperators and turbines become mission critical. While wrought Alloy 625 material still offers the best resistance, LPBF with targeted heat treatment provides a viable balance, enabling exploitation of AM's design benefits. Industry efforts must therefore integrate standardized post-AM heat and surface treatments to ensure adequacy in cycle environments. It suggests that, under tightly controlled post-processing (e.g., careful polishing and stress relief), LPBF-produced components may reach or exceed the oxidation performance of conventionally wrought materials. This is particularly promising for components operating in the intermediate to high-temperature range (650–800°C), typical of recuperators and primary heat exchangers in sCO_2 Brayton cycles.

The decision to investigate surface roughness effects on LPBF Alloy 625 arises from a practical necessity. Manufacturing constraints during the COVID-19 pandemic, such as disrupted supply chains, increased costs, and labor shortages, forced engineers to reassess conventional routes for producing complex heat exchanger geometries. Additive manufacturing (AM), specifically LPBF, presented a compelling alternative owing to its near-net shape capability, geometrical design freedom, and reduced lead times. Yet, these advantages are

offset by a lack of standardization in post-processing steps, especially surface finishing, which directly impacts the material's resistance to oxidation and mechanical degradation in sCO_2 environments.

9 Conclusion

This thesis explored the oxidation behaviour of nickel-based superalloys, with an emphasis on environmental contaminants (N and SO_2) found in an Allam cycle environment, manufacturing route, and how surface conditions influence high-temperature performance. The research investigated the role of impurities in a baseline 800°C, SO_2, H_2O, N_x, which are present in real power plant conditions. These impurities were found to impact oxidation behaviour significantly, practically affecting the protective oxide layers and promoting internal oxidation and nitridation. The presence of these impurities led to substantially higher mass gains across most alloys, indicating accelerated oxidation and degradation processes. The mass change versus the square root of time plots showed that many alloys, including IN939 and Rene 80, initially followed parabolic oxidation kinetics, suggesting diffusion-controlled oxide growth. Rene 80 and IN738, both chromia-forming alloys, exhibited accelerated mass gain in the presence of impurities. In the case of Rene 80, the oxidation kinetics deviated from parabolic behaviour, suggesting possible breakdown of the oxide layer or accelerated internal degradation mechanisms. IN738 showed a persistent rise in mass gain, implying that a strong diffusion barrier had not been established. These results are consistent with findings from Paper 4, which reported that SO_2 and N_2 significantly affected the protective nature of chromia layers likely through the formation of internal nitrides. Interestingly, alloys such as CM247 and MARM247 exhibited the least change in mass in both clean and contaminated environments. These alloys, which contain moderate Cr (8–11 wt%) and higher Al levels, favoured the formation of a thin alumina scale over chromia. Alumina-forming alloys exhibited superior oxidation resistance in environments rich in impurities. Further EPMA analysis of Rene 80 revealed the formation of Ti-rich nitrides along grain boundaries which are known to embrittle grain boundaries.

Another important aspect of this study was the evaluation of thermal barrier coatings (TBCs) as a protective strategy. In particular, CM247 was coated with a multi-layer TBC system consisting of a YSZ ceramic topcoat and an SC2464 bond coat. While the coated samples did not show dramatically lower weight gain than bare samples, they exhibited superior oxidation behaviour and minimal internal degradation. The TBCs acted as diffusion barriers, effectively suppressing the ingress of N, S, O, and C species. SEM and EDX analyses confirmed the formation of a stable Al_2O_3-rich thermally grown oxide (TGO) at the bond coat interface, which is thermodynamically compatible with YSZ and critical to TBC longevity. These results confirmed that alumina-forming bond coats are essential for TBC stability, especially in environments YSZ acts as a fast oxygen ion conductor. The formation of Al_2O_3 at the BC–TBC interface slows oxygen transport and suppresses oxidative attack on the underlying superalloy. In contrast, uncoated CM247 samples exposed to contaminants experienced internal oxidation and elemental depletion (e.g., Ti, Ta), reinforcing the protective value of the coating system.

The study also presented a detailed investigation of LPBF Alloy 625, focusing on a comparative analysis of the effects of surface conditions and manufacturing technique, particularly in the presence of contaminants on the oxidation behaviour. The findings showed the beneficial effect of surface treatment, especially polishing, on the oxidation resistance of LPBF Alloy 625. Polished samples demonstrated superior oxidation behaviour compared to as-built, ground, or solution-treated specimens. This enhancement is attributed to the smoother surface finish, reducing surface area for oxidation and promoting the development of thin, adherent, and continuous Cr_2O_3 protective scales. These protective scales are critical in sCO_2 systems due to their ability to limit the ingress of oxygen and other reactive species. The work also demonstrated that the polished solution heated at 1172°C for 1 hour and water quenching exhibited oxidation behaviour almost comparable to conventional wrought material. While mechanical polishing showed effectiveness, future work must include electro-polishing methods that can be automated.

9.1 Limitations and Future Work

While this study has provided new insights into the effects of impurities, manufacturing routes, and surface conditions on the oxidation behaviour of nickel-based superalloys, several limitations remain. These limitations naturally lead to important avenues for future work, particularly if more time, resources, and funding were available.

1. Limitations in pressure-controlled testing infrastructure
A key limitation was the inability to complete and commission the high-pressure chamber facility at Cranfield University. This restricted the experimental programme to 1 bar exposures, whereas real Allam cycle turbomachinery operates at pressures up to 30 MPa. If time allowed, the priority would be the full construction, certification, and commissioning of this pressure chamber. High-pressure, high-temperature tests are essential for understanding how supercritical CO_2 environments alter oxidation kinetics, volatile species formation, and the behaviour of impurities such as N_2 and SO_2. Higher pressure is expected to accelerate oxidation rates through increased oxygen activity and enhanced transport processes, but the magnitude of this acceleration—and its interaction with N and S chemistry could not be established within this study.

With a fully functional pressure chamber, I would design and perform a test comparing low-pressure vs supercritical exposures to quantify how pressure shifts in areas such as the oxide growth mechanism, i.e. parabolic or not, internal oxidation, sulphidation and nitridation rates, and Chromium depletion. These data are crucial for translating laboratory findings into realistic predictions of component performance.

2. Isolating impurity effects (N_2 vs SO_2 vs combined environments)
Another limitation was that nitrogen and sulphur impurities were introduced together in Test 2. While this simulated a realistic contaminated Allam-cycle environment, it prevented a clean separation of their individual effects on oxide disruption, nitridation kinetics, and chromia stability.

If revisiting the work, a dedicated programme of exposures would be performed where:

1. N_2 is added independently at controlled concentrations
2. SO_2 is also added independently
3. Combined N_2 and SO_2 exposures are then used to examine the effects
4. N_2 is added independently at controlled concentrations

This would clarify, for example, whether the observed deep Ti-rich nitridation is dominated by nitrogen alone or enhanced by sulphur-driven destabilisation of chromia. It would also allow quantification of which impurity contributes most strongly to internal attack and loss of protective behaviour.

With substantial funding, a far more comprehensive research programme could be pursued, including:

- **Completion and expansion of the high-pressure test facility**, enabling long-duration supercritical CO_2 exposures up to 30 MPa with full impurity control (N_2, SO_2, H_2O, O_2, trace metals).
- **Advanced characterisation**, such as atom probe tomography (APT) for nanoscale mapping of nitrides, oxides, and sulphur segregation at grain boundaries.
- **Computational thermodynamic and kinetic modelling**, incorporating pressure-dependent phase equilibria and reactive transport modelling to predict oxide breakdown, nitride formation, and volatile species generation.
- **Exposure of full-scale components**, including coated and uncoated blade segments, to validate coupon-scale results under realistic geometries and thermal gradients.

This integrated approach would produce the first comprehensive oxidation-nitridation-sulphurisation model for Allam cycle materials, significantly advancing understanding beyond the constraints of this thesis.

In summary, although this study provides valuable insights into the oxidation behaviour of superalloys in contaminated sCO_2 environments, future work should focus on high-pressure testing, isolated impurity studies, advanced characterisation, and modelling. These steps are essential for bridging the gap between laboratory conditions and real power-plant operation.

References

1. Nations U. Causes and Effects of Climate Change | United Nations. United Nations; Available at: https://www.un.org/en/climatechange/science/causes-effects-climate-change (Accessed: 1 November 2024)

2. IEA. Global electricity generation by source, 2014-2025 – Charts – Data & Statistics - IEA. 2024. Available at: https://www.iea.org/data-and-statistics/charts/global-electricity-generation-by-source-2014-2025 (Accessed: 22 May 2025)

3. Department of Energy U. An Assessment of Energy Technologies and Research Opportunities. 2015.

4. National Grid: Live. https://grid.iamkate.com/.

5. Rovira A., Muñoz M., Sánchez C., Barbero R. Advanced thermodynamic cycles for finite heat sources: Proposals for closed and open heat sources applications. Applied Thermal Engineering. Pergamon; 25 February 2020; 167: 114805. Available at: DOI:10.1016/J.APPLTHERMALENG.2019.114805 (Accessed: 24 September 2024)

6. Khan MN., Tlili I., Khan WA. Thermodynamic Optimization of New Combined Gas/Steam Power Cycles with HRSG and Heat Exchanger. Arabian Journal for Science and Engineering. Springer Verlag; 1 November 2017; 42(11): 4547–4558. Available at: DOI:10.1007/S13369-017-2549-4/METRICS (Accessed: 24 September 2024)

7. Alklaibi AM., Khan MN., Khan WA. Thermodynamic analysis of gas turbine with air bottoming cycle. Energy. Pergamon; 15 July 2016; 107: 603–611. Available at: DOI:10.1016/J.ENERGY.2016.04.055 (Accessed: 24 September 2024)

8. Ahn Y., Lee JI. A Study of S-CO2 Power Cycle for Waste Heat Recovery Using Isothermal Compressor. Proceedings of the ASME Turbo Expo. American Society of Mechanical Engineers Digital Collection; 20 September 2016; 9. Available at: DOI:10.1115/GT2016-57151 (Accessed: 26 May 2022)

9. Marchionni M., Bianchi G., Tassou SA. Review of supercritical carbon dioxide (sCO2) technologies for high-grade waste heat to power conversion. SN Applied Sciences. Springer Nature; 2020. Available at: DOI:10.1007/s42452-020-2116-6

10. Garg P., Srinivasan K., Dutta P., Kumar P. Comparison of CO2 and Steam in Transcritical Rankine Cycles for Concentrated Solar Power. Energy Procedia. Elsevier; 1 January 2014; 49: 1138–1146. Available at: DOI:10.1016/J.EGYPRO.2014.03.123 (Accessed: 7 October 2024)

11. Dostal V., Hejzlar P., Driscoll MJ. High-Performance Supercritical Carbon Dioxide Cycle for Next-Generation Nuclear Reactors. Nuclear Technology. Taylor & Francis; 2006; 154(3): 265–282. Available at: DOI:10.13182/NT154-265 (Accessed: 24 September 2024)

12. White MT., Bianchi G., Chai L., Tassou SA., Sayma AI. Review of supercritical CO2 technologies and systems for power generation. Applied Thermal Engineering. Pergamon; 25 February 2021; 185: 116447. Available at: DOI:10.1016/J.APPLTHERMALENG.2020.116447 (Accessed: 3 May 2022)

13. Mecheri M., Le Moullec Y. Supercritical CO2 Brayton cycles for coal-fired power plants. Energy. Pergamon; 15 May 2016; 103: 758–771. Available at: DOI:10.1016/J.ENERGY.2016.02.111 (Accessed: 24 September 2024)

14. Allam RJ., Fetvedt JE., Forrest BA., Freed DA. The Oxy-Fuel, Supercritical CO2 Allam Cycle: New Cycle Developments to Produce Even Lower-Cost Electricity From Fossil Fuels Without Atmospheric Emissions. Proceedings of the ASME Turbo Expo. American Society of Mechanical Engineers Digital Collection; 18 September 2014; 3B. Available at: DOI:10.1115/GT2014-26952 (Accessed: 3 November 2022)

15. Allam RJ., palmer M., Brown JR GW. US8596075B2: System and Method for High Efficiency Power Generation Using a Carbon Dioxide Circulating Working Fluid . 2013.

16. Chan W., Morosuk T., Li X., Li H. Allam cycle: Review of research and development. Energy Conversion and Management. Elsevier Ltd; 2023. Available at: DOI:10.1016/j.enconman.2023.117607

17. Allam R., Martin S., Forrest B., Fetvedt J., Lu X., Freed D., et al. Demonstration of the Allam Cycle: An Update on the Development Status of a High Efficiency Supercritical Carbon Dioxide Power Process Employing Full Carbon Capture. Energy Procedia. Elsevier; 1 July 2017;

114: 5948–5966. Available at: DOI:10.1016/J.EGYPRO.2017.03.1731 (Accessed: 24 January 2023)

18. Pint BA., Brese RG. High-temperature materials. In: Brun K, Friedman P, Dennis Richard (eds.) Fundamentals and Applications of Supercritical Carbon Dioxide (SCO2) Based Power Cycles. Woodhead Publishing; 2017. pp. 67–104. Available at: DOI:10.1016/B978-0-08-100804-1.00004-9 (Accessed: 12 October 2022)

19. Donachie M., Donachie S. Superalloys: A technical report . ASM International . 2002. Available at: https://www.asminternational.org/documents/10192/1849770/ACFAACF.pdf (Accessed: 26 May 2022)

20. Sims CT., Stoloff NS., Hagel WC. Superalloys II: High temperature materials for aerospace and industrial power. Wiley & Sons. Wileys & sons ; 1987. 640 p. Available at: https://www.wiley.com/en-au/Superalloys+II%3A+High+Temperature+Materials+for+Aerospace+and+Industrial+Power-p-9780471011477 (Accessed: 4 April 2022)

21. High Temperature Nickel-Based Superalloys for Turbine Discs: Part One :: Total Materia Article. Available at: https://www.totalmateria.com/page.aspx?ID=CheckArticle&site=ktn&NM=259 (Accessed: 3 May 2022)

22. Reed RC. The superalloys: Fundamentals and Applications. Cambridge: Cambridge University Press; 2006.

23. Sims CT., Stoloff NS., Hagel WC. Superalloys II: High temperature materials for aerospace and industrial power. Wiley & Sons. 1987. 640 p.

24. Decker RF. The evolution of wrought age-hardenable superalloys. JOM. Minerals, Metals and Materials Society; 2006. pp. 32–36. Available at: DOI:10.1007/s11837-006-0079-8

25. ASTM International. ASTM F2792-09e1 Standard Terminology for Additive Manufacturing Technologies. West Conshohocken; June 2010. Available at: DOI:10.1520/F2792-10 (Accessed: 23 November 2023)

26. Attaran M. The rise of 3-D printing: The advantages of additive manufacturing over traditional manufacturing. Business Horizons. Elsevier Ltd; 1 September 2017; 60(5): 677–688. Available at: DOI:10.1016/J.BUSHOR.2017.05.011 (Accessed: 6 August 2023)

27. Chen L., He Y., Yang Y., Niu S., Ren H. The research status and development trend of additive manufacturing technology. International Journal of Advanced Manufacturing Technology. Springer London; 1 April 2017; 89(9–12): 3651–3660. Available at: DOI:10.1007/S00170-016-9335-4/METRICS (Accessed: 8 August 2023)

28. Additive Manufacturing: Siemens uses innovative technology to produce gas turbines | Press | Company | Siemens. Available at: https://press.siemens.com/global/en/feature/additive-manufacturing-siemens-uses-innovative-technology-produce-gas-turbines (Accessed: 11 September 2024)

29. Chyrkin A., Gunduz KO., Fedorova I., Sattari M., Visibile A., Halvarsson M., et al. High-temperature oxidation behavior of additively manufactured IN625: Effect of microstructure and grain size. Corrosion Science. Pergamon; 15 August 2022; 205: 110382. Available at: DOI:10.1016/J.CORSCI.2022.110382 (Accessed: 19 August 2024)

30. Chyrkin A., Gunduz KO., Fedorova I., Sattari M., Visibile A., Halvarsson M., et al. High-temperature Oxidation Behavior of Additively Manufactured IN625: Effect of Microstructure and Grain Size. Corrosion Science. Elsevier Ltd; 15 August 2022; 205. Available at: DOI:10.1016/J.CORSCI.2022.110382 (Accessed: 21 April 2023)

31. Guo Q., Zhao C., Escano LI., Young Z., Xiong L., Fezzaa K., et al. Transient dynamics of powder spattering in laser powder bed fusion additive manufacturing process revealed by in-situ high-speed high-

energy x-ray imaging. Acta Materialia. Pergamon; 1 June 2018; 151: 169–180. Available at: DOI:10.1016/J.ACTAMAT.2018.03.036 (Accessed: 12 October 2023)

32. Guillen D., Wahlquist S., Ali A. Critical Review of LPBF Metal Print Defects Detection: Roles of Selective Sensing Technology. Applied Sciences (Switzerland). Multidisciplinary Digital Publishing Institute (MDPI); 2024. Available at: DOI:10.3390/app14156718

33. Gusarov A V., Yadroitsev I., Bertrand P., Smurov I. Model of radiation and heat transfer in laser-powder interaction zone at selective laser melting. Journal of Heat Transfer. July 2009; 131: 1–10. Available at: DOI:10.1115/1.3109245

34. Li Y., Yang H., Lin X., Huang W., Li J., Zhou Y. The influences of processing parameters on forming characterizations during laser rapid forming. Materials Science and Engineering: A. Elsevier BV; November 2003; 360: 18–25. Available at: DOI:10.1016/S0921-5093(03)00435-0

35. Deodeshmukh VP., Pint BA. Long-Term Performance of High Temperature Alloys in Oxidizing Environments and Supercritical CO2. 2019 Joint EPRI – 123HiMAT International Conference on Advances in High-Temperature Materials. ASM International; 2024. pp. 953–966. Available at: DOI:10.31399/asm.cp.am-epri-2019p0953

36. Kim SH., Kim C., Subramanian O., Jang C. Corrosion and Carburization Behaviour of Ni-Cr-Mo-Nb Superalloys in a High Temperature Supercritical-CO 2 Environment. Available at: DOI:10.1007/978-3-319-89480-5_10 (Accessed: 14 February 2025)

37. Follett WW., Moore IJ., Sylvain JW., Manager P. The STEP 10 MWe sCO2 Pilot Installation and Commissioning Status Update. The 8th International Supercritical CO2 Power Cycles Symposium . San Antonio; 2024.

38. A step forward for sCO2 power cycles - Modern Power Systems. Available at: https://www.modernpowersystems.com/analysis/a-step-forward-for-sco2-power-cycles-11423286/?cf-view (Accessed: 14 May 2025)

39. Department for Business E& IS. Net Zero Strategy: Build Back Greener. 2021.

40. Wright IG., Stevenson JW., Singheiser L. Materials for supercritical CO_2 power cycles: Challenges and advancements. Journal of Materials Science & Engineering. 2021; 9(4).

41. Lance MJ., Haynes JA., Pint BA. Oxidation behavior of nickel-based alloys in high-temperature CO_2 environments. Corrosion Science. 2020; 167.

42. Cengel YA., Boles MA., Kanoglu M. Thermodynamics: An Engineering Approach. 10th edn. McGraw Hill; 2023.

43. Thermodynamic cycle.

44. Patel R., Karamchandani CJ. Elements of Heat Engines. Acharya Publication; 1997.

45. Winterton RHS. The Brayton Cycle: A review of its uses and performance in modern power generation. Energy. 1983; 8(6): 537–552.

46. Zhao Q. Conception and optimization of supercritical CO2 Brayton cycles for coal-fired power plant application. Available at: http://www.culture.gouv.fr/culture/infos-pratiques/droits/protection.htm (Accessed: 16 February 2022)

47. Differentiate between closed cycle and open cycle gas turbine | Mechanical Engg Diploma Simple Notes ,Solved papers and Videos. Available at: https://www.mechdiploma.com/differentiate-between-closed-cycle-and-open-cycle-gas-turbine (Accessed: 16 February 2022)

48. United States Department of Energy. Gas Turbines Combined Heat and Power Technology Fact Sheet Series . 2016. Available at: https://www.energy.gov/sites/prod/files/2016/09/f33/CHP-Gas%20Turbine.pdf (Accessed: 27 February 2022)

49. Chen Y. Novel Cycles using Carbon Dioxide as Working Fluid. Stockholm; 2006.

50. Chen Y., Lundqvist P., Johansson A., Platell A. A Comparative Study of the Carbon Dioxide Transcritical Power Cycle Compared with an Organic Rankine Cycle with R123 as Working Fluid in Waste Heat Recovery. Applied Thermal Engineering. 2006; : 2142–2147.

51. Dostal V., Hejzlar P., Driscoll MJ. The supercritical carbon dioxide power cycle: Comparison to other advanced power cycles. Nuclear Technology. American Nuclear Society; 2006; 154: 283–301. Available at: DOI:10.13182/NT06-A3734

52. Li MJ., Zhu HH., Guo JQ., Wang K., Tao WQ. The development technology and applications of supercritical CO2 power cycle in nuclear energy, solar energy and other energy industries. Applied Thermal Engineering. Pergamon; 5 November 2017; 126: 255–275. Available at: DOI:10.1016/J.APPLTHERMALENG.2017.07.173 (Accessed: 24 September 2024)

53. Feher EG. The supercritical thermodynamic power cycle. Energy Conversion. 1968; 8(2): 85–90. Available at: DOI:10.1016/0013-7480(68)90105-8 (Accessed: 20 February 2022)

54. Sodeifian G., Sajadian SA., Ardestani NS. Determination of solubility of Aprepitant (an antiemetic drug for chemotherapy) in supercritical carbon dioxide: Empirical and thermodynamic models. The Journal of Supercritical Fluids. Elsevier; 1 October 2017; 128: 102–111. Available at: DOI:10.1016/J.SUPFLU.2017.05.019 (Accessed: 20 February 2024)

55. Min L., Liu M., Xi D., He M., Liu X., Huang Y. Study of Supercritical CO2 Physical Property Calculation Models. Frontiers in Energy Research. Frontiers Media S.A.; 25 February 2022; 10: 835311. Available at: DOI:10.3389/FENRG.2022.835311/BIBTEX (Accessed: 20 February 2024)

56. Zhu Q. Innovative power generation systems using supercritical CO2 cycles. Clean Energy. Oxford Academic; 29 December 2017; 1(1): 68–79. Available at: DOI:10.1093/CE/ZKX003 (Accessed: 2 March 2022)

57. Intergovernmental Panel on Climate Change. IPCC special report on Carbon Dioxide Capture and Storage. New York ; 2005.

58. Dostal V., Driscoll MJ., Hejzlar P., Todreas NE. A Supercritical CO2 Gas Turbine Power Cycle for Next-Generation Nuclear Reactors. International Conference on Nuclear Engineering, Proceedings, ICONE. American Society of Mechanical Engineers Digital Collection; 4 March 2009; 2: 567–574. Available at: DOI:10.1115/ICONE10-22192 (Accessed: 7 October 2024)

59. Dostal V. A supercritical carbon dioxide cycle for next generation nuclear reactors. Prague; 2004. Available at: https://dspace.mit.edu/handle/1721.1/17746 (Accessed: 22 February 2022)

60. Turchi CS., Ma Z., Dyreby J. Supercritical Carbon Dioxide Power Cycle Configurations for Use in Concentrating Solar Power Systems. Proceedings of the ASME Turbo Expo. American Society of Mechanical Engineers Digital Collection; 9 July 2013; 5: 967–973. Available at: DOI:10.1115/GT2012-68932 (Accessed: 26 May 2022)

61. Ahn Y., Bae SJ., Kim M., Cho SK., Baik S., Lee JI., et al. Review of supercritical CO2 power cycle technology and current status of research and development. Nuclear Engineering and Technology. Elsevier; 1 October 2015; 47(6): 647–661. Available at: DOI:10.1016/J.NET.2015.06.009 (Accessed: 13 July 2022)

62. Weiland NT., Dennis RA., Ames R., Lawson S., Strakey P. Fossil energy. Fundamentals and Applications of Supercritical Carbon Dioxide (SCO2) Based Power Cycles. Duxford: Woodhead Publishing; 2017. pp. 293–338. Available at: DOI:10.1016/B978-0-08-100804-1.00012-8 (Accessed: 15 June 2022)

63. Sulzer G. 269599: Verfahren zur Erzeugung von Arbeit aus Warme. Patent Swiss Patent CH; 1950.

64. Angelino G. Perspectives for the Liquid Phase Compression Gas Turbine. Journal of Engineering for Power. American Society of Mechanical Engineers Digital Collection; 1 April 1967; 89(2): 229–236. Available at: DOI:10.1115/1.3616657 (Accessed: 9 March 2023)

65. Angelino G. Real Gas Effects in Carbon Dioxide Cycles. International Gas Turbine Conference and Product Shows. Cleveland, Ohio: AMSE; 1969. Available at: DOI:10.1115/69-GT-102 (Accessed: 9 March 2023)

66. Ma Z., Turchi CS. Advanced Supercritical Carbon Dioxide Power Cycle Configurations for Use in Concentrating Solar Power Systems: Preprint. 2011; Available at: http://www.osti.gov/bridge (Accessed: 7 October 2024)

67. Persichilli M., Kacludis A., Zdankiewicz E., Held T. Supercritical CO 2 Power Cycle Developments and Commercialization: Why sCO 2 can Displace Steam Ste am. Available at: www.echogen.com (Accessed: 7 October 2024)

68. Span R., Wagner W. Equations of state for CO_2 and other substances in the supercritical region. Journal of Supercritical Fluids. 1996; 9(3): 247–259.

69. Molière M., Privat R., Jaubert JN., Geiger F. Supercritical CO2 Power Technology: Strengths but Challenges. Energies 2024, Vol. 17, Page 1129. Multidisciplinary Digital Publishing Institute; 27 February 2024; 17(5): 1129. Available at: DOI:10.3390/EN17051129 (Accessed: 25 July 2024)

70. Wright SA., Conboy TM., Ames DE. CO2-based mixtures as working fluids for geothermal turbines. Albuquerque, NM, and Livermore, CA (United States); January 2012. Available at: DOI:10.2172/1049477 (Accessed: 21 June 2022)

71. Esteves AF., Santos FM., Magalhães Pires JC. Carbon dioxide as geothermal working fluid: An overview. Renewable and Sustainable Energy Reviews. Pergamon; 1 October 2019; 114: 109331. Available at: DOI:10.1016/J.RSER.2019.109331 (Accessed: 30 September 2022)

72. Geddes B., Leon H., Huang X. Superalloys: Alloying and Performance. ASM . 2010. Available at: www.asminternational.org (Accessed: 26 May 2022)

73. Pollock TM., Tin S. Nickel-Based Superalloys for Advanced Turbine Engines: Chemistry, Microstructure, and Properties. JOURNAL OF PROPULSION AND POWER. 22(2).

74. ASM Handbook. Ni (Nickel) Binary Alloy Phase Diagrams. In: Okamoto H, Schlesinger ME, Mueller EM (eds.) Alloy Phase Diagrams. ASM International; 2016. pp. 520–533. Available at: DOI:10.31399/ASM.HB.V03.A0006189 (Accessed: 17 June 2025)

75. Huang HE., Koo CH. Characteristics and Mechanical Properties of Polycrystalline CM 247 LC Superalloy Casting. Materials Transactions. Japan Institute of Metals (JIM); 2004; 45: 562–568. Available at: DOI:10.2320/matertrans.45.562

76. Chiou MS., Yeh AC., Jian SR., Kuo CM. High temperature oxidation behavior of CM-247LC nickel base superalloy. Advanced Materials Research. Trans Tech Publications; 2014. pp. 61–66. Available at: DOI:10.4028/www.scientific.net/AMR.922.61

77. Jalowicka A., Nowak WJ., Naumenko D., Quadakkers WJ. Effect of SO2 Addition on Air Oxidation Behavior of CM247 and CMSX-4 at 1050°C.

JOM. Minerals, Metals and Materials Society; November 2016; 68: 2776–2785. Available at: DOI:10.1007/s11837-016-2072-1

78. ASM International. Metal Handbook . 2nd edn. Davis J (ed.) Taylor & Francis; 1988.

79. Hadjiapostolidou D., Shollock BA. Long Term Coarsening in RENÉ 80 Ni-Base Superalloy. 2008.

80. Mallikarjuna HT., Richards NL., Caley WF. Effect of alloying elements and microstructure on the cyclic oxidation performance of three nickel-based superalloys. Materialia. Elsevier; 1 December 2018; 4: 487–499. Available at: DOI:10.1016/J.MTLA.2018.11.004 (Accessed: 17 June 2025)

81. Cui CY., Gu YF., Ping DH., Harada H., Fukuda T. The evolution of η phase in Ni-Co base superalloys. Materials Science and Engineering: A. Elsevier BV; June 2008; 485: 651–656. Available at: DOI:10.1016/j.msea.2007.08.047

82. Murata Y., Hashizume A., Yoshinari A., Aoki N., Morinaga M., Fukui Y. Alloying Effects on Surface Stability and Creep Strength of Nickel Based Single Crystal Superalloys Containing 12 Mass% Cr. In: Pollock TM (ed.) 9th, International symposium on superalloys . Seven Springs, PA: TMS; 2000.

83. Jahangiri MR., Arabi H., Boutorabi SMA. Development of wrought precipitation strengthened IN939 superalloy. Materials Science and Technology (United Kingdom). SAGE PublicationsSage UK: London, England; December 2012; 28(12): 1470–1478. Available at: DOI:10.1179/1743284712Y.0000000073;JOURNAL:JOURNAL:MSTB (Accessed: 23 July 2025)

84. Vaezi M., Soleymani M. Creep Life Prediction of Inconel 738 Gas Turbine Blade. Journal of Applied Sciences. May 2009; 9: 1950–1955. Available at: DOI:10.3923/jas.2009.1950.1955

85. Heydari D., Fard AS., Bakhshi A., Drezet JM. Hot tearing in polycrystalline Ni-based IN738LC superalloy: Influence of Zr content. Journal of Materials Processing Technology. Elsevier; 1 March 2014; 214(3): 681–687. Available at: DOI:10.1016/J.JMATPROTEC.2013.10.001 (Accessed: 17 March 2025)

86. Egbewande AT., Zhang HR., Sidhu RK., Ojo OA. Improvement in laser weldability of INCONEL 738 superalloy through microstructural modification. Metallurgical and Materials Transactions A: Physical Metallurgy and Materials Science. Springer; 1 September 2009; 40(11): 2694–2704. Available at: DOI:10.1007/S11661-009-9962-6/FIGURES/20 (Accessed: 17 March 2025)

87. Collier JP. Effects of Replacing the Refactory Elements W, Nb and Ta with Nickel-based Superalloys on Microstructural, Microchemical and Mechanical Properties. Metallurgical transactions. A, Physical metallurgy and materials science. Springer; 1986; 17 A(4): 651–661. Available at: DOI:10.1007/BF02643984/METRICS (Accessed: 17 March 2025)

88. Ojo OA., Richards NL., Chaturvedi MC. On incipient melting during high temperature heat treatment of cast Inconel 738 superalloy. Journal of Materials Science. Springer; 15 December 2004; 39(24): 7401–7404. Available at: DOI:10.1023/B:JMSC.0000048761.32712.EB/METRICS (Accessed: 17 March 2025)

89. Ojo OA., Richards NL., Chaturvedi MC. Contribution of constitutional liquation of gamma prime precipitate to weld HAZ cracking of cast Inconel 738 superalloy. Scripta Materialia. March 2004; 50: 641–646. Available at: DOI:10.1016/j.scriptamat.2003.11.025

90. Honey T. A step forward for sCO2 power cycles. https://www.modernpowersystems.com/analysis/a-step-forward-for-sco2-power-cycles-11423286/?cf-view. 2024.

91. INCONEL ® alloy 625. Special Metal. 2013. Available at: www.specialmetals.com

92. Mathew MD., Parameswaran P., Bhanu Sankara Rao K. Microstructural changes in alloy 625 during high temperature creep. Materials Characterization. Elsevier; 1 May 2008; 59(5): 508–513. Available at: DOI:10.1016/J.MATCHAR.2007.03.007 (Accessed: 5 October 2023)

93. Li C., White R., Fang XY., Weaver M., Guo YB. Microstructure evolution characteristics of Inconel 625 alloy from selective laser melting to heat treatment. Materials Science and Engineering: A. Elsevier; 29 September 2017; 705: 20–31. Available at: DOI:10.1016/J.MSEA.2017.08.058 (Accessed: 25 November 2024)

94. Suave LM., Cormier J., Villechaise P., Soula A., Hervier Z., Bertheau D., et al. Microstructural evolutions during thermal aging of alloy 625: Impact of temperature and forming process. Metallurgical and Materials Transactions A: Physical Metallurgy and Materials Science. Springer Boston; 19 March 2014; 45(7): 2963–2982. Available at: DOI:10.1007/S11661-014-2256-7/FIGURES/15 (Accessed: 17 June 2025)

95. Sundararaman M., Mukhopadhyay P., Banerjee S. Precipitation of the δ-Ni3Nb phase in two nickel base superalloys. Metallurgical Transactions A. Springer-Verlag; March 1988; 19: 453–465. Available at: DOI:10.1007/BF02649259

96. Zhou L., Miller J., Vezza J., Mayster M., Raffay M., Justice Q., et al. Additive Manufacturing: A Comprehensive Review. Sensors. Multidisciplinary Digital Publishing Institute (MDPI); 2024. Available at: DOI:10.3390/s24092668

97. Wong M., Owen I., Sutcliffe CJ., Puri A. Convective heat transfer and pressure losses across novel heat sinks fabricated by Selective Laser Melting. International Journal of Heat and Mass Transfer. Pergamon; 15 January 2009; 52(1–2): 281–288. Available at: DOI:10.1016/J.IJHEATMASSTRANSFER.2008.06.002 (Accessed: 11 September 2024)

98. Bag S., Deneault JR., Durstock MF. Aerosol-Jet-Assisted Thin-Film Growth of CH3NH3PbI3 Perovskites—A Means to Achieve High Quality, Defect-Free Films for Efficient Solar Cells. Advanced Energy Materials. John Wiley & Sons, Ltd; 1 October 2017; 7(20): 1701151. Available at: DOI:10.1002/AENM.201701151 (Accessed: 11 September 2024)

99. Yao X., Moon SK., Bi G. A hybrid machine learning approach for additive manufacturing design feature recommendation. Rapid Prototyping Journal. Emerald Group Publishing Ltd.; 2017; 23(6): 983–997. Available at: DOI:10.1108/RPJ-03-2016-0041 (Accessed: 11 September 2024)

100. Bhavar V., Kattire P., Patil V., Khot S., Gujar K., Singh R. A review on powder bed fusion technology of metal additive manufacturing. Additive Manufacturing Handbook. 1st edn. CRC Press; 2017. pp. 251–253. Available at: DOI:10.1201/9781315119106-15 (Accessed: 20 May 2025)

101. 8 Essential Design Tips for SLS 3D Printing | Xometry Pro. https://xometry.pro/en/articles/3d-printing-sls-design-tips/.

102. Hager EM., O'Hara RP., Cobb GR., Flater PJ., Payton EJ., Sinha V., et al. Development of high density parts in the low-alloy, high-performance steel AF9628 using laser powder bed fusion. Materials Science and Engineering: A. Elsevier Ltd; March 2022; 838. Available at: DOI:10.1016/j.msea.2022.142656

103. Gordon J V., Narra SP., Cunningham RW., Liu H., Chen H., Suter RM., et al. Defect structure process maps for laser powder bed fusion additive manufacturing. Additive Manufacturing. Elsevier B.V.; December 2020; 36. Available at: DOI:10.1016/j.addma.2020.101552

104. Cunningham RW. Defect Formation Mechanisms in Powder-Bed Metal Additive Manufacturing. Carnegie Mellon University; 2018.

105. Coniglio N., Cross CE. Initiation and growth mechanisms for weld solidification cracking. International Materials Reviews. 2013. pp. 375–397. Available at: DOI:10.1179/1743280413Y.0000000020

106. DebRoy T., Wei HL., Zuback JS., Mukherjee T., Elmer JW., Milewski JO., et al. Additive manufacturing of metallic components – Process, structure and properties. Progress in Materials Science. Elsevier Ltd; 2018. pp. 112–224. Available at: DOI:10.1016/j.pmatsci.2017.10.001

107. Eliasu A., Czekanski A., Boakye-Yiadom S. Effect of laser powder bed fusion parameters on the microstructural evolution and hardness of 316L stainless steel. International Journal of Advanced Manufacturing Technology. Springer Science and Business Media Deutschland GmbH; April 2021; 113: 2651–2669. Available at: DOI:10.1007/s00170-021-06818-9

108. Carter LN., Martin C., Withers PJ., Attallah MM. The influence of the laser scan strategy on grain structure and cracking behaviour in SLM powder-bed fabricated nickel superalloy. Journal of Alloys and Compounds. Elsevier; 5 December 2014; 615: 338–347. Available at: DOI:10.1016/J.JALLCOM.2014.06.172 (Accessed: 17 June 2025)

109. Sames WJ., List FA., Pannala S., Dehoff RR., Babu SS. The metallurgy and processing science of metal additive manufacturing. International Materials Reviews. Taylor and Francis Ltd.; 2016; 61(5): 315–360. Available at: DOI:10.1080/09506608.2015.1116649 (Accessed: 16 June 2025)

110. Birks N., Meier GH., Pettit FS. Introduction to the high temperature oxidation of metals, Second edition. Introduction to the High Temperature Oxidation of Metals, Second Edition. Cambridge University Press; 2006. 1–338 p. Available at: DOI:10.1017/CBO9781139163903 (Accessed: 13 August 2024)

111. Young DJ. High Temperature Oxidation and Corrosion of Metals: Second Edition. 2nd edn. High temperature Oxidation and Corrosion of Metals: Second Edition. Sdyney: Elsevier Inc.; 2016. 1–733 p. Available at: DOI:10.1016/C2014-0-00259-6 (Accessed: 29 September 2022)

112. Kofstad P. High temperature corrosion . 2nd edn. Essex: Elsevier applied science ; 1988.

113. Thijs L., Verhaeghe F., Craeghs T., Humbeeck J Van., Kruth JP. A study of the microstructural evolution during selective laser melting of Ti-6Al-4V. Acta Materialia. May 2010; 58: 3303–3312. Available at: DOI:10.1016/j.actamat.2010.02.004

114. King WE., Anderson AT., Ferencz RM., Hodge NE., Kamath C., Khairallah SA., et al. Laser powder bed fusion additive manufacturing of metals; physics, computational, and materials challenges. Applied Physics Reviews. AIP Publishing; 1 December 2015; 2(4): 041304. Available at: DOI:10.1063/1.4937809 (Accessed: 17 June 2025)

115. Körner C., Attar E., Heinl P. Mesoscopic simulation of selective beam melting processes. Journal of Materials Processing Technology. Elsevier; 1 June 2011; 211(6): 978–987. Available at: DOI:10.1016/J.JMATPROTEC.2010.12.016 (Accessed: 17 June 2025)

116. Dinda GP., Dasgupta AK., Mazumder J. Laser aided direct metal deposition of Inconel 625 superalloy: Microstructural evolution and thermal stability. Materials Science and Engineering: A. Elsevier; 25 May 2009; 509(1–2): 98–104. Available at: DOI:10.1016/J.MSEA.2009.01.009 (Accessed: 17 June 2025)

117. Amato KN., Gaytan SM., Murr LE., Martinez E., Shindo PW., Hernandez J., et al. Microstructures and mechanical behavior of Inconel 718 fabricated by selective laser melting. 2012; Available at: DOI:10.1016/j.actamat.2011.12.032 (Accessed: 17 June 2025)

118. Li C., Liu ZY., Fang XY., Guo YB. Residual Stress in Metal Additive Manufacturing. Procedia CIRP. Elsevier B.V.; 2018. pp. 348–353. Available at: DOI:10.1016/j.procir.2018.05.039

119. Kreitcberg A., Brailovski V., Turenne S. Effect of heat treatment and hot isostatic pressing on the microstructure and mechanical properties of

Inconel 625 alloy processed by laser powder bed fusion. Materials Science and Engineering: A. Elsevier Ltd; March 2017; 689: 1–10. Available at: DOI:10.1016/j.msea.2017.02.038

120. Marchese G., Garmendia Colera X., Calignano F., Lorusso M., Biamino S., Minetola P., et al. Characterization and Comparison of Inconel 625 Processed by Selective Laser Melting and Laser Metal Deposition. Advanced Engineering Materials. Wiley-VCH Verlag; March 2017; 19. Available at: DOI:10.1002/adem.201600635

121. Tucho WM., Cuvillier P., Sjolyst-Kverneland A., Hansen V. Microstructure and hardness studies of Inconel 718 manufactured by selective laser melting before and after solution heat treatment. Materials Science and Engineering: A. Elsevier Ltd; March 2017; 689: 220–232. Available at: DOI:10.1016/j.msea.2017.02.062

122. Criales LE., Arısoy YM., Lane B., Moylan S., Donmez A., Özel T. Laser powder bed fusion of nickel alloy 625: Experimental investigations of effects of process parameters on melt pool size and shape with spatter analysis. International Journal of Machine Tools and Manufacture. Elsevier Ltd; October 2017; 121: 22–36. Available at: DOI:10.1016/j.ijmachtools.2017.03.004

123. Pantazopoulos GA. Failure mechanisms in alloys. Metals. MDPI AG; 2020. Available at: DOI:10.3390/met10010117

124. Grabke HJ., Wolf I. Carburization and oxidation. Materials Science and Engineering. 1987; 87: 23–33. Available at: DOI:10.1016/0025-5416(87)90357-0

125. Rouillard F., Charten F., Moine G. Corrosion Behavior of Different Metallic Materials in Supercritical Carbon Dioxide at 550°C and 250 bars. Corrosion. Association for Materials Protection and Performance; 1 September 2011; 67(9): 095001-095001–095007. Available at: DOI:10.5006/1.3628683 (Accessed: 18 March 2025)

126. Grabke HJ. Thermodynamics, Mechanisms and Kinetics of Metal dusting. Materials and Corrosion. Kluwer Academic Publishers-Plenum Publishers; 28 January 1999; 49(5): 303–308. Available at: DOI:10.1007/BF00664665 (Accessed: 18 March 2025)

127. Lai GY. High-Temperature Corrosion and Materials Applications. High-Temperature Corrosion and Materials Applications. ASM International; 2007. Available at: DOI:10.31399/ASM.TB.HTCMA.9781627083041 (Accessed: 18 March 2025)

128. Gleeson B. High-Temperature Corrosion of Metallic Alloys and Coatings. Materials Science and Technology: A Comprehensive Treatment. wiley; 2008. pp. 173–228. Available at: DOI:10.1002/9783527619306.ch14

129. Yang L., Qian H., Kuang W. Corrosion Behaviors of Heat-Resisting Alloys in High Temperature Carbon Dioxide. Materials. MDPI; 1 February 2022; 15(4): 1331. Available at: DOI:10.3390/MA15041331 (Accessed: 17 June 2025)

130. Pint BA., Keiser JR. Initial Assessment of Ni-Base Alloy Performance in 0.1 MPa and Supercritical CO2. JOM. Minerals, Metals and Materials Society; September 2015; 67: 2615–2620. Available at: DOI:10.1007/s11837-015-1661-8

131. Firouzdor V., Cao GP., Sridharan K., Anderson M., Allen TR. Corrosion resistance of PM2000 ODS steel in high temperature supercritical carbon dioxide. Materials and Corrosion. John Wiley & Sons, Ltd; 1 February 2015; 66(2): 137–142. Available at: DOI:10.1002/MACO.201307223 (Accessed: 17 June 2025)

132. McCarroll IE., La Fontaine A., Nguyen TD., Smith AF., Zhang J., Young DJ., et al. Performance of an FeCrAl alloy in a high-temperature CO2 environment. Corrosion Science. Pergamon; 15 July 2018; 139: 267–274. Available at: DOI:10.1016/J.CORSCI.2018.05.007 (Accessed: 17 June 2025)

133. Beckmann JA., Woodford DA. Grain-boundary Penetration of Sulphur in Ni and Ni-based alloys. Metallurgical Transactions. 1970; 1(3): 675–682.

134. Lees DG. On the reasons for the effects of dispersions of stable oxides and additions of reactive elements on the adhesion and growth-mechanisms of chromia and alumina scales-the 'sulfur effect'. Oxidation of Metals. Kluwer Academic Publishers-Plenum Publishers; February 1987; 27: 75–81. Available at: DOI:10.1007/BF00656731

135. Huczkowski P., Young DJ., Olszewski T., Chyrkin A., Quadakkers WJ. Effect of Sulphur on the Oxidation Behaviour of Possible Construction Materials for Heat Exchangers in Oxyfuel Plants in the Temperature Range 550–700 °C. Oxidation of Metals. Springer New York LLC; June 2018; 89: 651–681. Available at: DOI:10.1007/s11085-017-9809-2

136. Oleksak RP., Tylczak JH., Holcomb GR., Doğan ÖN. High temperature oxidation of steels in CO2 containing impurities. Corrosion Science. Elsevier Ltd; March 2020; 164. Available at: DOI:10.1016/j.corsci.2019.108316

137. Krupp U., Christ HJ. Internal nitridation of nickel-base alloys. Part I. Behavior of binary and ternary alloys of the Ni-Cr-Al-Ti system. Oxidation of Metals. Kluwer Academic/Plenum Publ Corp; 1999; 52: 277–298. Available at: DOI:10.1023/a:1018843612011

138. Lai GY. High-Temperature Corrosion and Materials Applications. High-Temperature Corrosion and Materials Applications. ASM International; 2007. Available at: DOI:10.31399/asm.tb.htcma.9781627083041

139. Krupp U., Christ H-J. Internal Nitridation of Nickel-Base Alloys Part II: Behavior of quaternary NiCrAlTi alloys and computer-based description. Oxidation of Metals. 1999; 52(3/4): 299–320.

140. Krupp U., Christ H-J. Internal Nitridation of Nickel-Base Alloys Part I: Behavior of binary and ternary alloys of the Ni-Cr-Al-Ti system. Oxidation of Metals. 1999; 52(3/4): 277–298.

141. Basoalto H., Sondhi SK., Dyson BF., McLean M. A Generic Microstructure-explicit Model of Creep in Nickel-base Superalloys. Superalloys. 2004; : 897–906.

142. Miao J., Pollock TM., Jones JW. Fatigue Crack Initiation in Nickel-based Superalloy René 88 DT at 593 °C. Superalloys. 2008; : 589–597. Available at: https://www.tms.org/superalloys/10.7449/2008/Superalloys_2008_589_597.pdf?utm_source=chatgpt.com (Accessed: 18 June 2025)

143. Giggins CS., Pettit FS. Oxidation of Ni-Cr-Al Alloys Between 1000° and 1200°C. Journal of The Electrochemical Society. The Electrochemical Society; 1 November 1971; 118(11): 1782. Available at: DOI:10.1149/1.2407837/XML (Accessed: 1 November 2024)

144. Clarke DR., Oechsner M., Padture NP. Thermal-barrier coatings for more efficient gas-turbine engines. MRS Bulletin. October 2012; 37: 891–898. Available at: DOI:10.1557/mrs.2012.232

145. Ogawa K. High Temperature Oxidation Behavior of Thermal Barrier Coatings. Gas Turbines - Materials, Modeling and Performance. InTech; 2015. Available at: DOI:10.5772/59794

146. Taylor TA., Walsh PN. Thermal expansion of MCrAlY alloys. Surface and Coatings Technology. Elsevier; January 2004; 177–178: 24–31. Available at: DOI:10.1016/j.surfcoat.2003.05.001

147. Noveed E., Liaqat A., Akhlaq A., Muhammad M., Muhammad MA., Abdul R., et al. Thermo-physical properties measurement of advanced TBC materials with pyrochlore and perovskite structures. Key Engineering Materials. Trans Tech Publications Ltd; 2018. pp. 236–244. Available at: DOI:10.4028/www.scientific.net/KEM.778.236

148. Paul S. Assessing coating reliability through pore architecture evaluation. Journal of Thermal Spray Technology. 2010. pp. 779–786. Available at: DOI:10.1007/s11666-010-9474-3

149. Yang Z. Evaluation and characterisation of thermal barrier coatings. https://research.manchester.ac.uk/en/studentTheses/evaluation-and-characterisation-of-thermal-barrier-coatings. 2013.

150. Wu BC., Chang E., Chao CH., Tsai ML. Oxide pegging spalling mechanism and spalling modes of ZrO2 8wt% Y2O3/Ni-22Cr-10Al-1Y thermal barrier coatings under various operating conditions. Journal of Materials Science. 1990; 25: 1112–1119. Available at: DOI:10.1007/BF03372212

151. Maier RD., Scheuermann CM., Andrews CW. Degradation of a two-layer thermal barrier coating under thermal cycling. Ceramic Bulletin. 1981; 60(5): 555–560.

152. Wright IG., Pint BA., Shingledecker JP., Thimsen D. Materials considerations for supercritical CO2 turbine cycles. Proceedings of the ASME Turbo Expo. American Society of Mechanical Engineers (ASME); 2013. Available at: DOI:10.1115/GT2013-94941

153. Sanicro® 625. https://www.alleima.com/en/technical-center/material-datasheets/bar-and-hollow-bar/bar/sanicro-625/.

154. Potter A., Sumner J., Simms N. The effects of water vapour on the hot corrosion of gas turbine blade materials at 700 °C. 2022; Available at: DOI:10.1080/09603409.2022.2056299 (Accessed: 9 March 2023)

155. International standard ISO. Corrosion of metals and alloys-Method for metallographic examination of samples after exposure to high-temperature corrosive environments. 2012.

156. Mori S., Pidcock A., Sumner J., Simms N., Oakey J. Fireside Corrosion of Heat Exchanger Materials for Advanced Solid Fuel Fired Power Plants. Oxidation of Metals. Springer; April 2022; 97: 281–306. Available at: DOI:10.1007/s11085-021-10094-z

157. Lee R. Coating and Alternatives for SEM Microscopy. INTER/MICRO’93. Chicago; 1993. pp. 1–20.

158. Scanning Electron Microscopy | Nanoscience Instruments. https://www.nanoscience.com/techniques/scanning-electron-microscopy/.

159. How Does EDX Analysis with a Scanning Electron Microscope (SEM) Work? https://www.azom.com/article.aspx?ArticleID=16256.

160. JEOL USA blog | Why Use SEM-EDS for Advanced Materials Analysis? https://www.jeolusa.com/NEWS-EVENTS/Blog/why-use-sem-eds-advanced-materials-analysis. 2024.

161. Hou PY. Beyond the Sulfur Effect. Oxidation of Metals. 52: 1999.

162. The principle of APT. https://myscope.training/APT_The_principle_of_APT.

163. Electron probe micro-analyzer (EPMA). https://serc.carleton.edu/research_education/geochemsheets/techniques/EPMA.html.

164. Alaves B. • Electricity demand in the UK 2021 | Statista. 2022. Available at: https://www.statista.com/statistics/323381/total-demand-for-electricity-in-the-united-kingdom-uk/ (Accessed: 21 June 2022)

165. Department of Energy U. Chapter 4: Advancing Clean Electric Power Technologies. 2015. Available at: https://www.energy.gov/sites/default/files/2016/06/f32/QTR2015-4R-Supercritical-Carbon-Dioxide-Brayton%20Cycle.pdf (Accessed: 22 June 2022)

166. Department of Energy U. Advancing Clean Electric Power Technologies . 2015.

167. Angelino G. Carbon Dioxide Condensation Cycles for Power Production . Journal of Engineering for Power . 1 July 1968; 90(3): 287–295. Available at: https://asmedigitalcollection.asme.org/gasturbinespower/article/90/3/287/

405421/Carbon-Dioxide-Condensation-Cycle-For-Power (Accessed: 1 March 2022)

168. Ma Y., Liu Z., Tian H. A review of transcritical carbon dioxide heat pump and refrigeration cycles. Energy. Pergamon; 15 June 2013; 55: 156–172. Available at: DOI:10.1016/J.ENERGY.2013.03.030 (Accessed: 22 June 2022)

169. Sarkar J. Ejector enhanced vapor compression refrigeration and heat pump systems—A review. Renewable and Sustainable Energy Reviews. Pergamon; 1 December 2012; 16(9): 6647–6659. Available at: DOI:10.1016/J.RSER.2012.08.007 (Accessed: 22 June 2022)

170. Turchi CS., Ma Z., Dyreby J. Supercritical Carbon Dioxide Power Cycle Configurations for Use in Concentrating Solar Power Systems. Proceedings of the ASME Turbo Expo. American Society of Mechanical Engineers Digital Collection; 9 July 2013; 5: 967–973. Available at: DOI:10.1115/GT2012-68932 (Accessed: 21 June 2022)

171. Ian Hunter., Daleo J., Wilson J., Ellison K. Analysis of Hot Section Failures on Gas Turbines in Process Plant Service. Proceedings of the 28th Turbomachinery Symposium. pp. 9–20.

172. Pollock TM., Tin S. Nickel-Based Superalloys for Advanced Turbine Engines: Chemistry, Microstructure and Properties. https://doi.org/10.2514/1.18239. American Institute of Aeronautics and Astronautics Inc.; 23 May 2012; 22(2): 361–374. Available at: DOI:10.2514/1.18239 (Accessed: 21 July 2022)

173. Sumner J., Potter A., Simms NJ., Oakey JE. Hot corrosion resistance of gas turbine materials in combusted syngas environments. 2015; 32: 177–187. Available at: DOI:10.1179/0960340914Z.00000000098

174. United Nations. Net Zero Coalition | United Nations. Available at: https://www.un.org/en/climatechange/net-zero-coalition (Accessed: 12 October 2023)

175. Pollock TM., Tin S. Nickel-Based Superalloys for Advanced Turbine Engines: Chemistry, Microstructure and Properties. https://doi.org/10.2514/1.18239. American Institute of Aeronautics and Astronautics Inc.; 23 May 2012; 22(2): 361–374. Available at: DOI:10.2514/1.18239 (Accessed: 8 December 2023)

176. Leary M., Mazur M., Williams H., Yang E., Alghamdi A., Lozanovski B., et al. Inconel 625 lattice structures manufactured by selective laser melting (SLM): Mechanical properties, deformation and failure modes. Materials & Design. Elsevier; 5 November 2018; 157: 179–199. Available at: DOI:10.1016/J.MATDES.2018.06.010 (Accessed: 12 October 2023)

177. Shankar V., Bhanu Sankara Rao K., Mannan SL. Microstructure and mechanical properties of Inconel 625 superalloy. Journal of Nuclear Materials. North-Holland; 1 February 2001; 288(2–3): 222–232. Available at: DOI:10.1016/S0022-3115(00)00723-6 (Accessed: 4 October 2023)

178. De Luca A., Kenel C., Griffiths S., Joglekar SS., Leinenbach C., Dunand DC. Microstructure and defects in a Ni-Cr-Al-Ti γ/γ’ model superalloy processed by laser powder bed fusion. Materials & Design. Elsevier; 1 March 2021; 201: 109531. Available at: DOI:10.1016/J.MATDES.2021.109531 (Accessed: 9 January 2023)

179. Oleksak RP., Carney CS., Teeter L., Doğan ÖN., Oleksak RichardOleksak RP. Oxidation Behavior of Welded Fe-Based and Ni-Based Alloys in Supercritical CO 2. Oxidation of Metals. 2022; 97: 123–139. Available at: DOI:10.1007/s11085-021-10080-5 (Accessed: 7 December 2022)

180. Andersson JH. Weldability of Precipitation Hardening Superalloys – Influence of Microstructure. Sweden; 2011. Available at: https://research.chalmers.se/en/publication/140316 (Accessed: 23 June 2025)

181. Floreen S., Fuchs GE., Yang WJ. The Metallurgy of Alloy 625. Superalloys. The Minerals, Metals and Materials Society; 28 August 1994;

718(625): 13–37. Available at: DOI:10.7449/1994/superalloys_1994_13_37 (Accessed: 16 October 2023)

182. Liu G., Zhang X., Chen X., He Y., Cheng L., Huo M., et al. Additive manufacturing of structural materials. Materials Science and Engineering: R: Reports. Elsevier; 1 July 2021; 145: 100596. Available at: DOI:10.1016/J.MSER.2020.100596 (Accessed: 8 August 2023)

183. Statista. Global 3D Printing Industry Market Size. 2022. Available at: https://www.statista.com/statistics/315386/global-market-for-3d-printers/ (Accessed: 23 November 2023)

184. Calderon L., Wang W., Valentin R., Mingareev I., Richardson M., Kapat J. Characterization of Laser Additive Manufacturing-Fabricated Porous Superalloys for Turbine Components. 2017; Available at: DOI:10.1115/1.4035560 (Accessed: 26 February 2024)

185. Frazier WE. Metal additive manufacturing: A review. Journal of Materials Engineering and Performance. Springer New York LLC; 8 April 2014; 23(6): 1917–1928. Available at: DOI:10.1007/S11665-014-0958-Z/FIGURES/9 (Accessed: 16 February 2023)

186. Xu J., Kontis P., Lin Peng R., Moverare J. Modelling of additive manufacturability of nickel-based superalloys for laser powder b e d fusion. Acta Materialia. 2022; 240: 118307. Available at: DOI:10.1016/j.actamat.2022.118307 (Accessed: 24 August 2023)

187. Cieslak MJ., Headley TJ., Kollie T., Romig AD. Melting and solidification study of Alloy 625. Metallurgical transactions. A, Physical metallurgy and materials science. Springer; 1988; 19 A(9): 2319–2331. Available at: DOI:10.1007/BF02645056/METRICS (Accessed: 9 May 2025)

188. Zhao R., Zhao Z., Bai P., Du W., Zhang L., Qu H. Effect of Heat Treatment on the Microstructure and Properties of Inconel 718 Alloy Fabricated by Selective Laser Melting. Journal of Materials Engineering

and Performance. Springer; 1 January 2022; 31(1): 353–364. Available at: DOI:10.1007/s11665-021-06212-2

189. Gu DD., Meiners W., Wissenbach K., Poprawe R. Laser additive manufacturing of metallic components: Materials, processes and mechanisms. International Materials Reviews. Maney Publishing; 2012. pp. 133–164. Available at: DOI:10.1179/1743280411Y.0000000014

190. Han JW., Jung SH., Cho H., Lee HW. Investigation of the Weld Properties of Inconel 625 based on Nb Content. International Journal of Electrochemical Science. Elsevier; 1 March 2018; 13(3): 2829–2841. Available at: DOI:10.20964/2018.03.01 (Accessed: 13 October 2023)

191. Catchpole-Smith S., Aboulkhair N., Parry L., Tuck C., Ashcroft IA., Clare A. Fractal scan strategies for selective laser melting of ‘unweldable’ nickel superalloys. Additive Manufacturing. Elsevier; 1 May 2017; 15: 113–122. Available at: DOI:10.1016/J.ADDMA.2017.02.002 (Accessed: 6 October 2023)

192. Paolini A., Kollmannsberger S., Rank E. Additive manufacturing in construction: A review on processes, applications, and digital planning methods. Additive Manufacturing. Elsevier; 1 December 2019; 30: 100894. Available at: DOI:10.1016/J.ADDMA.2019.100894 (Accessed: 4 October 2023)

193. Ataee A., Li Y., Brandt M., Wen C. Ultrahigh-strength titanium gyroid scaffolds manufactured by selective laser melting (SLM) for bone implant applications. Acta Materialia. Pergamon; 1 October 2018; 158: 354–368. Available at: DOI:10.1016/J.ACTAMAT.2018.08.005 (Accessed: 27 October 2023)

194. Wohlers. Wohlers Report: Additive Manufacturing and 3D Printing State of the Industry. 2013.

195. Wang Y., Guo W., Zheng H., Xie Y., Zhang X., Li H., et al. Microstructure, crack formation and improvement on Nickel-based superalloy fabricated

by powder bed fusion. Journal of Alloys and Compounds. Elsevier; 5 November 2023; 962: 171151. Available at: DOI:10.1016/J.JALLCOM.2023.171151 (Accessed: 16 October 2023)

196. Gruber K., Stopyra W., Kobiela K., Madejski B., Malicki M., Kurzynowski T. Mechanical properties of Inconel 718 additively manufactured by laser powder bed fusion after industrial high-temperature heat treatment. Journal of Manufacturing Processes. Elsevier; 1 January 2022; 73: 642–659. Available at: DOI:10.1016/J.JMAPRO.2021.11.053 (Accessed: 6 December 2024)

197. Li C., White R., Fang XY., Weaver M., Guo YB. Microstructure evolution characteristics of Inconel 625 alloy from selective laser melting to heat treatment. Materials Science and Engineering: A. Elsevier; 29 September 2017; 705: 20–31. Available at: DOI:10.1016/J.MSEA.2017.08.058 (Accessed: 7 May 2024)

198. Tian Z., Zhang C., Wang D., Liu W., Fang X., Wellmann D., et al. A Review on Laser Powder Bed Fusion of Inconel 625 Nickel-Based Alloy. Applied Sciences 2020, Vol. 10, Page 81. Multidisciplinary Digital Publishing Institute; 20 December 2019; 10(1): 81. Available at: DOI:10.3390/APP10010081 (Accessed: 8 December 2023)

199. Chyrkin A., Nowak WJ., Gunduz KO., Fedorova I., Sattari M., Froitzheim J., et al. Intergranular oxidation of additively manufactured Ni-base alloy 625: The role of Si. Corrosion Science. Pergamon; 15 July 2023; 219: 111234. Available at: DOI:10.1016/J.CORSCI.2023.111234 (Accessed: 3 October 2023)

200. Chowdhury S., Yadaiah N., Prakash C., Ramakrishna S., Dixit S., Gupta LR., et al. Laser powder bed fusion: a state-of-the-art review of the technology, materials, properties & defects, and numerical modelling. Journal of Materials Research and Technology. Elsevier Editora Ltda; 2022. pp. 2109–2172. Available at: DOI:10.1016/j.jmrt.2022.07.121

201. Lewis ER., Taylor MP., Attard B., Cruchley N., Morrison APC., Attallah MM., et al. Microstructural characterisation and high-temperature oxidation of laser powder bed fusion processed Inconel 625. Materials Letters. North-Holland; 15 March 2022; 311: 131582. Available at: DOI:10.1016/J.MATLET.2021.131582 (Accessed: 12 October 2023)

202. Karmuhilan M., Kumanan S. A Review on Additive Manufacturing Processes of Inconel 625. Journal of Materials Engineering and Performance. Springer; 1 April 2022; 31(4): 2583–2592. Available at: DOI:10.1007/S11665-021-06427-3/TABLES/5 (Accessed: 9 October 2023)

203. Parizia S., Marchese G., Rashidi M., Lorusso M., Hryha E., Manfredi D., et al. Effect of heat treatment on microstructure and oxidation properties of Inconel 625 processed by LPBF. Journal of Alloys and Compounds. Elsevier; 15 December 2020; 846: 156418. Available at: DOI:10.1016/J.JALLCOM.2020.156418 (Accessed: 12 October 2023)

204. Smialek J. Origins of a Low-Sulfur Superalloy Al2O3 Scale Adhesion Map. Crystals 2021, Vol. 11, Page 60. Multidisciplinary Digital Publishing Institute; 13 January 2021; 11(1): 60. Available at: DOI:10.3390/CRYST11010060 (Accessed: 5 October 2023)

205. Edwards P., Ramulu M. Fatigue performance evaluation of selective laser melted Ti–6Al–4V. Materials Science and Engineering: A. Elsevier; 26 March 2014; 598: 327–337. Available at: DOI:10.1016/J.MSEA.2014.01.041 (Accessed: 26 October 2023)

206. Jinoop AN., Paul CP., Bindra KS. Laser-assisted directed energy deposition of nickel super alloys: A review. Available at: DOI:10.1177/1464420719852658 (Accessed: 9 August 2024)

207. Nguejio J., Szmytka F., Hallais S., Tanguy A., Nardone S., Godino Martinez M. Comparison of microstructure features and mechanical properties for additive manufactured and wrought nickel alloys 625. Materials Science and Engineering: A. Elsevier; 9 September 2019; 764:

138214. Available at: DOI:10.1016/J.MSEA.2019.138214 (Accessed: 9 August 2024)

208. de Leon Nope G., Wang G., Alvarado-Orozco JM., Gleeson B., de Leon Nope G., Wang G., et al. Role of Elemental Segregation on the Oxidation Behavior of Additively Manufactured Alloy 625. JOM. Springer; 2022; 74(4): 1698–1706. Available at: DOI:10.1007/S11837-022-05200-8 (Accessed: 9 August 2024)

209. Sanviemvongsak T., Monceau D., Macquaire B. High temperature oxidation of IN 718 manufactured by laser beam melting and electron beam melting: Effect of surface topography. Corrosion Science. Pergamon; 15 August 2018; 141: 127–145. Available at: DOI:10.1016/J.CORSCI.2018.07.005 (Accessed: 9 August 2024)

210. Ramenatte N., Vernouillet A., Mathieu S., Vande Put A., Vilasi M., Monceau D. A comparison of the high-temperature oxidation behaviour of conventional wrought and laser beam melted Inconel 625. Corrosion Science. Pergamon; 1 March 2020; 164: 108347. Available at: DOI:10.1016/J.CORSCI.2019.108347 (Accessed: 27 November 2024)

211. Sames WJ., List FA., Pannala S., Dehoff RR., Babu SS. The metallurgy and processing science of metal additive manufacturing. International Materials Reviews. Taylor & Francis; 2016; 61(5): 315–360. Available at: DOI:10.1080/09506608.2015.1116649 (Accessed: 9 August 2024)

212. Zhao R., Zhao Z., Bai P., Du W., Zhang L., Qu H. Effect of Heat Treatment on the Microstructure and Properties of Inconel 718 Alloy Fabricated by Selective Laser Melting. Journal of Materials Engineering and Performance. Springer; 1 January 2022; 31(1): 353–364. Available at: DOI:10.1007/s11665-021-06212-2

213. Marchese G., Lorusso M., Parizia S., Bassini E., Lee JW., Calignano F., et al. Influence of heat treatments on microstructure evolution and mechanical properties of Inconel 625 processed by laser powder bed fusion. Materials Science and Engineering: A. Elsevier; 27 June 2018;

729: 64–75. Available at: DOI:10.1016/J.MSEA.2018.05.044 (Accessed: 9 August 2024)

214. Parizia S., Marchese G., Rashidi M., Lorusso M., Hryha E., Manfredi D., et al. Effect of heat treatment on microstructure and oxidation properties of Inconel 625 processed by LPBF. Journal of Alloys and Compounds. Elsevier; 15 December 2020; 846: 156418. Available at: DOI:10.1016/J.JALLCOM.2020.156418 (Accessed: 9 August 2024)

215. Bricknell RH., Woodford DA. The mechanism of cavity formation during high temperature oxidation of nickel. Acta Metallurgica. Pergamon; 1 January 1982; 30(1): 257–264. Available at: DOI:10.1016/0001-6160(82)90064-5 (Accessed: 26 October 2023)

216. Sundararaman M., Mukhopadhyay P., Banerjee S. Carbide Precipitation in Nickel Base Superalloys 718 and 625 and Their Effect on Mechanical Properties. The Minerals, Metals and Materials Society; 28 August 2012; : 367–378. Available at: DOI:10.7449/1997/SUPERALLOYS_1997_367_378 (Accessed: 28 November 2024)

217. Xuebing H., Yan K., Huihua Z., Yun Z., Zhuangqi H. Influence of heat treatment on the microstructure of a unidirectional Ni-base superalloy. Materials Letters. North-Holland; 1 July 1998; 36(1–4): 210–213. Available at: DOI:10.1016/S0167-577X(98)00028-7 (Accessed: 16 October 2023)

218. White MT., Bianchi G., Chai L., Tassou SA., Sayma AI. Review of supercritical CO2 technologies and systems for power generation. Applied Thermal Engineering. Pergamon; 25 February 2021; 185: 116447. Available at: DOI:10.1016/J.APPLTHERMALENG.2020.116447 (Accessed: 12 October 2022)

219. Pint BA., Keiser JR. The effect of impurities of oxidation in supercritical CO 2 at 750C . The 6th international symposium - supercritical CO2 power cycles. Pittsburgh; 2018. Available at:

https://sco2symposium.com/papers2018/materials/008_Paper.pdf (Accessed: 16 November 2022)

220. Oleksak RP., Holcomb GR., Carney CS., Teeter L., Doğan ÖN. Effect of Surface Finish on High-Temperature Oxidation of Steels in CO2, Supercritical CO2, and Air. Oxidation of Metals. Springer New York LLC; 1 December 2019; 92(5–6): 525–540. Available at: DOI:10.1007/S11085-019-09938-6/FIGURES/8 (Accessed: 24 January 2023)

221. Oleksak RP., Rouillard F. Materials Performance in CO2 and Supercritical CO2. Comprehensive Nuclear Materials: Second Edition. Elsevier; 1 January 2020; : 422–451. Available at: DOI:10.1016/B978-0-12-803581-8.11622-4 (Accessed: 6 March 2025)

222. Shankar V., Valsan M., Rao KBS., Mannan SL. Effects of temperature and strain rate on tensile properties and activation energy for dynamic strain aging in alloy 625. Metallurgical and Materials Transactions A: Physical Metallurgy and Materials Science. Minerals, Metals and Materials Society; 2004; 35 A(10): 3129–3139. Available at: DOI:10.1007/S11661-004-0057-0/METRICS (Accessed: 10 April 2024)

223. INCONEL ® alloy 625. Available at: www.specialmetals.com (Accessed: 1 March 2024)

224. Berman B. 3-D printing: The new industrial revolution. Business Horizons. Elsevier; 1 March 2012; 55(2): 155–162. Available at: DOI:10.1016/J.BUSHOR.2011.11.003 (Accessed: 20 March 2024)

225. Status of additive manufacturing for gas turbine components | Laser Focus World. Available at: https://www.laserfocusworld.com/industrial-laser-solutions/article/14221303/status-of-additive-manufacturing-for-gas-turbine-components (Accessed: 20 March 2024)

226. Carter LN., Wang X., Read N., Khan R., Aristizabal M., Essa K., et al. Process optimisation of selective laser melting using energy density model for nickel based superalloys. Materials Science and Technology

(United Kingdom). Taylor and Francis Ltd.; 21 June 2016; 32(7): 657–661. Available at: DOI:10.1179/1743284715Y.0000000108 (Accessed: 1 March 2024)

227. Sudbrack CK., Beckett DL., MacKay RA. Effect of Surface Preparation on the 815°C Oxidation of Single-Crystal Nickel-Based Superalloys. JOM. Minerals, Metals and Materials Society; 23 September 2015; 67(11): 2589–2598. Available at: DOI:10.1007/S11837-015-1639-6/TABLES/4 (Accessed: 17 April 2024)

228. Tolpygo VK., Clarke DR. Materials at High Temperatures Microstructural study of the theta-alpha transformation in alumina scales formed on nickel-aluminides. Materials at High Temperatures. 2000; 17(1): 59–70. Available at: DOI:10.1179/mht.2000.011 (Accessed: 16 April 2024)

229. Uran S., Veal B., Grimsditch M., Pearson J., Berger A. Effect of Surface Roughness on Oxidation: Changes in Scale Thickness, Composition, and Residual Stress. Oxidation of Metals. 2000; 54.

230. Leistikow S., Wolf I., Grabke HJ. Effects of cold work on the oxidation behavior and carburization resistance of Alloy 800. Materials and Corrosion. John Wiley & Sons, Ltd; 1 October 1987; 38(10): 556–562. Available at: DOI:10.1002/MACO.19870381003 (Accessed: 7 May 2024)

231. Serafin D., Nowak WJ., Wierzba B. The effect of surface preparation on high temperature oxidation of Ni, Cu and Ni-Cu alloy. Applied Surface Science. Elsevier B.V.; May 2019; 476: 442–451. Available at: DOI:10.1016/j.apsusc.2019.01.122

232. Nowak WJ., Siemek K., Ochał K., Kościelniak B., Wierzba B. Consequences of Different Mechanical Surface Preparation of Ni-Base Alloys during High Temperature Oxidation. Materials. Multidisciplinary Digital Publishing Institute (MDPI); 1 August 2020; 13(16). Available at: DOI:10.3390/MA13163529 (Accessed: 16 April 2024)

233. Allam RJ., Fetvedt JE., Forrest BA., Freed DA. The Oxy-Fuel, Supercritical CO2 Allam Cycle: New Cycle Developments to Produce Even Lower-Cost Electricity From Fossil Fuels Without Atmospheric Emissions. Proceedings of the ASME Turbo Expo. American Society of Mechanical Engineers Digital Collection; 18 September 2014; 3B. Available at: DOI:10.1115/GT2014-26952 (Accessed: 30 September 2022)

234. Allam R., Martin S., Forrest B., Fetvedt J., Lu X., Freed D., et al. Demonstration of the Allam Cycle: An Update on the Development Status of a High Efficiency Supercritical Carbon Dioxide Power Process Employing Full Carbon Capture. Energy Procedia. Elsevier; 1 July 2017; 114: 5948–5966. Available at: DOI:10.1016/J.EGYPRO.2017.03.1731 (Accessed: 17 November 2022)

235. Milewski J., Lis P., Szczęśniak A., Szabłowski Ł., Dybinski O., Futyma K. Prospects for the use of supercritical CO2 cycles. Journal of Power Technologies. 2021.

236. Molière M., Privat R., Jaubert J-N., Geiger F. Supercritical CO 2 Power Technology: Strengths but Challenges. 2024; Available at: DOI:10.3390/en17051129 (Accessed: 24 January 2025)

237. Allam R., Martin S., Forrest B., Fetvedt J., Lu X., Freed D., et al. Demonstration of the Allam Cycle: An Update on the Development Status of a High Efficiency Supercritical Carbon Dioxide Power Process Employing Full Carbon Capture. Energy Procedia. Elsevier Ltd; 2017; 114: 5948–5966. Available at: DOI:10.1016/J.EGYPRO.2017.03.1731 (Accessed: 26 September 2022)

238. Safari J., Nategh S. On the Heat Treatment of Rene-80 Nickel-base Superalloy. Journal of Materials Processing Technology. June 2006; 176: 240–250. Available at: DOI:10.1016/j.jmatprotec.2006.03.165

239. Neidel A., Riesenbeck S., Ullrich T., Völker J., Yao C. Hot cracking in the HAZ of laser-drilled turbine blades made from René 80.

Materialpruefung/Materials Testing. Carl Hanser Verlag; 2005. pp. 553–559. Available at: DOI:10.3139/120.100695

240. Pint., Bruce A. Both indirect-and direct-fired supercritical CO 2 (sCO 2) cycles for.

241. Beckman JP., Woodford DA. INTERGRANULAR SULFUR ATTACK IN NICKEL AND NICKEL-BASE ALLOYS. The Metallurgy Society . 1988;

242. Bricknell RH., Mulford RA., Woodford DA. ROLE OF SULFUR IN THE AIR EMBRITTLEMENT OF NICKEL AND ITS ALLOYS. Metallurgical transactions. A, Physical metallurgy and materials science. 1982; 13 A: 1223–1232. Available at: DOI:10.1007/BF02645505

243. Ikeda Y., Tosa M., Yoshihara K., Nii K. Adherence of Al2O3 coating layers to steels: The detrimental effect of sulphur and the beneficial effect of rare earth metals. Materials Science and Engineering A. November 1989; 120–121: 179–184. Available at: DOI:10.1016/0921-5093(89)90737-5

244. Krupp U., Christ H-J. InternalNitridationofNi-BasedAlloysduring High-Temperature Corrosion by Nitrogen. Available at: DOI:10.1002/(SICI)1527-2648(199912)1:3/4<194::AID-ADEM194>3.0.CO;2-N (Accessed: 31 March 2025)

245. Grabke HJ. Surface and interface segregation in the oxidation of metals. Surface and Interface Analysis. John Wiley & Sons Ltd; August 2000; 30: 112–119. Available at: DOI:10.1002/1096-9918(200008)30:1<112::AID-SIA777>3.0.CO;2-G

246. Oleksak RP., Tylczak JH., Holcomb GR., Doğan ÖN. High temperature oxidation of Ni alloys in CO2 containing impurities. Corrosion Science. Elsevier Ltd; August 2019; 157: 20–30. Available at: DOI:10.1016/j.corsci.2019.05.019

247. Nickel Institute. NICKEL ALLOY TOOL STEELS A PRACTICAL GUIDE TO THE USE OF NICKEL-CONTAINING ALLOYS N O 472. 2021. Available at: www.nickelinstitute.org (Accessed: 11 June 2025)

248. Giggins CS., Pettit FS. Corrosion of metals and alloys in mixed gas environments at elevated temperatures. Oxidation of Metals. Kluwer Academic Publishers-Plenum Publishers; October 1980; 14: 363–413. Available at: DOI:10.1007/BF00603609

249. Hancock P. The Influence of Nitrogen on the Oxidation of nickel-based Superalloys . Materials Science and Technology. 1987; 3(7): 546–541.

250. Leng W., Pillai R., Naumenko D., Galiullin T., Quadakkers WJ. Effect of substrate alloy composition on the oxidation behaviour and degradation of aluminide coatings on two Ni base superalloys. julic;

251. Krupp U., Christ HJ. Internal nitridation of nickel-base alloys. Part II. Behavior of quaternary Ni-Cr-Al-Ti alloys and computer-based description. Oxidation of Metals. Kluwer Academic/Plenum Publ Corp; 1999; 52: 299–320. Available at: DOI:10.1023/a:1018895628849

252. Wang YC., Mei QS., Zhang P., Yan JB., Ma Y., Liao LY., et al. Effect of nitrogen on the microstructure evolution and mechanical properties of Ni-Fe base superalloys during long-term thermal exposure. Materials Characterization. Elsevier Inc.; September 2023; 203. Available at: DOI:10.1016/j.matchar.2023.113058

253. Jiang R., Chen B., Hao X., Ma Y., Li S., Liu K. Micro-segregation and Precipitation of Alloy 690 during Isothermal Solidification: the Role of Nitrogen Content. Journal of Materials Science & Technology. Elsevier; 1 May 2012; 28(5): 446–452. Available at: DOI:10.1016/S1005-0302(12)60081-4 (Accessed: 26 June 2025)

254. Clarke DR., Levi CG. Materials design for the next generation thermal barrier coatings. Annual Review of Materials Research. 2003; 33: 383–417. Available at: DOI:10.1146/annurev.matsci.33.011403.113718

255. Faludi J., Bayley C., Bhogal S., Iribarne M. Comparing environmental impacts of additive manufacturing vs traditional machining via life-cycle assessment. Rapid Prototyping Journal. Emerald Group Publishing Ltd.; 19 January 2015; 21(1): 14–33. Available at: DOI:10.1108/RPJ-07-2013-0067

256. Marchese G., Bassini E., Aversa A., Lombardi M., Ugues D., Fino P., et al. Microstructural evolution of post-processed Hastelloy X alloy fabricated by laser powder bed fusion. Materials. MDPI AG; February 2019; 12. Available at: DOI:10.3390/ma12030486

257. Kopec M., Mierzejewska I., Gorniewicz D., Sitek R., Jóźwiak S. High-temperature oxidation behaviour of additively manufactured and wrought HAYNES 282. Journal of Materials Science. Springer; October 2024; 59: 17647–17665. Available at: DOI:10.1007/s10853-024-10207-4

Appendix A Ethical approval letter

Dear Phoebe

Reference: CURES/26124/2025
Project ID: 29629
Title: The degradation of gas turbine blade materials and additively manufactured Alloy 625 in high temperature CO2 environments

Thank you for your application to the Cranfield University Research Ethics System (CURES).

Your proposed research activity has been confirmed as Level 1 risk in terms of research ethics. Your letter of approval will be sent by email within 24 hours. If you do not receive this, please contact CURES Support.